SEAKEEPING BEHAVIOUR OF HIGH SPEED SHIPS

An experimental and numerical study

Pepijn de Jong

SEAKEEPING BEHAVIOUR OF HIGH SPEED SHIPS

An experimental and numerical study

PROEFSCHRIFT

ter verkrijging van de graad van doctor
aan de Technische Universiteit Delft,
op gezag van de Rector Magnificus Prof. ir. K.C.A.M. Luyben,
voorzitter van het College voor Promoties,
in het openbaar te verdedigen op dinsdag 11 oktober 2011 om 12.30 uur
door

Pepijn de JONG

scheepsbouwkundig ingenieur
geboren te Leeuwarden.

Dit proefschrift is goedgekeurd door de promotor:

Prof. dr. ir. R.H.M. Huijsmans

Samenstelling promotiecommissie:

Rector Magnificus	voorzitter
Prof. dr. ir. R.H.M. Huijsmans	Technische Universiteit Delft, promotor
Dr. ir. J.A. Keuning	Technische Universiteit Delft, copromotor
Prof. dr. M.R. Renilson	University of Tasmania
Prof. dr. P.A. Wilson	University of Southampton
Prof. dr. ir. H. Bijl	Technische Universiteit Delft
Prof. dr. ir. M.L. Kaminski	Technische Universiteit Delft
Dr. ir. F. van Walree	Maritime Research Institute Netherlands
Prof. dr. ir. T.J.C. van Terwisga	Technische Universiteit Delft, reservelid

The work presented in this thesis was carried out as part of the FAST research program, funded by:

United States Coast Guard	Baltimore, USA
Damen Shipyards High Speed Craft Department	Gorinchem, the Netherlands
Damen Schelde Naval Shipbuilding	Vlissingen, the Netherlands
Ministry of Defense	Den Haag, the Netherlands
Maritime Research Institute	Wageningen, the Netherlands

ISBN 978-94-6190-263-4

Copyright © 2011 by Pepijn de Jong.

All rights reserved.

Cover illustrations:

Front and bottom back: Dutch Coast Guard patrol vessel ‘Visarend’ experiencing a slam. These photos are reproduced with the kind permission of Damen Shipyards.
Top back: Computed pressure distribution on the hull of the same vessel.

Printed by Gildeprint drukkerijen, Enschede, The Netherlands

To my parents, Jan and Elly de Jong.

Table of symbols

Latin Letters

$\boldsymbol{A}$	Added mass matrix	kg,kgm^2	
a_z	Vertical acceleration level	m/s^2	
AR	Aspect ratio		
B_{wl}	Beam on waterline	m	
b_p	Linear roll damping coefficient	N/s	
b_{pp}	Quadratic roll damping coefficienty	N/s^2	
c	Chord	m	
C_b	Block coefficient		
C_d	Drag coefficient		
C_{di}	Induced drag coefficient		
C_{dv}	Cross flow drag coefficient		
C_l	Lift coefficient		
$C_{l\alpha}$	Lift curve slope	$1/deg$	
C_p	Pressure coefficient		
C_p	Prismatic coefficient (only chapter 2)		
dt	Time step	s	
$\boldsymbol{F}$	Force vector (generalised)	N,Nm	
F	Principal form of the time derivative of the free surface part of the Green function		
F_{hg}	Hypergeometric function, see Abramowitz and Stegun (1972, 15.1)		
Fn	Froude number based on ship length		
Fn_c	Froude number based on foil chord		
Fn_h	Froude number based on submergence depth		
Fn_{panel}	Froude number based on panel length		
G	Green function	m^2/s	
g	Gravity acceleration	m/s^2	
G^0	Rankine and biplane part of Green function	m^2/s	
G^f	Free surface part of Green function	m^2/s	
GM	Metacenter height	m	
$\boldsymbol{H}$	Angular momentum vector	kgm^2/s	
H	Wave height	m	$H = 2\zeta_a$
$H_{1/3}$	Significant wave height	m	
$\boldsymbol{i}$	Unit vector in x-direction		
i	Imaginary number or integer counter		
I_{xx}	Mass moment of inertia about x-axis	kgm^2	
$\boldsymbol{j}$	Unit vector in y-direction		
J_0	Bessel function of order zero		
$\boldsymbol{k}$	Unit vector in z-direction		
k	Wave number	rad/m	
$1+k$	Form factor		
KG	Height center of gravity above base	m	

K_p	Additional roll damping moment	Nm	
k_{yy}	Pitch radius of gyration	m	
L	Ship length	m	
L_{hist}	History length	m	
LCG	Longitidinal position center of gravity w.r.t. a.p.p.	m	
L_{pan}	Panel length	m	
LT	Leading term		
l_w	Body waterline intersection		
L_{wl}	Length waterline	m	
$\boldsymbol{M}$	Mass matrix	kg,kgm^2	
m	Mass	kg	
$\boldsymbol{n}$	Normal vector		
M	Number of spanwise panels		
N	Number of (chordwise) panels		
n	Normal direction		
N_{cut}	Number of cut-off history time steps		
N_{hist}	Number of history time steps		
p	Pressure	N/m^2	
$p\left(\boldsymbol{x}_0\right)$	Field or collocation point		
$P\left(x_a > a\right)$	Probability of exceedance of amplitude x_a over threshold value a		
P_l^ν	Legendre function of order ν, see Abramowitz and Stegun (1972, 8.4,8.5)		
p_d	Hydrodynamic pressure	N/m^2	
p_∞	Ambient pressure	N/m^2	
p_s	Hydrostatic pressure	N/m^2	
p_w	Incident wave pressure	N/m^2	
$q\left(\boldsymbol{\xi}\right)$	Source point		
$\boldsymbol{r}$	Body-fixed location of point on hull surface	m	
R	Absolute value distance source panel and collocation point	m	
R_0	Absolute value distance biplane source panel and collocation point	m	
Rn	Reynolds number		
R_v	Viscous resistance	N	
S	Fluid bounding surface		
S	Wetted area	m^2	
s	Span	m	
t	Foil thickness (only chapter 4)	m	
t	Time	s	
T_2	Wave spectrum zero crossing period	s	
T_{base}	Baseline draft	m	
t_{cut}	Cut-off history length measured in time	s	
t_{hist}	History length measured in time	s	
T_{max}	Maximum draft	m	
T_p	Wave spectrum peak period	s	
U	Constant forward ship speed	m/s	
$\boldsymbol{u}^0$	Induced velocities by Rankine and biplane terms	m/s	$\left[u^0, v^0, w^0\right]$
$\boldsymbol{u}^f$	Induced velocities by free surface memory terms	m/s	$\left[u^f, v^f, w^f\right]$
$\boldsymbol{V}$	Translational rigid body velocity	m/s	$[u, v, w]$
$\boldsymbol{v}$	Fluid velocity vector	m/s	
V	Fluid domain		
v_G	Induced velocity due to Green function influences	m/s	
V_N	Normal velocity on waterline	m/s	

v_w	Velocity due to incident waves	m/s	
$w(\boldsymbol{x}_0)$	Wake sheet point		
$\boldsymbol{x}$	Body-fixed spatial coordinates	m	$[x, y, z]$
$\boldsymbol{x}_0$	Space-fixed spatial coordinates	m	$[x_0, y_0, z_0]$
z_T	Transom immersion depth	m	

Greek Letters

α	Angle of attack	deg	
β	Non-dimensional temporal parameter (only chapter 4)		
$\boldsymbol{\delta}$	Instantaneous location body point	m	
ϵ	Infinitesimal distance	m	
ε	Numerical and/or truncation error		
$\varepsilon_{x\zeta}$	Phase angle of motion response x w.r.t. wave	deg	
Γ	Circulation strength	m^2/s	
Γ	Gamma function, see Gradshteyn and Ryzhik (1980, 8.31)		
γ	JONSWAP peak enhancement factor		
$\boldsymbol{\gamma}$	Vorticity vector	rad/s	
η	Free surface elevation	m	
η	Non-dimensional parameter (only chapter 4)		
$\boldsymbol{\eta}$	Body state vector	m, rad	
$\boldsymbol{\eta}_r$	Instantaneous rotation of body (Euler angles)	rad	$[\varphi, \theta, \psi]$
$\boldsymbol{\eta}_t$	Instantaneous location body origin	m	$[x_0, y_0, z_0]$
κ	Wave steepness ratio		$\kappa = H/\lambda$
λ	Non-dimensional parameter (only chapter 4)		
λ	Wave length	m	
μ	Doublet strength	m^2/s	
μ	Non-dimensional spatial parameter (only chapter 4)		
∇	Displacement of volume	m^3	
∇	Gradient operator		
ν	Kinematic viscosity	m^2/s	
ω	Wave frequency	rad/s	
$\boldsymbol{\Omega}$	Angular rigid body velocity	rad/s	$[p, q, r]$
Φ	Disturbance potential	m^2/s	
ϕ	Disturbance potential, steady part	m^2/s	
Φ_w	Wave potential	m^2/s	
Ψ	Total velocity potential	m^2/s	
ψ_w	Wave direction	rad	
ρ	Density	kg/m^3	
σ	Source strength (only chapters 3 and 4)	m/s	
σ	Standard deviation of a signal		
τ	Past time	s	
∇	Volume of displacement	m^3	
$\boldsymbol{\xi}$	Source location vector (space-fixed)	m	$[\xi, \eta, \zeta]$
ζ	Wave elevation	m	
ζ_a	Wave amplitude	m	

Subscripts

a	Amplitude of signal
ϵ	Infinitesimal surface
F	Fluid free surface

H	Submerged part of hull surface
∞	Bounding surface at infinity
i	Panel index
L	Surface of submerged lifting foils
S	Fluid bounding surface in integration
s	Steady force
u	Unsteady force
V	Fluid domain in integration
W	Wake sheet

Contents

Table of Symbols **i**

1 Introduction **1**
1.1 Historical background review 1
1.2 Review of computational methods for the seakeeping of ships 7
1.3 Research questions 14
1.4 Reading guide 16

2 Experimental Work and Criteria Development **17**
2.1 Introduction 17
2.2 Full scale measurements and criteria development 18
2.3 Model experiments 22
2.4 Discussion 61

3 Development of a Computational Model **63**
3.1 Introduction 63
3.2 Choice of computational model 64
3.3 Potential flow theory 65
3.4 Notation and sign conventions 67
3.5 Mathematical formulation 69
3.6 Numerical solution 75
3.7 Pressure evaluation approaches 88
3.8 Inclusion of viscous flow effects 99
3.9 Solution of the equations of motion 100

4 Numerical Aspects **103**
4.1 Introduction 103
4.2 Free surface Green function 104
4.3 Submerged foils 121
4.4 Transom flow model 137
4.5 Free surface elevation 151
4.6 Convergence study for seakeeping computations 162
4.7 Discussion 167

5 Validation **171**
5.1 Introduction . . . 171
5.2 Calm water trim and sinkage . . . 172
5.3 Regular head waves . . . 176
5.4 Irregular head waves . . . 190
5.5 Discussion . . . 199

6 Conclusions and Recommendations **201**
6.1 Introduction . . . 201
6.2 Limiting behaviour of high speed ships in waves . . . 201
6.3 Development, verification, and validation of a computational model . . . 203
6.4 Recommendations and future work . . . 205

Appendices

A Reynolds Transport Theorem **211**

B Time Derivatives in Moving Reference Frames **213**
B.1 Convective derivative . . . 213
B.2 Bernoulli equation in a moving reference frame . . . 213
B.3 Euler equations of motion . . . 214

C Potential Flow Details **219**
C.1 Elimination of the free surface integral . . . 219
C.2 Inspection of the waterline integral . . . 221

D Uncertainty Analysis **225**
D.1 Introduction . . . 225
D.2 Approach . . . 225
D.3 Elemental bias limits . . . 229
D.4 Elemental precision limits . . . 232
D.5 Uncertainty assessment . . . 234
D.6 Concluding remarks . . . 244

Bibliography **247**

Summary **257**

Samenvatting **261**

Acknowledgements **265**

Curriculum Vitae **267**

Chapter 1

Introduction

1.1 Historical background review

The appearance of torpedo boats around 1870 marks the dawn of high speed ships. The torpedo boat type of ship followed the invention of the torpedo in 1860 by Giovanni Luppis of Austria-Hungary. Because torpedo boats were relatively cheap, naval forces could purchase dozens instead of one large battleship. Moreover, the torpedo boats could easily outrun and outmanoeuvre the heavily armoured battleships of the time and their slow firing guns. They could deliver substantial damage with their torpedoes. In the late 19^{th} century steam engine powered torpedo boats of 30 to 50 m in length appeared in many navies, sailing at 20 to 30 knots. The first torpedo boat capable of launching self-propelled torpedoes was the HMS Lightning, launched in 1877 by the United Kingdom.

The threat that torpedo boats posed resulted in the birth of a larger type of fast ship to counter them, initially known as torpedo boat destroyer. Early torpedo boat destroyers were severely hindered by the weight of the steam engine resulting in ineffectively slow speeds and under-armament. A key factor in the successful development of this type of ship was yet another invention, the steam turbine, by Sir Charles Parsons in 1884. The capabilities of this new power plant were demonstrated with the infamous unauthorised show of the Turbinia at the Spithead Navy Review of 1897. It was conceived by Parsons and capable of reaching speeds of 34 knots. The lighter and powerful steam turbine engine provided high power at a significantly improved power to weight ratio, enabling higher speeds for the relatively small torpedo boat destroyers. By 1910 the steam turbine was widely adopted for use in fast naval vessels.

Both types, the torpedo boat and the destroyer, significantly evolved during and in between both World Wars. The introduction of the internal combustion engine lead to a smaller and much faster torpedo boat, the Motor Torpedo Boat (MTB) in the United Kingdom (figure 1.1(a)), of 15 to 30 m length sailing at 30 to 50 knots. In the United States it was known as the PT-boat and as the S-boote in Germany. The final class of MTBs used by the UK was the 100 ft, 100 ton Brave class, commissioned in 1958, capable of cruise speeds in excess of 40 knots and a maximum speed of 52 knots.

The destroyer was essentially an escort providing protection against torpedo boats and later against submarines and aircraft. Initially it was a fast displacement ship, operating at high speeds to be able to keep up with the small fast torpedo boats. Figure 1.1(b) shows a typical World War II era destroyer, length 114 m, displacement 2500 ton, capable of 36.5 knots. With the introduction of guided missile technology in the early 1960s the necessity



(a) MTB 5 of the Royal Navy



(b) Destroyer USS Fletcher under way at sea, circa 1960

Figure 1.1: *Military application of high speed ships*[1]

to keep up with the now obsolete fast motor torpedo boats vanished. The design speed of most destroyers was reduced from 35 to 40 knots in 1945 to maximum 30 knots currently, depending on their role. After World War II the displacement of destroyers significantly increased due to the addition of anti-submarine warfare and guided missile systems, radar and sonar equipment, and more recently cruise missiles. Ever since, frigates and corvettes have filled the gap at the lower end of the displacement range.

On the topic of research, up to the end of the 1960s research and design optimisation for high speed monohulls was mainly restricted to calm water resistance and stability (Savitsky 1968). Before the 1960s extensive research was published regarding the planing characteristics of prismatic hulls as well as systematic hull form series (Sottorf 1932, Savitsky 1964, Clement and Blount 1963). In spite of this, no sufficiently systematic research was performed to gain understanding of the seakeeping characteristics of high speed and planing craft. In reaction to this gap, noteworthy work has been carried out by Van den Bosch (1970), Fridsma (1969; 1971), Martin (1978) amongst others. Van den Bosch noted the importance of the deadrise angle for the seakeeping behaviour. Fridsma was the first to carry out extensive systematic model tests in regular and irregular waves with planing monohulls, and noted that motions responses and accelerations were strongly non-linearly related to the wave height. Martin (1978) also concluded that non-linear effects in the motion responses were strong at high speeds. Finding an acceptable seakeeping behaviour for planing monohulls proved to be a difficult task as planing hulls with their low deadrise angles suffer from large peaks in their vertical accelerations. Savitsky and Brown (1976) summarised the research into planing craft performed in previous years in the Davidson Laboratory. They published empirical formulations for use by designers of fast monohulls, forming the state-of-art used in the design community for high speed craft ever since.

Blok and Beukelman (1984) noted in their paper that seakeeping predictions in the 1980s finally enabled the designer not only to estimate the motion behaviour of fast ships at sea but

[1] Left: Photo No. A 55 from the Imperial War Museum collection No. 4700-01. This artistic work created by the United Kingdom Government is in the public domain. Right: Photo No. NH 68912 from Naval Historical Center. As a work of the U.S. federal government, the image is in the public domain.

also to improve upon it. They also noted, like Savitsky previously, that until then seakeeping of ships was still often looked upon as a field where improvement was difficult to achieve: 'ships do move anyway'. Instead, typically optimisation was sought in low resistance and high speed in calm water (Keuning 1994).

The new focus on seakeeping behaviour came with the realisation that almost all operations with ships at sea are limited by motion levels aboard the vessels used. Optimising for high speed in calm water does not necessarily result in a high speed in increasingly severe waves. Although the systematic research into smooth water behaviour of high speed craft continued throughout the 1980s (Keuning and Gerritsma 1982, Keuning et al. 1993) comfort, operability, and safety became important research and optimisation topics for high speed operations both in civilian and naval settings. As an example, Blok and Roeloffs (1989) reported on the influence on the section shape near the bow on the calm water performance and the motion response and accelerations in waves.

The search for more economical viable solutions to provide a better ride for passengers and crew led to new advanced design concepts for high speed craft. Besides fast displacement and planing monohulls, hydrofoil craft were the first of the advanced concepts to make commercial sense (Trillo 1991). The early beginnings of hydrofoil craft can be probably traced back to 1891, when Count de Lambert tested a foil assisted craft on the Seine, soon followed by Thornycroft in England. The first commercial service was on Lake Maggiore between Italy and Switzerland in 1953 with a hydrofoil boat launched by Supramar and Rodriguez (Meyer and Wilkens Jr. 1992). In 1975 the Boeing Jetfoil proved that also hydrofoil craft were able to provide an economical and fast travel and a comfortable ride. The hydrofoil craft was followed by the commercially less successful hovercraft in around 1959, the Surface Effect Ship appeared in 1960. Lavis (1992) provides an excellent overview of the development history of the hovercraft and the SES. The hovercraft was invented by Christopher Cockerell; the first commercial prototype launched in England in 1959. Both concepts, the hydrofoil and the air cushion vehicle, had their limitations especially with respect to motion behaviour in waves -seakeeping was not the main drive behind their development- and economical efficiency as well as technical complexity.

In particular the introduction of the catamaran in the 1970s lead to a boost in the application of high speed ferries. The Small Waterplane Area Twin Hull (SWATH) concept is a derivative of the catamaran, optimised for a reduction in the wave exciting force in the heave and pitch modes. It features an improved ride quality in especially head seas at the cost of a relatively complex structural design and the need for an extensive ride control system as these ships tend to suffer from longitudinal or pitch instability. When the Iron Curtain fell in 1989 yet another alternative came into view: the Wing In Ground vehicle or Ekranoplan. Although not new and not exclusively researched in Russia, soviet engineers managed to apply the WIG concept on an unexpected and unprecedented scale.

Figure 1.2 shows a schematic representation of the design alternatives for high speed craft. At the start of the 1990s a plethora of concepts for fast sea transportation was available as well as tools to study their merits, this is easily demonstrated by studying the contents of the FAST'91 conference and the overview paper of Trillo (1991) presented at the same conference. There seemed to be a large uncertainty as to the arguments to be used to choose the right concept for the right purpose.

Generally, these advanced concepts are designed to minimise the resistance by minimizing the volume of displacement and wetted surface or both (Keuning and Van Walree 2006).

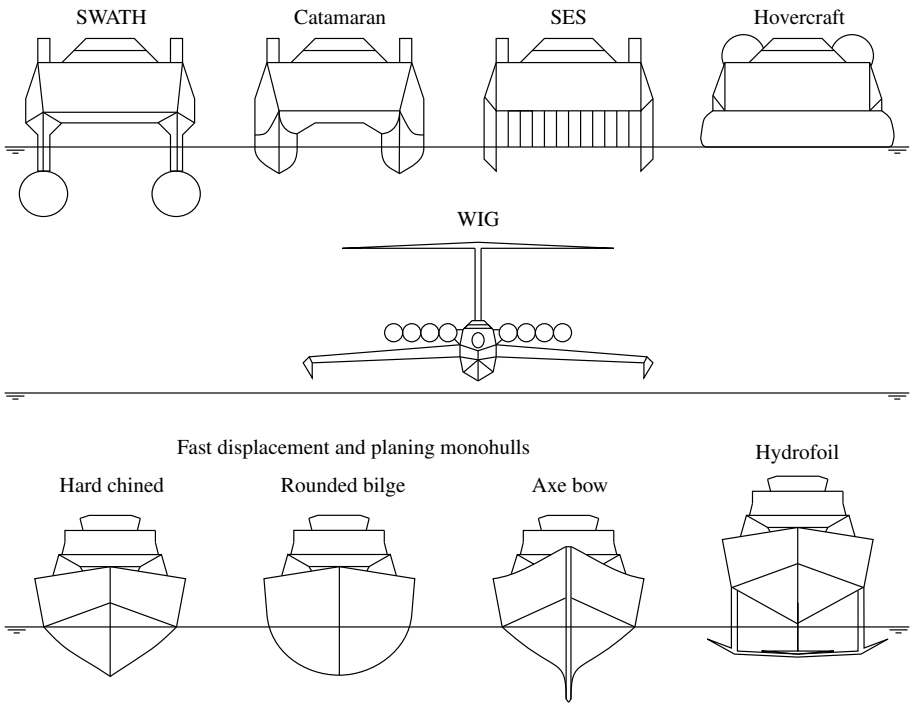


Figure 1.2: *High speed craft concepts, partly based on Keuning (1994).*

A secondary effort is made to minimise the motion response by either reducing the wave excitation or by adding motion control devices. Blok and Beukelman (1984), when selecting a base design for their high speed displacement ship hull forms (FDS) noted that the advanced concepts still only provided advantages over slender high speed displacement monohulls when the sea does not get too rough. Hydrofoils, whether operating in platforming or in contouring modes are restricted to mild weather conditions. For air cushion vehicles, maintaining the air cushion proves to be difficult if not impossible in severe sea states. SWATHs rely heavily on control surfaces to limit their motions and need to maintain enough clearance between the deck and the waves. This last point is also valid for catamarans and trimarans, and moreover multihulls are known to suffer from poor motion behaviour in beam and following seas. These advanced concepts rely on far more complex systems, resulting in a considerably higher construction and operational costs. For this reason many ship owners, in particular in military and patrol applications as well as in the offshore industry, tend to favour the much more simple and proven design of the fast monohull (Keuning 1994; 2006), whereas the high speed ferry market seems to favour large high speed multi-hulls (Armstrong 2009).

The focus on the seakeeping of high speed monohulls received another boost as these ships were increasingly employed in coastal waters and even open sea for patrol and offshore duties. Drawing on the lessons learned with the research from the 1970s on, new concepts for seaworthy high speed monohulls were developed. Keuning (2006) summarises the distinct



(a) Dutch coast guard patrol vessel Visarend, Damen Stan Patrol 4207



(b) Offshore crew supplier Silni, Damen Fast Crew Supplier 3507

Figure 1.3: *Enlarged Ship Concept (left) and Axe Bow Concept (right)*[2]

features of the behaviour of high speed monohulls in waves:

- The development of non-linear hydrodynamic lift on the hull.
- Non-linear wave exciting forces, particularly in the forward part of the hull.

From full scale observations it was concluded that speed reductions in waves mostly were voluntary applied by the crew, reacting on the motion response and accelerations that the ship was experiencing in the seaway. Usually, limiting criteria were (and often still are) set on significant motion responses and acceleration levels. For high speed monohulls, peaks in the vertical acceleration levels were identified as limiting (Keuning 1994). The identification of these peaks requires a different analysis that regards the non-linear behaviour of fast vessels in waves. The following determining parameters were identified for the seakeeping behaviour as well as the calm water resistance of high speed monohulls:

1. The above and below water geometry.
2. Length to beam ratio.
3. Length to displacement ratio.
4. The running attitude of the vessel.
5. The longitudinal ratio of gyration (only seakeeping0.

High speed ships operating in waves suffer from large relative motions and hence large submerged body variations. These same large relative motions (and velocities) are the root cause of the peaks in the vertical acceleration. They can partly be attributed to the relatively small ship length with respect to the wave length and height, but more importantly in head waves the peak of the motion response occurs at larger wave lengths (thus larger waves) due to the higher encounter frequency caused by the higher forward speed (Keuning 1994).

Application of this knowledge on the design and operability of a fast monohull led in 1995 to the introduction of the Enlarged Ship Concept (Keuning and Pinkster 1995) and subsequently the Axe Bow Concept in 2001 (Keuning et al. 2001), refer to figure 1.3. The philosophy behind the Enlarged Ship Concept and the Axe Bow Concept is summarised by Keuning (2006). He observed that in a large number of cases vessels were restricted in length

[2]Both photos are reproduced with the kind permission of Damen Shipyards Group.

due to a perceived linear relationship between length and building cost. Increasing the length by 20 to 50% while keeping the other main dimensions, displacement, and the functionality as constant as possible led to the introduction of void space in the design. This space was added in the bow region; moving the functional crew spaces aft where motion levels are naturally significantly reduced. The result was that the length to beam ratio and the length to displacement ratio were increased, a decrease of longitudinal radius of gyration, and a substantial increase of the deadrise angle in the bow region. The latter resulted in minimizing the wave exciting forces as well as the hydrodynamic lift in the bow region. The outcome is a much more 'linear' motion response with only a marginal increase of the building cost since only 'empty' hull was added to the design. It was concluded that operability in a North Sea environment improved with 35 to 50% compared to a non-optimised design. The design concept has been successfully applied on cutters of the Dutch coast guard (Keuning 2000) and on numerous other patrol vessels, among them 34 US Coast Guard cutters - the Sentinel class, the first is to be delivered in 2011.

The Axe Bow Concept (Keuning et al. 2001) featured a bow modification resulting in even more reduced non-linear hydrodynamic lift and wave exciting forces. The bow flare was completely removed resulting in nearly vertical sections in the bow region. The centreline sloped downward toward the bow, resulting in a maximum draft at the fore foot. This substantially tempered the occurrence of large peaks in the vertical accelerations and slamming. To maintain the same reserve buoyancy and pitch restoring moment the deck sheer was increased significantly towards the bow. Keuning (2006) emphasised that it was the void space of the Enlarged Ship Concept that enabled the radical shape change of the bow. The Axe Bow Concept showed another 40 to 50% improvement in operability compared to the Enlarged Ship Concept, a fact that has been confirmed by extensive model testing (Keuning and Van Walree 2006) that will be further elaborated in chapter 2 of this thesis. Since its introduction in the market in 2006, numerous fast monohulls according to the Axe Bow Concept have been sold, especially in the role of fast crew supplier.

Although the main focus of research into the seakeeping of high speed ships is the behaviour in head seas, also the limiting behaviour in stern-quartering and following waves is of importance for the operability of this type of vessels. The latter behaviour is characterised by the risk of bow-diving and the occurrence of broaching possibly followed by capsizing. Bow diving is the phenomenom that a ship sailing in stern-quartering and following waves plows or buries the bow in the water (Matsuda et al. 2004). This may lead to large amounts of green water on deck and in extreme cases to capsizing. The capsizing occurs at large pitch angles that may exceed 20 degrees associated with surf-riding. Broaching can be typified as a coupled yaw-roll instability and occurs mainly in following waves with a celerity close to the ship's Froude number (Umeda 2000, Spyrou 2000). Extreme cases can also cause a vessel to capsize.

Research is ongoing to further improve the Axe Bow Concept. The focus of this research is shifting toward motion control. One research line is directed at further reducing peaks in the vertical accelerations actively by using real-time motion prediction to control the vessel's speed and control surfaces, a process dubbed 'smart control' (Van Deyzen et al. 2011). Another research line is directed at controling the tendency to broach when sailing at speed in stern-quartering and following waves of fast ships in general (Keuning and Visch 2008; 2009). Keuning and Visch (2009) showed the successful application of a magnus rotor mounted under the bow as a bow rudder to improve the motion control in following waves. A

bow rudder generates a stabilizing rolling moment when countering a yaw motion, whereas a conventional rudder increases the rolling moment and consequently increasing the risk of a broach.

Typical of this new generation of fast monohulls is that they sail at relatively low speeds of about 30 knots. Their length typically is about 30 to 50 metres, leading to a Froude number of 0.7 to 0.9. Although at these speeds significant dynamic lift is generated carrying part of the ship's weight and resulting in a considerable change in running attitude, by no means these ships are fully planing. These ships are built of steel or aluminium or a combination of both, for instance a steel hull with a aluminium superstructure. They are more and more deployed further offshore in increasingly adverse weather conditions, setting greater demands on their hydrodynamic design to ensure a safe and comfortable environment for crew and passengers.

1.2 Review of computational methods for the seakeeping of ships

1.2.1 General seakeeping methods

Over the years numerous computational methods have been derived and applied to the problem of a ship advancing through waves. Earlier methods rely heavily on the assumption that the problem of ship moving in a seaway can be represented by a linear system, meaning that the motion response amplitudes are linearly related to the incoming wave amplitude. This assumption is only valid when assuming that the ship moves with infinitesimal motion amplitudes around its equilibrium position and that the incoming waves are only of very limited steepness. Applying this assumption, the motions in irregular waves can be computed by using the superposition principle for both waves as body motions, a procedure pioneered by St.Denis and Pierson (1953) in the field of marine engineering. This procedure results in the so-called frequency domain approach, where the incoming irregular waves are represented by series of sinusoidal waves of varying frequency and the response of the ship to each frequency is evaluated independently.

The first successful and widely adopted method using the assumption of linearity is the so-called linear strip theory. In strip theory the ship's hull is represented with a series of two-dimensional cross-sectional stations or strips on each of which the hydrodynamic forces are computed independently. It relies on an assumption of slenderness of the ship under consideration. The method was first successfully applied to a ship by Korvin-Kroukovski and Jacobs (1957) who presented a method for calculating heave and pitch motions of ship in regular waves. Their work used a series of building blocks reported as early as in 1896 by Krylov (1896) who pioneered the slender body approach, followed by work of Ursell (1957) who provided a method to compute added mass and damping forces on heaving cylinders and of Grim (1953) (and later Tasai (1959)) that generalised these results to arbitrary cross-sections. Gerritsma and Beukelman (1967), Ogilvie and Tuck (1969) and later Vugts (1970) and Salvesen et al. (1970) further refined and verified the strip theory method. The two-dimensional added mass and damping are either determined for a cylindrical shape and subsequently mapped to an arbitrary sectional shape or obtained by applying two-dimensional diffraction theory based on potential flow theory. In strip theory forward speed is taken into account by correcting the lengthwise distribution of added mass and damping.

Blok and Beukelman (1984) compared the outcome of linear strip theory calculations with the results of their experiments with the High Speed Displacement Hull Form Series. They found good correlation between the calculated and the measured motions for speeds up to Froude numbers of 1.14, pushing the linear strip theory far beyond its generally accepted limits. Keuning (1994) subsequently showed results of forced oscillation experiments with the parent of the same hull form series. He showed that although linear strip theory predicted the motions quite accurately, the predicted added mass and damping distributions showed large discrepancies with the measured added mass and damping distributions, especially at the higher Froude number of 1.14. Only for very high frequencies the comparison seemed reasonable. Keuning (1994) also showed that taking into account the actual running trim and sinkage could improve the distributions of added mass and damping significantly.

It is especially difficult for strip theory to cope with large asymmetrical motions such as roll, sway and yaw motions where three-dimensional flow with large longitudinal interactions between the steady and unsteady flow and the ship geometry becomes of importance. Yet, due to the fact that strip theory is remarkebly cheap in terms of computational effort and gives a reasonable estimate of the motion behaviour of ships in waves it is still widely used in the industry for a wide range of seakeeping applications.

Strip theory was followed by the linear frequency domain three-dimensional diffraction theory. This theory employs the same assumption of linearity and superposition principle as used in strip theory and is originally developed for computations of the motion response of offshore structures in waves. These structures are of similar dimensions in all directions, invalidating the slender body assumption behind strip theory and demanding a three-dimensional approach. Generally, use is made of boundary element methods were potential sources are distributed over the submerged geometry that is linearised to its calm water position. Another linearisation is used at the free surface condition that is linearised to the calm water free surface, allowing for the use of source influence functions (or Green function, Wehausen and Laitone (1960)) that automatically satisfy the linearised free surface condition. The latter eliminates the need for distributing sources over the free surface, dramatically improving the computational efficiency at the cost of much more complex influence functions and a less accurate description of the fluid dynamics, especially near the free surface. This method was pioneered amongst others by Faltinsen and Michelsen (1974), Hogben and Standing (1975), Guëvel et al. (1977) for zero forward speed cases, such as offshore structures, with substantial contributions by Noblesse (1982) and Newman (1984; 1985) to the efficient evaluation of the free surface Green function, highly important for the efficiency of the method.

The linear diffraction theory described above is limited to cases with zero forward speed. Including forward speed in linear frequency domain diffraction theory rigorously is not a straightforward task. Several authors have managed to adapt the method to include low forward speed or current velocities by expanding the integral equation and Green function around a current velocity based on the assumption that this velocity is small compared to the incident wave celerity (Inglis and Price 1982, Guëvel and Bougis 1982, Zhao et al. 1988, Huijsmans and Hermans 1989, Grue and Palm 1991). Yet, this approach is not satisfactory for ships travelling at much higher Froude numbers. Chang (1977), Inglis and Price (1980) and Beck and Loken (1989) have developed another approximate approach by employing the forward speed corrections borrowed from linear strip theory, as presented by Salvesen et al. (1970), combined with the zero-forward speed linear diffraction coefficients. Nevertheless the efforts of numerous authors to include the forward speed, the satisfactory inclusion of

forward speed is troublesome due to the complexity of the corresponding frequency domain Green function involved (Beck and Reed 2001).

To retain a free surface Green function eliminates the need to solve the boundary value problem on the free surface and by moving to the time domain an appropriate Green function can be formulated that retains a much more simple form despite the forward speed. Early efforts to formulate the corresponding initial value time domain diffraction problem are by Cummins (1962), who formulated the retardation function or memory integral, and Finklestein (1957), who derived the time domain solution for the Rankine singularity. This method leads to the so-called body-exact approach for large amplitude ship motions. In this approach the body boundary condition is satisfied on the exact body surface, whereas the free surface boundary condition is linearised to the calm water surface.

Although the computational effort needed is considerable compared to the linear frequency domain approach this time domain approach is able to deal with significant forward speed. King et al. (1988), following work of Liapis and Beck (1985) and Beck and Liapis (1987), have developed a method for linearised problem with forward speed, the so-called Neuman-Kelvin approach. This was later extended by Beck and Magee (1990) and Lin and Yue (1990) to problems with arbitrary large amplitude motions, while still retaining the linearised free surface condition. Lin and Yue (1990) achieve this by formulating the problem in a space-fixed reference frame and the concise implementation of an appropriate waterline integral. Bingham (1994) and Van Walree (2002) have developed similar methods. Van Walree (2002) in particular applied the method for a ship equipped with ride control systems to include the interaction of the ship and the control surfaces.

To reduce calculation time often the body-exact approach is traded for the body-linear approach and all involved authors (Beck and Magee 1990, Lin and Yue 1990, Bingham 1994, van Walree 2002) describe this process. This is done to substantially improve the calculation efficiency of the approach that in its body-exact form still requires the use of a supercomputer or at least a substantial capability for parallel computing. Although this body-linear approach retains its ability to deal with the presence of forward speed, it loses part of its validity for large amplitude motions.

Another approach, also founded on inviscid, potential flow theory, is based on the work of Dawson (1977). In this approach the potential flow is linearised around the steady double-body potential. This class of methods does not rely on a free surface Green function, but instead simple Rankine sources are distributed over the free surface and the body surface satisfying a quasi-linearised free surface condition at the free surface resulting from the double-body flow. Bertram (1990), Nakos et al. (1993) and Van 't Veer (1998) amongst others developed and applied methods based on Dawson's method to ship motions at forward speed. Pawlowski (1992) introduced the weak-scatterer hypothesis for double-body flow, assuming that the ship only weakly disturbs the steady and incident wave flows. He proposed to linearise the free surface boundary condition using the steady and incident wave potentials as a basis flow.

Blended methods, refer to for instance Finn et al. (2003), use a blend of any previously mentioned methods to obtain the hydrodynamic forces together with non-linear models for force components that are easily computed. The latter are usually the hydrostatic forces and the Froude-Krylov forces. Although often inconsistent in nature due to combining forces

obtained on different parts of the ship's geometry, blended methods do provide an engineering approach to the non-linear problem of wave loads and motions of ship in waves.

Finally, there are the fully non-linear potential flow methods, where both the body-exact and the fully non-linear free surface boundary conditions are solved. For steady problems a number of iterative boundary value methods have been developed (Jensen et al. 1989, Raven 1996), where each step solves a linearised problem based on the previous iteration leading to the full non-linear solution. These methods are very successful for the ship wave resistance problem. Bunnik (1999) proposed a seakeeping method taking into account the non-linear steady waves computed with the non-linear steady method presented by Raven (1996).

Another approach for unsteady problems, such as the seakeeping problem, are the Mixed Eulerian-Lagrangian methods (MEL), originating from the work of Longuet-Higgins and Cokelet (1976). This is a time stepping method where the free surface boundary condition is used to update the potential value and position of the free surface. At each time step a linear boundary value problem is solved in the Eulerian frame, subsequently the fully non-linear boundary conditions are used to update the Lagrangian points forming the boundaries of the problem. Mostly Rankine panel methods are used for the solution of this method. The method is highly dependent on advanced and accurate numerical schemes to remain stable. Two-dimensional problems have been investigated as early as 1977 by Faltinsen (1977), whereas three-dimensional problems are much more computationally demanding. Lin et al. (1984), Dommermuth and Yue (1987), Cao (1991) have obtained results for the three-dimensional case.

Table 1.1 provides an overview of the available potential flow methods for the ship motion problem and their linearisation in terms of potential decomposition and boundary conditions. The overview in the table is simplified and there are more methods available, often using a hybrid approach; borrowing and combining ideas and linearisations from a number of different methods. Additionally, choices can be made as to how to deal with hydrostatics and Froude-Krylov forces (the blended approach), as well as other methods of free surface linearisation (for instance the weak scatter assumption).

For the body-exact and fully non-linear methods the radiation and diffraction potentials are combined into one disturbance potential to reflect the fact that the diffraction problem is solved at the same time as the radiation potential on the instantaneous body surface. The free stream potential is added between brackets to the potential decomposition of the body-exact method to show that the mean forward speed, although solved for with the disturbance potential, in fact is treated as an independent motion component. When the body boundary condition of the body-exact method is linearised to the mean body position and orientation the method reduces to the Neumann-Kelvin method.

Finally, when using the steady double body basis flow, whether linear or non-linear, it is possible to solve the potential problem in the time-domain and to combine it with a body-exact approach. Most authors though, seem to favour the frequency domain approach with a linearised body boundary condition that is computationally much less demanding. Using non-linear steady double body flow, combined with a non-linear body boundary condition the solution methods starts to border on the fully non-linear solution.

Approach	Domain	Potential decomposition	Free surface boundary condition	Body boundary condition
Linear strip theory Linear diffraction	frequency	free stream diffraction radiation incident wave	linear	linear
Neumann-Kelvin	time	free stream diffraction radiation incident wave	linear	linear
Body-exact Large amplitude motions	time	(free stream) disturbance incident wave	linear	non-linear
Linear double body flow	frequency (time possible)	linear double body flow radiation diffraction incident wave	linear	linear (non-linear)
Non-linear double body flow	frequency (time possible)	non-linear double body flow radiation diffraction incident wave	mixed	linear (non-linear)
Fully non-linear	time	disturbance incident wave	non-linear	non-linear

Table 1.1: *Overview of potential flow methods for ship motion problems*

1.2.2 Seakeeping methods for planing craft

For planing craft a separate development of seakeeping methods has taken place over the years. In this development the planing of a vessel is compared to the problem of a two-dimensional wedge impacting on the water surface. The problem of two-dimensional wedges has been intensively studied starting with the pioneering works of von Karman (1929) and Wagner (1932), who studied the impact of the floats of landing seaplanes on the water surface. This led to a strip theory for planing vessels, also known as $2.5D$ or $2D + t$ theory.

First Martin (1978) based a linear semi-empirical strip theory for constant deadrise prisms in regular waves on the results of Wagner (1932) for constant deadrise impacting wedges. In this method no free surface deformations are taken into account except for a correction for pile-up, leading to very simple analytical formulations for the added mass coefficients and a very efficient method. Later Zarnick (1978) extended the method to a non-linear semi-empirical strip theory for planing constant deadrise prisms. Keuning (1994) further extended the basic model of Zarnick (1978) to variable deadrise hulls in irregular waves and added empirical formulations for the trim and sinkage based on model tests, in this way stretching the applicability of the method into a wider speed range.

Besides the non-linear strip theory for planing craft described above, several authors followed a more fundamental approach by solving two-dimensional impact of a wedge with potential flow boundary element methods with varying degrees of complexity in a follow-up on the work of Wagner (1932). Most of this work was based on potential flow assuming zero gravity; leading to a greatly simplified free surface condition.

The zero deadrise case of Wagner (amongst others) was extended to finite deadrise angles, arbitrary sectional shapes and the inclusion of the effect of spray plumes (Tulin 1957, Tulin and Hsu 1986, Zhao and Faltinsen 1993, Vorus 1996) to finally fully non-linear (zero-gravity) free surface conditions and flow separation (Zhao et al. 1996). Typically these methods are used either the slamming problem and for high-speed planing, the latter very often only in calm water. Garme (2005) used a combination of the semi-empirical non-linear strip theory of Zarnick and Keuning, combined with precomputed sectional hydrodynamic coefficients based on Tulin (1957) and Tulin and Hsu (1986) for planing craft in waves. This class of methods also is referred to as high frequency added mass methods.

Also three-dimensional methods have been developed for planing craft. Typically these methods rely as well on zero-gravity free surface boundary conditions and seek the analogy with the flow around a delta wing, that features leading edge separation similar to the flow around a planing vessel. Work has been done by Lai (1994) applying a three-dimensional vortex lattice method to the steady planing problem with special jet regions to treat the flow separation at the leading and the side edges. They applied a wake sheet at the transom edge to ensure smooth separation. No results of seakeeping simulations applying this method seem to have been published.

1.2.3 Transom flow

Modern high speed ships are in most cases fitted with a cut-off or transom stern. Besides some practical advantages, such as easier construction, more practical water jet installation, and larger and more practical shaped internal space, this design can offer significant hydrodynamic advantages, especially resistance reduction for particular hull configurations at

specific speed ranges (Maki et al. 2005a, Doctors et al. 2007). Additionally, transom flow is often linked to the increased motion damping high speed ships experience, especially for the pitch motion. For this reason transom flow can be an important flow feature that needs to be considered for successfully computing the wave resistance and motion behaviour of high speed ships.

Two distinct flow regimes can be observed near a transom, depending on its design and the forward speed of the ship: wetted and unwetted. In the case of a fully, or partly wetted (also known as partly ventilated) transom there exists a dead water region behind the transom. The recirculation flow in this region causes a reduction of the pressure, therefore the water level is a small distance below the surrounding water level (Starke et al. 2007).

The unwetted case is also known as fully ventilated or the dry-transom regime. At sufficient high forward speeds the water flow leaves the transom smoothly, cleanly separating from the transom, leaving the transom fully unwetted. In the case of an unwetted transom the presence of the free surface immediately behind the transom causes the pressure to drop to atmospheric pressure at the transom edge, whereas if the hull would continue smoothly at the transom the pressure would be significantly different and probably higher, dependent on the features of the hull design.

The pressure reduction towards the transom edge results in an upwards curved flow behind the transom, resulting in a wave crest behind the transom hollow. This wave crest increases in height when the transom immersion increases, as the pressure reduction increases, eventually resulting in a breaking wave behind the transom (Starke et al. 2007) also known as the ‘rooster tail’.

Guidelines for the speed where ventilation occurs were provided by Saunders (1957) for fully ventilated transom flow and later by Oving (1985) for partly ventilated transom sterns. Saunders stated that fully ventilated transom flow would occur at transom draft Froude numbers between 4 and 5. Oving related this ‘critical transom Froude number to the beam over draft ratio of the transom. More recent studies show a critical transom draft Froude number of 3 to 3.5 for naval surface combatants (Maki et al. 2005b). More detailed prediction methods employing empirical formulas based on experiments are presented by Maki et al. (2005a) for the unwetting of the transom and by Doctors and Day (1997) and Doctors et al. (2007) for the both the unwetting of the transom as prediction of the resistance.

Methods for computation of transom flow have evolved over time from fully non-linear two-dimensional locally applied potential flow models (Vanden-Broeck 1980, Scorpio and Beck 1997) to fully non-linear three-dimensional models describing the flow around the complete ship, such as developed by Raven (1998) for the wave making resistance. In more recent years also more detailed viscous CFD methods have been applied to prediction of transom flows, for example by Starke et al. (2007). As the hydrodynamic motive for using a transom stern mostly is dominated by the possibly advantageous resistance, these methods focus on the correct estimation of the wave system behind the transom, its impact on the resistance and the exact ship speed at which fully ventilated flow occurs.

Alternatively, the implementation of transom flow in a potential flow method with a linearised free surface is of a different nature. Here problems arise due to inconsistencies of the depressed free surface behind the transom and the linearised free surface. Due to the implementation of the free surface Green function, both in the frequency domain as in the

time-domain, correct evaluation of the influence of the dry transom becomes extremely difficult, if not impossible. Also in the two-dimensional high-frequency added mass approaches described in the previous section implementation of transom flow is not evident due to the lack of longitudinal coupling between subsequent transverse strips.

Several solutions are proposed for the modelling of transom flow for linearised potential flow methods and in some cases for two-dimensional high frequency added mass methods:

Virtual or dummy appendage

In order to force the flow to separate smoothly from the transom dummy panels are applied behind the transom. In its most crude way the hull is continued by a few rows of panels behind the transom. Several authors have proposed more elaborated dummy shapes. These shapes are either based on empirical data on the shape of the hollow behind the transom (Couser et al. 1998, Doctors and Day 1997), or by using another non-linear free surface method to find the shape of the hollow (Du et al. 2003).

Empirical near-transom pressure correction

Garme (2005) proposed the usage of a pressure reduction function that reduces the pressure over a certain length towards the transom to zero. Based on pressure measurements on several stations towards the transom he adopted a reduction shape in the form of a hyperbolic tangent function. The coefficients he found by tuning the function using trim and sinkage data from model tests with a large variety of different high speed hulls. This methods will be further elaborated in section 4.4.

Kutta-type transom pressure condition

Reed et al. (1991) proposed the usage of a transom flow condition at the transom for fully ventilated sterns. The used an analogy with the Kutta condition applied at the trailing edge of foils in inviscid flow to ensure smooth flow separation, combined with forcing the pressure to atmospheric at the transom edge. For this end, source-doublet panels are used with a wake sheet extending from the transom. In the vortex lattice methods presented by Lai (1994) a similar approach was used, yet they do not seem to enforce the pressure at the transom edge and instead use a pure Kutta condition.

1.3 Research questions

The research presented in this thesis is aimed at answering the following three research questions:

1. *What is the limiting behaviour with respect to safety and operability of high speed ships operating in waves?*
2. *What criteria are applied to evaluate the limiting behaviour of high speeds operating in waves?*

3. *Can a numerical method be formulated and implemented for the analysis of the seakeeping behaviour of high speed ships? One that provides more fundamental insight than currently available methods, while remaining practically usable.*

The approach to answer these questions is twofold. First, a literature review and an experimental study are performed, aimed at qualifying and where possible quantifying the seakeeping behaviour of high speed ships at model scale and at full scale. Previously obtained experimental material available at the Delft University of Technology, both at full scale and at model scale, have been re-examined to present an overview and to identify the characteristics of the seakeeping behaviour of fast ships.

Second, a computational model is formulated that incorporates the lessons learned in the first stage. The aim of this computational method is to provide designers of fast vessels, operating at moderate to high speeds, with a method that gives more fundamental insight than currently widely-used methods such as linear strip theory. Importantly, the method should still have the capability to be run in a normal desktop environment with reasonable computational times, as large computational infrastructures are not feasible in the design environment. The research is concluded by the validation of the computational model with the experimental results obtained in the first stage of the research.

Although the application of the findings and the computational method developed in this thesis is not limited to monohulls, the discussion presented in this thesis is specifically targeted at these vessels. The reason for this is that the market of high speed ships for patrol and offshore supply duties is dominated by the relative simple and reliable fast monohulls as outlined previously in this chapter.

The speed range considered in the research is defined by the speeds attained by present-day fast patrol and crew supply vessels as described in the first section of this chapter. This speed range entails Froude numbers from 0.5 to around 1.0. At these forward speeds a significant portion of the weight is carried by hydrodynamic lift and ships have significant trim and sinkage and the motion response can be strongly non-linear with respect to the incoming waves.

At same time gravity effects and radiation and diffraction of waves are still of great importance (Ogilvie 1967). The result is that both 'traditional' seakeeping methods such as linear strip theory and frequency domain diffraction theory as zero-gravity planing slender body theories are not applicable and an intermediate method should be found and applied. Additionally in this speed range the transom will be largely unwetted and the influence of this on the running attitude and the seakeeping should be taken into consideration.

Besides the main objective of estimating the motions and accelerations in waves in a practical manner, secondary and future objectives of the computational method are:

- To provide pressures and loads on fast ships in waves as an input for global strength and fatigue assessment with structural computational methods.
- To predict the behaviour of fast ships for large amplitude horizontal motions and manoeuvres and to study directional stability, the influence of roll stability and broaching behaviour.
- Next to predicting significant motion levels also providing insight in peak acceleration levels.

1.4 Reading guide

Chapter 2 presents a literature review and an experimental study into the limiting seakeeping behaviour of fast ships in head, bow quartering, stern quartering, and following seas. The aim is to provide insight into the limiting behaviour of and criteria set to the seakeeping behaviour of in particular high speed ships. This chapter provides the physical background needed to successfully set-up a computational method and material to validate this method against.

In chapter 3 a computational model for the seakeeping of high speed craft in the speed range of Froude numbers of 0.5 to 1.0 is presented. The choice for the method will be discussed, as well as the fundamentals and assumptions behind the method. Finally the computational details of the method and simplifications to improve the efficiency of the method will be discussed.

In chapter 4 a number of numerical aspects of the computational method are studied in detail. The aim is to verify the code by ensuring confidence in the implementation of the method in the form of a computer code and to obtain a general idea of the correct use of the method and its input.

In chapter 5 a number of case studies are presented where the outcome of the computational method is compared to the results of the experiments presented in chapter 2 in order to validate it. Comparisons will be performed in calm water, regular head waves, and irregular head waves for two design concepts of high speed ships.

Finally, chapter 6 closes this thesis with the conclusions and recommendations. It provides the answers to the first two research questions based on the experimental work of chapter 2 followed by the answer to the third research question based on the computational work presented in chapters 3, 4, and 5. Finally, the recommendations and future work are described.

Chapter 2

Experimental Work and Criteria Development

2.1 Introduction

Over the past 20 years significant progress has been made in optimizing the seakeeping behaviour of fast planing or semi-planing monohulls. Especially impacts of the bow in waves and the subsequent levels of the vertical acceleration on board have been shown to severely affect the comfort level experienced by crew and passengers (Keuning 1994). Accordingly, research and design effort has been focused at improving on this behaviour. In spite of the important improvement of the seakeeping behaviour of fast monohulls already achieved it was felt that the consistent formulation of limiting criteria with respect to vertical acceleration levels on board such vessels could have an even further impact on their design and operability (Keuning 1994, Keuning and Van Walree 2006, Keuning and Gelling 2007).

To address the formulation of limiting criteria of fast ships and to compare three new and improved designs for fast monohulls in 2004 a joint industry project, named FAST I, was set up by the Ministry of Defense of the Netherlands, the U.S. Coast Guard, Damen Shipyards High Speed Craft Department, Damen Schelde Naval Shipbuiling, and the Maritime Research Institute Netherlands (MARIN) commissioned at the Ship Hydromechanics Laboratory of the Delft University of Technology (DUT).

The first part of this research project consisted of full scale measurements on board an 'Enlarged Ship Concept' (Keuning and Pinkster (1995), refer to chapter 1), the *Valiant* of the U.K. Customs and Excise. A team of experts went on board and monitored the motions and accelerations, along with wave measurements using wave buoys and video recordings. The information was gathered to provide more material in order to formulate limiting criteria for the operation of such ships in a seaway and was combined with experimental data collected earlier on board rescue lifeboats of the Royal Netherlands Sea Rescue Institution (Ooms and Keuning 1997).

The second part consisted of model experiments of three comparable designs of a fast monohull patrol boat. The main objective of this part of the research project was formulated as follows:

> To acquire data on three possible design concepts, in order to develop the knowledge on the hydromechanics involved in the design, construction, and safe oper-

ation of fast marine vehicles, in particular those employed in patrol and surveillance tasks through navies, coast guard, law enforcement agencies, amongst others.

More concretely, the aim of the model experiments was twofold: (1) to gain insight in the hydromechanic performance of three design concepts for fast patrol vessels and their mutual ranking and (2) to gather data to be used for the development and validation of mathematical tools for the behaviour of fast vessels in waves. The second point serves as the basis of the validation of the computational method presented in chapter 3 of this thesis. In fact, the development of such a computational model is phase 2 of the of the FAST research project. Besides the data obtained during FAST I, the experimental data set was further extended during this second project to enable more systematic material to validate the method against.

The following two sections describe both parts of the research in more detail. Section 2.2 deals with the full scale measurements and the subsequent criteria development and section 2.3 describes the model experiments and their results. Part of the information presented in these sections has been previously published by Keuning and Van Walree (2006) and Keuning and Gelling (2007). Without aiming to repeat an overview of both works will be provided; mainly to highlight their outcomes, to place the work into a broader perspective, and to elaborate on a number of important points raised. Particularly the discussion in section 2.4 aims at providing this broader perspective.

Most experimental data presented in the graphs of this chapter is accompanied by 95% confidence bounds. The way these confidence bounds were determinated is presented in detail in appendix D.

2.2 Full scale measurements and criteria development

In order to compare the operability of high speed monohull designs in a seaway it seems necessary to first obtain an idea as to what criteria are important for the operability of this type of ship and how these criteria should be applied. In order to answer these questions a series of full scale experiments was set-up. The aim of these was threefold. First, to gain insight into what played a role when considering the operability of this type of vessel and what characteristics should be used to formulate a suitable criterion. Second, to quantify actual limiting values for the criteria to be used and third to identify aspects that ensure a safe operation for these type of vessels.

Keuning (1994) already showed that the operability of fast ships in a seaway can not be judged by using the linear approach of setting limits to the root mean square values or significant values (equal to the average of the largest one-third of the amplitudes occurring in an irregular signal) of the motion and acceleration levels. Generally, the linear approach implies that an irregular sea state can be split in independent harmonic components each with their own amplitude, frequency, and phase angle. The motion response of the ship is assumed to consist of the sum of the motion responses to each individual wave component. The amplitude of each individual wave component is transferred onto the motion amplitude by assuming a fixed amplitude magnification factor for each motion component. This leads to the concept of a transfer function, or Response Amplitude Operator (RAO) linking the wave amplitudes to the motion amplitudes for each motion component at each frequency.



Figure 2.1: *UK Customs and Excise patrol vessel 'Vigilant' and Dutch Coast Guard patrol vessel 'Zeearend', both of the type Damen StanPatrol 4207*[1]

In the linear approach, the value of the RAO is independent of the significant wave height and there exists a fixed relation between the significant values of the wave and motion signals and the maximum values. For instance, the one in thousand waves occurring extreme value has a magnitude of roughly twice the significant value (section 2.3.5 will elaborate on this). For this reason limits set to the significant values have a direct relation to the occurrence of maxima. Keuning (1994) showed that both assumptions are violated when considering the motions of high speed ships in a seaway, as these ships behave non-linear in both senses: the RAOs are dependent of the magnitude of the waves and the motions of the ship itself and the relation between significant values and the occurrence of maxima is not fixed any more.

The actual distribution of peaks and troughs of the responses in a seaway now determines the operability. The implication is that time domain simulations, either computational or by means of model experiments, need to be performed for each one of the wave spectra selected from the wave scatter diagram to analyse the operability of this type of vessels. This entails a far more time consuming procedure than usual for 'linear' operability assessments. Section 2.3.6 will elaborate on methods to be used in a 'non-linear' seakeeping analysis.

In combination with previous full scale experiments carried out by the Ship Hydromechanics Laboratory of the Delft University of Technology with fast Search And Rescue (SAR) vessels (reported by Ooms and Keuning (1997)) now the following full scale empirical data was available:

- Full scale measurements aboard the 'Valiant', a 42 meter fast patrol boat according to the 'Enlarged Ship Concept' capable of 27 knots of the UK Customs and Excise at the west coast of Scotland.
- Extensive data from measurements and observations on board of lifeboats of the Royal Netherlands Sea Rescue Institution, boats ranging from 10 to 16 metres capable of sailing 25 to 35 knots.

[1] Reproduced with the kind permission of Damen Shipyards.

- Interviews with the crews of three Coast Guard cutters, StanPatrol 4207 (figure 2.1), the same type as the 'Valiant'.

Where full scale trials were carried out the ships were instrumented and monitored in order to obtain information about the ship motions and the acceleration levels in the wheelhouse and on the bow as well as environmental conditions as wind and waves, the latter using wave buoys. On top of this the 'throttle control' applied by the crew was recorded and video recordings were made of the view from the bridge. The crews were instructed to perform their usual tasks under real circumstances. During the tests experts from the Delft University of Technology (DUT) and in some cases from Maritime Research Institute Netherlands (MARIN) and the US Coast Guard were present. The 'hard' recorded data was supplemented with information obtained from interviews with the crews after the measurements.

The main conclusion from this full scale research was summarised by Keuning and Van Walree (2006) and can be broken down into the following statements:

- All crews imposed voluntary speed reduction in roughly similar conditions, in terms of the vessels' motions and the occurrance of acceleration peaks.
- It was very clear that the incentive for voluntary speed reduction did not come from the prevailing magnitude of the significant amplitude of the motions or the vertical accelerations but instead from the occurrence of a single or a few large peaks in particular in the vertical acceleration level just prior before the actual instant of voluntary speed reduction.
- In that case the crew applied a speed reduction in order to prevent any further occurrence of these peaks.

These three points can be linked to a well known general aspect of human nature, that humans are more inclined to react to well defined extremes that occur at one particular instance rather than to averages that slowly change over time (Keuning and Van Walree 2006). In fact, the voluntary speed reductions proved to be a very useful instrument in determining what the crew looked upon as acceptable in terms both of safety and of crew and passenger comfort. The fact that the speed reductions were so clearly linked to the occurrence of peaks in the vertical acceleration levels confirms what Keuning (1994) had already found based on theoretically studying the motion behaviour of high speed craft in a seaway. It also clearly indicates that any successful criteria of the operability of this kind of vessels, in particular in head waves, should be based on setting limits to the occurrence of maxima in the vertical acceleration levels.

Voluntary speed loss due to extreme accelerations is not specific to high speed ships. Lloyd (1989) already mentions in his work that for most conventional ships slamming is the primary reason for voluntary speed loss. Nevertheless, high speed ships do encounter relatively more often extreme vertical accelerations. In fact, in the more severe sea states almost every wave encounter in head waves results in a slam.

When studying the differences between the larger Enlarged Ship Concept type of vessels and the smaller SAR boats some marked differences can be observed:

- For the larger vessels -their design already underwent a cycle of optimisation of their motions behaviour- the occurrence of large peaks in the acceleration level at the bow

and the subsequent structural vibrations due to impact, or slam, of the bow in the wave surface proved to be the determining factor for speed reduction.
- For the smaller vessels a higher level of acceleration was accepted, but typically the vertical acceleration measured in the wheelhouse proved to be far more important for the behaviour of the crew.
- 'Active' throttle control proved to be an important aspect on the smaller SAR boats. By actively controlling the throttle by anticipating the waves that were about to reach the ship a higher average speed was attained, than by fixing the throttle at a 'safe' level.

The larger vessels were already optimised for the level of accelerations in the wheelhouse. The crews judged the limiting behaviour in a different way than the crews of the smaller vessels. In absence of the direct sensation of the vertical acceleration levels on their own body due to the optimisations of the motion behaviour they needed to rely on far more indirect signals of the bow taking a hit from a wave and the subsequent structural response. This raises an interesting and important question: does the optimisation of the motion behaviour to increase the workability on board and the comfort of the crew impair the safety and integrity of the vessel? As the crew gets less direct feedback as to how severe the environmental conditions are, the risk of putting the ship, crew, and passengers in a more dangerous situation increases.

The final point about 'active' throttle control raises the question whether this can be used as a mechanism to further improve the operability of small vessels, while optimizing, or better maximizing, their speed. This is in particular of interest of SAR boats and at the moment of writing this thesis research is ongoing at the Delft University of Technology into this particular topic (Van Deyzen et al. 2011).

Finally, during this research the following criteria were defined and quantified (Keuning and Van Walree 2006):

For the larger vessels (roughly 40 metres) the maximum accepted vertical accelerations were:

- 8.0 m/s^2 at the wheelhouse and 20.0 m/s^2 at the bow.

For the smaller vessels (roughly 20 metres or less) the maximum accepted vertical accelerations were:

- 13.0 m/s^2 at the wheelhouse and 25.0 m/s^2 at the bow.

Conventional criteria for the evaluation of vertical acceleration levels experienced on board are derived from ISO standard 2631 or for warships from NATO standard STANAG 4154 and are usually based on RMS or significant values. The ISO 2631 standard (ISO 1997; 1985) provides discomfort boundaries for motion sickness dependent on acceleration frequency, and duration of exposure. These boundaries are formulated with respect to RMS values of the vertical acceleration level. The seakeeping citeria for warships, formulated in the STANAG 4154 standard (NATO STANAG 1997), are defined in terms of the Single Significant Amplitudes (SSA, the mean value of the one-third highest amplitudes). The limit to the vertical acceleration SSA is set at $0.4g$ in STANAG 4154.

NORDFORSK (1987) published an extensive table summarising seakeeping criteria for merchant vessels, navy vessels, and fast small craft and mentions limits of $0.65g$ RMS for the vertical acceleration level at the forward perpendicular and $0.275g$ RMS at the bridge.

Next to these specific criteria, implicit criteria are proposed to the number of slams per hour dependent on the sea state and the forward speed, instead of to the severity of these slams (Lloyd 1989). These (proposed) criteria are based on interviews with captains, similar to the work presented here for high speed ships.

At the moment of writing, research is ongoing at the DUT on the development of criteria for the seakeeping of high speed ships. These developments are focused on obtaining more full scale data and feedback from crews of fast patrol vessels and SAR boats and not only at motions and accelerations in head waves, but also at directional stability and broaching in following and stern-quartering waves and bow-diving.

2.3 Model experiments

2.3.1 Development of conceptual designs

The second part of the FAST I project consisted of extensive model experiments with three comparable designs for a High Speed Naval Vessel (HSNV), a patrol boat for offshore service. To ensure that the designs were realistic, significant effort was invested in generating the parameters for a generic design as a starting point for the three comparable designs. The Top Level Requirements (TLR) for the HSNV resulted in a top speed of 45 knots and a maximum draft of 3.05 metres (Brower and Cleary 2003). The design process was carried out using a design synthesis computer program to modify the design to meet the TLR and to investigate the effect on the Total Cost of Ownership (TCO) at the U.S. Coast Guard (Sheinberg et al. 2007).

The endurance was set at 7 days with a crew of 20 heads. The speed profile was set at 80% of the time at 10 knots, 15% at 17 knots and 5% at 50 knots. The speed range 30-40 knots was considered reasonable for present day designs, while the target maximum speed of 50 knots was set as a challenge for the future. The main parameters of the concept design of the HSNV are given in table 2.1 and the lines of the base boat as well as the inboard profile in figure 2.2. The design employs a triple water jet set-up with a combined diesel and gas turbine propulsion plant. For the hull and superstructure aluminium was selected, although a CRP option (Composite Reinforced Plastics) was considered.

Table 2.1: *Main particulars concept design HSNV*

Quantity	Symbol	Unit	Value
Length waterline	L_{wl}	m	52.58
Beam on waterline	B_{wl}	m	8.40
Maximum draft	T_{max}	m	2.68
Volume of displacement	∇	m^3	$\pm$ 526.00
Prismatic coefficient	C_p	$-$	0.75
Block coefficient	C_b	$-$	0.44
Power (diesel)		BHP	2$*$3900
Power (gas turbine)		BHP	1$*$29500

Using the HSNV design as a basis three conceptual designs were crafted at the Ship Hydromechanics Laboratory of the Delft University of Technology. The first conceptual design,

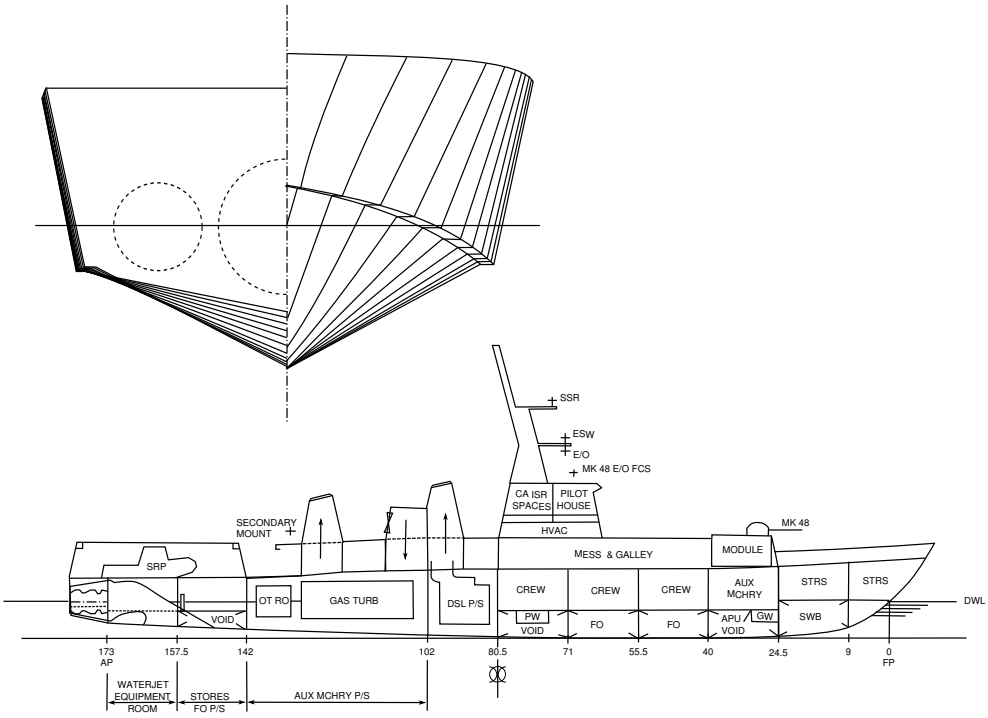


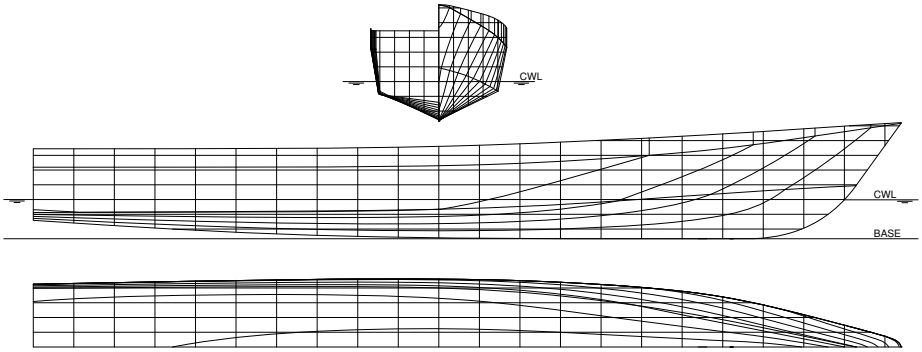
Figure 2.2: *Concept HSNV design body plan and general arrangement (Keuning and Van Walree 2006)*

the Parent Hull Form was generated by the application of the 'Enlarged Ship Concept' (Keuning and Pinkster 1995) to a patrol boat using the operational parameters and functionality specifications defined by the U.S. Coast Guard for the HSNV. The other two conceptual designs were adaptations of the ESC, one applying the 'Axe Bow Concept' (Keuning and Pinkster 2002), the other applying the 'Wave Piercer Concept' (Van Diepen 2003b). The resulting three conceptual designs were:

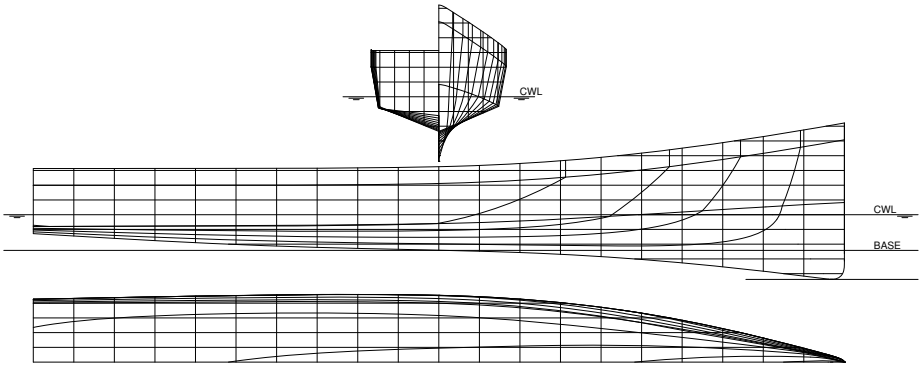
1. Enlarged Ship Concept (ESC), Parent Hull Form (PHF)
2. Axe Bow Concept (ABC)
3. Wave Piercer Concept (WPC)

Both the Enlarged Ship Concept and the Axe Bow Concept were already introduced in detail in chapter 1. The application of the Wave Piercer Concept has been reported over the last few decades by various authors, especially for multi hulls like trimarans. The application of the Wave Piercer Concept to monohulls has been patented by Van Diepen (Van Diepen 2003a). Another well known application to monohulls is the Very Slender Vessel (VSV) by Thompson (Thompson 2000). The idea is to minimise the wave exciting forces by taking away the above water part of the buoyancy in the bow region resulting in a backward sloping bow profile. In effect a large part of the reserve buoyancy at the bow is removed, while the usable deck area is significantly reduced.

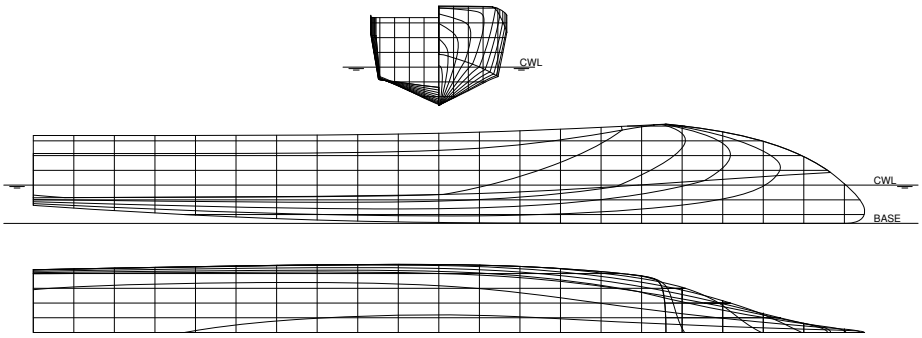
One of the main tasks in this design process was retaining the same functionality and specifications for all three designs in order to ensure that the comparison of the hydromechanical



(a) Enlarged Ship Concept



(b) Axe Bow Concept



(c) Wave Piercer Concept

Figure 2.3: *Body plans of the FAST-I conceptual designs*[a]

[a]The original plans and the models have integrated spray rails along nearly the entire length. These are not depicted in the body plans presented here.

behaviour occurred on the basis of comparable designs. However, to meet the minimum deck area criterion of the HSNV much larger overall dimensions would be required for the Wave Piercer Concept. As this would severely affect the hydromechanic comparison of the three designs and it was decided not to apply this particular design criterion to the Wave Piercer design.

Table 2.2: *Main particulars FAST conceptual designs*

Quantity	Symbol	Unit	ESC	ABC	WPC
Length waterline	L_{wl}	m	55.00	55.00	55.10
Beam on waterline	B_{wl}	m	8.46	8.46	8.46
Maximum draft	T_{max}	m	2.66	4.39	2.60
Baseline draft	T_{base}	m	2.66	2.42	2.60
Volume of displacement	∇	m^3	516.00	517.40	515.90
Wetted area	S	m^2	480.58	512.84	492.16
Vertical position CoG	KG	m	3.85	3.53	3.79
Longitudinal position CoG[a]	LCG	m	22.49	24.36	22.47
Metacentre height	GM	m	1.52	1.52	1.52
Pitch radius of gyration	k_{yy}	m	13.75	13.75	13.75

[a]The longitudinal position of the centre of gravity is defined with respect to the aft perpendicular.

Body plans of the three designs are depicted in figure 2.3, while their main particulars are presented in table 2.2. The beam was selected to yield an adequate stability while retaining the favourable seakeeping characteristics of relatively slender ships. Although no complete structural analysis of the designs was performed the vertical location of the centre of gravity of all three designs, necessary to obtain sufficient transverse stability, were considered to be feasible. Due to the design choices for an identical aft half, the same waterline length, and the same transverse metacentric height, the three different bow shapes led to differences in the volume of displacement and the height of the center of gravity.

2.3.2 Test program

The test program consisted of calm water resistance tests, tests in irregular head waves, tests in regular following waves, and finally tests in stern-quartering waves. The latter, involving stern-quartering waves, have been carried out at MARIN with only the two best performing designs, the ESC and the ABC.

The tests in waves were performed in ever worsening environmental conditions in terms of wave height and forward speed in order to assess the operational limits of each of the designs. Besides acceleration levels other types of limiting behaviour were anticipated. This included shipping of green water in head waves, bow diving in following waves, and broaching and subsequent capsizing in stern-quartering waves (Keuning and Van Walree 2006, Keuning and Gelling 2007). Special care was taken to include the worst possible, but still realistic, environmental conditions in the test program.

The experiments described above were carried out during the FAST I research project. The validation of the computational model presented in this thesis with this data consisted mainly

of the comparison of statistical properties of time traces, giving only a very general view of the quality of the computations. Also the tuning of the irregular wave conditions was done prior to the actual model test, in absence of the model, to ensure generated waves according to the given spectra. No reliable deterministic time trace was obtained during the actual model experiments, due to disturbance waves generated by the model and ventilation of the wire-type wave probes at high forward speed.

During the development of this thesis it was found that the data obtained in irregular waves provided too little basis for the validation proces and an extra set of towing tank tests was setup specifically for the purpose of validation. This new set was focused at regular head waves, allowing for a more deterministic and complete comparison between experiment and computation. The relatively simple, predominantly harmonic signals are far easier to compare and interpret than the more complex irregular signals, while the generated waves are easily deterministic quantifiable in terms of frequency, amplitude, and phase angles. Moreover, it can be ensured that the exact same wave train is used in both the experiments and the computations. Besides the regular wave experiments, a limited amount of tests has been performed in irregular head waves. In order to fulfil the requirement of a deterministic wave train that could be fed to a computational model special attention was paid to reliable wave measurement and reconstruction at high forward speeds.

To limit the amount of tests it was decided to only perform these additional tests with two of the three design concepts, the Enlarged Ship Concept and the Axe Bow Concept. These experiments have been carried out at the Ship Hydromechanics Laboratory of the DUT.

2.3.3 Experimental set-up

The tests in head waves and following waves have been carried out in the towing tank No. 1 of the Shiphydromechanic Laboratory of the Delft University of Technology. The dimensions of this towing tank are: 142.00 m length, 4.22 m width, and maximum 2.50 m of water depth. The towing tank is fitted with a hydraulically actuated flap type wave generator and the towing carriage is able to attain speeds of 7 m/s. A model scale of 1/20 was chosen leading to a model waterline length of 2.75 metres. At this scale the required maximum model velocity was a little under 6 m/s, well within the capacity of the towing carriage of the towing tank used.

The models were constructed of glass fibre reinforced polyester (GRP). They were ballasted to obtain the correct weight, mass moment of inertia, longitudinal, and vertical location of the centre of gravity according to the specifications obtained in the design process. The models were fitted under the towing carriage using a support hinge and bearing system allowing them to heave and pitch, while preventing them from carrying out motions in other directions. The hinge of the support system was exactly positioned at the centre of gravity. An overview of the test set-up is provided in figure 2.4.

A model was towed at constant forward speed by the towing carriage. During the experiments the following quantities were measured: forward speed, heave and pitch motions, vertical accelerations at the bow and at the centre of gravity, and the resistance. The forward speed was read from the control system of the towing carriage. The motions were measured using an optical tracking system, the resistance using a strain-gauge type force transducer and the accelerations by two dedicated gravity based accelerometers placed at the centre of gravity and at the bow. IR LEDs were positioned on the model to enable optical motion tracking with a dedicated IR camera system.

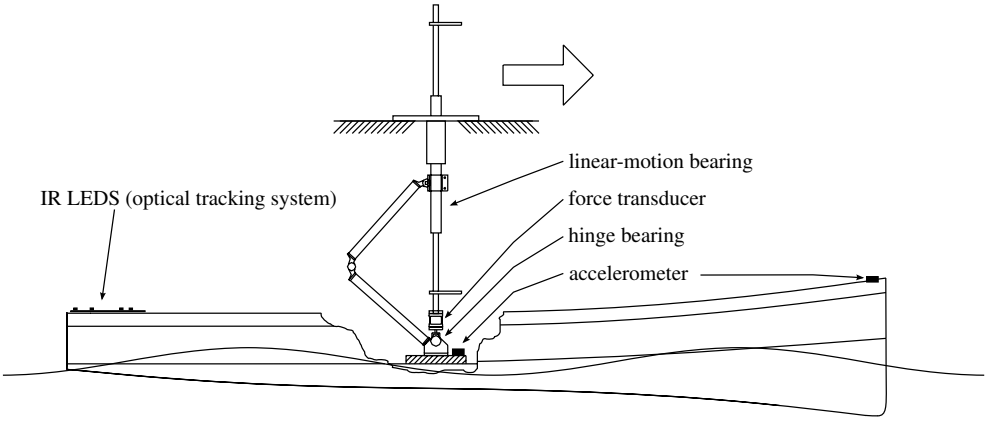


Figure 2.4: *Experimental set-up of the DUT tests*

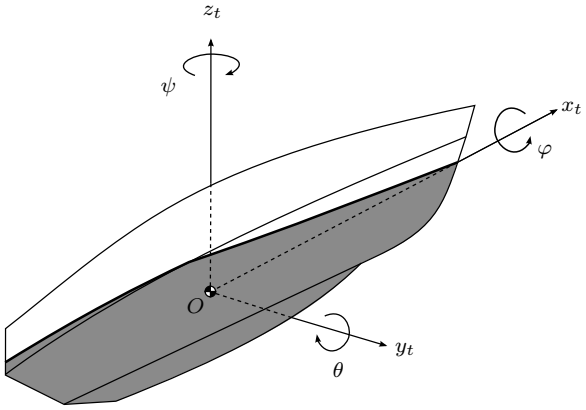


Figure 2.5: *Coordinate system used for the measurements*

The heave and pitch motions were measured in a steady translating axis system $Ox_ty_tz_t$ with its origin in the center of gravity of the model, depicted in figure 2.5. The acceleration levels were measured body-fixed and corrected for the gravity acceleration. The influence of the pitch angle on the action of the gravity acceleration was neglected. The maximum pitch angle was about 5 degrees, resulting in a maximum deviation of less than 0.5% of g.

The forward accelerometers (at the bow) were located at 1.32 metres in front of the center of gravity for the ESC and the ABC. Due to its bow shape the forward accelerometer of the WPC was mounted at 0.985 metres in front of the center of gravity. The accelerometers at the center of gravity were in fact located 65 millimeters in front of the center of gravity for all three design concepts; it was impossible to locate them exactly at the center of gravity due to the mounting bracket of the tow system. As all three models had an identical aft part combined with a different bow shape, the longitudinal position of the center of buoyance (and thus the LCG) was different (particularily for the ABC, refer to table 2.2). It should be noted that this resulted in a different longitudinal placement of the accelerometers.

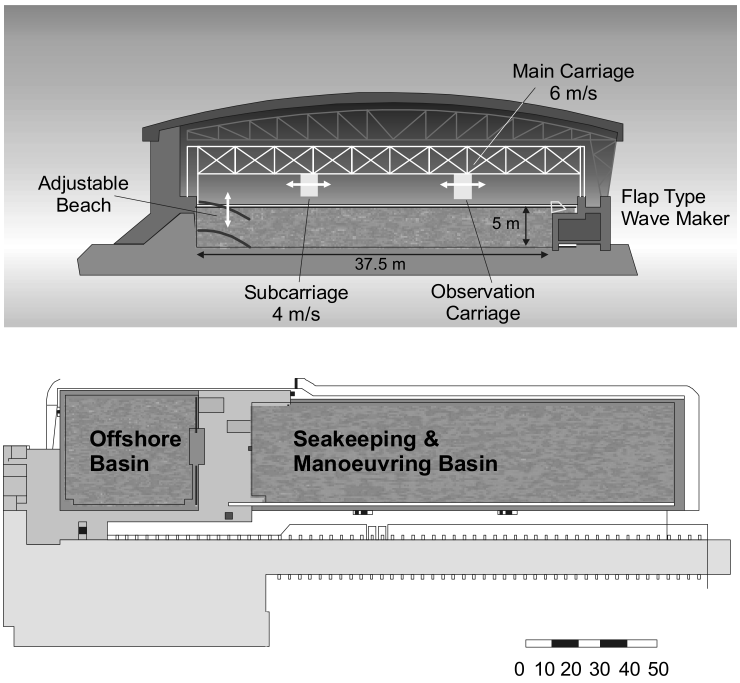


Figure 2.6: *Seakeeping model basin at Marin*

For the experiments in deterministic irregular waves one wave probe was located forward of the model and was specially selected to be able to follow the exact wave profile at high forward speeds. This (servo-type) probe consisted of a vertical rod that was actuated vertically by an electrical motor. Its tip was held exactly at the water surface by using electrical conductivity. Transverse of the centre of gravity of the model a second wave probe of a conventional wire resistance type was located in order to provide a check of the phase angles of the individual wave components. This same result could not have been achieved by using a single wave probe at the centre of gravity as at this location the incident waves already may be severely disturbed by the diffraction and radiation waves of the model and their reflections.

The tests in stern-quartering seas have been performed in the Seakeeping and Manoeuvring Basin of MARIN. The dimensions of this basin are: 170.00 m length, 40.00 m width, and maximum 5.00 m of water depth. The basin is equipped with wave generators along one long side and one short side. The wave generators consist of a series of independent segments consisting of hinged flaps and are capable of generating waves (regular and irregular) in all directions. The towing carriage is capable of velocities up to 6 m/s and has a sub-carriage moving in transverse direction capable of 4 m/s. Figure 2.6 provides a schematic overview of this facility.

In order to allow the models, pictured in figures 2.7 to 2.9, to move freely in six degrees of freedom the models were self propelled and only connected to the towing carriage by means of a ‘umbilical cord’ for data transfer. To facilitate this, the models were fitted out with two electrical powered water jets with steerable nozzles using an autopilot to follow a

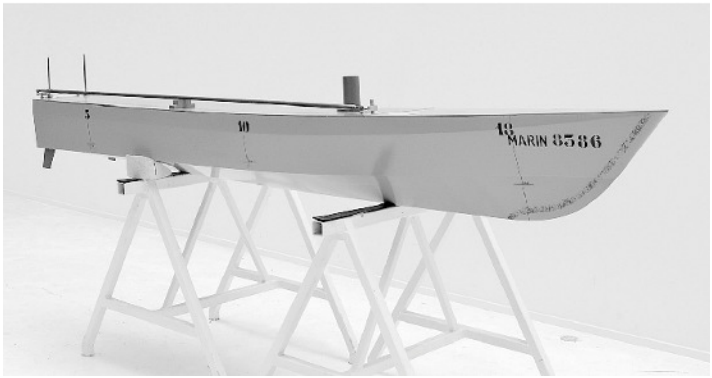


Figure 2.7: *Photograph of ESC model used in the Marin experiments*

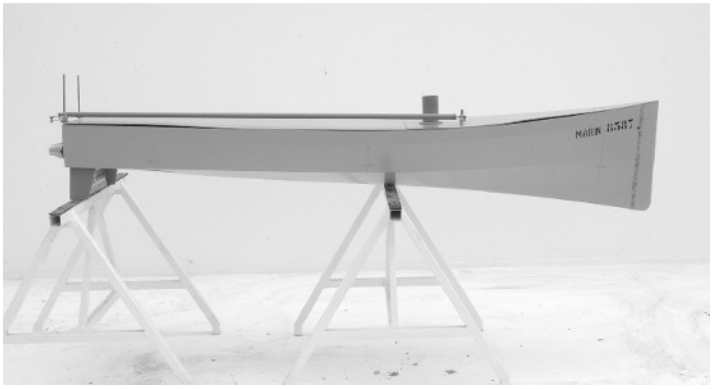


Figure 2.8: *Photograph of ABC model used in the Marin experiments*

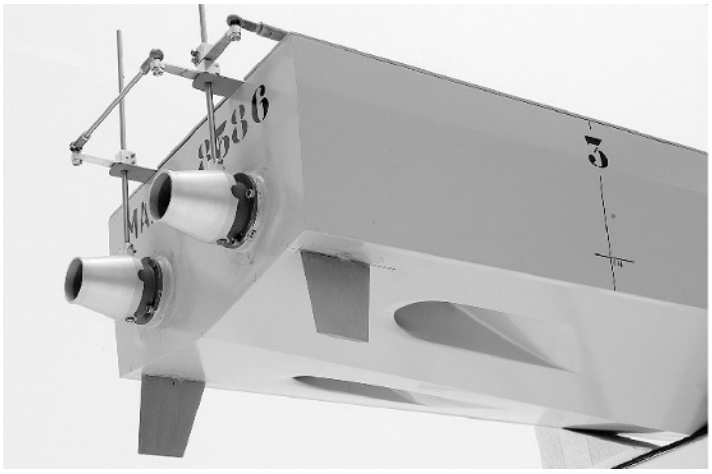


Figure 2.9: *Detail of skeg and water jet arrangement*

pre-set course following the standards used at MARIN. The maximum nozzle angular rate was 10 degrees per second and the maximum nozzle angle was 23 degrees to both port side as starboard side. Due to the absense of propellor shafts and rudders it was felt that twin skeg arrangement was necessary to improve directional stability for all models. The skegs of the Axe Bow Concept were chosen to be twice as large as those of the Enlarged Ship Concept. The sub-carriage follows the model in order to measure its motions optically and enable data-recording using the umbilical cord.

2.3.4 Calm water behaviour

In order to determine the calm water resistance of three designs the models (without appendages) have been towed in the No. 1 towing tank of the Delft Ship hydromechanics Laboratory. This has been done according to the standard procedure used by the Laboratory. In this procedure three carborundum strips are placed on the model at three stations along its forward half to ensure a fully turbulent boundary layer at model scale. In order to discount the parasitic drag due to strips themselves two runs were performed for each forward speed in the measurement range. For the second set of runs the width of the carborundum strips was doubled with respect to the first set to obtain the additional parasitic drag and to relate this to the wetted surface area of the strips.

To obtain the full scale calm water resistance Froude's extrapolation method was used, applying the plate friction coefficient computed with the ITTC'57 formula. No form factor was used, and the form resistance was treated as a part of the residuary resistance. In the extrapolation procedure only the static wetted surface was taken into account. The resulting total calm water resistance is presented in figure 2.10 for all three models.
Omission of the dynamic wetted surface introduces an error in the resistance extrapolation. In this particular case, the maximum error in wetted surface can be roughly estimated as about 4% (due to 0.20 meter rise over a length of about 50 meters), resulting in a 4% higher (model) frictional resistance. The frictional resistance is assigned a relative lower scaling factor than the residual resistance (as the plate friction coefficient decreases for increasing Reynolds number). The result is a lower total resistance. This under-estimation however is limited by the fact that the frictional resistance only is minor part of the total resistance, especially for high forward speeds. At Froude number 0.8 the frictional resistance is about 25 to 30 % of the forward speed and 4% thereof is assigned a too small scaling factor. Therefore the maximum error that is introduced is less than 1% of the value of the total resistance. The effect of the trim on the wetted surface is neglected in this estimate.

The Wave Piercer has generally a lower resistance than the other two models. The Axe Bow model has a favourable calm resistance below 35 knots with respect to the parent hull form (ESC), above 35 knots this reversed. A further explanation of this may be found in the running attitude of the vessels, i.e. the trim and sinkage (or rise) in calm water, shown in figures 2.11 and 2.12. The Wave Piercer experiences a larger rise with respect to the other two; its flatter body shape near the bow apparently results in a higher hydrodynamic lift. This larger rise will translate itself in a lower wetted surface and less water displacement by the body, probably causing the lower resistance. Nevertheless, the trim angles and even more so their differences are very small, implicating that the different body shapes and subsequent different lifting forces (concentrated at the fore part of the hull) do not cause very pronounced differences in trimming moments.

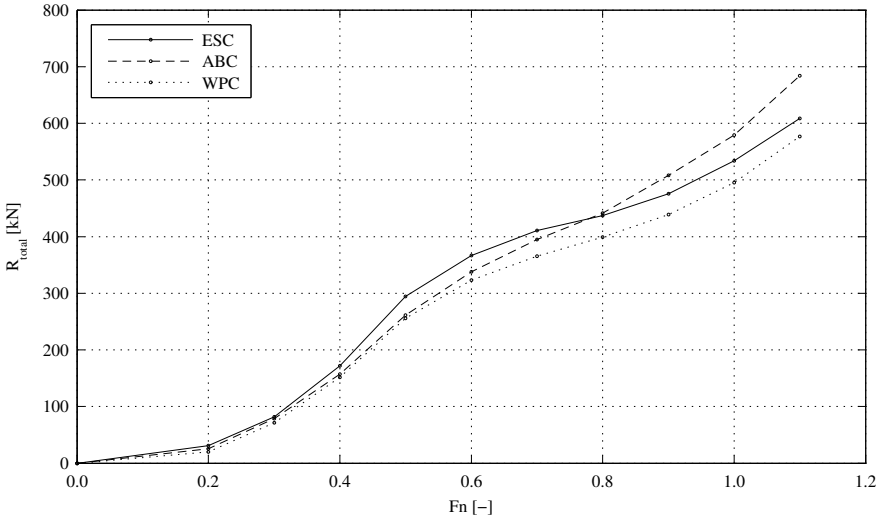


Figure 2.10: *Calm water total resistance*

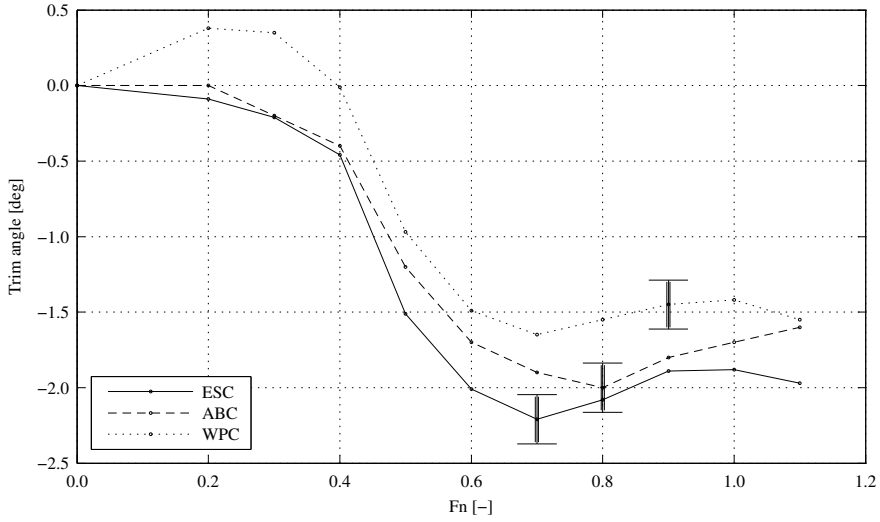


Figure 2.11: *Calm water trim (positive: bow down)*

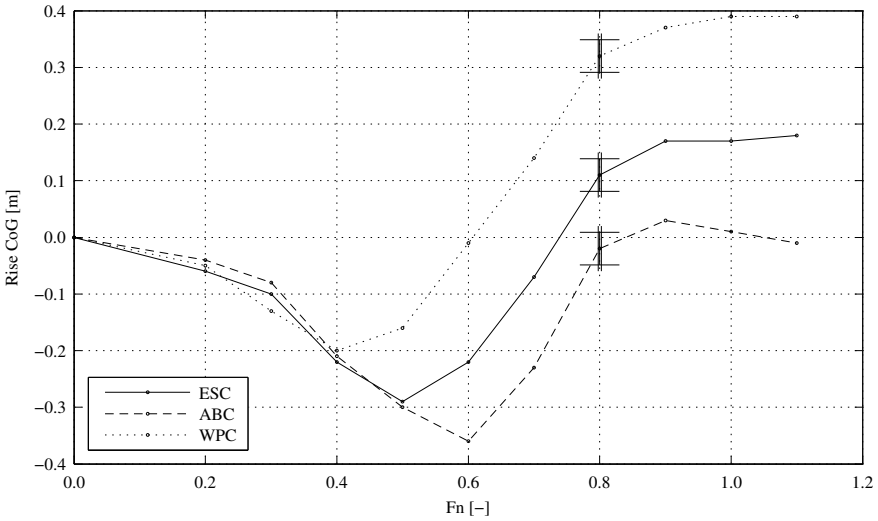


Figure 2.12: *Calm water sinkage and rise at centre of gravity*

One factor that could influence the resistance, the trim, and the rise and their comparison is the location of the tow point. This point was located at the center of gravity of all three models, nevertheless the center of gravity was not at the same height for the three models (refer to table 2.2), as the metacentric height was kept constant. In real life situations, the propulsion force attaches at the propellor or at the water jet shaft. This influences mainly the trimming moment and the trim angle, and therefore indirectly also may influence the resistance and the rise. Figure 2.4 is on scale and shows that the point of attachment is positioned relatively low in the model. For this reason, the magnitude of the trimming moment may be relatively small.

2.3.5 Regular head waves and the usage of RAOs

As discussed before in section 2.3.2 during the development of the numerical model it was realised that the use of experimental data obtained in irregular waves as validation material only led to a partial overview of the quality of the predicted motions by the numerical method. For this reason addional testing has been carried out in regular head waves, especially setup for the work presented in this thesis, giving a more complete picture of the quality of the motion predictions in a wide range of wave conditions and allowing for deterministic comparison of computed and empirical data, instead of only statistical comparison.

To limit the amount of tests, the regular tests have been performed with only the ESC and the ABC models at two forward speeds of 25 and 35 knots full scale. In order to investigate the dependence of the motion response with respect to the wave amplitude a variation of three ratios of wave height with respect to wave length have been tested (or wave steepness ratio κ), 1/60, 1/30, and 1/20. For 'normal' regular wave experiments to obtain the motion response

of a vessel the ITTC recommends to either keep this ratio constant at a value of 1/50, or to keep the ratio of wave height with respect to the length between the perpendiculars constant (ITTC 2002b). The regular wave tests have been performed for a range of wave periods, corresponding to wave lengths from one half the waterline length to three times the waterline length (the ITTC recommends one half to two times the length between the perpendiculars). Table 2.3 summarizes the chosen wave frequencies and shows the relation to the wave length and the encounter periods at both forward speeds.

Table 2.3: *Regular waves; wave length, frequencies, and periods*

ω	$\omega\,(L/g)^{1/2}$	T	λ/L	T_e $25kts$	T_e $35kts$
$[rad/s]$	$[-]$	$[s]$	$[-]$	$[s]$	$[s]$
0.60	1.42	10.47	3.11	5.86	4.98
0.70	1.66	8.98	2.29	4.68	3.93
0.80	1.89	7.85	1.75	3.83	3.18
0.90	2.13	6.98	1.38	3.20	2.63
1.00	2.37	6.28	1.12	2.72	2.22
1.10	2.60	5.71	0.93	2.34	1.89
1.20	2.84	5.24	0.78	2.03	1.63
1.30	3.08	4.83	0.66	1.79	1.43

A minimum of 14 wave cycles were measured during one run, more than the minimum 10 cycles advised by the ITTC for statistical reliable data processing (ITTC 2002b). A number of tests could not be performed in accordance with the testing program. This considered the tests at the highest wave steepness and the lowest frequencies, i.e. long waves. In some cases the waves were too large to be generated in the towing tank, and a reduced wave steepness was chosen in these cases. In other cases the motions of the vessels became too violent for the support bearings; these cases have been discarded. The effect of the tank bottom on the wave dynamics (shallow water waves) was not taken into account.

In order to process the data the measured motion responses were expressed by using Response Amplitude Operators (RAO). These RAOs were determined by applying a harmonic analysis at a single frequency to the input signal (the measured wave height) and the output signals (the motion responses). The single frequency at which to perform this analysis, the encounter frequency of the incident waves, was extracted from the wave signal by a least squares fit of a sine function. In this way the amplitudes of the input and the output, as well as their relative phase angles were obtained, allowing the computation of the Response Amplitude Operators. It can easily shown, however, that there are significant shortcomings applying this linear analysis procedure to the seakeeping problem of high speed ships.

In the remainder of this section, first, the shortcomings of using a linear analysis with RAOs to the non-linear seakeeping problem of high speed ships and the occurrence of peaks in the vertical acceleration is discussed using the experimental results of the Enlarged Ship Concept. Second, the motion responses of the Enlarged Ship Concept and the Axe Bow Concept are compared, taking into account non-harmonic and non-linear behaviour in the motion and acceleration responses.

Response Amplitude Operators and high speed ships

The main assumptions behind the usage of a Response Amplitude Operators are (1) a harmonic input (and output) and (2) linearity of the system, i.e. a linear relation between input and output. This linear relation is not only limited to the amplitude of the in- and output signals -meaning that a factor times the original input will yield the original output multiplied by the same factor- but also to the harmonics of the in- and output signals. In a linear system, when assuming that the wave elevation is a harmonic signal, automatically the output signal becomes a harmonic signal of the same frequency (or frequencies) as the time trace of the wave elevation with a fixed amplification factor for each frequency component. Another consequence of linearity is the superposition principle, that allows the simple summation of harmonic components without taking into account any (non-linear) interactions.

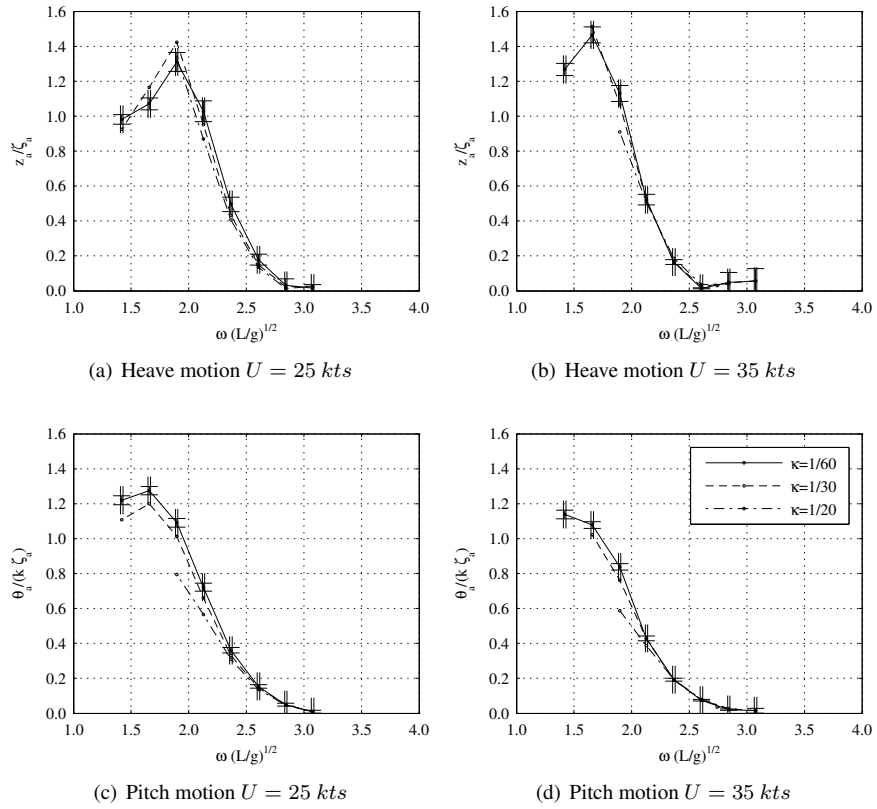
One way of taking into account the non-linearity of the system is to compute RAOs for a range of wave heights or steepness. Although the dependence of the motion response on the wave amplitude may be taken into account in this way, still energy transfer to other frequencies than the wave frequency and non-harmonic responses pose difficulties that invalidate the usage of RAOs. Specifically in the non-linear system of high speed craft sailing in waves these two effects do take place:

First, large amplitude motions may take place, related to the often relatively small size of fast ships with respect to the waves and the large accelerations that these vessels may experience in waves due to their large forward speed. The resulting large variations of the submerged body shape may cause higher and lower order harmonics in the motion responses. Clear examples can be found in the work of De Jong and Keuning (2006), showing the results of forced oscillation experiments with a frigate-type hull at forward speed. They showed that in particular the submergence and emergence of the transom stern as well as the bow-flare can be associated with large non-linearities in the heave and pitch hydrodynamic derivatives, especially in the form of lower order harmonics. It should be noted that this non-linear behaviour does not necessarily lead to an increase of the responses. Instead, often decreases of the motion responses can be observed due to this type of motion responses (De Jong and Keuning 2006).

Second, non-harmonic responses may occur. A prime example of non-harmonic response is seen in the vertical accelerations of high speed ships in large head waves. Impacts may occur, and will occur if circumstances are severe enough, that typically show a large peak once per wave cycle on top of a harmonic signal.

Turning to the experimental data it turns out that the measured heave and pitch time traces are dominated by a harmonic response at the excitation frequency. Apparently the occurrence of lower and higher order harmonics is very limited. In fact, both designs underwent already a process of optimisation for seakeeping behaviour that essentially makes them perform in a more linear fashion than traditional high speed monohulls with low deadrise angles in the bow area.

At the larger excitation frequencies the time traces show disturbance of the harmonic motion responses. This disturbance stems from the very small magnitude of excitation and the response at large wave frequencies due to the constant wave steepness. Interferences due to noise and other harmonics caused by the moving towing carriage are then relatively large with respect to the motion response.



(a) Heave motion $U = 25\ kts$

(b) Heave motion $U = 35\ kts$

(c) Pitch motion $U = 25\ kts$

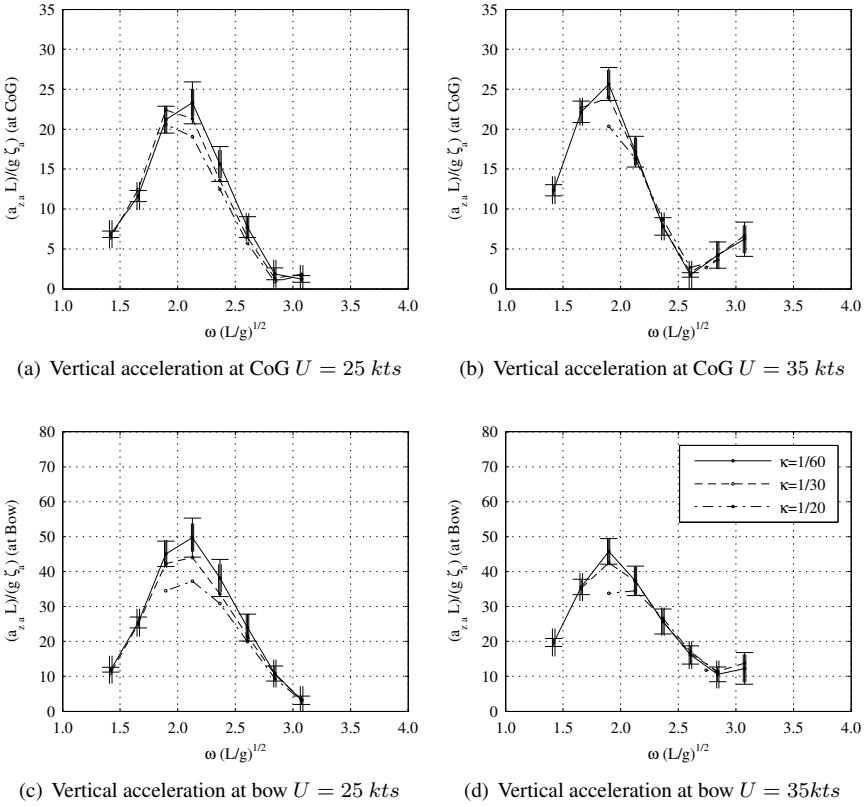
(d) Pitch motion $U = 35\ kts$

Figure 2.13: *Motion Response Amplitude Operators and their dependence on the wave steepness, ESC*

In fact the latter is a trade-off caused by the choice between either performing the regular wave experiments at constant wave amplitude or at constant wave steepness. Choosing the former, maximising the wave amplitudes in the search for non-linear effects will cause very short waves at high wave frequencies. These waves may break, or when avoiding this, the wave amplitude for longer waves is very limited. Choosing the latter, wave breaking is avoided at the cost of relatively small wave amplitudes at higher frequencies and a worsening signal to noise ratio and relatively large wave amplitudes at lower frequencies.

Although the heave and pitch signals share the single harmonic nature with the wave signals, still there is a noticeable amount of amplitude non-linearity visible in the motion response; the motion RAOs for increasing wave steepness are not coinciding but rather show a slightly decreasing trend in figure 2.13. Additionally the response is dependent on the forward speed; the pitch motion response is decreased by increasing the forward speed and obviously the peak in the response is shifted to a lower wave frequency due to the increased frequency of encounter.

Whereas for the motion response the Response Amplitude Operators seem to provide a nearly complete description of the behaviour in regular waves, this is not the case for the vertical



(a) Vertical acceleration at CoG $U = 25\ kts$ (b) Vertical acceleration at CoG $U = 35\ kts$

(c) Vertical acceleration at bow $U = 25\ kts$ (d) Vertical acceleration at bow $U = 35kts$

Figure 2.14: *Vertical acceleration Response Amplitude Operators and their dependence on the wave steepness, ESC*

accelerations due to non-harmonic behaviour. Figure 2.14 presents the RAOs for the vertical accelerations, that have been measured by dedicated accelerometers positioned at the bow and at the centre of gravity. Observing the figure, nearly the same conclusion may be drawn as from the motion RAOs: the acceleration RAOs are dependent on the wave amplitude with a decreasing trend for increasing wave amplitude and the acceleration levels at the bow are reduced with increasing forward speed. The latter seems related to the increased pitch damping at higher forward speeds.

Nonetheless, when studying the fit of the single harmonic sine to the acceleration signals it appears that the accelerations are non-harmonic in a large number of cases. Figure 2.15 shows an example of such time trace and the corresponding single harmonic fit for the vertical acceleration level at the bow. In particular large peaks occur in the bow accelerations during the part of the motion cycle that the bow moves downward to meet the water surface; i.e. impacting or slamming occurs. Obviously, this slamming is not recorded when extracting a single harmonic sine from the acceleration responses and is absent in the RAOs.

In order to quantify this effect further, the positive and negative acceleration maxima have

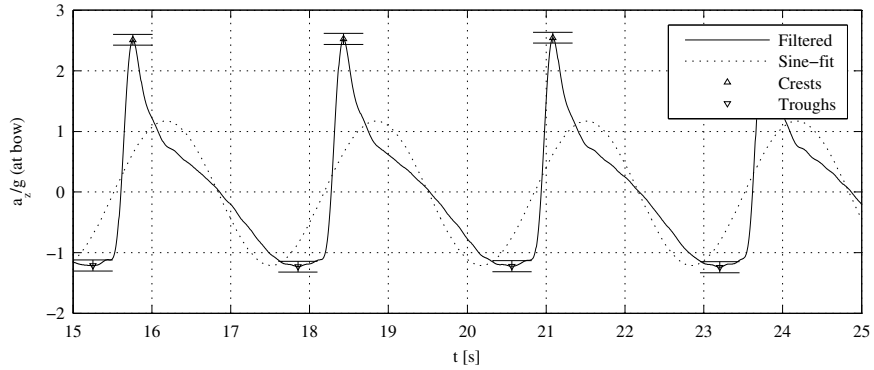
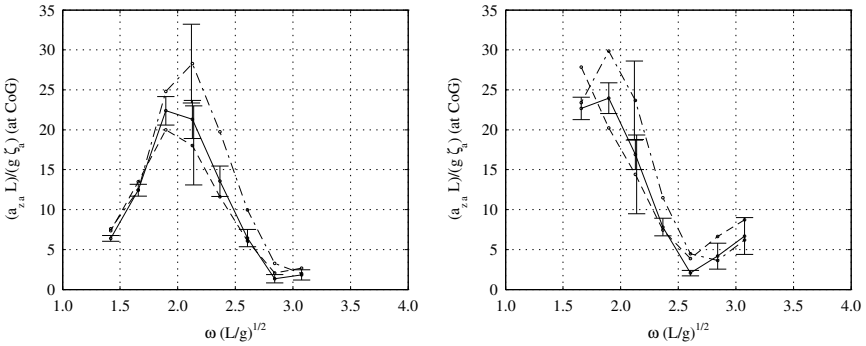
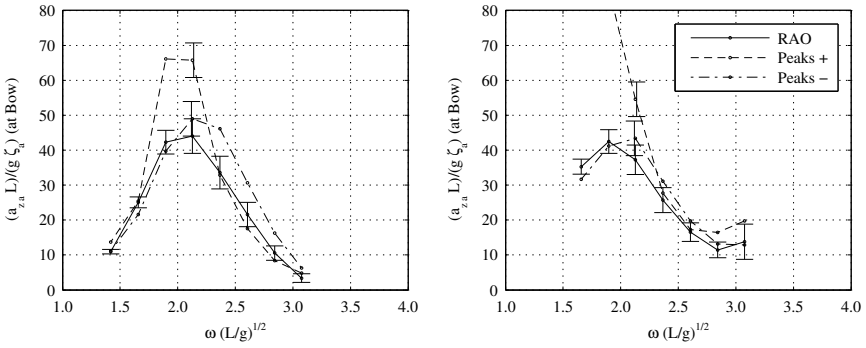


Figure 2.15: *Time trace of the vertical acceleration level measured at the bow, ESC,* $\kappa = 1/20$ $\omega = 4.02\ rad/s$ $U = 35\ kts$



(a) Vertical acceleration at CoG $U = 25\ kts$

(b) Vertical acceleration at CoG $U = 35\ kts$



(c) Vertical acceleration at bow $U = 25kts$

(d) Vertical acceleration at bow $U = 35kts$

Figure 2.16: *Vertical acceleration Response Amplitude Operators and (positive and negative) peaks, ESC,* $\kappa = 1/30$

been plotted together with the acceleration RAOs in figure 2.16 at the intermediate wave steepness of $\kappa = 1/30$. The positive and negative maximum values have been obtained by finding the peaks and troughs in the filtered acceleration signals and averaging the peak values and the trough values for each time trace. They are made dimensionless with respect to the wave amplitude in the same way as the acceleration RAO values, analogous to the RAO the result could be termed a 'Response Maximum Operator' (RMO). Although essentially non-linear, its usage alongside the RAO could be to quantify the occurrence of non-harmonic (and non-linear) maxima.

For a linear system the acceleration time traces would consist of a single frequency harmonic, and the peaks and troughs would closely correspond to the positive and negative amplitudes of the single harmonic function fitted trough the data. On the contrary, figure 2.16 shows large differences between the amplitudes and the peak values, particularly for the positive peaks occurring in the bow accelerations. This effect is highly dependent on both the wave amplitude and the forward speed. Although for brevity the graphs are omitted here, at a wave steepness of 1/60 peaks in the acceleration levels are virtually non-existent, whereas at a wave steepness of 1/20 they are even more pronounced.

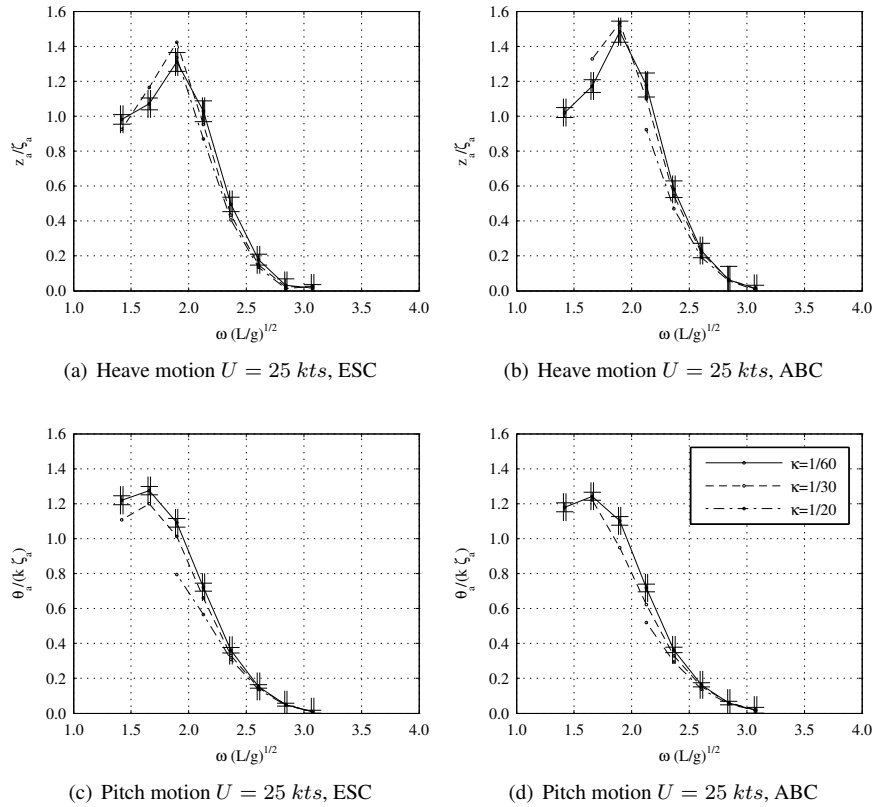
Interesting to note is that the RAOs suggest that the motions and acceleration levels relatively *decrease* for increasing wave steepness. In contrast to this, when studying the peaks that occur in the vertical acceleration levels, especially at the bow, it shows that these become relatively *more* extreme as the wave steepness increases. As pointed out when discussing full scale measurements and the development of criteria for the seakeeping of high speed vessel in section 2.2, the occurrence of these peaks are the limiting factor for the comfort and safety experienced on board and the operability of the vessel and its crew.

Comparison of Enlarged Ship Concept and Axe Bow Concept

A comparison of the motion responses of the Enlarged Ship Concept and the Axe Bow Concept in regular head waves is presented in figure 2.17, for a forward speed of 25 knots. Although very similar in appearance, the heave response of the Axe Bow Concept is larger than the heave response of the Enlarged Ship Concept, in particular near the resonance frequency. As the main difference between both designs is formed by the difference in the bow shape, apparently the Axe bow results in lower damping for the heave motion. Interestingly, the pitch responses show the opposite: the pitch response of the ESC is larger than the pitch response of the Axe Bow Concept. The reason may be the bow flare of the ESC.

Again when inspecting the measured heave and pitch time traces no large deviations from a single harmonic function are found. The motion responses of both design concepts can be considered close to linear with respect to the incident regular waves. An exception may be found in a mild amplitude dependence shown by the slight differences in the RAOs for different values of the wave steepness.

The larger vertical motion response of the Axe Bow Concept is confirmed by the fact that a larger number of experiments in the towing tank at the higher wave amplitudes needed to be stopped or cancelled for this concept. Due to the larger vertical motions, the model of the Axe Bow Concept was more prone to reach the limits of the vertical guide bearing in the test set-up (refer to figure 2.4). This effect was amplified by the choice to keep the wave steepness constant over the wave frequency, leading to relatively large wave and motion amplitudes for the longer regular waves.



(a) Heave motion $U = 25\ kts$, ESC

(b) Heave motion $U = 25\ kts$, ABC

(c) Pitch motion $U = 25\ kts$, ESC

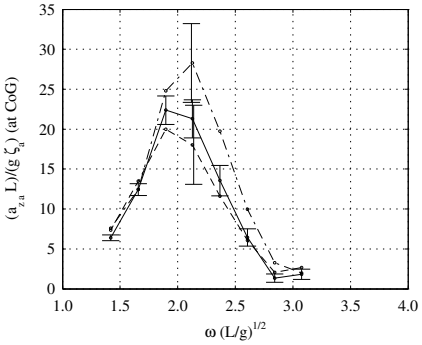
(d) Pitch motion $U = 25\ kts$, ABC

Figure 2.17: *Motion Response Amplitude Operators and their dependence on the wave steepness, comparison between Enlarged Ship Concept and Axe Bow Concept*

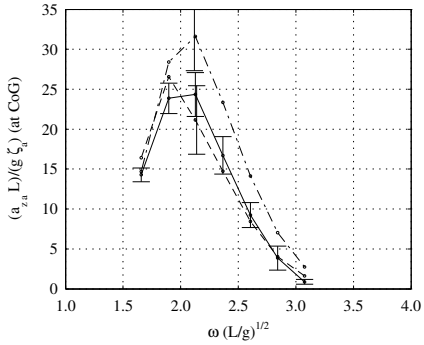
This behaviour especially occurred at the higher forward speed of 35 knots, where the heave motion response was larger than at 25 knots. For this reason the comparison between both designs is carried out at 25 knots; as a more complete picture can be given over the wave frequencies. The comparison at 35 knots, omitted here, shows very similar trends to the ones at 25 knots, but with a number of data points missing due to the bearing problems.

As outlined in the previous section, to compare the vertical acceleration levels the peak values need to be taken into account. In order to do this, besides the RAOs for the vertical acceleration levels at the bow and at the centre of gravity, also the positive and negative peak values of the acceleration time traces are plotted in figure 2.18 for the middle wave steepness of $\kappa = 1/30$.

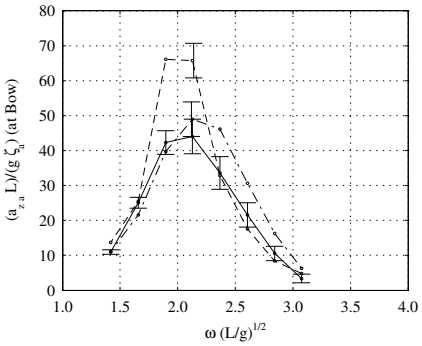
In figure 2.18 it can be noted that the vertical acceleration levels at the centre of gravity of the Axe Bow Concept are larger than the ones of the Enlarged Ship Concept. The peak values in the acceleration signals only differ to a small extend from the single harmonic amplitude. This corresponds to the already earlier observed relatively large heave motion response of the Axe Bow Concept. Nevertheless, it should be noted that the accelerometers at the center



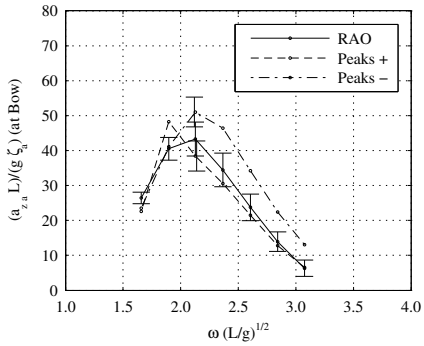
(a) Vertical acceleration at CoG $U = 25\ kts$, ESC



(b) Vertical acceleration at CoG $U = 25\ kts$, ABC



(c) Vertical acceleration at bow $U = 25\ kts$, ESC



(d) Vertical acceleration at bow $U = 25\ kts$, ABC

Figure 2.18: *Vertical acceleration Response Amplitude Operators and (positive and negative) peaks, $\kappa = 1/30$, comparison between Enlarged Ship Concept and Axe Bow Concept*

of gravity were placed on a different longitudinal position for both designs, caused by the fact that the longitudinal position of the center of gravity is different for both designs (refer to table 2.2). This difference could possibly explain part of the difference found in the measured vertical acceleration levels at the center of gravity.

In contrast to the acceleration levels at the center of gravity, the vertical acceleration levels at the bow show a entirely different picture. Although the 'linear' response -the one found applying the principle of the RAO- is nearly identical for both designs, the Enlarged Ship Concept suffers far more from the (positive) peaks in the vertical acceleration levels occurring at the bow. In fact, these peaks at the bow are nearly non-existent for the Axe Bow Concept.

This behaviour is confirmed when studying the time traces of both design concepts in an identical wave train. Figure 2.19 shows the time trace of the vertical acceleration at the bow for the Axe Bow Concept. This time trace can be directly compared to the time trace given in figure 2.15 for the Enlarged Ship Concept. Both time traces were obtained in the steepest regular wave near the resonance frequency at the the forward speed of 35 knots. Both figures

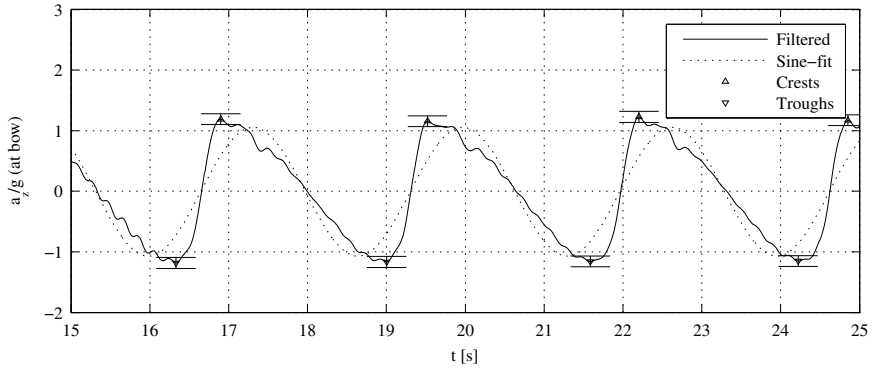


Figure 2.19: *Time trace of the vertical acceleration level measured at the bow, ABC,* $\kappa = 1/20$ $\omega = 4.02\ rad/s$ $U = 35\ kts$

show the filtered vertical acceleration signal, the sine fit at the wave encounter frequency, and the positive and negative peaks.

Clearly, the 'linear' sine fit is nearly identical for both design concepts, as well as the main part of the actual time trace. Nevertheless, the peaks in the time trace for the ABC are significantly reduced in comparison to the ESC, with a factor 3 from nearly $3g$s to $1g$. This reduction becomes even larger when moving to lower wave frequencies, unfortunately these experiments with the ABC could not be carried out due to the limitations of the test set-up in combination with the fixed values of the wave steepness described above.

It can be concluded that RAOs are not a valid tool for describing the entire motion response of fast ships in head waves, and in particular the vertical acceleration levels. Although peaks can be found in the vertical accelerations during regular wave towing tank testing, and even can be quantified next to the RAO, using the 'Response Maximum Operator', no clear indication as to how often these peaks occur can be obtained from regular wave tests. Either they do occur in the signal at each wave cycle or they do not.

Often the occurrence of peaks is attributed to the relative velocity of the impact of the bow in the instantaneous water surface. In a regular wave train this either occurs each wave cycle or it does not occur at all. Whether or not such threshold velocity is exceeded in an irregular seaway is dependent on the local superposition of wave components and is difficult to relate to peaks occurring in independent regular waves. Automatically this means that the RMO has little value in translating the information regarding the occurrence of peaks and their magnitude in regular waves to to irregular waves. Towing tank tests have to be performed in irregular head waves in order to further quantify the occurrence of peaks in the vertical accelerations.

One additional remark about the interpretation of the acceleration levels measured by means of accelerometers is that the actual measured acceleration level is highly dependent on a number of factors. First, an important role is played by factors related to the measurement, including but not limited to the type and capabilities of the sensor, the sampling frequency used to sample the measured time trace, and the level of low pass filtering to avoid noise and

anti-aliasing. Second, the structural properties, in particular the local structural properties in the area where the accelerometer is mounted, play a vital role in determining the acceleration levels that are measured.

On model scale, often but not always rightfully, the model is assumed to be fully rigid and hence the structural properties are often not taken into account, even if they are known. On full scale, it is nearly impossible to avoid the influence of the local and global structural response in the measured acceleration signals. In order to be able to compare the measured acceleration levels of different ships or models one should at least ensure that the influence of the structural response of model or full scale ship are of the same order of magnitude by carefully selecting where the accelerometers are mounted and how they are supported within the structure of ship or model.

When investigating the experimental results in regular head waves deeper than on the level of RAOs, it can be concluded that the further optimisation of the hull form from the Enlarged Ship Concept to the Axe Bow Concept for minimisation of the occurrence of these peaks to improve the safety and ride comfort is a successful one. Ironically, this optimisation (as was already described in chapter 1) results in hull forms that perform more and more in 'linear' way, from a conventional high speed monohull to the Enlarged Ship Concept and finally the Axe Bow Concept.

2.3.6 Irregular head waves

The experiments in irregular head waves have been performed using a JONSWAP wave spectrum with a peak period of 7.8 seconds and a gamma of 3.3. In order to keep the amount of data and the number of towing tanks runs to be performed manageable, it was decided to use a wave spectrum with only one particular peak period and to gradually increase the significant height. Table 2.4 summarises the wave conditions used in these experiments. Based on scatter diagrams of the wave conditions on the North Sea these wave conditions are considered to be representative of the worst conditions that can be found on the North Sea.

Table 2.4: *Wave conditions*

$H_{1/3}$	T_2	T_p	γ
$[m]$	$[s]$	$[s]$	$[-]$
2.0	6.0	7.8	3.3
2.5	6.0	7.8	3.3
3.0	6.0	7.8	3.3
3.5	6.0	7.8	3.3
4.0	6.0	7.8	3.3

The chosen peak period of 7.8 seconds results in a non-dimensional peak frequency of $\omega\sqrt{L/g} = 1.9$. The resulting encounter frequency corresponds closely to the frequency of maximum response of the ESC and ABC in head waves at 25 knots; refer for instance to figure 2.13. Forward speeds of 25, 35 and 50 knots full scale have been used. Special care was taken to obtain signals with enough length to obtain reliable statistical data. To do this repeated runs have been performed in spatial (or temporal) different parts of the wave realisation of the spectrum to obtain a run length equal to at least 200 to 300 peak periods.

The same test set-up has been used as with the calm water experiments and the tests in regular head waves, discussed in the previous sections. In addition to the Enlarged Ship and Axe Bow Concepts, the Wave Piercer Concept has been used again in these experiments.

The general findings of the experiments in irregular head waves are summarised by Keuning and Van Walree (2006):

1. All three designs share roughly the same significant values for the heave, pitch and vertical acceleration responses in comparable wave conditions.
2. Only the Axe Bow Concept complied with the limiting criteria (outlined in section 2.2).
3. Large differences were found between the peaks occurring in the vertical acceleration levels at the centre of gravity but particularly at the bow for the three design concepts. The Wave Piercer Concept in general experienced 40 percent lower values at the bow than the Enlarged Ship Concept, whereas the Axe Bow Concept even showed a reduction of 65 percent compared to the Enlarged Ship Concept.
4. Although showing a favourable occurrence of peaks in the vertical acceleration levels, the Wave Piercer Concept suffered severely from shipping of green water. This made testing in the towing tank in higher sea states impossible. On full scale this will pose highly impractical requirements on water tightness and streamlining of the above water part of the hull and the superstructure. Visibility requirements and deck wetness criteria will require the use of breakwaters that will experience severe loadings.

Rayleigh plots as a tool for non-linear analysis

The previous section demonstrated that the motions of high speed vessels in head waves and in particular the vertical acceleration levels are non-linear with respect to the wave elevation. By using a linear analysis of the seakeeping behaviour of high speed vessels, important data, such as the occurrence of peaks in the acceleration levels, are simply neglected. Furthermore, it was shown that even when studying the occurrence of peaks in the vertical acceleration levels in independent regular wave components it is extremely difficult to relate these to the occurrence of peaks in a stochastic, irregular seaway.

For this reason, it is important to study the seakeeping behaviour in actual irregular sea states, albeit that this comes with additional difficulties. These difficulties are related to the limited length of the towing tank meaning that a large number of runs has to be performed for the same sea state to provide statistical reliable data. It is important to come up with analysis tools that enable at least visualisation of non-linear behaviour. One such tool that is extensively used at the Ship Hydromechanics Laboratory of the Delft University of Technology is the Rayleigh plot.

$$f(x) = \frac{x}{\sigma^2} \exp\left(-\frac{x}{\sigma\sqrt{2}}\right) \tag{2.1}$$

Theoretically, the envelope of a band-limited (or narrow banded), normally distributed signal follows the Rayleigh distribution, given in (2.1). Longuet-Higgins (1952) applied this argument to ocean waves. He demonstrated that the crest-to-trough wave height follows the Rayleigh distribution provided that the free surface elevation is distributed sufficiently narrow banded. When this is the case it can be shown (Longuet-Higgins 1952) that the envelope

of the wave elevation is symmetrical with respect to the zero-line; considering the crest-to-trough wave height is in that case equivalent to considering the magnitudes of the crests and troughs separately.

Following Ochi (1973), crests are defined as local maxima occurring above the zero-line and troughs as local minima below the zero-line. Local negative maxima and positive minima are discarded. Refer to figure 2.20 for a graphical clarification. Formally written by Ochi (1973), the maxima of a random $X(t)$ are given by: $\left\{X(t) > 0, \dot{X}(t) = 0, \ddot{X}(t) < 0\right\}$ and the minima by: $\left\{X(t) < 0, \dot{X}(t) = 0, \ddot{X}(t) > 0\right\}$. Ochi's reasoning is that negative maxima and positive minima are unnecessary for engineering purposes. At the same time, relating them to an envelope can be awkward.

Several authors have put forward (Thompson 1974, Haring et al. 1976, Forristal 1978) that in fact the application of the Rayleigh distribution led to an over-prediction of the wave heights when studying actual measured records of wave elevations. Eventually, the inaccurate fit of the Rayleigh distribution to the wave height distribution was linked to the spectral shape of the wave elevation distribution, in particular the spectral width (Forristal 1984) and in fact the wave elevation distribution was found to be not always sufficiently narrow banded. Subsequently, several adjusted probability distributions have been proposed to provide an improved prediction of the wave heights (Longuet-Higgins (1980) amongst others). In spite of this, the Rayleigh distribution remains a reliable and well-used tool for the estimation of the design wave used in the design of ship and offshore constructions, where over-prediction often is considered an extra safety factor.

Another usage of the Rayleigh distribution is to determine the non-linear characteristics of ship motions. This technique works as follows: assuming that the incident wave elevation is a narrow banded, normally distributed signal, the wave amplitudes are Rayleigh distributed. Assuming the ship behaves in a linear fashion then also the motion time traces (motions and acceleration levels) should abide the narrow-banded Gaussian distribution and also their minima and maxima (crest and trough values) should follow the Rayleigh distribution. In the case of non-linearities, these should show up in the form of deviations of the minima and maxima distributions with respect to the Rayleigh distribution.

This is visualised by plotting the probability of exceedance of the minima and maxima in a so-called Rayleigh plot. The horizontal axis, showing the probability of exceedance, is deformed using in such way that that the probability of exceedance of Rayleigh distributed minima or maxima shows up as a straight line. According to the Rayleigh distribution the probability of exceedance of amplitude x_a over a threshold value a is given by:

$$P(x_a > a) = \int_a^\infty \frac{x}{\sigma^2} \exp\left(-\frac{x}{\sigma\sqrt{2}}\right) dx = \exp\left(-\frac{a^2}{2\sigma^2}\right) \tag{2.2}$$

This can be rewritten as in (2.3). This relation is used to deform the horizontal axis. At the same time the axis is inverted so that a probability of exceedance of 100 % (corresponding threshold value is zero) coincides with the intersection with the vertical axis.

$$a = \sigma\sqrt{-2\ln\left(P(x_a > a)\right)} \tag{2.3}$$

The standard deviation is related to the significant amplitude by means of:

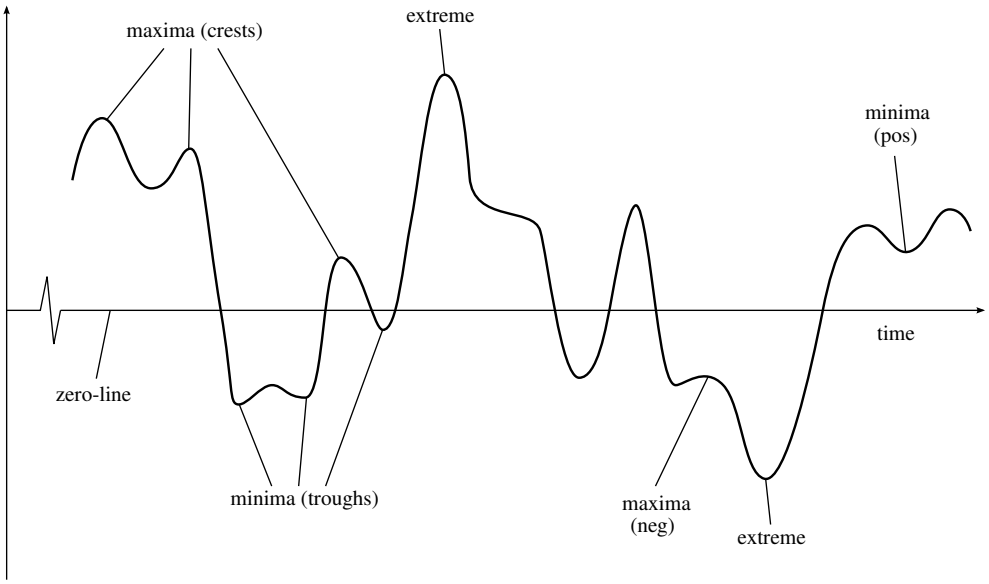


Figure 2.20: *Definition of maxima and minima of a time trace (based on Ochi (1973))*

$$x_{a1/3} = 2\sigma \tag{2.4}$$

The result is that the probability of exceedance of Rayleigh distributed maxima and minima show up as straight lines. The link between the time trace containing the maxima and minima and the resulting straight line is formed by the significant value of time trace; in particular the inclination of this line. Any deviations from this line mean that the minima or maxima are not Rayleigh distributed. If the input signals (the wave elevation maxima and minima) are Rayleigh distributed then this means that the ship behaves in a non-linear fashion.

One of the implications of the validity of the Rayleigh distribution is that the peak value, for instance occurring once in every thousand wave cycles, is directly linked to the significant value of the time series. When the ship motion behaviour would be linear then criteria posed on the significant value of the motion response would suffice in capturing the maximum values. In the case that the vessel behaves in a non-linear way, peak values are not any more directly linked to significant values. This behaviour can be visualised and quantified using the Rayleigh plot.

The measured time series are analysed to find the crests and troughs that occur in the measured time traces. This process should be carried out carefully; a large number of local maxima occur due to high frequency disturbances not related to the rigid body motions in noisy signals -especially acceleration levels- and require low-pass filtering. If not sufficiently filtered this results in a large number of crests and troughs and therefore distortion of the Rayleigh plot. Nevertheless, too aggressive filtering will affect the peak values and remove extremes; although at the same time peak values may be distorted by noise.

The resolution sought here is by setting a minimum time lag between two subsequent crests or troughs of 0.5 seconds, combined with low-pass filtering at 20 Hz. With a peak

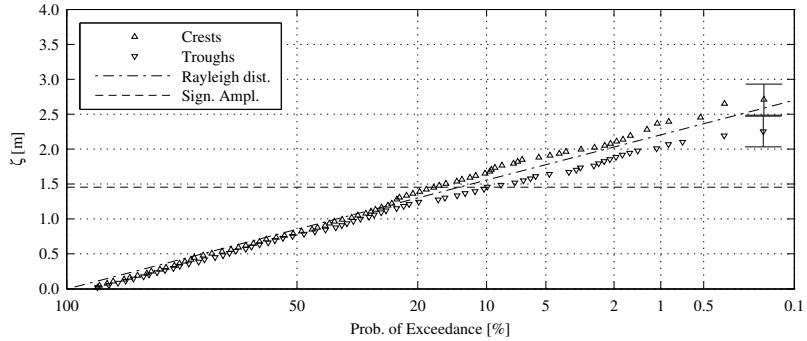


Figure 2.21: *Rayleigh plot of peaks and troughs and significant amplitude of wave elevation, condition:* $T_p = 7.8\ s$*,* $H_{1/3} = 3.5\ m$*, and* $U = 35\ kts$

period of 7.8 seconds, and peaks occurring normally only two times per wave period (one slamming peak and one rigid body motion peak due to the wave induced motions) a value of 0.5 seconds is reasonable and yields satisfactory results. Another resolution that was tried was to assume only one maximum between two zero-crossings and to discard maxima and minima of less than 10% of the standard deviation of the signal combined with low-pass filtering at 20 Hz. This yielded comparable results, however (minor) distortion was visible in the lower part of the Rayleigh plot, while peak values were largely retained.

In some cases a vertical 'stack' of peaks or troughs at one probability value may be observed in Rayleigh plots, in particular for low probabilities of exceedance of around 0.1 to 0.5 %. This is caused by the occurrence of a single or a few maxima occurring in one frequency 'bin' while the neighbouring 'bins' are empty. A 'bin' is the discrete portion of local maximum values that is used to compute the probability of exceedance. Especially for high valued local maxima (and minima) that only occur a once or twice during the time series this may happen. In that case, each of the bins that does not contain values is assigned the same probability of exceedance as the previous bin. Once or twice in about 300 wave cycles results in a probability of 0.3 to 0.6 %. Extending the length of the time series would probably skew the vertical stacks towards lower probabilities. In this thesis these vertical stacks are removed by not plotting empty bins in the graphs.

An example of these Rayleigh plots is given in figure 2.21. In the figure a Rayleigh plot is shown for a wave realisation of a wave spectrum with a peak period $T_p = 7.8\ s$ and a significant wave height $H_{1/3} = 3.5\ m$, measured on the towing carriage moving at a high forward speed (35 kts full scale). Four plots are shown in the graph: the triangles show the probability of exceedance of maxima and minima (troughs and crests) in the measured wave elevations, the inclined dash-dotted line shows the corresponding 'Rayleigh line', related to the measured signal by means of the significant value, and finally the horizontal dashed line presents the significant amplitude of the signal. Both lines intersect at $\exp(-2) \approx 13.5\%$, by definition.

Comparison of the three design concepts

For the purposes of this discussion detailed results will only be shown for the medium high forward speed of 35 knots at a significant wave height of 3.5 metres. After studying the extensive data set, these results represent the typical differences in motion behaviour between the three design concepts. Moreover, the forward speed of 35 knots represents much better the typical maximum operational speeds of current high speed monohulls in patrol and SAR roles -more than the 50 knots that within the scope of the research project should be seen as a 'future challenge'. In the final part of this comparison a brief overview will be presented of all results and an evaluation of the criteria set to the HSNV design.

Unfortunately no results are available at 3.5 metres significant wave height for the WPC and instead results at 3.0 metres are used in this comparison for this vessel. In fact, when studying the wave elevation time traces of all three cases (ESC, ABC, and WPC) it becomes apparent that the actual realised significant wave heights are respectively: 3.3 m and 3.1 m for the ESC and ABC, and 2.9 m for the WPC. These values are relatively unreliable, because of accuracy problems with the measurement of waves with wire type wave probes at high forward speeds caused by spray and ventilation of the probe wires.

Table 2.5: *Significant values*

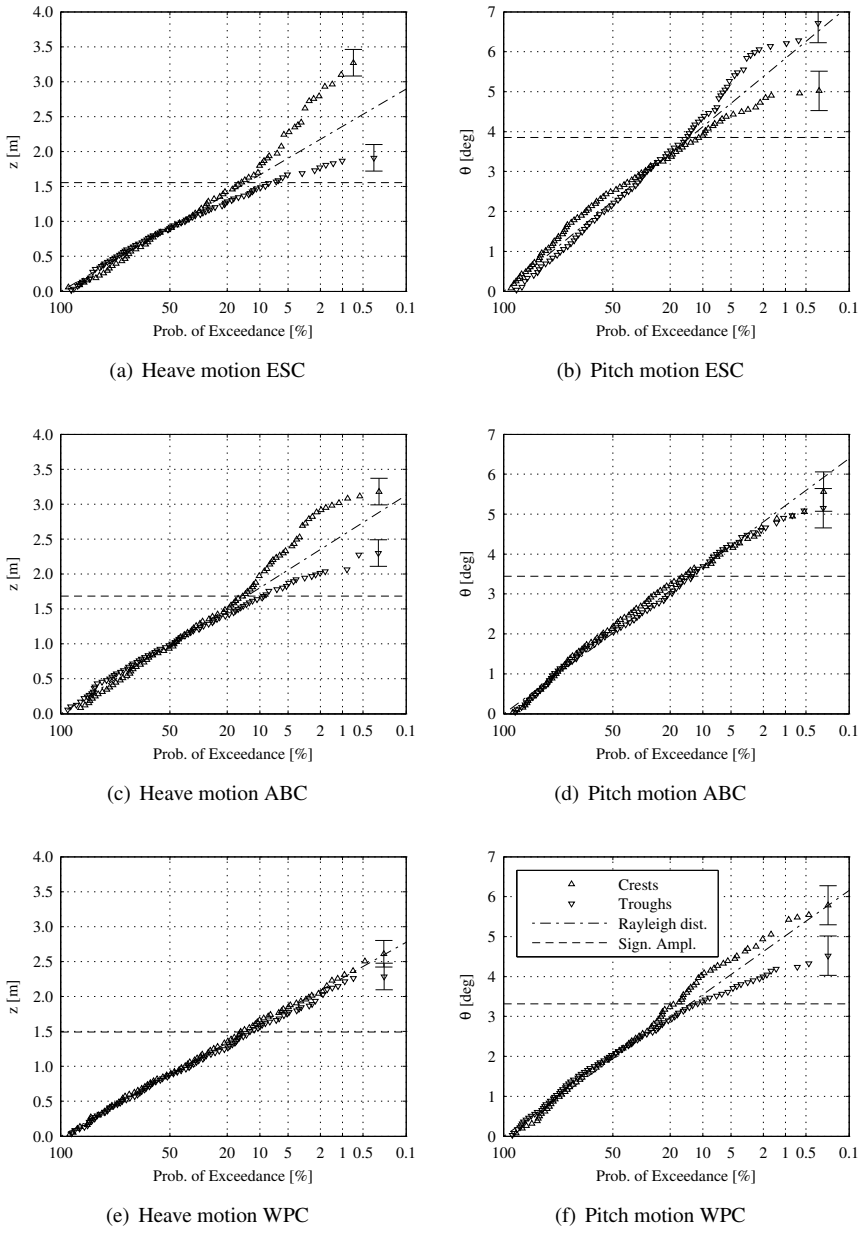
Quantity	Symbol	Unit	ESC	ABC	WPC
Wave amplitude	ζ_a	m	3.50	3.50	3.00
Heave amplitude	z_a/ζ_a	–	0.89	0.96	0.99
Pitch amplitude	$\theta_a/(k\zeta_a)$	–	32.98	29.53	33.82
Vert. acc. amplitude (at CoG)	$a_{zacog}L/(g\zeta_a)$	–	19.14	19.82	18.38
Vert. acc. amplitude (at bow)	$a_{zabow}L/(g\zeta_a)$	–	36.02	33.18	29.37

Table 2.5 presents an overview of the significant wave amplitude and the non-dimensional significant motion and acceleration amplitudes, made non-dimensional using the significant wave amplitude. This significant wave amplitude was the one achieved during the tuning of the wave signals in absense of the model as the measurement of the wave elevation obtained during the actual experiments were unreliable (as was outlined above). Although all three experiments were performed in slightly different wave conditions, in particular for the WPC, this way of presenting provides a way of discounting the differences in the wave conditions.

Only slight differences are generally found between the three designs. The WPC seems to produce the lowest acceleration levels and the ESC the highest. The trend for the heave motion is exactly the reverse. The pitch motions are smallest for the ABC. The comparison between the behaviour of the ABC and the ESC confirms the results based on the RAOs determined in the regular wave experiments presented in the previous section.

In the light of the discussion above, before comparing the motion and accelerations of the three designs using Rayleigh plots, one should first check whether the maxima and minima of the wave elevation are Rayleigh distributed. This check can be performed by observing figure 2.21 showing a Rayleigh plot of a wave realisation. Although sometimes small deviations were found, generally the maxima in the generated waves were in fact Rayleigh distributed.

The Rayleigh plots for the heave and pitch motions are presented in figure 2.22. The heave motions become progressively more linear moving from the ESC to the WPC. In con-

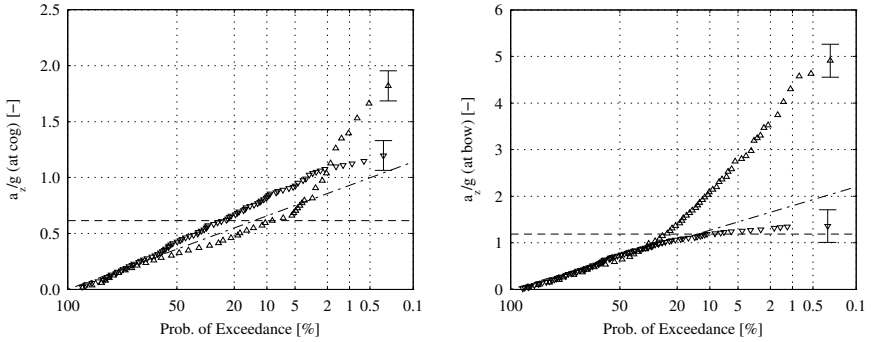


(a) Heave motion ESC (b) Pitch motion ESC

(c) Heave motion ABC (d) Pitch motion ABC

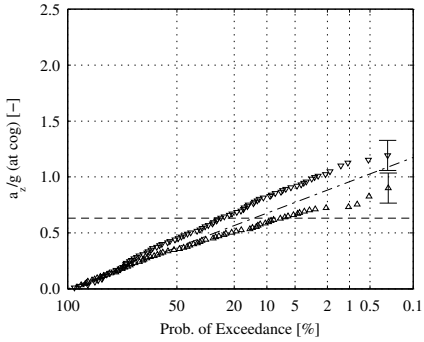
(e) Heave motion WPC (f) Pitch motion WPC

Figure 2.22: *Rayleigh plots of peaks and troughs and significant amplitudes of heave and pitch motions, condition:* $T_p = 7.8\ s$*,* $H_{1/3} = 3.5\ m$*, and* $U = 35\ kts$

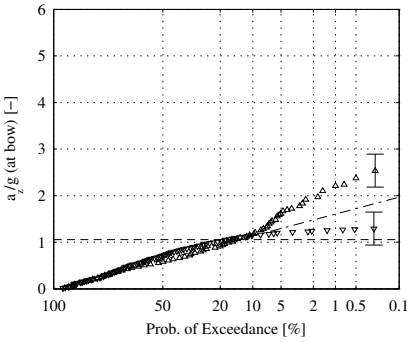


(a) Vertical acceleration at CoG ESC

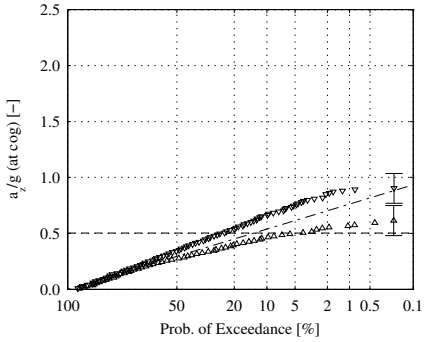
(b) Vertical acceleration at bow ESC



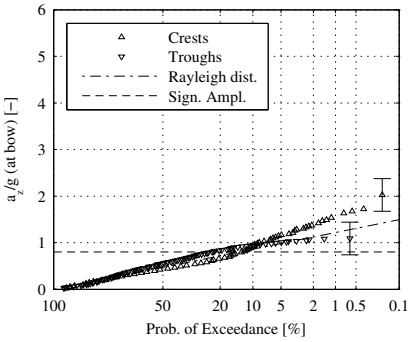
(c) Vertical acceleration at CoG ABC



(d) Vertical acceleration at bow ABC



(e) Vertical acceleration at CoG WPC



(f) Vertical acceleration at bow WPC

Figure 2.23: *Rayleigh plots of peaks and troughs and significant amplitude of vertical acceleration levels at the CoG and at the bow, condition:* $T_p = 7.8\ s$, $H_{1/3} = 3.5\ m$, *and* $U = 35\ kts$

trast, the pitch motions show another trend: the pitch motions of the ABC are nearly linear and symmetric, while those of the other two designs are significantly more non-linear. The ESC shows significant less bow down pitch amplitude, and the WPC the other way around significant less bow up amplitudes. Observing the different bow lines, with V-shapes for the ESC, a 'linear' vertical shape for the ABC and the Wave Piercer bow for the WPC this different behaviour seems logical.

In fact, similar conclusions may be drawn by studying the Rayleigh plots instead of the significant values or the RAOs for the heave and pitch motions. Nevertheless, a more complete picture of the underlying behaviour is obtained by studying the Rayleigh plots. This becomes even more apparent when studying the Rayleigh plots in figure 2.23 depicting the vertical acceleration levels at the centre of gravity and at the bow.
The vertical accelerations at the centre of gravity show a very similar behaviour for all three designs. The levels are slightly lower for the WPC; this may be attributed to the lower significant value of the wave elevations signal discussed above. Those of the ESC, especially the upward directed crests show a relatively large occurrence of peaks above $1g$. Apparently the large upward peaks measured at the bow translate partly to the acceleration levels at the centre of gravity.

The vertical accelerations level at the bow shows a very interesting behaviour. The downward peaks (troughs) and the significant values are relatively close for the three designs and do not become much larger than $1g$; the downward motion is dominated by the gravity force pulling the ship downwards and the effects of rotational motions on the accelerations are of minor importance. The upward peaks however, show large differences: the ESC suffers from large peaks exceeding $5g$s, whereas the other two designs did not exceed $3g$s. The lower values of the WPC may again be offset by the lower significant wave height.

To complete the comparison in irregular head waves, an overview of the operability of the three design concepts in the tested wave conditions is presented in table 2.6. The criteria outlined in section 2.2 are applied in table. Summarising the criteria for the maximum accepted vertical acceleration levels:

- $8.0\ m/s^2 = 0.8g$ at the wheelhouse ($13.0\ m/s^2 = 1.3g$ for vessels smaller than approx. 20 metres in length).
- $20.0\ m/s^2 = 2.0g$ at the bow ($25.0\ m/s^2 = 2.5g$ for vessels smaller than approx. 20 metres in length).

Furthermore, limits to the deck wetness were set in the HSNV design specification. Unfortunately, this criterion has not been applied using a verifiable measurement procedure and threshold value, but its estimation was left to expert opinion. For this estimation, visual observation ('eyeball' verification) during the model experiments and video material obtained during these experiments were used.

Though this approach was lacking in consistency, in practice it turned out to be a feasible one. Both the ESC and the ABC hardly shipped any green water, whereas the Wave Piercer Concept shipped large amounts of green during the experiments. In fact, due to this shipping of green water a significant amount of the test program of the WPC, at high forward speeds in the more severe wave conditions, could not be completed. In one particular case the model of the WPC was even lost during the experiment due to large quantities of Green water inside the model. The cases where shipping of green water was limiting are indicated with a $*$-

superscript, and are in fact the main reason for non-compliance of the WPC monohull to the requirements set to the HSNV.

Table 2.6: *Operability in tested wave conditions using developed criteria (Keuning and Van Walree 2006)*

U	$H_{1/3}$	ESC	ABC	WPC
$[kts]$	$[m]$			
25	2.0	$\surd^a$	$\surd$	$\surd$
25	2.5	$\surd$	$\surd$	$\surd$
25	3.0	$\times^b$	$\surd$	$\surd$
25	3.5	$\times$	$\surd$	$\times^{*c}$
25	4.0	$\times$	$\times$	$\times^*$
35	2.0	$\surd$	$\surd$	$\surd$
35	2.5	$\times$	$\surd$	$\surd$
35	3.0	$\times$	$\surd$	$\times$
35	3.5	$\times$	$\times$	$\times^*$
50	2.0	$\times$	$\surd$	$\surd$
50	2.5	$\times$	$\surd$	$\surd$
50	3.0	$\times$	$\surd$	$\times^*$
50	3.5	$\times$	$\surd$	$\times^*$
50	4.0	$\times$	$\surd$	$\times^*$

[a] $\surd$ - meets all criteria
[b] $\times$ - exceeds one or more criteria
[c] $*$ - run not completed due to excessive deck wetness

The maximum acceleration levels measured on the ABC decreased with increasing forward speed. The maximum acceleration levels measured on the ESC were worst for the medium forward speed of 35 knots. The acceleration levels measured on the WPC increased with increasing forward speed, although it was difficult to obtain a very clear picture for this particular design concept. This was caused by the excessive shipping of green water preventing the completion a large amount of runs for the WPC (indicated with the asterisks in table 2.6).

The Axe Bow Concept was the only design concept capable of sailing at 50 knots in the highest sea state during the experiments presented here. This concept hardly suffered from slamming nor from shipping of green water in all tested sea states. Only in two cases the Axe Bow Concept did not meet the the design criteria. Both these cases occurred at the lower forward speeds; either indicating an increase of motion damping with forward speed, or a shift of the encounter frequency away from the resonance frequency of the ABC, or both.

Based on the RAOs obtained during the tests in regular head waves in 25 and 35 knots the resonance frequency of the ABC equals approximately 1.8 rad/s. Based on the forward speed this is equivalent to a wave period of 7.3 s at 25 knots, 8.3 s at 35 knots, and 9.3 s at 50 knots. In the latter case the resonance period has indeed moved relatively far from the peak in the wave spectrum (refer to figure 2.24), resulting in lower motion responses at the highest forward speed.

Based on typical scatter diagrams of the North Sea and the results presented above, it can be stated that the Axe Bow Concept achieves a 100% all year round operability. Based

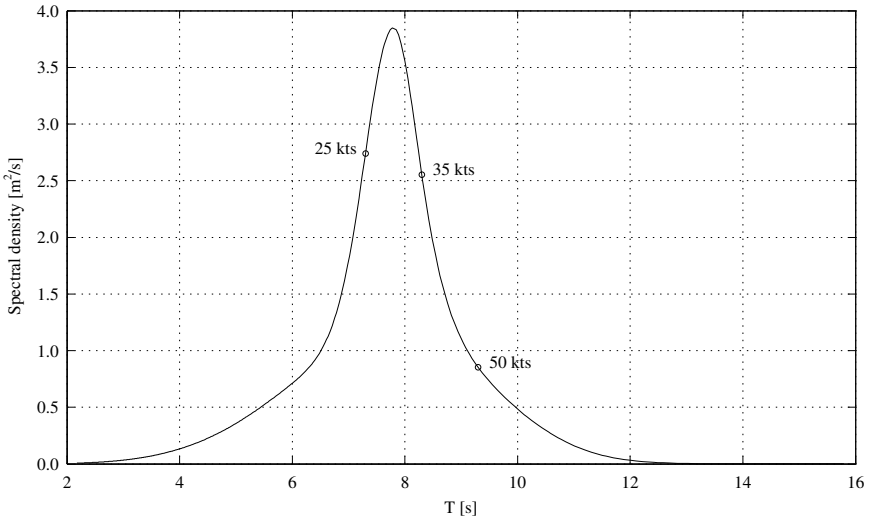


Figure 2.24: *JONSWAP spectrum, $T_p = 7.8\ s$, $H_{1/3} = 4.0\ m$ and estimated resonance periods ABC at three forward speeds*

on the vertical acceleration levels, the Enlarged Ship Concept achieves a significantly lower operability, whereas the Wave Piercer Concept suffers from shipping of green water in a substantial part of its operational envelope.

In conclusion, the Rayleigh plot can be useful for the comparison of the seakeeping behaviour of high speed ships, in particular for vertical acceleration levels and the occurrence of maxima, that directly impose limits on the safety and operability of such vessels. Not only insight is gained in the occurrence of maxima but also their relation to significant values becomes apparent. In this way the Rayleigh plot provides a deeper understanding of the motion behaviour than the 'classical' tools as RAOs and significant values of time traces.

2.3.7 Regular following waves

To investigate the impact of bow diving and shipping of green water in following waves, limited model tests have been carried out in regular following waves with all three design concepts at three forward speeds, 20, 35, and 50 knots full scale. The experiments were carried out at the Delft University of Technology using the test set-up identical to the previously presented tests, but now running the towing carriage away from the wave maker instead of towards the wave maker in head waves.

These tests were meant as a limited and simplified comparison of the design concepts. The model setup prevented the models from carrying out surge motions. Although surge motions may have a large influence on the motion behaviour in following waves and the occurrence of bow-diving, it was reasoned that because of the identical aft ship of the design

concepts, the action of the (aft incoming) waves on the vessels would be of a very comparable nature.

A variation of wave lengths was used to obtain encounter frequencies around the zero encounter frequency. In this way, runs in all possible situations were performed: waves overtaking the model, identical wave celerity and model speeds, and the model overtaking the waves. Again the wave height was gradually increased in order to assess the limits of operability of the models in following waves. The criteria used for this assessment were:

1. The occurrence of bow diving.
2. Shipping of green water and deck wetness.

The assessment of these criteria was carried out by visual observation and by the analysis of video recordings of the experiments. Moreover RAOs were obtained for the heave and pitch motions and vertical acceleration levels. In order to quantify non-linear behaviour in terms of the wave amplitude RAOs were determined at each frequency for a number of wave heights. Besides the amplitude non-linearity, also non-harmonic behaviour was observed due to of shipping green water; resulting in some cases in severe harmonic disturbance and noisy signals.

Just as for the shipping of green water in head seas, again no easily verifiable quantification and threshold values for the criteria were set. Still the differences in behaviour between three design concepts were sufficiently large to justify the following conclusions:

1. Non-harmonic behaviour in terms of non-sinusoidal motion responses was limited to the cases with bow diving combined with shipping of green water.
    - The heave response was linear with the wave height and more or less identical for all three vessels.
    - The pitch response was nearly linear with the wave steepness, largest for the WPC and nearly identical for the ESC and the ABC.
2. The vertical acceleration levels were in all cases moderate and did not pose any limitation to the operability.
3. Neither bow diving nor deck wetness occurred with either the ESC or the ABC.
4. Bow diving did occur with the WPC, combined with extreme deck wetness and shipping of green water.
    - The tendency of bow diving diminished with increasing forward speed.
    - The effects of bow diving, in terms of shipping of green water, increased with forward speed.

That the tendency to bow dive diminished with forward speed could be attributed to two diffent mechanisms. First, it is known that ships are most sensitive to bow diving when their forward speed is close to the wave celerity. At the higher forward speeds the model started to overtake the following waves. The forward speed was shifted away from the wave celerity, resulting in a different, negative, encounter frequency. Second, the running attitude changed with forward speed. The larger trim at larger forward speeds naturally decreased the tendency to bow dive. Nevertheless, when bow diving did occur for the WPC at higher forward speeds, its bow shape, combined with the higher forward speed resulted in severe shipping of green water.

2.3.8 Stern-quartering waves

The motivation behind model experiments in stern-quartering waves were the concerns about the higher risk of broaching of the Axe Bow Concept in following and stern-quartering waves. It was feared that yaw angles would cause relatively strong lift forces on the bow due to the vertical foil-like appearance of the bow. These lift forces, if limited to the bow region, would cause a de-stabilizing hydrodynamic moment in the direction of the yaw amplitude. When this moment cannot be counter acted by the rudder force than broaching may occur. Similarly, (sideways) sway velocities combined with the forward speed would cause lift forces to be generated. Although this force is directed opposite to the sway velocity, and seems stabilizing, it may cause both yaw and roll moments, suggesting a strong coupling between sway, yaw and roll.

In order to observe and quantify this type of behaviour, it was decided to perform the experiments with self-propelled models in Seakeeping and Manoeuvring Basin of MARIN in stern quartering waves (as outlined in section 2.3.3). As the WPC was already disqualified due to excessive shipping of green water in head seas, only the 'best' two designs were considered in these tests. The waves were generated using again a JONSWAP wave spectrum with a significant wave height of 2.5 metres and a peak period of 6.75 seconds, a representative spectrum for the North Sea area, with probabilities of exceedance of the wave height of 15 % of the time. A limited amount of tests have been performed in waves with a significant height of 3.5 metres, using a JONSWAP spectrum with the same peak period of 6.75 seconds. Wave directions between 300 and 330 degrees were tested and two forward speeds, 20 and 50 knots full scale.

Furthermore, tests have been performed in a bi-chromatic wave train. This is a semi-regular wave train with two regular sine components of nearly the same wave length, resulting in a nearly regular wave train with slowly varying amplitude over time. The primary wave length was selected in such way that a sensitive situation arose for broaching for the particular model and forward speed, in this case 1 to 1.4 times the waterline length. The wave height was gradually increased to identify the limiting height for each of the two models for broaching. In irregular waves brouching is a rare event that requires a large simulation time to be measured with statistcal reliability or even to be measured at all. The idea behind the choice for bi-chromatic waves was that conditions under which broaching occurred could be replicated more easily; in effect making the broaching behave more deterministically. In this work, the focus will be on the analysis of the results obtained in irregular waves.

In this research a broach was defined in very broad terms as simultaneously exceeding a heel angle of 50 degrees and a yaw angle of 40 degrees. The general findings of these test were summarised by Keuning and Van Walree (2006) as follows:

1. Both the Enlarged Ship Concept as the Axe Bow Concept did not experience a real broach during any of the tests.
2. There was no large difference in tendency to broach between both models.
3. The Axe Bow Concept experienced larger roll angles than the Enlarged Ship Concept, although the difference was not very large.
4. Maximum (crest to trough) roll angles did not exceed 35 degrees and maximum (crest to trough) yaw angles did not exceed 40 degrees, for both designs.
5. There was a relatively large influence of the heading (wave direction) on both the roll and the yaw motions.

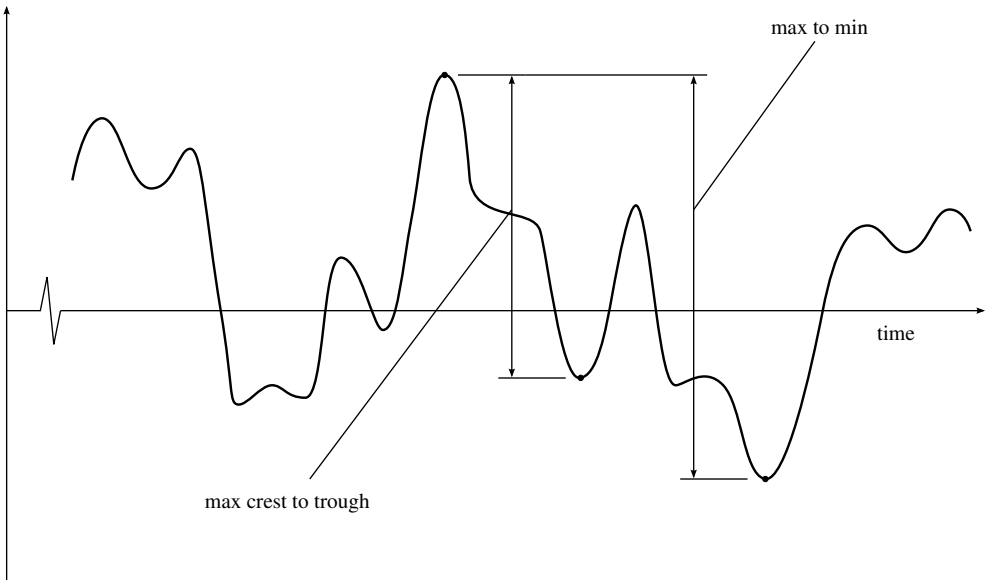


Figure 2.25: *Relation maximum crest to trough and maximum to minimum value of a time trace*

To judge the motion behaviour in stern-quartering waves, it is more logical to consider these crest to trough values instead of individual maxima and minima. Unlike the heave, roll, and pitch motions, the horizontal plane motions surge, sway, and yaw do not posses a clear neutral value. From the perspective of course keeping and broaching the extent of individual motion excursions irrespective of their relation to the neutral value are far more important than the magnitude of individual maxima and minima.

The crest to trough values were found by first identifying the individual local maxima and minima in the same manner as described in section 2.3.6, followed by linking adjacent maxima and minima to obtain the crest to trough values. Their maximum generally is lower than the difference of the maximum and the minimum of the same time trace, as the maximum and minimum of the time trace do not necessarily occur in the same or in adjacent cycles (refer to figure 2.25).

Two differences were introduced here. First, also negative valued maxima and positive valued minima were included instead of only including positive maxima and negative minima. This was mainly done to accomodate the large (and low frequent) excursions made in the surge and sway motions (and therefore the fact that these responses were not narrow banded). Figure 2.26 shows an example of a surge time trace, showing the wave frequent motion on top of a low frequent motion. Although the low frequent behaviour could be removed by high pass filtering, it was feared that this filtering would remove too much information from the time traces. Second, the minimum required distance between individual maxima or minima was increased to 4 seconds. This value was obtained by slowly increasing it from 0.5 seconds, until the measured wave elevation time trace was behaving accordingly the Rayleigh distribution.

Figure 2.27 shows the significant and maximum crest to trough values of the surge motion and

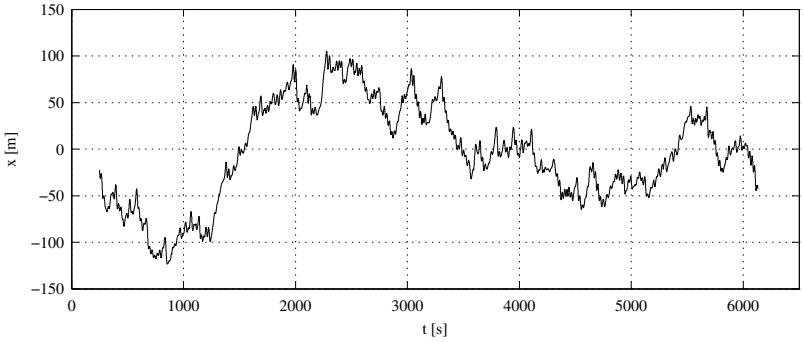


Figure 2.26: *Time trace of surge motion (Axe Bow Concept), condition:* $\psi_w = 315\ deg$, $T_p = 6.75\ s$, $H_{1/3} = 2.5\ m$, *and* $U = 20\ kts$

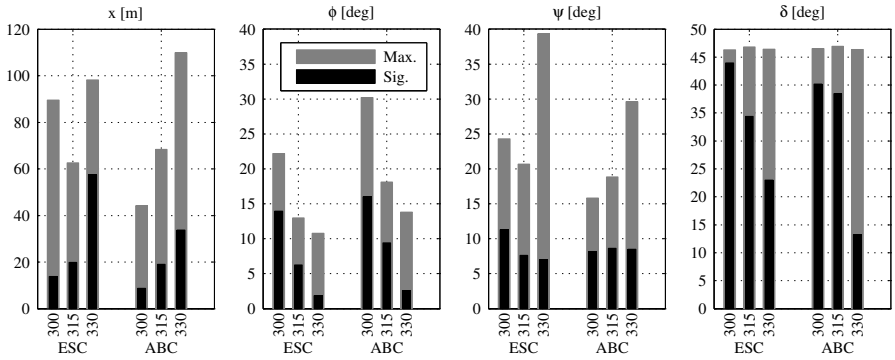


Figure 2.27: *Comparison significant and maximum crest to trough values ESC and ABC for roll, yaw, and nozzle angle at three headings, condition:* $T_p = 6.75\ s$, $H_{1/3} = 2.5\ m$, *and* $U = 20\ kts$

the roll, yaw, and nozzle angles for both design concepts in irregular waves at three different headings of 300, 315, and 330 degrees and a forward speed of 20 knots (Froude number 0.44). Based on figure 2.27, it can be seen that the surge motion displayed by the Enlarged Ship Concept, in terms of the significant value, is larger than for the Axe Bow Concept. At a heading of 330 degrees the ABC shows a much larger maximum value.

The maximum behaviour of the surge motion may be of more importance than its significant value as it may indicate the occurrence of surf-riding. Surf-riding, a large and fast excursion in the surge direction on the front face of a wave, often is a precursor to broaching. Nevertheless, the fact that maxima are rare events, and therefore of a highly stochastic nature, makes direct comparison of both design concepts difficult. This is even further complicated by the fact that self-steering and self-propulsion introduce a relatively large randomness in the location of the model in the wave train and therefore in the action of the waves on the model and its response.

Like the surge motion, also the roll motion shows a large dependence on the heading

both in terms of maximum crest to trough values and the significant values. The roll motion peaks at a heading of 300 degrees, whereas the yaw motion peaks at 330 degrees for both designs. The significant value of the yaw motion seems less dependent on the heading. The ABC clearly suffers more from rolling than the ESC, while for the yaw motion the opposite is true. This may indicate a stronger coupling between yaw and roll for the ABC. Due to its bow shape a yaw motion can introduce a relatively large roll moment.

The nozzle angles show that in all conditions presented here the maximum nozzle steering angle is reached. At headings of 300 and 315 degrees the maximum and significant crest to trough values of the nozzle angle are relatively close, meaning that the maximum nozzle angle was reached relatively often. Curiously, this does not coincide with the largest yaw motion. The nozzle angle was controlled by an autopilot, the control parameters of the autopilot were identical for both design concepts.

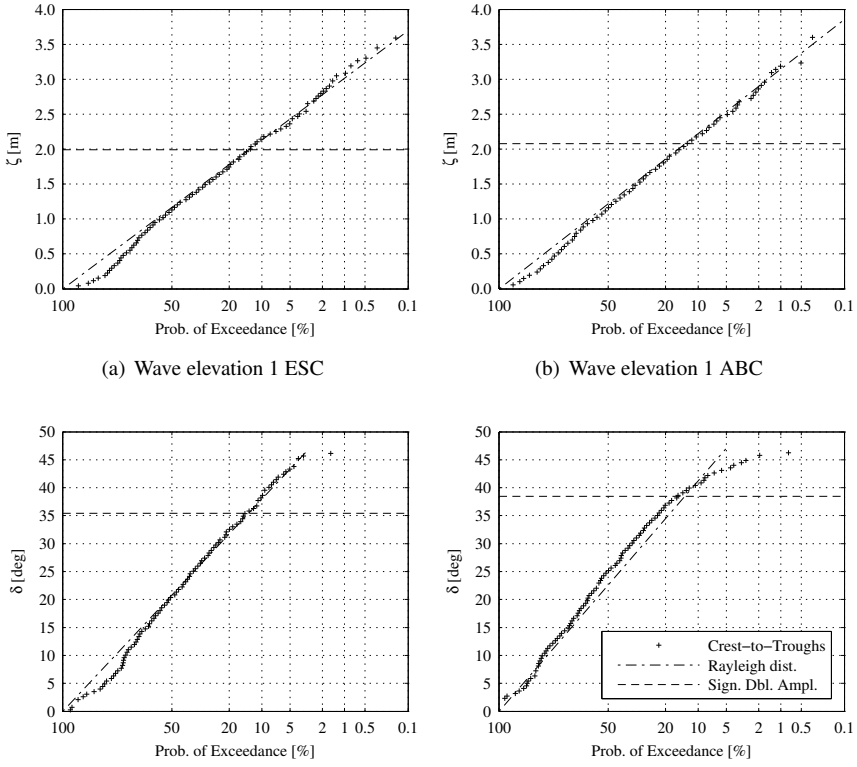
Additional results, not presented here, show that the yaw motions as well as the nozzle angles significantly decrease when the forward speed is increased to 50 knots. In fact, at 50 knots the frequency of encounter becomes negative: the ship is overtaking the waves. The main reason for this decrease seems to be the increase in lift force generated by the skegs due to the increased forward speed, although also the shift in frequency of encounter may cause large differences.

To obtain a more complete picture Rayleigh plots of the crest to trough values of both designs at 315 degrees heading are depicted in figures 2.28, 2.29, and 2.30. Figure 2.28 shows Rayleigh plots of the wave elevation and the nozzle angles for both designs. The wave elevation, measured at a location that was relatively undisturbed by radiated and diffracted waves from the model, closely follows the Rayleigh line. The wave conditions match closely for both designs. The Rayleigh plot of the nozzle angles show that the nozzle angle of the ABC relative more often reached the maximum nozzle range of 46 degrees (two times 23 degrees), confirming the trend in figure 2.27(d).

Figure 2.29 contains the Rayleigh plots of the surge, sway, and heave motions, figure 2.30 those of the roll, pitch, and yaw motions. The surge and sway motions show a large emphasis on extreme reponses and do not adhere to the Rayleigh distribution. The main cause of this seems to be the non-narrow bandedness of both motions, possibly partly caused by the interaction of the autopilot controlled steering and the wave induced motions. As was illustrated before in figure 2.26, the surge and sway motions show a relatively large low frequent motion on top of which the wave frequent responses occur. Although in the identification of crest to trough values the lower valued higher frequent oscillations were favoured by the search algorithm, still the influence of low frequent excursions seems to visible in the distribution of the crest to trough values. In spite of this, the distributions are remarkebly similar for both designs for both the surge and the sway motions.

Although not the main focus here, the heave and the pitch motions show a much more linear behaviour. The ESC shows considerably larger heave motions, especially in terms of the significant crest to trough values. The pitch motions are nearly identical for both designs. The maximum pitch angles are relatively large at around 8 degrees, larger than was found in head waves.

The comparison of the roll motion shows that over the whole range the roll motions are larger for the Axe Bow Concept. The yaw motion shows a more curious behaviour. The ESC suffers from a relative large amount of higher valued crest to trough values than the ABC, while the significant value of the yaw crest to trough values is larger for the ABC. Both the



(a) Wave elevation 1 ESC

(b) Wave elevation 1 ABC

(c) Nozzle angle ESC

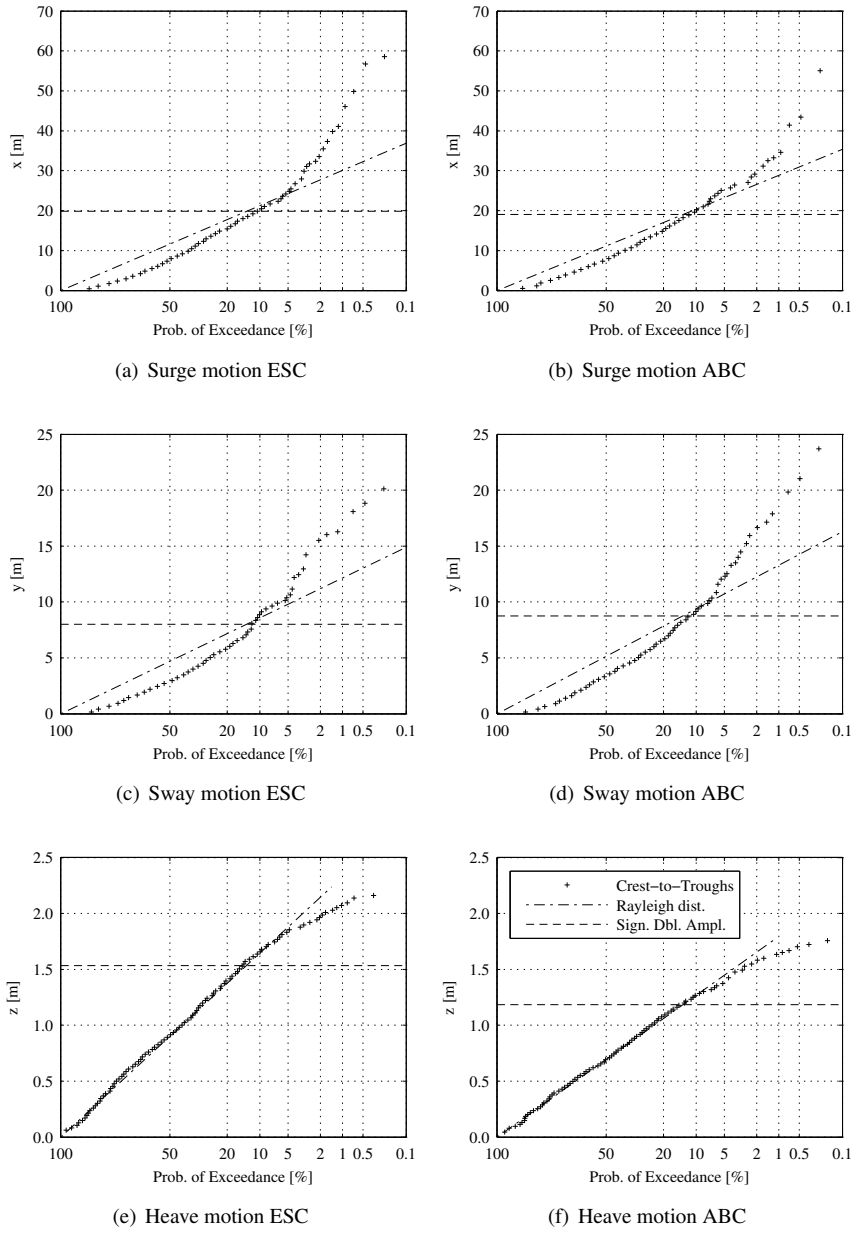
(d) Nozzle angle ABC

Figure 2.28: *Rayleigh plots of peaks and troughs and significant amplitude for stern quartering waves, condition:* $\psi_w = 315\ deg$, $T_p = 6.75\ s$, $H_{1/3} = 2.5\ m$, *and* $U = 20\ kts$

roll and the yaw motions of the ABC follow the Rayleigh line much more closely than those of the ESC, and in that sense perform more linear.

In conclusion, although no real broach was encountered during the experiments in stern-quartering waves, both tested designs showed some interesting differences in their motion responses under similar conditions. The Axe Bow Concept performed much more linear than the Enlarged Ship Concept when considering the yaw and roll responses, while the Enlarged Ship Concept showed relatively more emphasis on maximum responses. The roll motion of the Axe Bow Concept was shown to be significantly larger than that of the Enlarged Ship Concept. Depending on the heading, the yaw responses showed a more mixed behaviour in terms of maxima, its significant values remained however nearly constant for both designs.

Both designs show large differences in the surge motion, especially in terms of maximum crest to trough values. These may be related to the inherently larger randomness introduced in self-steered and self-propelled model tests, and are indicative of the challenges of successful comparison of the results obtained with this kind of model test. Rather than just using significant values and maxima for the comparison of motion reponses in stern-quartering waves,



(a) Surge motion ESC

(b) Surge motion ABC

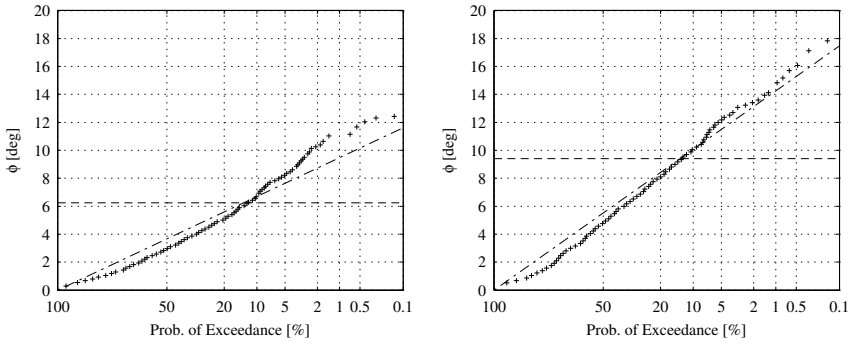
(c) Sway motion ESC

(d) Sway motion ABC

(e) Heave motion ESC

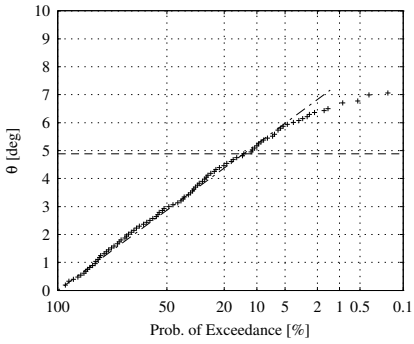
(f) Heave motion ABC

Figure 2.29: *Rayleigh plots of peaks and troughs and significant amplitude for stern quartering waves, condition:* $\psi_w = 315\ deg$, $T_p = 6.75\ s$, $H_{1/3} = 2.5\ m$, *and* $U = 20\ kts$

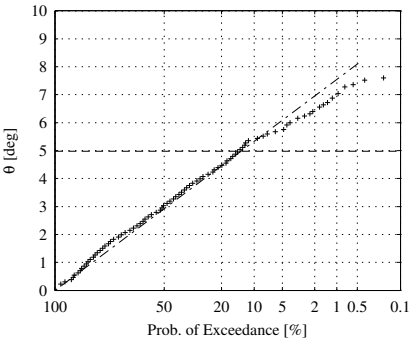


(a) Roll angle ESC

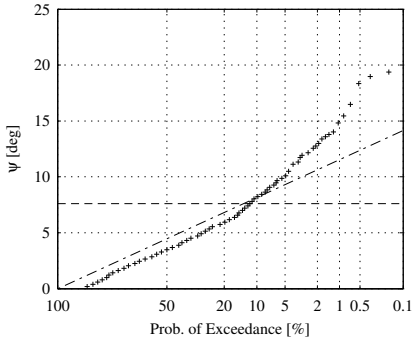
(b) Roll angle ABC



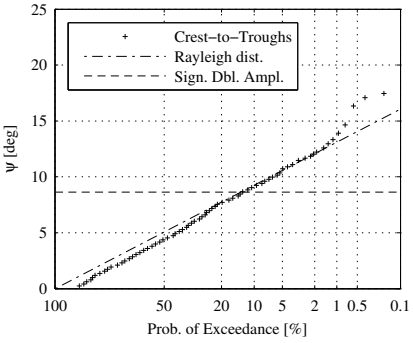
(c) Pitch angle ESC



(d) Pitch angle ABC



(e) Yaw angle ESC



(f) Yaw ABC

Figure 2.30: *Rayleigh plots of peaks and troughs and significant amplitude for stern quartering waves, condition:* $\psi_w = 315\ deg$, $T_p = 6.75\ s$, $H_{1/3} = 2.5\ m$, *and* $U = 20\ kts$

Rayleigh plots enable a more detailed comparison and avoid conclusions to be based on the occurrence of a single maximum value.

2.4 Discussion

Based on the previous two sections, the first one dealing with full scale behaviour of fast vessels at sea taking into account the viewpoint and behaviour of the crew and the second dealing with the seakeeping behaviour of these vessels at model scale in the laboratory, the following observations can be made:

- High speed vessels operating in head and bow-quartering waves are subjected to motions that are characterised by the occurrence of high peaks of several gs in the vertical acceleration level and these peaks in particular are limiting for both the crew as the ship's structural integrity. In fact, the occurrence of (too high) peaks in the vertical acceleration level is a direct incentive for the crew to react, mainly by means of (voluntary) speed reduction, impacting the operability profile.
- The limiting behaviour of high speed vessels operating in stern-quartering and following waves is characterised by the risk of bow diving and broaching. Bow diving was found to be highly dependent on bow shape and forward speed. The latter included two aspects. First, the frequency of encounter changes with forward speed and ships are mostly sensitive to bow diving at a encounter frequency close to zero, when the wave celerity is close to the forward speed. Second, the running attitude changes with forward speed and increased trim may reduce the risk on bow diving.
- Although a linear approach to the motions of these vessels gives a surprisingly accurate representation on the level of heave and pitch motions in head waves, the occurrence of peaks in the vertical acceleration is severely underestimated when using the linear approach. The linear approach assumes a fixed relation between significant motion levels and maximum levels and this relation is clearly violated by this kind of vessel.

To successfully analyse the seakeeping behaviour of fast vessels it does not suffice to use Response Amplitude Operators to compute the resulting motion behaviour in a sea state and setting limits to the significant values of the motions and accelerations levels as is done in a conventional seakeeping analysis. An alternative approach is to perform time domain analysis on computed or measured time traces and to construct Rayleigh plots of these time traces. These plots indicate the probability of exceedance of the peaks and troughs that occur in the motions and in particular in the acceleration levels. This tool enables not only a more accurate quantification of the occurrence of peaks, but also provides insight in to how often these peaks occur; more than by just identifying only the single maximum value in a time trace.

The application of Rayleigh plots is not limited to motions and acceleration in head waves, but may also be applied to motions in other wave directions. When applied to large horizontal plane motions crest to trough values should be considered instead of individual maxima and minima. When applied in this way, Rayleigh plots are shown to be a useful tool for the study of the motion behaviour in stern-quartering waves.

In this experimental study three designs concepts were compared that each already were optimised to some degree for better seakeeping behaviour. The Axe Bow Concept, being

a further development on the basis of the Enlarged Ship Concept, was selected as the best performing design of the three, with a 100% all year round operability under the conditions studied. The Wave Piercer Concept showed in some cases an even better motion behaviour than the Axe Bow, but nevertheless suffered disproportionally from shipping of green water and therefore was rejected on the basis of the requirements set.

On a side note, one particularly interesting point was raised in the discussion about the acceleration levels aboard the larger and optimised high speed vessels. As the acceleration levels at the wheelhouse were severely reduced due to the seakeeping optimisation, the crew relied on far more indirect feedback, such as structural vibrations following an impact at the bow, to judge the seakeeping behaviour. This change may have an impact on the safety on board these vessels and should be taken into account to provide the crew training or feedback on how to safely operate this kind of vessel.

Although clear criteria were set for the motions and accelerations in head waves, the criteria for deck wetness (shipping of green water) and broaching behaviour were more ambiguous. This may be attributed to a (still) limited knowledge of the phenomena involved, and in particular with respect to the quantification of these aspects in terms of crew safety, structural integrity, and finally operability. These topics warrant further research and usage of the knowledge generated in such research may lead to a next step in the evolution of high speed vessels for duty at sea.

Chapter 3

Development of a Computational Model

3.1 Introduction

In chapter 1 the need was argued for accurate and efficient computational tools for the assessment of the seakeeping behaviour of high speed vessels in terms of motions, acceleration levels, loads and dynamic behaviour. The present chapter presents the development of a numerical model for the seakeeping of fast ships. Fast in this context is defined as the range of Froude numbers over length from 0.5 to 1.2. Depending on the hull form, most ships are not fully planing in this speed regime, but hydrodynamic lift becomes of importance and can cause significant dynamic trim and rise of the centre of gravity. This change in running attitude can result in essentially different motion behaviour in a seaway (Keuning 1994) and will need to be included in the computational method.

The numerical model has been programmed in the Fortran programming language and the resulting program is termed *Panship*. The formulation of the numerical model is based on the work of Lin and Yue (1990) and further developed by Van Walree (1999; 2002) to study the interaction of submerged lifting surfaces and ships, in particular hydrofoils. The model is based on a three-dimensional time domain Green function method and is capable of dealing with significant forward speeds and arbitrary three-dimensional (large amplitude) motions due to the use of a transient Green function, as was demonstrated by for example King et al. (1988). The free surface boundary conditions are linearised to the undisturbed free surface, while it is possible to retain the body boundary condition on the actual submerged geometry. Practically, it is necessary to linearise the body boundary condition as well, to reduce the computational burden of the method, enabling the seakeeping analysis to run on a normal desktop computer.

Customisations of the method are implemented, specifically aimed at fast ships. This includes the formulation of a transom flow condition at the stern to ensure that the flow leaves the transom smoothly at high forward speed of the ship. Attention is paid to pressure evaluation methods that include the Froude-Krylov and hydrostatics pressures on the instantaneous submerged body with the option of using pressure profile stretching. Modules to include the forces due propulsion systems and due to motion control appendages such as rudders, trim flaps, interceptors and lifting surfaces into simulations have been implemented.

Although the method is linearised to the calm water submerged body surface, the reference position is adapted using the trim and sinkage at the forward speed of the ship. In effect, the body linearisation is performed around the calm water reference position at the correct forward speed. The development of this computational model for high speed ships has been reported earlier in several papers: De Jong et al. (2007), De Jong and Van Walree (2008), Van Walree and De Jong (2008), De Jong and Van Walree (2009).

The first section will discus the choice for this particular computational method. The subsequent two sections describe the assumptions behind potential flow theory and basic fluid mechanics as well as the choice of reference frames. Sections 3.5 and 3.6 contain the mathematical and numerical details of the potential flow method and its solution. Section 3.7 describes the pressure evaluation possibilities and section 3.8 deals with the empirical inclusion of viscous flow effects. Finally, section 3.9 details the solution of the equations of motion. A number of details of the derivations presented in this chapter can be found in appendices A, B, and C.

3.2 Choice of computational model

Summarising from chapters 1 and 2, the main characteristics of the seakeeping behaviour of fast ships are:

- The relatively large forward speed.
- The relatively large (relative) motions and consequent large submerged geometry variations.
- The occurrence of peaks in the vertical accelerations when the relative velocity of the bow and the free surface becomes large.
- The occurrence of rare events as bow-diving and broaching in stern quartering and following waves.
- Partly or fully ventilated transom stern flow.

Based on the discussion in the first chapter, linear strip theory and linear frequency domain diffraction methods are not taken into consideration. Linear strip theory does not satisfactorily deal with motions in all degrees of freedom as large longitudinal flow interactions (occurring with large sway and yaw motions in oblique seas) are not sufficiently dealt with. Moreover, both linear approaches are not capable to deal with large forward speed in a satisfactory manner.

One of the requirements for the computational model, as mentioned in chapter 1, is that it should be possible to operate the model in a research and design environment. Although fully non-linear potential flow methods are available and in theory are able to deal with the complete fluid flow problem of high speed seakeeping, with exception of viscous flow, in the current state-of-art they require too much computational effort at too much risk for large instabilities in their solution (Beck and Reed 2001). For these reasons this class of approaches is discarded in the current work.

An intermediate solution may be found in a non-linear two-dimensional approach (the 2D+t-approach), either empirical or based on non-linear $2D$ potential flow solutions. Although this class of methods is promising, especially in head seas, it is felt that they suffer

too much from the two-dimensional flow assumption to be successful in 3D problems, just as their linear counterpart mentioned above. Nevertheless, at least for the roll motion several authors have come up with promising numerical approaches (for instance Judge et al. (2004)).

Without resorting to fully three-dimensional CFD, with or without viscous models, the remaining options are either the body-exact large amplitude motion approach or the usage of a double body basis flow plus unsteady flow in a body linear or body-exact approach. Either approach can be coupled with so-called blended techniques, where a number of contributions, such as hydrostatics, are computed in a non-linear fashion and combined with the linear hydrodynamic solution. In the current work the prior model, the body-exact approach, is chosen and will be extended to deal with fully ventilated transom flow.

Nonetheless, in this work one major simplification will be made. The body boundary condition will be linearised to the mean forward speed orientation of the body, incorporating forward speed calm water trim and sinkage. Although this simplification offsets a main advantage of the method, the body exactness, it is necessary in order to reduce the computational load substantially. The code in its body-exact form requires a prohibitively large computational effort in order to be applied in a practical research and design environment. To partly reduce the impact of this simplification a blended approach is developed, where the Froude-Krylov forces, the added mass force, and the hydrostatics can be computed on the instantaneous wetted surface and a pressure stretching approach is introduced to apply the linearised hydrodynamic (radiation plus diffraction) pressures on the instantaneous wetted surface.

The reasoning behind this choice is that a practical applicable computational method is obtained that can be run in a desktop environment, though it remains possible to move to the body-exact approach when either more efficient methods arise to more rapidly deal with the history integrals due to the usage of the time domain free surface Green function, or the computational power on the desktop becomes sufficiently large. Several customisations that are introduced in this work can be directly carried over in the body-exact approach.

In fact at the moment work is ongoing in parallel to develop numerical techniques to compute the Green function integrals more efficiently. Preliminary results show a very promising run time speed up.

3.3 Potential flow theory

3.3.1 Conservation of mass

Conservation of mass in a moving and deforming volume $V(t)$ can be enforced by requiring that the rate of change of mass within the volume plus the net flux of mass over the boundary $S(t)$ of $V(t)$ equals zero.

$$\frac{d}{dt}\int_{V(t)} \rho \, dV + \int_{S(t)} \rho \boldsymbol{v}_r \cdot \boldsymbol{n} \, dS = 0 \tag{3.1}$$

Using the derivation of the Reynolds transport theorem given in appendix A with $\eta(\boldsymbol{x}, t) = 1$ and left hand side equal to zero this equation can be rewritten as:

$$\int_{V(t)} \left(\frac{\partial}{\partial t} \rho + \nabla \cdot \rho \boldsymbol{v} \right) dV = 0 \tag{3.2}$$

Assuming incompressible flow the equation of continuity reduces to:

$$\int_{V(t)} \nabla \cdot \boldsymbol{v} \, dV = 0 \tag{3.3}$$

The differential form of the equation of continuity is given by:

$$\nabla \cdot \boldsymbol{v} = \frac{\partial u}{\partial x} + \frac{\partial v}{\partial y} + \frac{\partial w}{\partial z} = 0 \tag{3.4}$$

3.3.2 Conservation of momentum

Conservation of momentum can be achieved by requiring that the rate of change of momentum within a moving and deforming volume $V(t)$ and the flux of momentum through the boundary $S(t)$ of $V(t)$ equals the net external force exerted on the fluid in $V(t)$.

$$\frac{d}{dt} \int_{V(t)} \rho \boldsymbol{v} \, dV + \int_{S(t)} \rho \boldsymbol{v} \left(\boldsymbol{v} \cdot \boldsymbol{n} \right) dS = \sum \boldsymbol{F} \tag{3.5}$$

Again the application of the Reynolds transport theorem (appendix A) enables the elimination of the boundary integral and the resulting equation can be rewritten by using the chain rule for differentiation:

$$\int_{V(t)} \boldsymbol{v} \left(\frac{\partial \rho}{\partial t} + \nabla \cdot \rho \boldsymbol{v} \right) + \rho \left(\frac{\partial \boldsymbol{v}}{\partial t} + \boldsymbol{v} \cdot \nabla \boldsymbol{v} \right) dV = \sum \boldsymbol{F} \tag{3.6}$$

Substitution of conservation of mass (3.2) eliminates the first term in each integral:

$$\int_{V(t)} \rho \left(\frac{\partial \boldsymbol{v}}{\partial t} + \boldsymbol{v} \cdot \nabla \boldsymbol{v} \right) dV = \sum \boldsymbol{F} \tag{3.7}$$

Assuming an inviscid, incompressible fluid, the external force on the fluid in the control volume $V(t)$ only consists of pressure acting on the boundary and gravity acting on the complete body of the fluid.

$$\int_{V(t)} \rho \left(\frac{\partial \boldsymbol{v}}{\partial t} + \boldsymbol{v} \cdot \nabla \boldsymbol{v} \right) dV = - \int_{S(t)} p \boldsymbol{n} \, dS + \int_{V(t)} \rho \boldsymbol{g} \, dV \tag{3.8}$$

Using the Gauss' divergence theorem outlined in appendix A to rewrite the surface integral for the pressure into a volume integral, Euler's equation for inviscid flow appears:

$$\int_{V(t)} \rho \left(\frac{\partial \boldsymbol{v}}{\partial t} + \boldsymbol{v} \cdot \nabla \boldsymbol{v} \right) dV = \int_{V(t)} \left(\rho \boldsymbol{g} - \nabla p \right) dV \tag{3.9}$$

The final step to arrive at potential flow is to assume the flow is irrotational. That means that the fluid elements posses zero angular velocity. The average angular velocity at a point in a fluid can be defined as one half the curl of the velocity at the same location. Instead often the

vorticity is used to describe the angular motion in a fluid, defined as the curl of the velocity field, effectively dropping the factor of one half of the average angular velocity:

$$\boldsymbol{\zeta} = \text{curl}\, \boldsymbol{v} = \begin{vmatrix} \boldsymbol{i} & \boldsymbol{j} & \boldsymbol{k} \\ \frac{\partial}{\partial x} & \frac{\partial}{\partial y} & \frac{\partial}{\partial z} \\ u & v & w \end{vmatrix} \tag{3.10}$$

The second term in the left hand side integral term in (3.9), an acceleration term, can be written as follows:

$$(\boldsymbol{v} \cdot \nabla)\, \boldsymbol{v} = \nabla \left(\frac{1}{2} V^2 \right) + \boldsymbol{\zeta} \times \boldsymbol{v} \tag{3.11}$$

The vorticity in an irrotational flow is zero, $\boldsymbol{\zeta} = \text{curl}\, \boldsymbol{v} \equiv 0$, reducing Euler's equation (3.9) to:

$$\int_{V(t)} \rho \left(\frac{\partial \boldsymbol{v}}{\partial t} + \nabla \left(\frac{1}{2} V^2 \right) \right) dV = \int_{V(t)} (\rho \boldsymbol{g} - \nabla p)\, dV \tag{3.12}$$

3.3.3 Velocity potential

A vector with zero curl must be the gradient of a scalar function. This gives rise to the velocity potential function, for consistence with the remainder of the work denoted Ψ:

$$\boldsymbol{v} = \nabla \Psi \tag{3.13}$$

Substituting (3.13) in (3.12) and integrating (3.12) over the fluid volume gives the Bernoulli equation for potential flow. Note that this equation is valid throughout the fluid under the assumption of an incompressible, irrotational, and inviscid fluid.

$$\frac{p}{\rho} + \frac{\partial \Psi}{\partial t} + \frac{1}{2} \nabla \Psi \cdot \nabla \Psi - gz = C \tag{3.14}$$

The Laplace equation is the governing equation for potential flow. It appears by substituting the velocity potential (3.13) in the continuity equation for incompressible flow (3.4):

$$\nabla^2 \Psi = 0 \tag{3.15}$$

3.4 Notation and sign conventions

The following notations are adopted in the derivation of the theory presented in this thesis.

- All normals to surfaces and panels are positive when pointing into the fluid.
- Earth fixed coordinates are denoted with a subscript '0'.
- A union of surfaces $S_H \cup S_B \cup S_W$ is abbreviated by S_{HBW}.

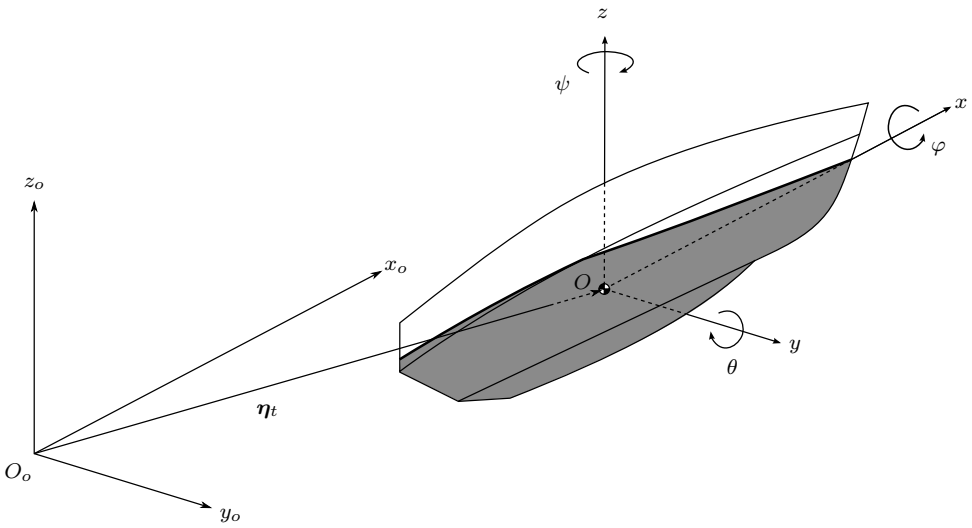


Figure 3.1: *Coordinate systems (note that for clarity both systems are drawn parallel)*

Two right handed Cartesian coordinate systems are defined. These two systems are depicted in figure 3.1. Firstly, an space-fixed coordinate system $O_0x_0y_0z_0$ with the $O_0x_0y_0$ plane coinciding with the undisturbed free surface and the z_0 axis directed upwards. Secondly, a body-fixed coordinate system $Oxyz$, the x-axis points from stern to bow, the y-axis to port and the z-axis up. The origin of the body-fixed system coincides with the center of gravity of the vessel.

The rigid body velocity vector consists of the translational rigid body velocity $\boldsymbol{V} = [u, v, w]$ and the angular rigid body velocities $\boldsymbol{\Omega} = [p, q, r]$; here both are defined in the body-fixed reference system:

$$\boldsymbol{u}\,(t) = [\boldsymbol{V}, \boldsymbol{\Omega}] \tag{3.16}$$

This leads to the instantaneous velocity vector $\dot{\boldsymbol{\delta}}$ of a body-fixed point at a location $\boldsymbol{r} = [x, y, z]$ in the body-fixed frame given in (3.17).

$$\dot{\boldsymbol{\delta}}\,(\boldsymbol{x}, t) = \boldsymbol{V} + \boldsymbol{\Omega} \times \boldsymbol{r} \tag{3.17}$$

The body translations can be either described in the body-fixed reference system, or in the earth-fixed reference system. A state vector $\boldsymbol{\eta}$ can be defined, that expresses the location and orientation of the body in the earth-fixed frame. The first three components are the translations in x_0, y_0, and z_0 directions given by the vector $\boldsymbol{\eta}_t = [x_0, y_0, z_0]$, whereas the latter three are the Euler orientation angles $\boldsymbol{\eta}_r = [\varphi, \theta, \psi]$.

$$\boldsymbol{\eta}\,(t) = [\boldsymbol{\eta}_t, \boldsymbol{\eta}_r] \tag{3.18}$$

The vector describing the instantaneous location in the earth-fixed reference frame of a point $\boldsymbol{r} = [x, y, z]$ (defined in the body-fixed frame) due to the rigid body motions is denoted as $\boldsymbol{\delta}_0$ and employs the Euler rotation transformation matrix $\boldsymbol{ABC}$, derived in appendix B. The

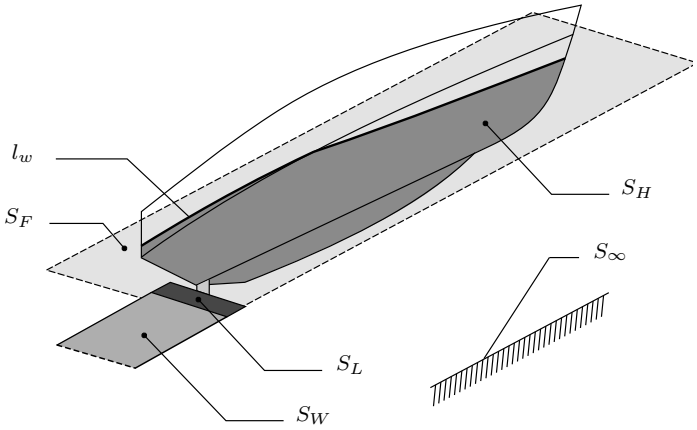


Figure 3.2: *Problem boundaries*

convention used for the order of the Euler rotations are the Tait-Bryan angles (yaw, pitch and roll).

$$\boldsymbol{\delta}_0(\boldsymbol{x},t) = \boldsymbol{\eta}_t + \boldsymbol{ABC}(\varphi,\theta,\psi)\,\boldsymbol{r} \tag{3.19}$$

This expression can be linearised for small rotation angles. Although not necessary in the large amplitude motion approach itself, this formulation is useful when linearising the hydrodynamic solution to the mean body geometry and the subsequent formulation of the so-called m-*terms*.

$$\boldsymbol{\delta}_0(\boldsymbol{x},t) \approx \boldsymbol{\eta}_t + \boldsymbol{\eta}_r \times \boldsymbol{r} \tag{3.20}$$

Finally, two more vectors will be used. First, the vector describing the instantaneous velocity due to the rigid body motions of any body-fixed point in the earth-fixed frame is denoted as $\dot{\boldsymbol{\delta}}_0$ and is the earth-fixed projection of $\dot{\boldsymbol{\delta}}$. Second, for convenience and consistance with literature a generalised (earth-fixed) velocity vector $\dot{\boldsymbol{\eta}}$ is defined for use in the m-terms. It is the earth-fixed equivalent of $\boldsymbol{u}$.

It should be noted that the relation between the Euler rotation angles and the angular velocity $\Omega = [p,q,r]$ is not entirely straightforward and depends on the body orientation. More about this relation can be found in appendix B, detailing several transformations between body-fixed and space-fixed reference frames.

3.5 Mathematical formulation

3.5.1 Domain decomposition

The fluid domain is considered, bounded by surface $S(t)$. $S(t)$ is decomposed as shown in figure 3.2, where:

- $S_F(t)$ is the free surface of the fluid.

- $S_H(t)$ is the submerged part of the hull of the ship in consideration.
- $S_L(t)$ is the surface of the submerged foil(s).
- $S_W(t)$ is the wake sheet.
- $S_\infty(t)$ is the surface bounding the fluid infinitely far from the body.
- $S_\epsilon(t)$ is a small (semi-)sphere containing the observation point (only necessary in a few parts of the derivation - not shown in the figure).

The line $l_w(t)$ denotes the instantaneous intersection between the free surface and the body surface: $l_w(t) = S_H(t) \cap S_F(t)$.

3.5.2 Decomposition of the potential function

The total potential Ψ can be split into two parts under the assumption of linearity. First, the incident wave potential Φ_w, representing the incoming waves. Secondly, the disturbance potential Φ, representing the disturbance of the flow caused by the diffraction of the waves and the motions of the body. In formula:

$$\Psi(\boldsymbol{x}_0, t) = \Phi_w(\boldsymbol{x}_0, t) + \Phi(\boldsymbol{x}_0, t) \tag{3.21}$$

In this formulation, adopted by Lin and Yue (1990), it is not necessary to distinguish between the steady and the unsteady disturbance flows. The problem is seen from the earth-fixed reference frame, with the body boundary moving through the problem domain. The body is allowed to carry out large amplitude motions and the steady forward translation is seen as part of these large amplitude body motions. In fact, this formulation means that the disturbance potential is linearised around the steady forward speed, similar to the Neumann-Kelvin approach.

For the sake of brevity the arguments of the potentials $\boldsymbol{x}_0$ and t will be dropped, only to appear where confusion can arise as to which reference frame is used. Φ_w is given in the earth-fixed reference frame by:

$$\Phi_w = \frac{\zeta_a g}{\omega} e^{kz_0} \sin\left(k\left(x_0 \cos\psi_w + y_0 \sin\psi_w\right) - \omega t\right) \tag{3.22}$$

3.5.3 Boundary and initial conditions

The following boundary conditions are imposed in order to solve the potential flow problem in the fluid domain V:

Free surface

Two conditions need to be imposed on S_F. First, a kinematic condition assuring that the velocity of a particle at the free surface is equal to the velocity of the free surface itself. Both conditions in their most pure form need to be applied at the *a priori* unknown location of the free surface.

The unsteady form of the non-linear kinematic free surface boundary condition follows appears by setting the substantial derivative of the Lagrangian vertical displacement of a water

particle minus the vertical coordinate of the free surface equal to zero on the free surface, as for example shown by Newman (1978).

$$\frac{\partial}{\partial t}\left(\eta - z_0\right) = 0 \quad \forall \quad \boldsymbol{x}_0 \in S_F \tag{3.23}$$

In this equation, z_0 is the vertical displacement of a water particle moving with the Lagrangian frame, thus only dependent on the variable t and $\eta\left(x_0, y_0, t\right)$ gives the free surface elevation at point (x_0, y_0) at time t. In other words, care needs to be taken when taken the time derivative of η (refer to appendix B).

Second, a dynamic condition assuring that the pressure at the free surface is equal to the ambient pressure (set to zero). The unsteady Bernoulli equation in a translating coordinate system is given by:

$$\frac{\partial \Psi}{\partial t} + g\eta + \frac{1}{2}\left(\nabla\Psi\right)^2 = 0 \quad \forall \quad \boldsymbol{x}_0 \in S_F \tag{3.24}$$

The statement $\forall\, \boldsymbol{x}_0 \in S_F$ can be replaced with 'at $z_0 = \eta$'. Both equations can be linearised to the undisturbed free surface by dropping the higher order terms under the assumption of small wave steepness. This results in the validity of the equations at the known surface $z_0 = 0$. The result is a condition that is much easier to satisfy computationally, at the cost of an accurate description of the fluid flow near the free surface. The remaining equations are:

$$\left.\begin{aligned} \frac{\partial \eta}{\partial t} &= \frac{\partial z_0}{\partial t} \\ \frac{\partial \Psi}{\partial t} + g\eta &= 0 \end{aligned}\right\} \quad \text{at } z_0 = 0 \tag{3.25}$$

By time derivation of the second equation and substitution of the first into the resulting expression, one condition remains:

$$\frac{\partial^2 \Psi}{\partial t^2} + g\frac{\partial \Psi}{\partial z_0} = 0 \quad \text{at } z_0 = 0 \tag{3.26}$$

The free surface boundary condition for steady cases can be obtained from (3.25) by applying the convective derivative for both time derivatives (of Φ and η), as explained in appendix B:

$$\left.\begin{aligned} \boldsymbol{V}\cdot\nabla\eta &= \frac{\partial z_0}{\partial t} \\ \boldsymbol{V}\cdot\nabla\Psi + g\eta &= 0 \end{aligned}\right\} \quad \text{at } z_0 = 0 \tag{3.27}$$

With a constant forward speed U in x-direction and combining both equations the result is the linearised free surface boundary condition for steady potential flow.

$$\frac{\partial^2 \Psi}{\partial x^2} + \frac{g}{U^2}\frac{\partial \Psi}{\partial z_0} = 0 \quad \text{at } z_0 = 0 \tag{3.28}$$

(3.28) can be rewritten in terms of the Froude number $Fn = U/\left(\sqrt{gL}\right)$, showing that when the Froude number approaches zero the second term approaches infinity, indicating possibly problematic behaviour of this condition at very low Froude numbers. In section 4.4.3 the

limiting behaviour with respect to the forward speed of the approach developed in this thesis will be studied closer.

$$\frac{\partial^2 \Psi}{\partial x^2} + \frac{1}{Fn^2}\frac{\partial \Psi}{\partial z_0} = 0 \quad \text{at } z_0 = 0 \tag{3.29}$$

Body surface

On the instantaneous body surface, consisting of hull surface $S_H\,(t)$ and lifting surface $S_L\,(t)$ a zero normal flow condition is imposed:

$$\dot{\boldsymbol{\delta}}_0 \cdot \boldsymbol{n} = \frac{\partial \Phi}{\partial n} + \frac{\partial \Phi_w}{\partial n} \quad \forall \quad \boldsymbol{x}_0 \in S_{HL} \tag{3.30}$$

This condition is a non-linear boundary condition, as the exact location of the body is unknown a priori and dependent on the solution of the potential flow problem and the subsequent solution of the equations of motion. Applying this condition in this form leads to the fully body exact approach.

Similar to the free surface boundary condition, also this condition can be linearised to its mean location. This linearisation results in a more simple approach that reduces the computational effort needed to a large extend. The price to be paid for this simplification is a less exact solution to the problem and the appearance of a number of extra terms in the body boundary condition, the so-called m-*terms*.

The linearisation of the body boundary condition has been formally carried out by Timman and Newman (1962) for an oscillatory motion of a spheroid. This procedure relies on splitting the disturbance potential in two separate parts: a steady disturbance potential, ϕ, and the unsteady disturbance potential. Now the decomposition of the total potential becomes the following:

$$\Psi = (\Phi - \phi) + \phi + \Phi_w \tag{3.31}$$

The result of Timman and Newman (1962) can be formulated in a more general form for arbitrary but small displacements around the steady translating body orientation. In that case the movement of the hull can be linearised to $\boldsymbol{\delta}$ as given in (3.20).

$$\frac{\partial \Psi}{\partial n} = \dot{\boldsymbol{\delta}}_0 \cdot \boldsymbol{n} - \left(\left(\boldsymbol{\delta}_0 \cdot \nabla\right)\nabla\phi - \left(\nabla\phi \cdot \nabla\right)\boldsymbol{\delta}_0\right) \cdot \boldsymbol{n} \quad \forall \quad \boldsymbol{x}_0 \in \bar{S}_{HL} \tag{3.32}$$

Finally, use can be made of m-terms adopted by Ogilvie and Tuck (1969) to rewite the linearised body boundary condition in a more elegant way, making use of the definition of $\boldsymbol{\delta}$ in (3.20).

$$\frac{\partial \Phi}{\partial n} + \frac{\partial \Phi_w}{\partial n} = \dot{\boldsymbol{\eta}} \cdot \boldsymbol{n} + \boldsymbol{\eta} \cdot \boldsymbol{m} \tag{3.33}$$

Where the definition of the unit normal $\boldsymbol{n}$ is extended to 6 degrees of freedom:

$$\begin{aligned} [n_1, n_2, n_3] &= \boldsymbol{n} \\ [n_4, n_5, n_6] &= \boldsymbol{x} \times \boldsymbol{n} \end{aligned} \tag{3.34}$$

And the m-terms are defined as:

$$\begin{aligned}[m_1, m_2, m_3] &= -(\boldsymbol{n} \cdot \nabla) \nabla \phi \\ [m_4, m_5, m_6] &= -(\boldsymbol{n} \cdot \nabla)(\boldsymbol{x} \times \nabla \phi) - \boldsymbol{n} \times \boldsymbol{V}\end{aligned} \tag{3.35}$$

The term $\boldsymbol{n} \times \boldsymbol{V}$, for a constant forward speed given by $\boldsymbol{V} = [U, 0, 0]$, reduces to $[Un_z, -Un_x]$. These terms are automatically included in the normal velocity components when transferring the body-fixed velocity components to the earth-fixed reference frame. This does happens in the current method as well, due to the fact that the equations of motion are solved in the body-fixed reference frame.

Infinity

At a large distance from the body (at infinity, S_∞) the radiation condition is imposed:

$$\begin{aligned}\Phi &\to 0 \\ \frac{\partial \Phi}{\partial t} &\to 0\end{aligned} \tag{3.36}$$

Initial condition

At the start of the process the fluid is at rest. When waves are present, they are started with a ramp-up function on their amplitude from $t = 0$. The ship is set in motion impulsively at $t = 0$.

$$\Phi = \frac{\partial \Phi}{\partial t} = 0 \tag{3.37}$$

3.5.4 Transient Green function

In this time-domain potential method the Green function given in (3.38) will be utilised. This Green function specifies the influence of a singularity with impulsive strength (submerged source or dipole) located at point $q(\xi, \eta, \zeta)$ on the potential at field point $p(x_0, y_0, z_0)$. The function has been derived by Newman (1985).

$$\begin{aligned}G(p, q, t - \tau) = G^0 + G^f = \\ \frac{1}{R} - \frac{1}{R_0} + 2 \int_0^\infty \left[1 - \cos\left(\sqrt{gk}\,(t - \tau)\right)\right] e^{k(z_0 + \zeta)} J_0(kR)\, dk \\ \text{for } p \neq q\,,\ t - \tau \geq 0\end{aligned} \tag{3.38}$$

In (3.38) G^0 is the source and biplane part, or Rankine part, the remaining part, G^f, is the free surface memory part of the Green function. J_0 is the Bessel function of order zero, given by:

$$J_0(x) = \frac{1}{\pi} \int_0^\pi e^{ix \cos\theta} d\theta \tag{3.39}$$

Further:

$$R = \sqrt{(x_0 - \xi)^2 + (y_0 - \eta)^2 + (z_0 - \zeta)^2}$$
$$R_0 = \sqrt{(x_0 - \xi)^2 + (y_0 - \eta)^2 + (z_0 + \zeta)^2} \tag{3.40}$$

It can be easily shown that the Green function given above satisfies the Laplace equation, the free surface boundary conditions and the condition at infinity (Wehausen and Laitone 1960).

$$\nabla^2 G = 0 \text{ in } V(t) \text{ excluding singular points, } t > \tau \tag{3.41}$$

$$\frac{\partial^2 G}{\partial t^2} + g\frac{\partial G}{\partial z_0} = 0 \text{ on } S_F(t), t > \tau \tag{3.42}$$

$$G, \frac{\partial G}{\partial t} \to 0 \text{ on } S_\infty(t), t > \tau \tag{3.43}$$

$$G, \frac{\partial G}{\partial t} = 0 \text{ on } S_F(t), t = 0 \tag{3.44}$$

3.5.5 Transient integral equation

To derive the transient integral equation, use is made of Green's second identity. When assuming that the functions $\Phi(\boldsymbol{x}_0, t)$ and $\Psi(\boldsymbol{x}_0, t)$ satisfy the boundary and initial conditions given in the previous sections and are regular functions in the fluid domain V, Green's second identity for these functions is given by:

$$\int_V \left(\Phi\nabla^2\Psi - \Psi\nabla^2\Phi\right) dV = \int_S \left(\Phi\Psi_n - \Psi\Phi_n\right) dS \tag{3.45}$$

Note that for brevity use is made of short hand notation for the derivatives and arguments of functions are dropped. The identity relates the integral over the fluid domain V to an integral over the boundary S of V. When functions Φ and Ψ are assumed to satisfy the Laplace equation, the left hand side of (3.45) equals zero:

$$\int_S \left(\Phi\Psi_n - \Psi\Phi_n\right) dS = 0 \tag{3.46}$$

Application of Green's second identity to functions $\Phi(\boldsymbol{\xi}, t)$ and $G_\tau(\boldsymbol{x}_0, \boldsymbol{\xi}, t - \tau)$ in the fluid domain V bounded by $S = S_\infty \cup S_\epsilon \cup S_{FHLW}$ (refer to figure 3.1) yields the relation given in (3.47). S_ϵ is introduced to exclude singular points from the domain to ensure that both functions are regular in the considered domain. It is to be understood that the field point p is not included in any of the boundary surfaces at this point in the derivation, except for S_∞.

$$\int_S \left(\Phi G_{\tau n} - G_\tau \Phi_n\right) dS = 0 \tag{3.47}$$

As this relation holds for all $\tau < t$ integration in time between $\tau = 0$ and $\tau = t$ is permitted. Functions Φ, $G_{\tau n}$, Φ_n and G_τ do not have singularities on S_ϵ their contribution will approach zero as $\epsilon \to 0$. In addition, using the boundary condition on S_∞, the contribution on S_∞ will approach zero as well. What remains is:

$$\int_0^t \int_{S_{FHLW}(\tau)} \left(\Phi G_{\tau n} - G_\tau \Phi_n\right) dS\, d\tau = 0 \tag{3.48}$$

The linearised free surface and body-exact integral equation for transient ship motions appears by using the free surface Green function's properties to eliminate the free surface integral from (3.48). The details of this process are included in appendix C, section C.1. The result is an alternative expression for the free surface integral of (3.48). The need for an integration over the entire (or at least a part of) the free surface is now removed.

$$\begin{aligned}\int_0^t \int_{S_F(\tau)} \left(\Phi G_{\tau n} - G_\tau \Phi_n\right) dS\, d\tau &= -4\pi T\Phi \\ &- \int_{S_{HLW}(t)} \left(\Phi G_n^0 - G^0 \Phi_n\right) dS + \frac{1}{g}\int_0^t \int_{l_w(\tau)} \left(\Phi G_{\tau\tau} - G_\tau \Phi_\tau\right) V_N\, dL\, d\tau\end{aligned} \tag{3.49}$$

V_N is the two dimensional normal velocity of the body at $l_w(\tau)$ in the plane of the linearised free surface. As explained in appendix C, according to Hunt (1980) T is defined as:

$$T(p) = \begin{cases} 1 & p \in V(t) \\ 1/2 & p \in S_{HL}(t) \\ 0 & \text{otherwise} \end{cases} \tag{3.50}$$

Combining (3.49) with (3.48) results in the integral equation for transient ship motions:

$$\begin{aligned}4\pi T\Phi(\boldsymbol{x_0}, t) = &- \int_{S_{HLW}(t)} \left(\Phi(\boldsymbol{\xi}, \tau)\, G_n^0 - G^0 \Phi_n(\boldsymbol{\xi}, \tau)\right) dS \\ &+ \int_0^t \int_{S_{HLW}(\tau)} \left(\Phi(\boldsymbol{\xi}, \tau)\, G_{\tau n}^f - G_\tau^f \Phi_n(\boldsymbol{\xi}, \tau)\right) dS\, d\tau \\ &+ \frac{1}{g}\int_0^t \int_{l_w(\tau)} \left(\Phi(\boldsymbol{\xi}, \tau)\, G_{\tau\tau}^f - G_\tau^f \Phi_\tau(\boldsymbol{\xi}, \tau)\right) V_N\, dL\, d\tau\end{aligned} \tag{3.51}$$

The first term is the source and dipole plus biplane image contribution, the second and third terms contain the free surface memory effects over the past time τ. It should be noted that the replacement of the free surface integral is allowed by virtue of a linear free surface boundary condition and the choice for a Green function that satisfies this condition. Note that in the time derivatives of the Green function the G-terms are replaced with the G^f-terms, as the G^0-terms are time independent.

3.6 Numerical solution

3.6.1 Source and dipole distribution

To obtain a governing equation in terms of singularity distributions, formulations are needed that relate different types of singularities on a surface to the potential induced by the surface

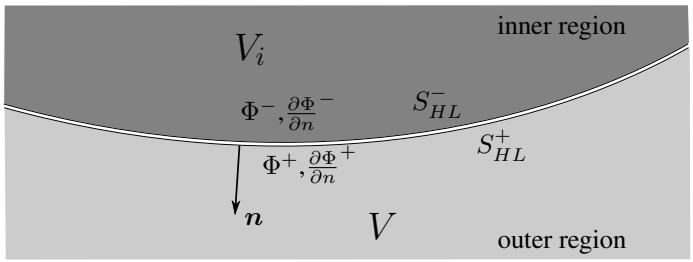


Figure 3.3: *Definition of inner and outer sides of a singularity distribution over a surface*

on a point $p\,(\boldsymbol{x}_0, t)$. It is assumed that p is lying within the volume V, and possibly on the boundary S_{HL}.

The hull and lifting surfaces will be modelled with a combination of source and dipole distributions, with a wake sheet extending downstream from the trailing edge. For the lifting surfaces, wake sheets are necessary to satisfy the Kutta condition at the trailing edge; for the hull surface a transom flow condition will be satisfied near the transom edge using a wake sheet. To obtain a formulation for this mixed source-dipole distribution on the hull and lifting surfaces the dipole strength is set equal to the jump of the potential across the inner (-) and outer (+) sides (refer to figure 3.3) of the surfaces and the source strength is set equal to the jump in the normal derivative of the potential between inner and outer surfaces:

$$\left.\begin{aligned} \Phi^+ - \Phi^- &= -\mu \\ \Phi_n^+ - \Phi_n^- &= \sigma \end{aligned}\right\} \forall \quad q \in S_{HL} \tag{3.52}$$

The wake sheets are considered infinitely thin volumes bounded by coinciding upper and lower boundary surfaces. This leads to the situation that the lower wake sheet boundary surface can be seen as the inner side of the upper wake sheet boundary surface. The dipole strength of a wake sheet is set equal to the jump of the potential across the lower (-) and upper (+) sides of the surface and the normal derivative of the potential is set equal for upper and lower surfaces.

$$\left.\begin{aligned} \Phi^+ - \Phi^- &= -\mu \\ \Phi_n^+ &= \Phi_n^- \end{aligned}\right\} \forall \quad q \in S_W \tag{3.53}$$

There is no contribution due to the waterline integral in the current method. The strength of the waterline contribution is set equal to the strength of the adjacent body surface. In terms of a panel distribution this means that a waterline element has the same strength as the adjacent body panel. In this way, no separate unknowns need to be solved at the waterline and no conditions need to be set at the waterline intersection. This may represent a suboptimal solution and future work may include quantification of the effect of this choice and if necessary a more consistent approach to include separate waterline elements.

Now the integral equation given in (3.51) can be applied over the inner and outer surfaces to obtain the potential induced at a point p lying on the boundary of the hull or lifting surfaces. Note that at first the point p is excluded from the boundary, to avoid a singular point at p. This is achieved by using the surface S_ϵ at a infinitesimal distance ϵ from p as shown in figure 3.4.

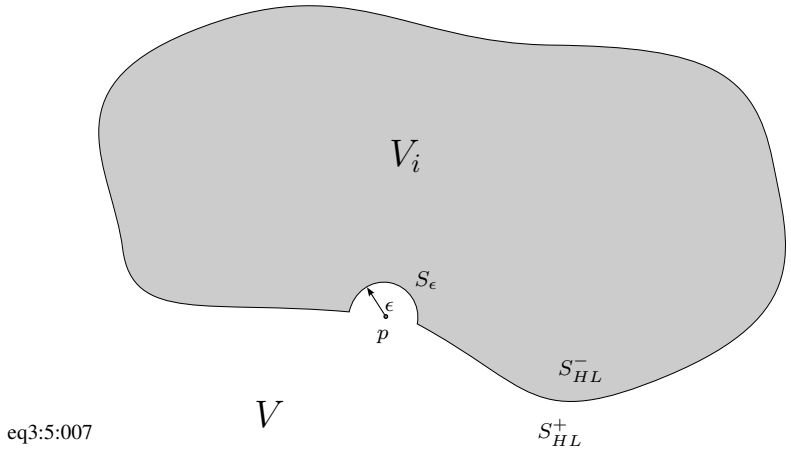


Figure 3.4: *Limiting analysis of field point p at the domain boundary*

Hunt (1980) shows with a limiting analysis that the contribution due to the G^0-integral equals $-4\pi T\Phi^+(p,t)$ for the outer potential and $4\pi(1-T)\Phi^-(\boldsymbol{x}_0,t)$ for the inner potential. The exclusion is not needed for the G^f (or memory) integrals, as these integrals are over the past-time geometry as the past-time geometry is naturally displaced relative to the current-time geometry.

The contributions due to the inner surfaces are negative due to reversal of the normals with respect to the corresponding outer surfaces. Collecting all contributions to the outer potential at p yields:

$$\begin{aligned}
&4\pi T\Phi^+(\boldsymbol{x}_0,t)+4\pi(1-T)\Phi^-(\boldsymbol{x}_0,t)= \\
&\qquad -\int_{S_{HLW}(t)}\left(\left[\Phi^+-\Phi^-\right](\boldsymbol{\xi},t)\,G_n^0-G^0\left[\Phi_n^{d+}-\Phi_n^{d-}\right](\boldsymbol{\xi},t)\right)dS \\
&\quad +\int_0^t\int_{S_{HLW}(\tau)}\left(\left[\Phi^+-\Phi^-\right](\boldsymbol{\xi},\tau)\,G_{\tau n}^f-G_\tau^f\left[\Phi_n^+-\Phi_n^-\right](\boldsymbol{\xi},\tau)\right)dS\,d\tau \\
&+\frac{1}{g}\int_0^t\int_{l_w(\tau)}\left(\left[\Phi^+-\Phi^-\right](\boldsymbol{\xi},\tau)\,G_{\tau\tau}^f-G_\tau^f\left[\Phi_\tau^{d+}-\Phi_\tau^{d-}\right](\boldsymbol{\xi},\tau)\right)V_N\,dL\,d\tau \qquad (3.54)
\end{aligned}$$

Of interest is the value of the potential at p on the outer side of the surface in terms of singularity distributions over the hull and lifting surface boundaries as well as over the wake surfaces. To arrive at a formulation for $\Phi^+(p)$ teq3:5:007he relations for the jump in potential and in the normal derivative of the potential given in (3.52) and (3.53) are substituted. Finally, as $p(\boldsymbol{x}_0,t)$ is lying on a smooth part of either S_H or S_L function T will be equal to $T=1/2$. The following equation results for the potential at field point $p(\boldsymbol{x}_0,t)$, located on $S_{HL}(t)$:

$$4\pi\Phi\left(p,t\right)=-2\pi\mu\left(p,t\right)+\int_{S_{HL}(t)}\sigma\left(q,t\right)G^{0}\,dS+\int_{S_{HLW}(t)}\mu\left(q,t\right)G_{n_q}^{0}\,dS$$
$$-\int_{0}^{t}\int_{S_{HL}(\tau)}\sigma\left(q,\tau\right)G_{\tau}^{f}\,dS\,d\tau-\int_{0}^{t}\int_{S_{HLW}(\tau)}\mu\left(q,\tau\right)G_{\tau n_q}^{f}\,dS\,d\tau$$
$$-\frac{1}{g}\int_{0}^{t}\int_{l_w(\tau)}\sigma\left(q,\tau\right)G_{\tau}^{f}V_N V_n\,dL\,d\tau-\frac{1}{g}\int_{0}^{t}\int_{l_w(\tau)}\mu\left(q,\tau\right)G_{\tau\tau}^{f}V_N\,dL\,d\tau$$
$$-\frac{1}{g}\int_{0}^{t}\int_{l_w(\tau)}G_{\tau}^{f}\left(\boldsymbol{V}\cdot\nabla\mu+\frac{d\mu}{d\tau}\right)V_N\,dL\,d\tau \quad (3.55)$$

$\sigma\left(q,t\right)$ and $\mu\left(q,t\right)$ are the source and dipole strengths at position $q\left(\boldsymbol{\xi},t\right)$ at time t, and $\partial/\partial n_q$ is the normal derivative at the singularity point $q\left(\boldsymbol{\xi},t\right)$. V_n is the normal velocity on a waterline panel.

A further elaboration of the derivation of the waterline term in (3.55) is given in appendix C. When combined source-doublet elements are used near the waterline, a quite complex waterline integral term appears due to the doublet strength and its derivatives. For practical purposes, combined source-doublet elements are mostly used either on fully submerged lifting foils (section 3.6.2) or on for satisfaction of the transom flow condition on the aft part of the hull (section 3.6.3). In the latter case, the waterline in the aft part is nearly or fully parallel to the longitudinal axis for ships fitted with a transom stern. This is especially true in the body-linear formulation that will be adopted in most cases, section 3.6.7. In this case V_N simply will become zero and the doublet waterline terms will vanish.

In the following, the doublet waterline integral terms are neglected. Nevertheless, in case doublet distributions are applied in regions where they are adjacent to the waterline and the waterline is not (nearly) parallel to the rigid body velocity then these terms are important aeq3:5:007nd need to be accounted for. Situations where this applies include:

- Doublets distributed over the entire submerged geometry, for instance in case of (body-linear) simulations where the body has an angle of attack in the horizontal plane.
- In body-exact simulations with large amplitude horizontal motions.

By applying the $\nabla\cdot\boldsymbol{n}_p$ operator to (3.55) and using the zero normal flow condition (3.30) on the hull and the lifting surfaces, an expression for the normal velocity at $p\left(\boldsymbol{x}_0,t\right)$ is obtained, given in (3.56). This derivation is equivalent to the one above, its details are omitted here, a number of which can be found in Hunt (1980). Note the appearance of the m-terms in the body boundary condition.

$$4\pi\left(\dot{\boldsymbol{\eta}}\cdot\boldsymbol{n}_p+\boldsymbol{\eta}\cdot\boldsymbol{m}_p-\Phi_{wn_p}\right)=2\pi\sigma\left(p,t\right)+\int_{S_{HL}(t)}\sigma\left(q,t\right)G^0_{n_p}\,dS+\int_{S_{HLW}(t)}\mu\left(q,t\right)G^0_{n_pn_q}\,dS-\int_0^t\int_{S_{HL}(\tau)}\sigma\left(q,\tau\right)G^f_{\tau n_p}\,dS\,d\tau-\int_0^t\int_{S_{HLW}(\tau)}\mu\left(q,\tau\right)G^f_{\tau n_pn_q}\,dS\,d\tau-\frac{1}{g}\int_0^t\int_{l_w(\tau)}\sigma\left(q,\tau\right)G^f_{\tau n_p}V_NV_n\,dL\,d\tau \quad (3.56)$$

In this equation subscript p for the normal derivative indicates a normal derivative at the field point $p\left(\boldsymbol{x}_0,t\right)$, and q at singularity point $q\left(\boldsymbol{\xi},t\right)$. (3.56) is the principal equation to be solved for the unknown source and dipole strengths $\sigma\left(q,t\right)$ and $\mu\left(q,t\right)$. To solve it numerically, the equation needs to be discretised. This is elaborated in section 3.6.4.

3.6.2 Wake model for lifting surfaces

When doublets are distributed over lifting surfaces an extra constraint needs to be set at the trailing edges of these lifting surfaces in the form of a wake model. This is necessary for obtaining an unique value for the circulation strength around lifting surfaces and in this way for an unique solution to the potential flow problem. The wake model relates the dipole strength at the trailing edge of lifting surfaces to the location and shape of a wake sheet. Usually this is done by applying the *Kutta* condition, used by W. M. Kutta in 1902 for the first time. The Kutta condition poses an additional constraint on the flow in a way that the flow leaves the sharp trailing edge smoothly and the velocity at the trailing edge is finite (Katz and Plotkin 2001). The Kutta condition holds for both steady and unsteady flows.

An additional condition should be satisfied, being that vorticity produced at the lifting surface must be shed from the lifting surface to the wake sheet in order to satisfy the requirement that the circulation Γ around a contour enclosing the lifting surface and its wake must be conserved (Kelvin's circulation theorem):

$$\frac{d\Gamma}{dt}=0,\text{ in }V\left(t\right) \quad (3.57)$$

These requirements are satisfied by transferring the nett circulation at the trailing edge onto the adjacent wake sheet elements. In the current method this is achieved by applying the two-dimensional Kutta condition for each longitudinal panel strip:

$$\mu_w=\mu_{upper}-\mu_{lower} \quad (3.58)$$

Where μ_w is the doublet strength of the first wake panel adjacent to the trailing edge and μ_{upper} and μ_{lower} the strengths of the upper and lower panel lifting surface panels adjacent to the trailing edge.

A final requirement is that the wake sheet should be force free. It is not a solid surface, so no pressure difference can be present between the upper and lower sides of the sheet. The force on a vortex sheet is given by the Kutta-Joukowsky law:

$$\boldsymbol{F} = \rho \boldsymbol{V} \times \boldsymbol{\gamma} \tag{3.59}$$

This means that for zero force the vorticity vector $\boldsymbol{\gamma}$ should be directed parallel to the velocity vector $\boldsymbol{V}$. This can be accomplished by displacing the vortex element corner points with the local fluid velocity.

Lifting surfaces and wake panels are modelled by constant-strength doublet panels and the wake sheet panels, using equivalent vortex ring elements with strength Γ equal to μ to compute the induced velocities efficiently (Katz and Plotkin 2001).

3.6.3 Transom flow model

As noted in chapter 1, fast vessels fitted with a cut-off or transom type stern experience smooth flow separation at the transom at sufficient high Froude numbers. Transom flow can have a significant impact on both the motion behaviour and the resistance. Also as pointed out in sections 1.2.3 and 3.2, plain potential flow theory with a linearised free surface boundary condition is not able to provide a reasonable approximation of transom flow.

Instead at the transom edge extremely high flow velocities may occur in potential flow computations, depending on forward speed and local panel discretisation. In reality finite velocities and pressures occur at the transom edge. In order to account for transom flow and to enforce smooth flow separation and finite flow velocities at the transom a wake model has been added, similar to the one proposed by Reed et al. (1991) for steady transom flow.

The transom flow wake model consists of the application of the unsteady linearised Bernoulli equation at the transom edge. This is combined with the distribution of source-doublet elements over the hull in front of the transom edge and a trailing wake sheet extending aft from the transom edge. The assumption behind the transom flow condition applied here is that the flow separates smoothly from the transom with a velocity at the trailing edge that is tangent to the hull. This similar to what was proposed by Reed et al. (1991) for steady cases.

Figure 3.5 shows a view on the centreline of a ship fitted with a transom stern, the linearised free surface ($z_0 = 0$), and a representation of the actual free surface. The wake sheet does not follow the actual free surface, but instead extends backward in a straight horizontal fashion, similar to the wake sheets of lifting surfaces described in the previous section. A further improvement could be to adapt the shape of the wake sheet to the physics of the flow, but is not investigated here.

Since the pressure should be continuous everywhere in the fluid domain, the pressure at the hull just forward of the transom edge should equal the pressure at the free surface just aft of the transom. The transom flow condition is obtained by using the Bernoulli equation to link the total pressure on the body just before the transom stern (the hydrodynamic pressure induced by the presence of the body and its motions, the incident wave pressure, and the hydrostatic pressure) to the pressure on the free surface just aft of the transom stern.

The Bernoulli equation derived in appendix B; (B.7) is applied to be able to use the induced potential derivatives in the non-inertial body-fixed frame. The condition is applied using the linearised rigid body velocity vector $[U, 0, 0]$ instead of the instantaneous rigid body velocity vector. This is related to the linearisation of the potential flow solution to the averaged body surface that will be discussed in section 3.6.7.

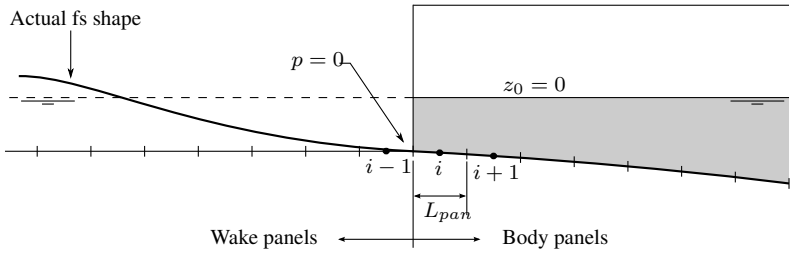


Figure 3.5: *Transom flow model: view on centreline of transom stern*

The reasoning behind using the linearised rigid body velocity is that otherwise the terms in the solution matrix become dependent on the solution of the equations of motion. This would require dealing with adaptations of the solution matrix and subsequent costly LU-decomposition of the solution matrix at each time step. Using the linearised rigid body velocity does not require this and the solution matrix can be LU-decomposed once, before the time simulation is started.

$$gz_T = U\left(\frac{\partial \Phi}{\partial x} + \frac{\partial \Phi_w}{\partial x}\right) - \left(\frac{\partial \Phi}{\partial t} + \frac{\partial \Phi_w}{\partial t}\right) \tag{3.60}$$

In (3.60) z_T is the local immersion at the transom edge. The condition will be approximately satisfied at the transom edge. In fact, it will not be satisfied exactly at the transom edge but at the collocation points of the last hull panels in front of the transom edge avoiding the need for additional influence functions to be computed at the transom edge. These collocation points are represented by i in figure 3.5.

The wave influence in both right hand side terms can be calculated by taking the appropriate derivatives of the wave potential function, given in (3.22). The tangential induced velocities of all singularities at source points $q(\boldsymbol{\xi}, t)$ at the transom edge panels $s(\boldsymbol{x}_0, t)$ are given by:

$$\begin{aligned} 4\pi \frac{\partial \Phi}{\partial x}(s,t) = &-2\pi \frac{\partial \mu(s,t)}{\partial x} \\ &+ \int_{S_H(t)} \sigma(q,t)\, G^0_x \, dS + \int_{S_{HW}(t)} \mu(q,t)\, n G^0_{xn_q} \, dS \\ &- \int_0^t \int_{S_H(\tau)} \sigma(q,\tau)\, G^f_{x\tau} \, dS \, d\tau - \int_0^t \int_{S_{HW}(\tau)} \mu(q,\tau)\, G^f_{xn_q\tau} \, dS \, d\tau \\ &- \frac{1}{g} \int_0^t \int_{l_w(\tau)} \sigma(q,\tau)\, G^f_{x\tau} V_N V_n \, dL \, d\tau \end{aligned} \tag{3.61}$$

Because constant strength singularities are used, it is not possible to directly obtain the x-derivative of μ at the centroid of the transom edge panel. This is solved by estimating this derivative at the transom edge panel using the value of μ at the panel just in front of this panel and at the panel just behind the transom edge panel, the first wake sheet panel, and dividing over the length. $i+1$ refers to the panel directly upstream and $i-1$ refers to first wake panel downstream of the transom panel as indicated in figure 3.5.

$$\frac{\partial \mu\left(w,t\right)}{\partial x} \approx \frac{\mu_{i+1} - \mu_{i-1}}{2L_{pan}} \tag{3.62}$$

The time derivative of the induced potential in the second term of (3.60) can be evaluated as follows:

$$\begin{aligned} 4\pi \frac{\partial \Phi}{\partial t}\left(w,t\right) = -2\pi \frac{\partial \mu}{\partial t}\left(p,t\right) \\ + \int_{S_H(t)} \frac{\partial \sigma}{\partial t}\left(q,t\right) G^0 \, dS + \int_{S_{HLW}(t)} \frac{\partial \mu}{\partial t}\left(q,t\right) G^0_{n_q} \, dS \\ - \int_0^t \int_{S_H(\tau)} \sigma\left(q,\tau\right) G^f_{t\tau} \, dS \, d\tau - \int_0^t \int_{S_{HW}(\tau)} \mu\left(q,\tau\right) G^f_{t\tau n_q} \, dS \, d\tau \\ - \frac{1}{g} \int_0^t \int_{l_w(\tau)} \sigma\left(q,\tau\right) G^f_{t\tau} V_N V_n \, dL \, d\tau \end{aligned} \tag{3.63}$$

The strength of the first row of wake panels, the row of wake elements attached to the transom edge, is set to unknown. Once shed into the wake their strength remains constant, to satisfy Kelvin's circulation theorem. For each body panel adjacent to the transom edge, there will be a wake panel with unknown strength generated in the first wake row. Likewise there is for each transom edge element one extra condition. Application of the transom flow condition in this manner adds an equal amount of unknowns and conditions to the system, a necessary precondition to obtain a solution. Yet, because of the use of combined source-doublet elements on the hull, or at least on a limited part in front of the transom edge, it is necessary to set the source strength of these panels. This can be done in (at least) two ways:

1. Pre-set the source strength of combined source-doublet elements to the vector sum of the undisturbed incoming velocity, the undisturbed wave velocity and possibly the induced velocity due to memory effects. Subsequently, solve for the source strengths of non source-doublet elements, doublet strengths, and transom wake row strengths.
2. First solve a source-only system with absence of transom flow condition, doublet elements, and transom wake elements. Subsequently, solve for the source strengths of non source-doublet elements, doublet strengths, and transom wake row strengths, using the source strengths obtained in the first solution for the source strength of the combined source-doublet elements. This method was favoured by Reed et al. (1991) as they experienced numerical instabilities applying the first method.

The implementation of (3.63) is slightly more complicated, especially for the time derivative of the induced potential. This complication is caused by the usage of a discrete time derivative (a simple first order backward scheme) resulting in numerically unstable results for the source terms. The solution is to apply a first order backward scheme only to the time derivatives of the doublet and wake element terms and using analytical derivatives for the source terms. This process is identical to obtaining the time derivative of the complete potential solution and is detailed in section 3.7.1.

The wake sheet shape should be tangent to the body at the transom and then the requirement of a force free wake sheet can be used to find the appropriate position of the transom wake elements once shed. The first wake elements behind the body are extending horizontally

backwards leading to a straight wake sheet with a profile identical to the transom stern profile. As the buttock lines near the transom generally here nearly horizontal no large difference in orientation of the final body panels and the first wake row panels exists.

For practical purposes it is not necessary to distribute doublet panels over the entire body geometry as the influence of the transom stern condition is limited to a small region near the stern. Generally, only doublet panels in a region of about 10% to 15% of the ship length in front of the transom will have a significant doublet strength. This issue will be further quantified in chapter 4.

3.6.4 Discretisation

The hull surface, lifting surfaces and wake surfaces are discretised using constant strength singularity elements, enabling the replacement of the surface integrals in (3.56) with summations over the singularity panels. The element types on each of these three surfaces are discussed below.

Hull

The ship hull is modelled with constant strength, quadrilateral source panels that can be combined with constant strength dipole panels. Near the transom a combination of constant strength, quadrilateral source and dipole panels can be used together with a trailing wake sheet to implement the transom flow condition described in section 3.6.2.

Lifting surface

Lifting surfaces are modelled with a combination of constant strength, quadrilateral source and dipole panels. The source strength is predefined by setting:

$$\begin{aligned} \sigma &= \left[-\boldsymbol{v}_w - \boldsymbol{v}_G + \dot{\boldsymbol{\delta}}_b\right] \cdot \boldsymbol{n} \\ \boldsymbol{v}_w &= \nabla\Phi_w \\ \boldsymbol{v}_G &= \nabla\Phi^d \\ \dot{\boldsymbol{\delta}}_b &\quad \text{refer to section 3.4} \end{aligned} \tag{3.64}$$

Wake sheet

Wake sheets are modelled with vortex ring elements, carrying a circulation strength Γ. These vortex elements consist of four discrete straight vortex lines of constant strength that enclose the quadrilateral element area. The induced velocity due to a vortex ring element is identical to that of a constant strength dipole element if $\Gamma = \mu$ (Katz and Plotkin 2001). The use of vortex ring elements still satisfies the Kelvin condition and at the same time the induced velocities due to vortex ring elements can be calculated with only a small effort.

(3.65) gives the discretised form of (3.56), dropping the short hand notation for the Green function derivatives. It implements the zero normal flow condition at panel i. In (3.65) NH is the number of hull panels, NL the number of lifting surface panels, NW the number of wake sheet elements and NWL the number of waterline panels. t is the present time,

τ the past time, i and j are element indices for collocation point p and singularity point q, respectively. $\partial/\partial n_{p_i}$ is the normal derivative to the surface at collocation point i, $\partial/\partial n_{q_j}$ is the normal derivative to the surface at singularity point j, both defined in the space-fixed axis system.

When either the source strength or the dipole strength is fixed to a pre-defined value, corresponding left hand side terms will contain known singularity strengths and will move to the right hand side.

The left hand side terms from left to right signify:

1. Contribution due to the local (Rankine) source strength
2. Normal induced velocities due to hull and lifting surface source and dipole panels Rankine terms and their biplane images.

In the same order, the terms on the right hand side signify:

1. Normal velocities due to body motions and incident waves.
2. Normal induced velocities due to wake sheet elements.
3. Normal induced velocity due to memory effect of hull and lifting surface source panels.
4. Normal induced velocity due to memory effect of waterline source panels.
5. Normal induced velocity due to memory effect of hull, lifting surface, and wake sheet dipole panels.

$$
\begin{aligned}
2\pi\sigma_i + \sum_{j=1}^{NH(t)+NL(t)} \left[\sigma_j^{(t)} \int_{S_j} \frac{\partial G^0\left(p_i, q_j\right)}{\partial n_{p_i}} \, dS + \mu_j^{(t)} \int_{S_j} \frac{\partial^2 G^0\left(p_i, q_j\right)}{\partial n_{p_i} \partial n_{q_j}} \right] dS = \\
4\pi \left(\dot{\boldsymbol{\eta}} \cdot \boldsymbol{n_{p_i}} + \boldsymbol{\eta} \cdot \boldsymbol{m_{p_i}} - \frac{\partial \Phi_w}{\partial n_{p_i}} \right) - \sum_{j=1}^{NW(t)} \mu_j^{(t)} \int_{S_j} \frac{\partial^2 G^0\left(p_i, q_j\right)}{\partial n_{p_i} \partial n_{q_j}} \, dS \\
+ \int_0^t \sum_{j=1}^{NH(\tau)+NL(\tau)} \sigma_j^{(\tau)} \int_{S_j} \frac{\partial^2 G^f\left(p_i, t; q_i, \tau\right)}{\partial \tau \partial n_{p_i}} \, dS \, d\tau \\
+ \int_0^t \sum_{j=1}^{NWL(\tau)} \sigma_j^{(\tau)} \int_{l_w} \frac{\partial^2 G^f\left(p_i, t; q_i, \tau\right)}{\partial \tau \partial n_{p_i}} V_N^{(\tau)} V_n^{(\tau)} \, dL \, d\tau \\
+ \int_0^t \sum_{j=1}^{NH(\tau)+NL(\tau)+NW(\tau)} \mu_j^{(\tau)} \int_{S_j} \frac{\partial^3 G^f\left(p_i, t; q_i, \tau\right)}{\partial \tau \partial n_{p_i} \partial n_{q_i}} \, dS \, d\tau
\end{aligned}
\tag{3.65}
$$

The induced potential and its derivatives due to the source elements Rankine and their biplane image parts $1/R$ and $1/R_0$ are computed using the 'Hess and Smith' formulations as given by Hess and Smith (1964). The induced potential and its spatial derivatives due to dipole elements and their biplane Green function parts $1/R$ and $1/R_0$ are obtained by applying the Biot-Savart law to the four sides of the equivalent vortex ring and its biplane image as follows (Katz and Plotkin 2001):

$$\int_{S_j} \frac{\partial^2 G\left(p_i, q_i\right)}{\partial n_{p_i} \partial n_{q_j}} dS = \int_{S_j} \boldsymbol{n}_{p_i} \cdot \nabla \left\{ \boldsymbol{n}_{q_i} \cdot \nabla \left[R^{-1}\left(p_i, q_i\right) - R_0^{-1}\left(p_i, q_i\right) \right] \right\} dS = \boldsymbol{n}_{p_i} \cdot \left[\boldsymbol{V}\left(p_i, q_i\right) + \boldsymbol{V}_0\left(p_i, q_i\right) \right] \quad (3.66)$$

The velocity vectors $\boldsymbol{V}$ and $\boldsymbol{V_0}$ are defined by (where $\boldsymbol{dl}$ is the vortex element vector of each of the four panel edges):

$$\boldsymbol{V} = \int \frac{\boldsymbol{dl} \times \boldsymbol{R}}{R^3} \quad (3.67)$$

$$\boldsymbol{V_0} = \int \frac{\boldsymbol{dl} \times \boldsymbol{R_0}}{R_0^3} \quad (3.68)$$

3.6.5 Time stepping

At the start, $t = 0$, the body is impulsively set into motion. Waves are started with a ramp-up function. At the first time step, source and dipole strengths are determined without wake sheet. At each subsequent time step the body is advanced to a new position with an instantaneous velocity. Both position and velocity are known from the equations of motion, refer to section 3.9. The gap that results behind each trailing edge dipole elements on lifting surfaces is filled with a vortex ring element. Together, the vortex ring elements form wake sheets. In this way, the orientation of the wake element at the trailing edge approximates the orientation of the flow leaving the lifting surface or transom stern to the first order. The circulation strength of new wake vortex elements in the trailing wake sheets of lifting surfaces is set equal to the difference in dipole strength of the upper and lower side trailing edge dipole elements for lifting surfaces. For transom flow, the new wake vortex strength are determined by simultaneously solving for the normal flow condition and for the transom flow condition described in section 3.6.3.

The above procedure is valid for the body-exact approach. Linearisation of the body boundary condition significantly simplifies this process and is discussed in section 3.6.7.

3.6.6 Solution

With the known position and velocity of hull, lifting surfaces and wake vortexes the governing equation (3.65) can be solved for the unknown source and dipole strengths. To solve (3.65), it can be cast in a set of linear equations with as unknowns the source and dipole strengths $X_j^{(t)}$:

$$\sum_{j=1}^{NT(t)} A_{ij} X_j^{(t)} = B_i \text{ with } i = 1, 2, 3, ..., NT\left(t\right) \quad (3.69)$$

Matrix terms A_{ij} contain the integral terms of the left hand side of (3.65), the Rankine and biplane image terms. Their evaluation will be detailed in section 4.2.2. On the other side, vector terms B_i contain the entire right hand side of (3.65). $NT\left(t\right)$ denotes the total number

of source and dipole panels at time t. This set of linear equations can be readily solved by using standard LU-decomposition techniques.

The right hand side term B_i contains three types of expressions:

1. Normal velocity due to the rigid body motions.
2. Normal velocity due to the undisturbed incident wave.
3. Induced normal velocity due to wake panels and memory effects.

The first two expressions can be evaluated straightforwardly. The wave velocities can be directly obtained from the spatial derivatives of the incident wave potential function and the rigid body motions follow from the time integration of the equation of motion up to the current time instant. The final type of expressions (numbered 2-5 on the right hand side in (3.65) in section 3.6.4) are much more cumbersome to obtain. They consist of wake Rankine and biplane image and free surface memory contributions and free surface memory contributions for the source and doublet panels.

The wake Rankine and biplane image terms are obtained using the same procedure as for the doublet G^0-terms, detailed in chapter 4, section 4.2.2. The memory terms require much more computational effort. Per control point the contributions to each free surface memory derivative of all singularity panels over all history time steps need to obtained. Moreover, each of these contributions involves a very accurate integration over the singularity panel. This procedure is detailed in chapter 4, section 4.2.1.

In the case of the application of the transom flow condition described in section 3.6.3 the solution scheme needs to be extended. As pointed out, although the number of extra conditions added to system equals the number of new unknown wake panel strengths in the first wake panel row, the combined source-doublet elements add extra unknowns to the problem. In section 3.6.3 two possibilities have been given to solve this: (1) pre-setting the source strength and solving for the doublet strengths, and (2) first solving a source-only system without wake elements, followed by a doublet solution with wake elements.

The second method was favoured by Reed et al. (1991) as they experienced numerical instabilities applying the first method. In this work also the second method is choosen. Figure 3.6 illustrates the system that is solved for the combined source-doublet system (the second solution in method 2 above). Now the influence matrix $\boldsymbol{A}$ is extended to include the transom flow condition. The parts indicated in the figure are:

$A1$ The normal G^0-influence terms of the doublet singularities of the body on the other panels and themselves.

$A2$ The normal G^0-influence terms of the first wake row singularities on the body panels.

$A3$ The tangential G^0-influences of the body singularities on the u-velocity in the pressure condition (applied on the last hull panel row at the transom edge) as well as the term used to construct the local doublet x-derivative in (3.62). Additionally the estimated terms for the time derivative at the transom condition that are dependent on the current doublet strength.

$A4$ The tangential G^0-influences of the first wake row singularities on the other first wake row and themselves as well as their contribution to the local doublet x-derivative in (3.62) and their contribution to the time derivative in the transom pressure condition.

The solution vector $\boldsymbol{X}$ contains the unknown source and doublet strengths on the body ($X1$) and the unknown doublet strengths of the first wake row ($X2$). The right hand side vector part

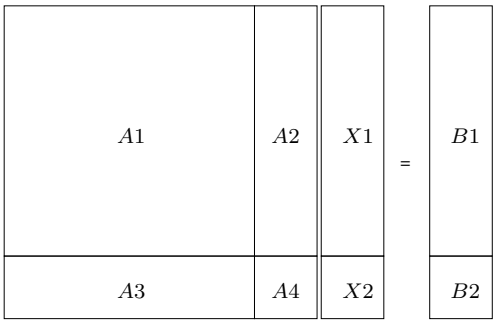


Figure 3.6: *Set-up of solution of combined source-doublet system*

$B1$ houses the normal velocity contributions of all memory integrals and known G^0-integrals on each body panel along with the local wave and rigid body normal velocities. The $B2$-part of the right hand side vector $\boldsymbol{B}$ holds all memory and known G^0-term contributions to the u-velocity and $d\Phi/dt$ at the transom panels along with the wave velocity in x-direction. The 'known' G^0-term contributions stem from the first source-only solution that was obtained before adding the transom flow condition.

3.6.7 Linearisation

As noted in the previous section, the evaluation of the free surface memory term of the Green function requires a large amount of computational time. These terms need to be evaluated at each control point for the entire time history at each time step. Moreover, due to the wake shedding process, the number of singularity elements increase in time.

To decrease this computational burden, the evaluation of the free surface memory contributions has been simplified. For low $(t-\tau)$ values use is made of interpolation of predetermined values for G^f and its derivatives, whereas for larger $(t-\tau)$ values polynomials and asymptotic expansions are used to approximate G^f and its derivatives. After a certain history time the history integrals are cut off alltogether, requiring a careful selection of a suitable cut off time. The evaluation of the Green function derivatives using this procedure is detailed in chapter 4, section 4.2.1.

Despite the significant reduction of the effort needed to evaluate the free surface memory contributions the computational effort needed is still excessive. To further limit the problem, a maximum is set to the number of wake elements to be used. Once this maximum is reached for each new row of wake elements the final row at the other end of the wake sheet is removed. Care needs to be taken that the wake sheet remains of sufficient length to avoid influence of the removal of wake rows on the body forces (refer to chapter 4).

A further reduction of the problem can be achieved by prescribing the wake sheet position and form. This prescription is simply that a wake element should remain stationary once shed. Now, no effort is needed to calculate the exact position of each wake element at each time step (requiring the calculation of the influence of all singularity elements on each wake element). This violates the requirement of a force free wake sheet, but for practical purposes this does not have significant influence as shown by Van Walree (1999) and Katz and Plotkin (2001) for (hydro) foils. In chapter 4 this matter is further investigated.

For the panels on the hull and lifting surfaces a similar problem is present. Due to the unsteady motions the position of the hull and lifting surfaces relative to the past time panels is not constant, so the influence of past time panels has to be recalculated for the entire time history. This results in a significant computational burden requiring the use of a supercomputer or at least distributed computing to keep the computational time within reasonable limits.

In order to reduce this, a major simplification has to be made. To avoid recalculation of the past time panels, the relative distance has to be kept constant. This requires linearisation of the unsteady position of hull and lifting surfaces to a average position (moving with a constant forward speed). This approach is called the *body-linear* approach, in contrast with the approach before this, the *non-linear* or more accurately the *body-exact* approach.

This reduction leads to a constant relative distance between the current panels and the past time panels, so that the memory integral can be calculated a priori for use at each time step during the simulation. This makes the matrix A in (3.69) a constant matrix, that needs to be inverted only once, instead of at each time step.

The prescription of the wake sheets in this linear approach leads to a flat wake sheet behind the lifting surface. Again a constant distance exist to the past time wake panels. Only the strengths of the first row of wake elements (the start vortex) need to be calculated at each time step, until the maximum wake sheet length is reached. For all other rows the induced velocity can be obtained by multiplying the influence by their actual circulation. This again reduces the computational effort needed.

An added benefit is that the waterline integral for wake sheets that intersect the free surface will disappear. This intersection will appear for instance when along the entire circumference of the transom stern wake elements are shed. When inspecting (3.51) it becomes apparent that a waterline integral will appear for this kind of wake sheets. Yet as long as the wake consists of flat surfaces parallel to the ship's velocity, the component of the linearised rigid body velocity normal to the wake sheet is naught. Hence this term disappears.

Practically, the body panels on the linearised submerged geometry are obtained by first running iterative simulations at the desired forward speed in calm water. The final location of the body geometry (in terms of trim and rise of the centre of gravity) is used to obtain new panels for the next iteration. As soon as the starting location of an iteration coincides with reasonable margins with the final location of the same iteration this procedure is stopped and the reference position of the ship at the corresponding forward speed is found and is used in the seakeeping analysis, this procedure will be detailed in chapter 5.

3.7 Pressure evaluation approaches

In order to obtain the distribution of the hydrostatic and -dynamic pressures acting on the body the Bernoulli equation is evaluated on the body surface. The unsteady Bernoulli equation in the body fixed reference frame is derived in appendix B and repeated in (3.70). In this equation the time derivative of the potential is obtained in the non-inertial body-fixed frame.

$$\frac{p - p_\infty}{\rho} + \frac{\partial \Phi}{\partial t} - \nabla\Phi \cdot (\boldsymbol{V} + \boldsymbol{\Omega} \times \boldsymbol{r}) + \frac{1}{2}\left(\nabla\Phi\right)^2 - g z_0 = 0 \tag{3.70}$$

The evaluation of (3.70) involves the computation of the spatial and temporal derivatives of the velocity potential on the body. At this point the spatial derivatives at all body panels have

already been obtained in the solution of the potential zero normal flow problem. The time derivative nevertheless, is still unknown and needs to be obtained. This process is described in section 3.7.1.

Next still a number of choices can be made as to how exactly the different components in the Bernoulli equation are computed. These components are split into the hydrostatic pressure, the induced hydrodynamic pressure (due to radiation and diffraction) and the incident wave pressure or Froude-Krylov pressure. Three alternative approaches for this pressure evaluation have been implemented. The first is to compute all pressure components, hydrodynamic (including Froude-Krylov) and hydrostatic at the linearised submerged geometry (fully body-linear approach, section 3.7.4). The second is to retain the linearised dynamic pressure of the first approach and to compute the Froude-Krylov pressures and hydrostatic pressures at the actual submerged geometry (blended approach, section 3.7.5). The third is to apply pressure profile stretching, described in section 3.7.6.

Two of these approaches involve the usage of the instantaneous wave elevation determined by applying the dynamic free surface boundary condition. This process is described in section 3.7.3.

3.7.1 Time derivative of the velocity potential

To obtain the time derivative of the velocity potential, the derivative can be split in an incident wave part and disturbance part, based on the assumption of linearity:

$$\frac{\partial \Phi}{\partial t} = \frac{\partial \Phi_w}{\partial t} + \frac{\partial \Phi}{\partial t} \tag{3.71}$$

The incident wave part can easily be calculated analytically:

$$\frac{\partial \Phi_w}{\partial t} = \frac{\partial}{\partial t}\left(\frac{\zeta_{wa} g}{\omega} e^{k_w z_0} \sin\left(k_w x_0 - \omega t\right)\right) \tag{3.72}$$

The time derivative of the disturbance part can be determined using the integral equation for the disturbance potential given in (3.55). Derivation with respect to time gives the following relation:

$$\begin{aligned} 4\pi \frac{\partial \Phi}{\partial t}(p,t) = -2\pi \frac{\partial \mu}{\partial t}(p,t) + \int_{S_{HL}(t)} \frac{\partial \sigma}{\partial t}(q,t)\, G^0\, dS + \\ \int_{S_{HLW}(t)} \frac{\partial \mu}{\partial t}(q,t)\, G^0_{n_q}\, dS - \int_0^t \int_{S_{HL}(\tau)} \sigma(q,\tau)\, G^f_{t\tau}\, dS\, d\tau - \\ \int_0^t \int_{S_{HLW}(\tau)} \mu(q,\tau)\, G^f_{t\tau n_q}\, dS\, d\tau - \frac{1}{g} \int_0^t \int_{l_w(\tau)} \sigma(q,\tau)\, G^f_{t\tau} V_N V_n\, dL\, d\tau - \end{aligned} \tag{3.73}$$

In this derivation use has been made of Leibniz theorem for differentiation of an integral, (3.74) (Gradshteyn and Ryzhik 1980). The terms due to the integration borders fortunately simply disappear as they contain single time derivatives of G^f, that become zero for $\tau = t$.

Note that the normal velocities V_N and V_n are constant with respect to time, due to the applied linearisation.

$$\frac{d}{dc}\int_{a(c)}^{b(c)} f\left(x,c\right)dx = \int_{a(c)}^{b(c)} \frac{\partial}{\partial c} f\left(x,c\right)dx + f\left(b,c\right)\frac{db}{dc} - f\left(a,c\right)\frac{da}{dc} \tag{3.74}$$

Part of the time derivative can be estimated by a simple first order backward scheme. This concerns the local dipole strength, the dipole Rankine contribution and the wake contributions. The estimation is impossible for the Rankine source part and the free surface memory source and dipole contributions as it leads to instabilities.

$$\frac{\partial \Phi}{\partial t} \approx \left[\frac{\partial \Phi}{\partial t}\right]_{an} + \left[\frac{\partial \Phi}{\partial t}\right]_{est} \tag{3.75}$$

The estimated part of the derivative can be calculated in a straightforward manner. The analytical part is split in a Rankine part and a free surface memory part.

$$4\pi\left[\frac{\partial \Phi}{\partial t}\right]_{an}^{0} = \int_{S_{HL}} \frac{\partial \sigma\left(q,t\right)}{\partial t} G^0\, dS \tag{3.76}$$

$$\begin{aligned} 4\pi\left[\frac{\partial \Phi}{\partial t}\right]_{an}^{f} = -\int_0^t \Bigg\{ &\int_{S_{HL}} \sigma\left(q,\tau\right) G^f_{t\tau}\, dS + \int_{S_{HL}} \mu\left(q,\tau\right) G^f_{t\tau n_q}\, dS + \\ &\frac{1}{g}\int_{L_W} \sigma\left(q,\tau\right) G^f_{t\tau} V_N V_n\, dL \Bigg\} d\tau + \end{aligned} \tag{3.77}$$

Of these equations only the time derivative of the source strength, (3.76), poses a difficulty as this term is unknown at the time of the solution. Nevertheless, it can be obtained by using the solution matrix of the potential flow problem.

$$\begin{aligned} \sigma =& A^{-1}\boldsymbol{v}_n \\ \frac{\partial \sigma}{\partial t} =& A^{-1}\frac{\partial \boldsymbol{v}_n}{\partial t} \end{aligned} \tag{3.78}$$

In this equation, A is the solution matrix relating the source strengths via the Rankine influences to the right hand side of the solution (containing the free surface memory effects, the incident wave and the rigid body motions). This matrix is available after setting up the solution in terms of normal velocities to obtain the source and dipole strengths and is independent of time in the body-linear formulation, allowing for a quite simple time derivative of the solution equation as shown in (3.78).

When a combined source-dipole formulation is used, the solution matrix A that needs to be used in (3.78) is somewhat different than the solution matrix used for the potential solution. This is due to the fact that in (3.78) A should only relate the source strengths to the normal flow velocity, as only the time derivative of the source strength is required. For that reason all dipole relations are removed from A and it only contains G^0-terms of all source elements.

$\boldsymbol{v}_n$ is a vector containing all influences due to incident wave, free surface memory and rigid body motions in terms of normal velocity on the panels:

$$\begin{aligned}\frac{\partial \boldsymbol{v}_n}{\partial t} &= \left[-\frac{\partial \boldsymbol{v}_w}{\partial t} - \frac{\partial \boldsymbol{v}_G}{\partial t} + \ddot{\boldsymbol{\delta}}\right] \cdot \boldsymbol{n} \\ \frac{\partial \boldsymbol{v}_w}{\partial t} &= \frac{\partial \nabla \Phi_w}{\partial t} \\ \frac{\partial \boldsymbol{v}_G}{\partial t} &= \frac{\partial \nabla \Phi^{df}}{\partial t}\end{aligned} \tag{3.79}$$

$\ddot{\boldsymbol{\delta}}$ refer to the definition of $\boldsymbol{\delta}$ in section 3.4

The wave accelerations follow from the analytical expression for the wave potential. The free surface memory contributions can be determined with the time derivative of the induced velocities due to the free surface memory influences. Again this time derivative can be obtained easily be realizing that due its definition the value of G^f and its derivatives are zero at $\tau = t$.

$$\frac{\partial \boldsymbol{v}_G}{\partial t} = \frac{1}{4\pi}\int_0^t \left[-\int_{S_{HL}(\tau)} \sigma(q,\tau)\, G^f_{t\tau n_p}\, dS - \int_{S_{HLW}(\tau)} \mu(q,\tau)\, G^f_{t\tau n_p n_q}\, dS - \frac{1}{g}\int_{l_w(\tau)} \sigma(q,\tau)\, G^f_{t\tau n_p} V_N V_n\, dL\right] \tag{3.80}$$

3.7.2 Added mass

For the solution of the equation of motion it is possible to include the $\ddot{\boldsymbol{\delta}}$-term, the rigid body acceleration, in the mass term as added mass. The term that will be transferred equals:

$$\int_{S_{HL}(t)} A^{-1}\ddot{\boldsymbol{\delta}}(q,t)\, G^0\, dS \tag{3.81}$$

The force vector on one panel due to this term can be written as:

$$\int_{S_{HL}(t)} A^{-1}\ddot{\boldsymbol{\delta}}(q,t)\, G^0\, dS \cdot A_{panel} \tag{3.82}$$

Or in terms of the partial time derivative of the body-fixed velocity vector:

$$\left(\int_{S_{HL}(t)} A^{-1}\ddot{\boldsymbol{\delta}}'(q,t)\, G^0 dS \cdot A_{panel}\right)\frac{\partial \boldsymbol{u}}{\partial t} \tag{3.83}$$

The matrix $\ddot{\boldsymbol{\delta}}'$ is a $(N \times 6)$ matrix containing the normal acceleration on a panel due to unit body acceleration components. For each panel at (x, y, z) it equals:

$$\ddot{\boldsymbol{\delta}}' = \begin{bmatrix} n_x \\ n_y \\ n_z \\ n_z y - n_y z \\ n_x z - n_z x \\ n_y x - n_x y \end{bmatrix} \tag{3.84}$$

(3.83) can be summed over all panels to obtain the total force on the body due to this term. Closer inspection learns that the expression consists of a term equivalent to the infinite frequency added mass found in frequency domain potential theory times the rigid body acceleration. When expanded, the added mass term turns out to be a (6×6) matrix that can be directly included in the mass matrix. To obtain the correct pressure distribution for visualisation and output, it is necessary to add this term to the resulting pressure distribution. This has to be done after the rigid body motion is solved, as the rigid body acceleration is needed to obtain this contribution.

Instead of constructing the influence matrices A and G^0 and the unit acceleration matrix $\ddot{\boldsymbol{\delta}}'$ for the linearised submerged geometry, it is also possible to set-up copies of these two matrices at run-time specifically for the computation of the added mass. In that case it is possible to set them up for the panels that are below $z_0 = 0$ on the exact time instant. This leads to a body-exact added mass term, that becomes time-dependent due to its dependence on the rigid body motions, following the concept of the blended approach also used for the computattion of Froude-Krylov and hydrostatic pressures.

The additional computational time is only marginal, as all three matrices are relatively simple to set-up and a still a large amount of the terms that used to contruct these matrices can be pre-computed before the time-domain loop commences.

3.7.3 Free surface elevation

The free surface elevation can be obtained by applying the dynamic free surface boundary condition given in (3.26). The linearised dynamic condition (3.25) can be used to obtain an expression for the free surface elevation:

$$\eta = -\frac{1}{g}\frac{\partial \Phi}{\partial t} \quad \text{at } z_0 = 0 \tag{3.85}$$

$\frac{\partial}{\partial t}$ is the time derivative for an earth-fixed (inertial) coordinate frame. The time derivative of the potential is only available on the body-fixed panels, making a transformation necessary as shown previously in (3.70). In this manner the free surface elevation becomes:

$$\eta = -\frac{1}{g}\frac{\partial \Phi}{\partial t} + \frac{1}{g}\left[\boldsymbol{V} + \boldsymbol{\Omega} \times \boldsymbol{r}\right] \cdot \nabla \Phi \tag{3.86}$$

For an unsteady problem, where the body boundary condition is linearised to the mean position of the body, the free surface elevation can be calculated by setting $\boldsymbol{V} = [U\ 0\ 0]$.

$$\eta = -\frac{1}{g}\frac{\partial \Phi}{\partial t} + \frac{U}{g}\frac{\partial \Phi}{\partial x} \tag{3.87}$$

In order to calculate the free surface elevation, both the spatial derivatives and the time derivative of the velocity potential are needed at the free surface. To obtain the spatial derivative in x-direction, (3.51) needs to be re-evaluated to obtain expressions for these derivatives at the free surface. Again field point p is located on a boundary of the fluid domain, in this case the undisturbed free surface, thus $T = 1/2$ is set according to (C.8). The result is similar to (3.56), but now p is positioned on the free surface instead of the body surface.

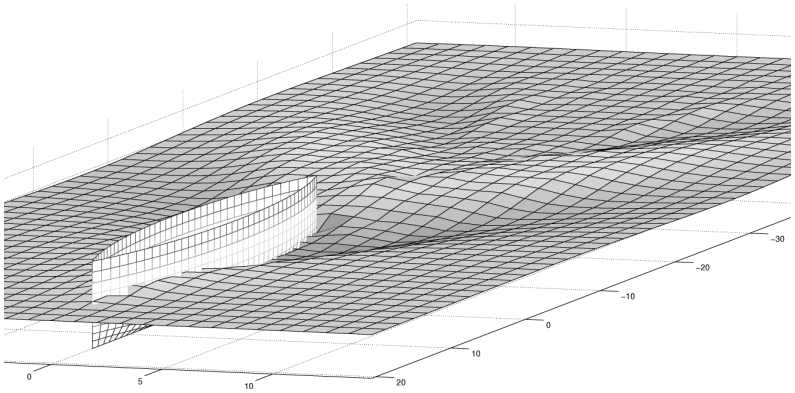


Figure 3.7: *(Calm water) free surface elevation due to a Wigley travelling at* $Fn = 0.6$

To compute the flow velocities at the free surface, it is sufficient to know the singularity strengths of the body panels together with the Green function derivatives evaluated for the field point or field point distribution on the free surface. The time derivative of the undisturbed wave potential can be calculated analytically, the time derivative of the singularity potential is computed using the approach introduced in section 3.7.1. When the potential derivatives are evaluated on a grid at the free surface, the elevation can be calculated at the grid points and a representation of the free surface shape can be obtained as shown in figure 3.7.

To obtain the instantaneous wetted surface of the body geometry, the body geometry is positioned in its current rigid body position (refer to figure 3.8) in the incident plus disturbed wave field. The next step is to find the instantaneous intersection of the body and the free surface. To do this, the free surface elevation is now split in two parts:

1. The undisturbed incident wave elevation that can be computed exactly everywhere.
2. The body and wake induced free surface elevation.

The first can be obtained at the x_0y_0-location of each panel without difficulties. The second, composed of the diffraction and radiation waves (or disturbance waves), is obtained by evaluating the induced free surface elevation at the linearised calm water intersection. The total wave elevation at the horizontal location of each panel centroid is found by computing the undisturbed wave elevation at the instantaneous vertical projection of each panel centroid on the x_0y_0-surface and adding the induced wave elevation of the nearest linearised waterline grid point. In other to avoid numerical problems in the Green function, the free surface grid points at the linearised waterline are not placed exactly on the intersection of the body panels with the free surface, but the grid points rather are displaced over a small distance outwards and downwards, as shown in figure 3.9. The implications of this procedure will be detailed in chapter 4, section 4.5.

The relative position of the free surface grid points with respect to the body and wake singularity panels remains constant. For this reason the calculation of the free surface memory influences of the body and wake singularity panels on the free surface grid can be precomputed in the same way as is done in setting up the potential flow solution.

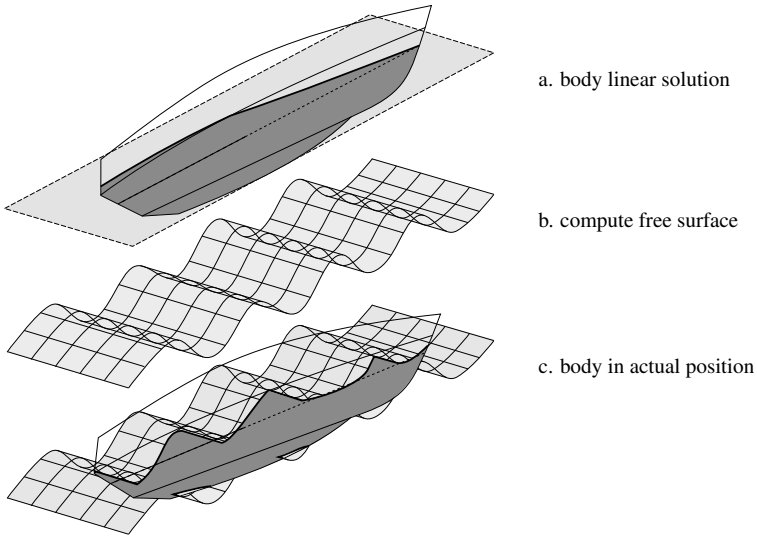


Figure 3.8: *Free surface evaluation on rectangular grid*

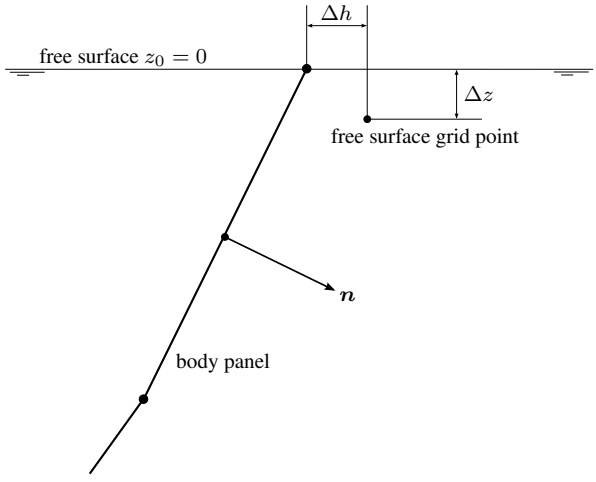


Figure 3.9: *Horizontal and vertical shift of free surface evaluation points*

3.7.4 Body linear approach

In the body linear approach, the hydrodynamic and hydrostatic pressures are evaluated on the linearised calm water submerged body surface. This surface is generally determined by iteratively finding the corresponding reference position of a body for each forward speed in calm water. The pressure is determined by applying (3.70), that for a constant forward speed U reduces to:

$$\frac{p - p_\infty}{\rho} + \frac{\partial \Phi}{\partial t} - U\frac{\partial \Phi}{\partial x} + \frac{1}{2}\left(\nabla\Phi\right)^2 - gz = 0 \tag{3.88}$$

The linearised hydrostatic pressures are simply evaluated at each panel centroid by using the reference position of the body in calm water. This is expressed in (3.70) by using the body-fixed z-coordinate, instead of the earth-fixed z_0-coordinate.

3.7.5 Blended pressure approach

Due to the geometric linearisation of the problem, the hydrodynamic pressure due to the disturbance potential is calculated at the still water wetted part of the body at all time instances. The variation of the wetted surface and its orientation caused by the incoming waves, the diffracted and radiated waves, and the rigid body motions is ignored. Nevertheless, the pressure distribution can be corrected by considering the real earth-fixed position of each collocation point relative to either the undisturbed wave surface or the actual free surface (the latter obtained with the method described in section 3.7.3) when computing the hydrostatic and Froude-Krylov pressures.

The combination of the induced hydrodynamic pressures at the linearised position of the body and Froude-Krylov and hydrostatic pressures at the actual body location is in literature often termed as 'the blended pressure' approach. In (3.89) the potential derivatives due to distributed singularities, or the induced potential derivatives are obtained in the same way as for the linear pressure approach described in the previous section, whereas the derivatives of the wave potential and the hydrostatics are obtained on the actual submerged rigid body geometry at the current time instant.

$$\frac{p - p_\infty}{\rho} + \frac{\partial \Phi}{\partial t} - U\frac{\partial \Phi}{\partial x} + \frac{1}{2}\left(\nabla\Phi\right)^2 - gz_0 = 0 \tag{3.89}$$

The hydrostatic, hydrodynamic and Froude-Krylov pressures are elaborated below. The still water free surface is $z_0 = 0$ and the actual free surface is $z_0 = \eta$; ζ is the incident wave elevation.

Hydrostatic pressure p_s

The actual earth-fixed rigid body position is used for the calculation of the pressure.

$$\begin{aligned} p_s &= -\rho g z_0 && \forall \quad z_0 \leq 0 \wedge z_0 \leq \eta \\ p_s &= -\rho g\left(z_0 - \eta\right) && \forall \quad z_0 > 0 \wedge z_0 \leq \eta \\ p_s &= 0 && \forall \quad z_0 > \eta \end{aligned} \tag{3.90}$$

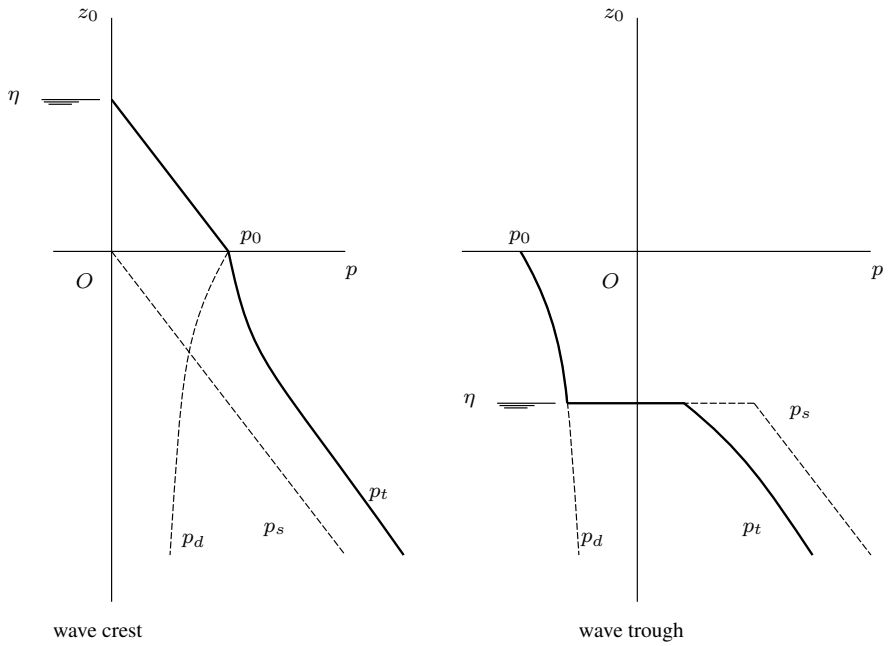


Figure 3.10: *Vertical pressure distribution for blended approach, wave crest - left, wave trough - right*

Hydrodynamic pressure p_d

The hydrodynamic pressure, working on the still water submerged geometry, will be left unmodified, even when the originally submerged geometry emerges. Experience shows that when the hydrodynamic pressure is changed only by setting it to zero in emerged regions, the force balance becomes unstable.

Froude-Krylov pressure p_w

The undisturbed wave pressure can be included by simply calculating the linear Froude-Krylov pressures directly at the actual submerged geometry up to the still water free surface. In wave troughs the Froude-Krylov pressure, in accordance with the hydrostatic pressure is set to zero. In wave crests a linear pressure variation is assumed between the pressure at the still water surface ($\rho g \eta$) and zero pressure at the instantaneous free surface. This pressure component has been included in the hydrostatic pressure above.

An interesting feature of this approach is that there is some 'leakage' of the rigid body motions into the linearised potential solution: in the application of the zero normal flow condition, the core of the potential solution (3.56) and (3.65), also the normal velocity due to the undisturbed waves is evaluated at the 'actual' instantaneous rigid body location, including the correction for the wave surface elevation.

Although the blended pressure approach partly takes into account the variation of the pressures due to the rigid body motions and the non-zero wave elevation, the approach re-

sults in an inconsistent pressure distribution on the hull. Due to the various assumptions in the pressure computation it is possible that jumps occur in the pressure distribution on the body. Those jumps are not occurring in the linear pressure approach, as that approach, nevertheless its limitations, is exactly consistent with the assumptions of linearity and small wave steepness.

The inconsistency is not of much importance when considering overall rigid body motions and acceleration levels. Still when local pressures become of importance, for example when using the pressure distribution for structural strength analysis, then the jumps in the pressure distribution could be a limiting factor.

A variation on the blended pressure approach has been implemented as well. In this variation instead of the undisturbed wave elevation ζ the disturbed wave elevation η is used to correct the Froude-Krylov and hydrostatic pressures. This disturbed wave elevation is determined as described in the next section for the pressure profile stretching approach.

Figure 3.10 shows how the modification of the hydrostatic pressure (dashed line marked p_s) impacts the total vertical pressure distribution (thick line marked p_t). Generally, wave crests do not pose problems. The pressure above the still water free surface is assumed to be hydrostatic and the hydrostatic pressure in the wave crest at the still waterline and the hydrodynamic pressure of the wetted surface at the waterline equal each other and no jump is present.

In a wave trough on the other hand, a jump in the pressure is occurring at the instantaneous free surface. One reason for this jump is the fact that the hydrodynamic pressure p_d is not set to zero in the wave trough above the free surface, as the dynamic pressure remains unaltered in this approach. Yet, even setting the hydrodynamic pressure in a wave trough to zero still results in a pressure jump. This jump is due to the linearisation of the free surface boundary condition and the retaining of the velocity squared term in the pressure distribution.

A further complication is the inclusion of the rigid body motions (not shown in figure 3.10). Although the rigid body motions can be implemented easily by substituting the actual z_0-coordinate when calculating the hydrostatics, even more jumps will occur in the total pressure distribution.

A similar approach has been used by Blandeau et al. (1999) for a local pressure model on the side shell of FPSOs. They used the hydrodynamic pressures at the waterline in a zero forward speed frequency domain panel method. The pressure at the waterline is corrected by applying a water column of height $\eta = p_0/\rho g$ in case of a wave crest and the pressure above a through is set to zero.

3.7.6 Pressure profile stretching approach

As pointed out in the previous section, the combination of hydrostatic and Froude-Krylov pressures on the instantaneous wetted surface with linearised hydrodynamic pressures (the blended pressure approach) yields inconsistencies resulting in jumps in the pressure distribution. For relatively large (with respect to wave length and height) and slow speed ships operating in non-steep waves generally these inconsistencies will not result in large deviations in the pressure distributions. These large deviations are prevented due to the fact that the disturbance part of the hydrodynamic pressure is relatively small in comparison with the hydrostatic and Froude-Krylov pressures under these conditions.

Problems arise when the hydrodynamic disturbance pressures are relatively large. This is especially the case for high speed ships, where the high rate of change of impulse of the water along the length of the ship, especially at the bow, causes regions with large gradients in the hydrodynamic pressure. The resulting loads cause significant lift and thereby significant trim and rise. Variations in the hydrodynamic pressures will have significant effect on the total force balance of the ship. Especially for ships with relatively large length over beam ratios and flared bow sections, large variations in submerged geometry and thus in hydrodynamic loads can occur.

Now a method is developed that considers the influence of body and free surface non-linearities (causing changes in the wetted surface) in the hydrodynamic loads as well. Hydrostatic pressures, hydrodynamic disturbance pressures and incident wave pressures again are considered separately.

Hydrostatic pressure p_s

The actual earth-fixed rigid body position is used for the calculation of the hydrostatic pressure, as has been done with the previous approach.

$$\begin{aligned} p_s &= -\rho g z_0 && \forall \quad z_0 \leq 0 \wedge z_0 \leq \eta \\ p_s &= -\rho g \left(z_0 - \eta\right) && \forall \quad z_0 > 0 \wedge z_0 \leq \eta \\ p_s &= 0 && \forall \quad z_0 > \eta \end{aligned} \tag{3.91}$$

Hydrodynamic pressure p_d

The hydrodynamic disturbance pressures are stretched by considering the original wetted depth (keel to (the nearest part of the) calm waterline) and the actual wetted depth (from keel to free surface elevation at the nearest waterline location, including rigid body motions) at each collocation point. The vertical pressure contour of p_d is determined at the x-location of the collocation point and stretched from original wetted depth to actual wetted depth as shown in figure 3.11 (the arrows).

Froude-Krylov pressure p_w

The pressure due to the incident waves is determined on the body surface below the still waterline of the body in its actual position (due to its motions), in the same way as the previous approach. For the wave profile the total free surface elevation is used (due to incoming waves and disturbance wave), pressures above the instantaneous free surface elevation are set to zero

In this approach, care is taken that in evaluating the incident wave pressure and normal velocity on the hull the same values are used as much as possible. This is to avoid treating the incident wave pressure and velocity differently in the solution of the boundary value problem and in computing the resultant pressure. In spite of this the result is that linear assumptions are violated in the process. Linearity assumes a uncoupling of wave excitation and hydrodynamic reaction, in the current process non-linear interactions or corrections are introduced that are not part of the underlying theoretical method.

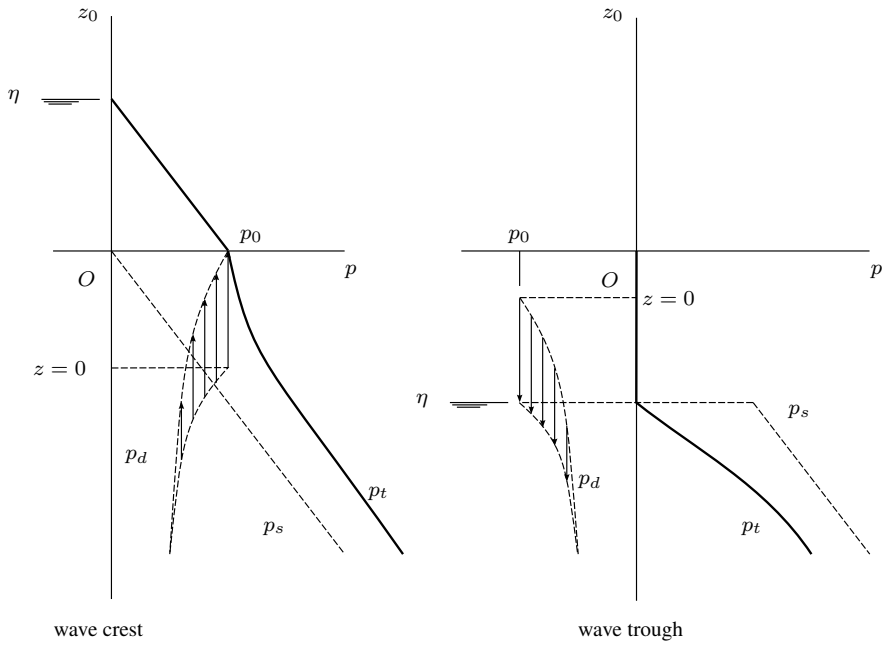


Figure 3.11: *Stretching of the hydrodynamic pressure (simplified; $z = 0$ indicates the location of the body-linear calm water intersection in the space-fixed frame). The arrows indicate the stretching process. Note that this figure only shows two possibilities of the possible combinations of rigid body position and wave elevation.*

In chapter 5, the implications of the different pressure techniques will be studied and quantified.

3.8 Inclusion of viscous flow effects

3.8.1 Viscous resistance

To calculate the viscous resistance R_v, empirical formulations are applied to each of the submerged parts of the geometry. The formulation used, is based on the ITTC'57 plate friction line and combined with a form factor $1 + k$.

$$R_v = \frac{1}{2}\rho U^2 \cdot S_{wet} \cdot C_f \,(1 + k) \tag{3.92}$$

$$C_f = \frac{0.075}{\left(\log_1 0Rn - 2\right)^2} \tag{3.93}$$

U is the ship speed, S_{wet} is the wetted surface area, k is a suitable form factor, and Rn is the Reynolds number of the body part considered. For the time being the wetted surface is computed by using the total area of the below water panels of the body in still water in its calm water forward speed reference position. The form factor is a user input value. The

choice of this value is beyond the scope of this thesis. Often for high speed ships fitted with a transom stern a form factor of 1 is applied.

3.8.2 Viscous damping

Especially for high speed vessels, possessing only slight potential damping, viscous damping can play an important role. This is especially true around the peak of vertical motions. Then forces that arise due to separation in the bilge region due to vertical motions can be of significance. The magnitude of these forces depends on oscillation frequency and amplitude, Froude number, and section shape. In the current model a cross flow analogy is used to account for these forces. Currently, the viscous damping coefficient is implemented in a simplyfied way and only depends on section shape, other influences are neglected. The following formulation is used in a strip wise manner:

$$F_z = -\frac{1}{2}\rho \left|V_r\right| V_r S C_{dv} \tag{3.94}$$

V_r is the vertical velocity of the section relative to the local flow velocity and S is the horizontal projection of the section area. The cross-flow drag coefficient C_{dv} has values in-between 0.25 and 1.33.

An additional term is incorporated for the hull roll damping, K_p:

$$K_p = -\left(b_p p + b_{pp}|p|p\right) \tag{3.95}$$

p is the roll velocity and b_p and b_{pp} are linear and quadratic roll damping coefficients respectively, determined by means of the MARIN FDS method (Blok and Aalbers 1991).

3.9 Solution of the equations of motion

To obtain the motions of the body in time, the equations of motion need to be solved. By assuming that the body is rigid and by choosing a convenient angular orientation vector $[\varphi, \theta, \psi]$ to define the position of the body in the space-fixed reference frame, application of linear and angular conservation of momentum in the body-fixed reference frame yields the Euler equations of motion. The derivation is given in appendix B and the resulting equations are repeated in (3.96).

$$\begin{aligned}
m\left(\dot{u} + qw - rv\right) &= X - mg\sin\theta \\
m\left(\dot{v} + ru - pw\right) &= Y + mg\cos\theta\sin\varphi \\
m\left(\dot{w} + pv - qu\right) &= Z - mg\sin\theta\cos\varphi \\
\dot{p}I_{xx} + qr\left(I_{zz} - I_{yy}\right) &= K \\
\dot{q}I_{yy} + rp\left(I_{xx} - I_{zz}\right) &= M \\
\dot{r}I_{zz} + pq\left(I_{yy} - I_{xx}\right) &= N
\end{aligned} \tag{3.96}$$

The vector $\boldsymbol{u} = [u, v, w, p, q, r]$ is the rigid body velocity in the body-fixed reference frame, the vector $\boldsymbol{F} = [X, Y, Z, K, M, N]$ contains the body-fixed hydromechanic force acting on

the body and the gravity terms express the action of the gravity force in the body-fixed reference frame. The mass matrix equals:

$$\boldsymbol{M} = \begin{bmatrix} m & 0 & 0 & 0 & 0 & 0 \\ 0 & m & 0 & 0 & 0 & 0 \\ 0 & 0 & m & 0 & 0 & 0 \\ 0 & 0 & 0 & I_{xx} & 0 & 0 \\ 0 & 0 & 0 & 0 & I_{yy} & 0 \\ 0 & 0 & 0 & 0 & 0 & I_{zz} \end{bmatrix} \tag{3.97}$$

As stated in section 3.7.1 the pressures contain a term due to the time derivative of the potential function that can be expressed by an added mass term times the acceleration. Transferring this term to the left hand side removes the unknown accelerations in the right hand side. When the equations of motion are expressed in matrix-vector form, the added mass matrix and the mass matrix can be simply joined into one (6×6) matrix. This enables the separation of the mass plus added mass times acceleration terms to the left hand side, resulting in the following form for the equations of motion:

$$\frac{\partial \boldsymbol{u}}{\partial t} = f\left(t, \boldsymbol{u}\right) \tag{3.98}$$

The right hand side contains the unknown acceleration (body-fixed) and the right hand side the unknown body-fixed velocity. Using the fourth order Runge Kutta method, refer to Burden and Faires (2001), (3.98) can be integrated in time to yield rigid body velocity at time step $i+1$ if the value of $\boldsymbol{u}$ is known at time step i:

$$\begin{aligned} \boldsymbol{u}_0 &= \boldsymbol{\alpha} \\ k_1 &= dt \cdot f\left(t_i, \boldsymbol{u}_i\right) \\ k_2 &= dt \cdot f\left(t_i + h/2, \boldsymbol{u}_i + 1/2k_1\right) \\ k_3 &= dt \cdot f\left(t_i + h/2, \boldsymbol{u}_i + 1/2k_2\right) \\ k_4 &= dt \cdot f\left(t_i + 1, \boldsymbol{u}_i + k_3\right) \\ \boldsymbol{u}_{i+1} &= \boldsymbol{u}_i + 1/6\left(k_1 + 2k_2 + 2k_3 + k_4\right) \end{aligned} \tag{3.99}$$

$\boldsymbol{\alpha}$ is the starting velocity of the body. Using the fourth order Runge-Kutta scheme means that the right hand side of (3.98) should be evaluated four times per time step. In particular the hydromechanic force should be evaluated four times per time step, meaning that the potential boundary value problem needs to be set-up and solved four times per time step.

For the most part the hydromechanic contributions to the solution of the boundary value problem are readily calculated. Yet the free surface memory functions do take a significant computational effort, especially when the linearisation described in section 3.6.7 are not performed. To reduce this effort one could choose to evaluate the induced normal velocities up to time step i and to keep them constant during the Runge-Kutta looping at the cost of some accuracy.

Effectively the influence of the changing rigid body velocity, wave orbital velocities, and control actions are taken into account, whereas the influence of the changing body position is not taken into account. This can be justified when the time step is small enough so that the

shift in rigid body position during a time step remains relatively small compared to the body dimensions.

In fact, a fifth evaluation of (3.98) is necessary to not only obtain the velocity (and by integration the position) of the body, but to also obtain the right, correctly balanced, forces, pressures and accelerations at time step $i + 1$.

Chapter 4
Numerical Aspects

4.1 Introduction

When a computational method, or for that manner any piece of software, is translated from idea and concept into computer code inevitably errors are introduced into the final program. These may come from different sources: from simple typographic mistakes and false matrix addresses, wrong interpretation of mathematical formulas to numerical errors such as round-off errors, truncation errors, and numerical instabilities. A number of these errors, especially typographic errors and programming errors may be signalled by a good compiler that translates the source code into an executable program, nevertheless this is to a large degree dependent on the correct usage of the compiler and even the compiler itself may introduce errors into the code.

For this reason, vital stages in the 'production' process of a computational code into an executable program are the verification stage and the validation stage. Although both stages are meant to ensure the quality of the program, they are two separate processes. In the verification stage the objective is to verify whether the program is producing expected results within the assumptions that are made in the basis of the method, or in other words whether the implementation of the method is correct. Often this is done by comparing the output of the program or separate parts of it (on the subroutine level or even a lower level) with results that have been obtained in a very controlled manner, such as analytical mathematical solutions or outcome of 'trusted' other programs. The validation stage on the other hand is meant to judge the quality of the program when it is applied to the cases it was developed for. The validation process deals with the assumptions at the basis of the method and is used to judge whether these are valid for the purposes the program is developed for.

Chapter 4 first deals with the verification of parts of the computational method introduced in the previous chapter. The verification is focused at the correct computation of the free surface Green function and its derivatives in section 4.2. Both the free surface memory part as the Rankine part are studied in detail to ensure the correct implementation. Guidelines for the correct truncation of the free surface memory effects and limiting behaviour of the Green function for zero and high Froude numbers are discussed.

In section 4.3 limited validation of the method is performed by studying the calculation of the lift on fully submerged foils, both deep and near the free surface. The computed results are compared to published experimental data. The following two sections 4.4 and 4.5 present numerical studies regarding the transom flow condition and the computation of the

free surface elevation. Section 4.6 discusses a convergence study investigating panel size and memory effect truncation for the complete numerical method applied to a high speed ship. In fact this section forms a final preparation for the seakeeping validation study presented in chapter 5. Chapter 4 is concluded with a discussion in section 4.7.

4.2 Free surface Green function

The choice for a time-domain Green function approach eliminates the need for distributing panels over the free surface to obtain a solution to the boundary value problem. Although for the latter approach a simple Rankine influence function would suffice, it would introduce a large number of extra unknowns as well as the need to explicitly deal with the radiation condition at the free surface edges, for instance by implementing numerical beaches.

Instead a much more complicated influence function, or Green function, was introduced in (3.38). This free surface Green function was designed to automatically satisfy the linear free surface boundary condition. This comes at the cost of a computationally much more complicated influence function with an improper integral and an oscillating argument. Especially when source and field point are close together in proximity of the calm water free surface the influence function of this form is heavily oscillating over the source panel. The accurate evaluation and panel integration of this integral is of utmost importance for the success of the entire method.

The current section deals with the numerical background of the chosen Green function. First, the computation and the spatial and temporal integration of the computationally challenging free surface memory part of the Green function is discussed. Checks are described to ensure correct implementation of the influence function. Second, the implementation of the Rankine and biplane parts is discussed. Finally, the low Froude number and high Froude number limits of the entire free surface Green function are studied, providing an integrated verification of the correct implementation of both the free surface memory part and the Rankine and biplane part of the Green function.

4.2.1 Free surface memory part

In the previous chapter, in particular in (3.65), (3.73), and (3.80), it became apparent that to set-up the solution and to calculate the dynamic pressure the following Green function derivatives are necessary to evaluate: time derivatives G^f_t, spatial derivatives of G^f_t of the form: G^f_{tx}, double spatial derivatives of G^f_t: of the form G^f_{txx}, double time derivatives G^f_{tt}, spatial derivatives of G^f_{tt} of the form: G^f_{ttx}, and double spatial derivatives of G^f_{tt}: of the form G^f_{ttxx}.

Each of these derivatives needs to be integrated over each source panel and multiplied by the constant panel strength over every history time step for each collocation point. The result is that for a symmetric body with N panels and N_{hist} history time steps $N \times N/2 \times N_{hist}$ accurate spatial and temporal integrations need to be carried out. The integration has been implemented in the computational method by applying Gaussian quadratures for the spatial integration over the source panel (Van Walree 1999) and by using the 10-point Gauss and 21-point Kronrod rule for the time integration.

What remains, is the accurate spatial and temporal evaluation of the derivatives of the free surface memory part of Green function in (3.38). In particular its time derivative, given in (4.1), is of interest.

$$\frac{\partial G^f\left(p,q,t-\tau\right)}{\partial t} = 2\sqrt{g}\int_0^\infty \left[\sin\left(\sqrt{gk}\left(t-\tau\right)\right)\right]\sqrt{k}e^{k(z_0+\zeta)}J_0\left(kR\right)dk$$
$$\text{for } p \neq q\ ,\ t-\tau \geq 0 \quad (4.1)$$

Direct numerical integration of this function and its derivatives requires a significant computational effort due to the oscillatory nature of the integrand and the infinite limit of the integral. In order to arrive at a more efficient procedure a number of solutions are suggested by different authors:

- Beck and Magee (1990), followed by Van Walree (1999), proposed to pre-calculate principal values of the Green function derivatives and store these values in tables. At runtime the correct principal values can be obtained by interpolation in these tables. In this way, a large portion of the computational effort is shifted out of the time domain calculation. By a proper change of variables it is possible to generate pre-calculated tables that are independent of the parameters of the problem that is being solved and can be computed only once and used indefinitely.

- Clément (1998a;b) proposed a different approach, realising that by a similar change of variables the principal form of each of the Green function derivatives satisfies a relatively simple fourth order Ordinary Differential Equation. Solving this fourth order ODE with appropriate coefficients yields the principal form of the desired Green function derivative.

In the computational model presented in this thesis both methods are combined. The method of Clément (1998a;b) is applied to fill the interpolation tables proposed by Beck and Magee (1990). Yet, these tables are limited to near-history to limit the necessary storage space. For the memory part further down in history use is made of computational efficient asymptotic expansions derived by Newman (1985; 1992). Both methods are detailed in the following sections.

Generation of interpolation tables

We define two non-dimensional parameters μ and β, along with two additional derived parameters η and λ. The parameter μ is a spatial parameter, ranging from 0 and 1. The parameter β is a temporal parameter, ranging from 0 to ∞. Despite that μ, λ and η in this section have different meanings than in the rest of the thesis, they are retained here to keep the formulation compatible with work of other authors.

$$\begin{aligned}
\mu\left(p,q,t-\tau\right) &= -\frac{z_0+\zeta}{R}, \quad \mu \in [0,1] \\
\beta\left(p,q,t-\tau\right) &= \sqrt{\frac{g}{R}}\left(t-\tau\right), \quad \beta \in [0,\infty\rangle \\
\eta &= \sqrt{1-\mu^2} \\
\lambda &= kR
\end{aligned} \tag{4.2}$$

Substitution of (4.2) into the time derivative of free surface part of the Green function, (4.1), gives the principal form of the time derivative of the free surface part of the Green function:

$$G_t^f\left(\mu,\beta\right) = 2\sqrt{\frac{g}{R^3}}\int_0^\infty \sqrt{\lambda}\sin\left(\sqrt{\lambda}\beta\right)e^{-\lambda\mu}J_0\left(\lambda\eta\right)d\lambda \tag{4.3}$$

were
Ignoring the leading term $2\sqrt{g/R^3}$, we obtain the function F given in (4.4). Function F and all its derivatives are non-dimensional and only dependent on the non-dimensional parameters $\beta \in [0,\infty\rangle$ and $\mu \in [0,1]$. These parameters are independent of the problem under consideration, making them suitable for pre-calculation and table interpolation. It has been chosen to pre-calculate function F and all necessary derivatives for $\beta \in [0,\beta_{lim}]$ and $\mu \in [0,1]$ and to store them in tables for interpolation at runtime. β_{lim} is a pre-determined value and is currently set to 20 so that the oscillatory behaviour of the Green function derivatives is mainly captured in the tabulated values. For values of $\beta > 20$ use is made of asymptotic expressions described in the next section.

$$F\left(\mu,\beta\right) = \int_0^\infty \lambda^{1/2}\sin\left(\sqrt{\lambda}\beta\right)e^{-\lambda\mu}J_0\left(\lambda\eta\right)d\lambda \tag{4.4}$$

To obtain the actual value of the Green function derivatives, they are written in terms of derivatives of F, μ, β and the leading term. This leads to ten derivatives of F that need to be pre-computed and stored: F, F_μ, $F_{\mu\mu}$, F_β, $F_{\beta\beta}$, $F_{\mu\beta}$, $F_{\mu\mu\mu}$, $F_{\mu\mu\beta}$, $F_{\mu\beta\beta}$, and $F_{\beta\beta\beta}$. These values will be interpolated at runtime and multiplied by the relatively easy to obtain derivatives of μ, β and the leading term. In fact, only the derivatives of μ, β and the leading term contain the problem-dependent information of the Green function derivatives.

Instead of the values of the derivatives of G^f, now pre-computed values need to be obtained for the derivatives of F. First the β-derivatives are given here:

$$F_\beta\left(\mu,\beta\right) = \int_0^\infty \lambda\cos\left(\sqrt{\lambda}\beta\right)e^{-\lambda\mu}J_0\left(\lambda\eta\right)d\lambda \tag{4.5}$$

$$F_{\beta\beta}\left(\mu,\beta\right) = -\int_0^\infty \lambda^{3/2}\sin\left(\sqrt{\lambda}\beta\right)e^{-\lambda\mu}J_0\left(\lambda\eta\right)d\lambda \tag{4.6}$$

$$F_{\beta\beta\beta}\left(\mu,\beta\right) = -\int_0^\infty \lambda^{2}\cos\left(\sqrt{\lambda}\beta\right)e^{-\lambda\mu}J_0\left(\lambda\eta\right)d\lambda \tag{4.7}$$

The μ-derivatives are slightly more complicated due to the dependence of μ in the argument of the Bessel functions. For the derivatives of the Bessel functions, and to simplify the equations, use has been made of Abramowitz and Stegun (1972).

$$F_{\mu}\left(\mu,\beta\right)=-\int_{0}^{\infty}\lambda^{3/2}\sin\left(\sqrt{\lambda}\beta\right)e^{-\lambda\mu}J_{0}\left(\lambda\eta\right)d\lambda+\frac{\mu}{\eta}\int_{0}^{\infty}\lambda^{3/2}\sin\left(\lambda\beta\right)e^{-\lambda\mu}J_{1}\left(\lambda\eta\right)d\lambda \quad (4.8)$$

$$F_{\mu\mu}\left(\mu,\beta\right)=\frac{3}{2}\int_{0}^{\infty}\lambda^{5/2}\sin\left(\sqrt{\lambda}\beta\right)e^{-\lambda\mu}J_{0}\left(\lambda\eta\right)d\lambda-2\cdot\frac{\mu}{\eta}\int_{0}^{\infty}\lambda^{5/2}\sin\left(\sqrt{\lambda}\beta\right)J_{1}\left(\lambda\eta\right)d\lambda+\frac{1}{2}\cdot\frac{\mu^{2}+1}{\eta^{2}}\int_{0}^{\infty}\lambda^{5/2}\sin\left(\sqrt{\lambda}\beta\right)e^{-\lambda\mu}J_{2}\left(\lambda\eta\right)d\lambda \quad (4.9)$$

$$F_{\mu\mu\mu}\left(\mu,\beta\right)=-\frac{5}{2}\int_{0}^{\infty}\lambda^{7/2}\sin\left(\sqrt{\lambda}\beta\right)e^{-\lambda\mu}J_{0}\left(\lambda\eta\right)d\lambda+\frac{15}{4}\cdot\frac{\mu}{\eta}\int_{0}^{\infty}\lambda^{7/2}\sin\left(\sqrt{\lambda}\beta\right)e^{-\lambda\mu}J_{1}\left(\lambda\eta\right)d\lambda-\frac{3}{2}\cdot\frac{1+\mu^{2}}{\eta^{2}}\int_{0}^{\infty}\lambda^{7/2}\sin\left(\sqrt{\lambda}\beta\right)e^{-\lambda\mu}J_{2}\left(\lambda\eta\right)d\lambda+\frac{1}{4}\cdot\frac{\mu^{3}+3\mu}{\eta^{3}}\int_{0}^{\infty}\lambda^{7/2}\sin\left(\sqrt{\lambda}\beta\right)e^{-\lambda\mu}J_{3}\left(\lambda\eta\right)d\lambda \quad (4.10)$$

The remaining mixed $\mu\beta$-derivatives of F needed can be easily obtained in a similar manner.

To obtain values for these derivatives use can be made of the fact that the function F and its derivatives satisfy a very simple fourth order ordinary differential equation; a lemma established by Clément (1998a;b). The form of this ODE is as follows:

$$\frac{\partial^{4}A_{\nu,l}}{\partial\tau^{4}}+\mu\tau\frac{\partial^{3}A_{\nu,l}}{\partial\tau^{3}}+\left(\frac{\tau^{2}}{4}+\mu\left(3+2l\right)\right)\frac{\partial^{2}A_{\nu,l}}{\partial\tau^{2}}+\left(l+\frac{5}{4}\right)\tau\frac{\partial A_{\nu,l}}{\partial\tau}+\left(\left(l+1\right)^{2}-\nu^{2}\right)A_{\nu,l}=0 \quad (4.11)$$

The solution of this ODE is given by:

$$A_{\nu,l}\left(\mu,\tau\right)=\int_{0}^{\infty}\lambda^{l}e^{-\lambda\mu}J_{\nu}\left(\lambda\sqrt{1-\mu^{2}}\sin\left(\sqrt{\lambda}\tau\right)\right)d\lambda\quad\forall\quad0<\mu\leq1 \quad (4.12)$$

Comparing this solution to function F and its derivatives shows that F and its derivatives can either be written as a leading term times $A_{\nu,l}$ -using a convenient choice for ν and l and by substituting β for τ-, or can be split in parts that can be written as such.

The objective is to construct an interpolation table based of F and a number of the μ and β-derivatives of F on a range of values of μ and β. To obtain values for F and its derivatives,

suitable ODEs of above form have to be solved as an initial-value problem. The ODEs that are solved are chosen such that the solution contains F or (part of) the derivatives of F. By solving for different values of μ and β the table can then be filled.

$$LT \cdot \int_0^\infty e^{-\mu\lambda} J_\nu(\eta\lambda)\, \lambda^{l+1} d\lambda = LT \cdot \Gamma(\nu + l + 1) P_l^{-v}[\mu] \tag{4.13}$$

$$LT \cdot \int_0^\infty e^{-\mu\lambda} J_\nu(\eta\lambda)\, \lambda^{l+1} d\lambda = LT \cdot \frac{\left(\frac{\eta}{2}\right)^\nu \Gamma(\nu + l + 1)}{\Gamma(\nu + 1)} F_{hg}\left(\frac{\nu + l + 1}{2}, \frac{-l + \nu}{2}; \nu + 1; \eta^2\right) \tag{4.14}$$

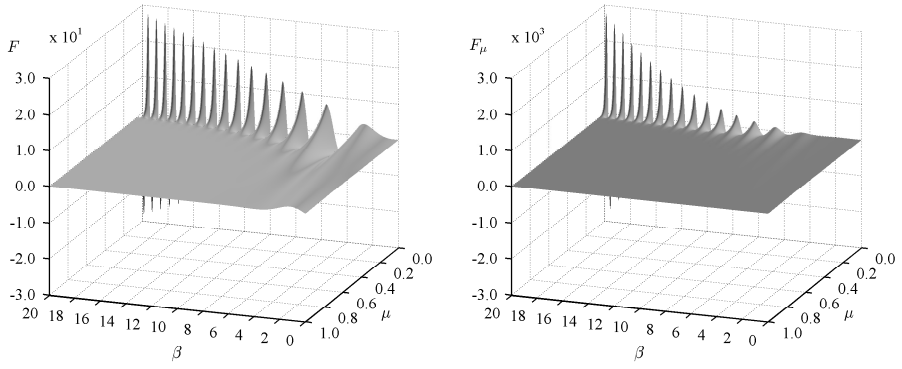
To solve the initial values problem, the starting values $A_{\nu,l}(\mu, 0)$ and its derivatives are required. They can be found, applying Gradshteyn and Ryzhik (1980) in two different ways. First, by using Legendre functions $P_l^{-\nu}$ (given in (4.13), Abramowitz and Stegun (1972)). Second, by using Hyper-geometric functions F_{hg} (given in (4.14) Abramowitz and Stegun (1972)). LT denotes an arbitrary leading term independent of λ that can be chosen such that the solution (or part of it) of the ODE matches the principal Green function derivative, Γ is the gamma function, defined in for example Abramowitz and Stegun (1972).

It has been found that the first option provides more accurate solutions. Moreover, the determination of the Hyper-geometric function for $\mu = 0$ does not converge. Yet, the Hyper-geometric functions can be used to check the outcome of the Legendre functions to locate calculation errors. Using the initial values, all the necessary ODEs can be solved for a range of μ and β values. Different parts of the same derivative (containing different leading terms and having different ν, l-values) can be solved separately and the results can added up afterwards.

Finally, instead of following the procedure described above at runtime, the derivatives are stored in an interpolation table that can be loaded at runtime. This makes for a very efficient method, as now only interpolation needs to be performed at runtime. Due to the non-dimensional formulation, yielding smoother and easier to evaluate and to integrate functions, the interpolation tables generated with this method are problem-independent and need to be generated only once.

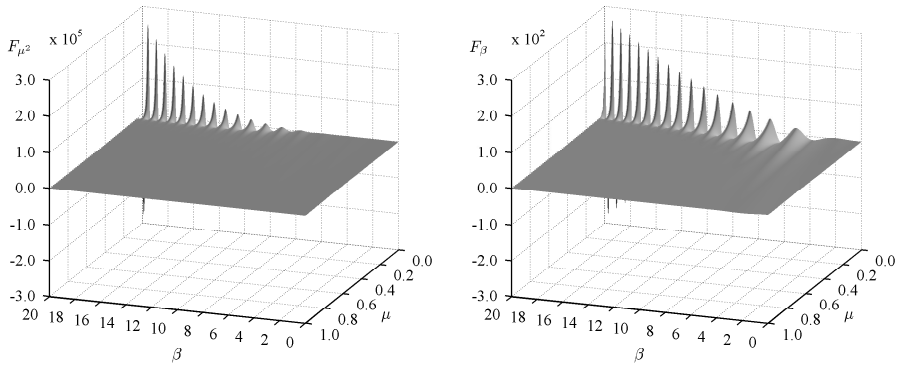
The drawback of this approach is the fact that one of the two parameters, β, has an unbounded range of possible values, whereas a relatively large resolution is necessary to capture the oscillatory behaviour of the derivatives with respect to β. This would lead to relatively large storage requirements. For this reason, only for low β-values of up to 20 use is made of the interpolation approach. For higher β-values use is made of series approximation, described in the next section.

In figure 4.1, three-dimensional representations of all ten principal Green function derivatives are plotted against the non-dimensional parameters μ and β. Clearly visible is the highly oscillatory behaviour for low values of the spatial parameter μ. This behaviour occurs for low values of the vertical source coordinate z_0 and vertical field point coordinate ζ and for high values of the distance between source and field point R with respect to $z_0 + \zeta$. Stated differently, all Green function derivatives show highly oscillatory behaviour when the source and



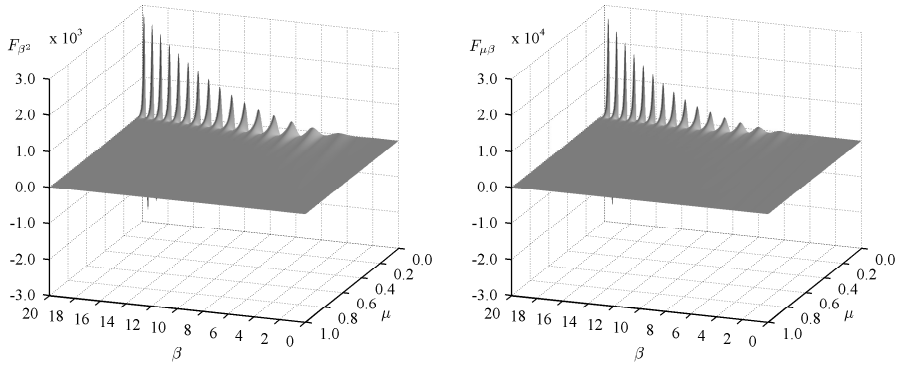
(a) F

(b) F_μ



(c) $F_{\mu 2}$

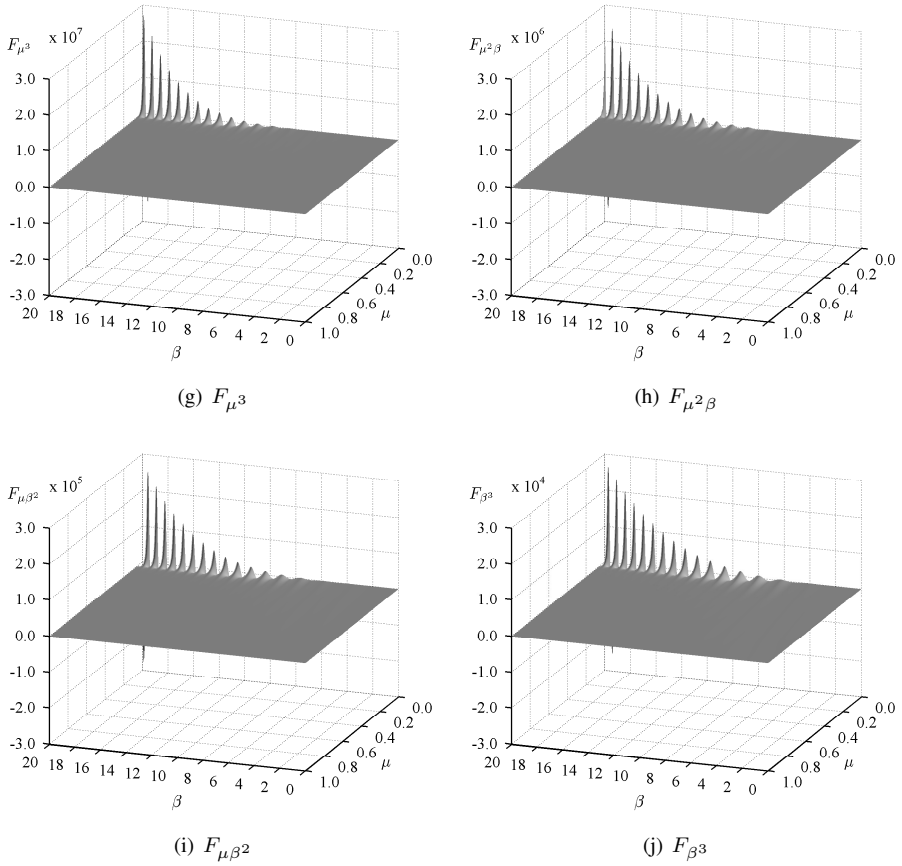
(d) F_β



(e) $F_{\beta 2}$

(f) $F_{\mu\beta}$

Figure 4.1: *Tabulated principal Green function derivatives*



(g) F_{μ^3} (h) $F_{\mu^2\beta}$

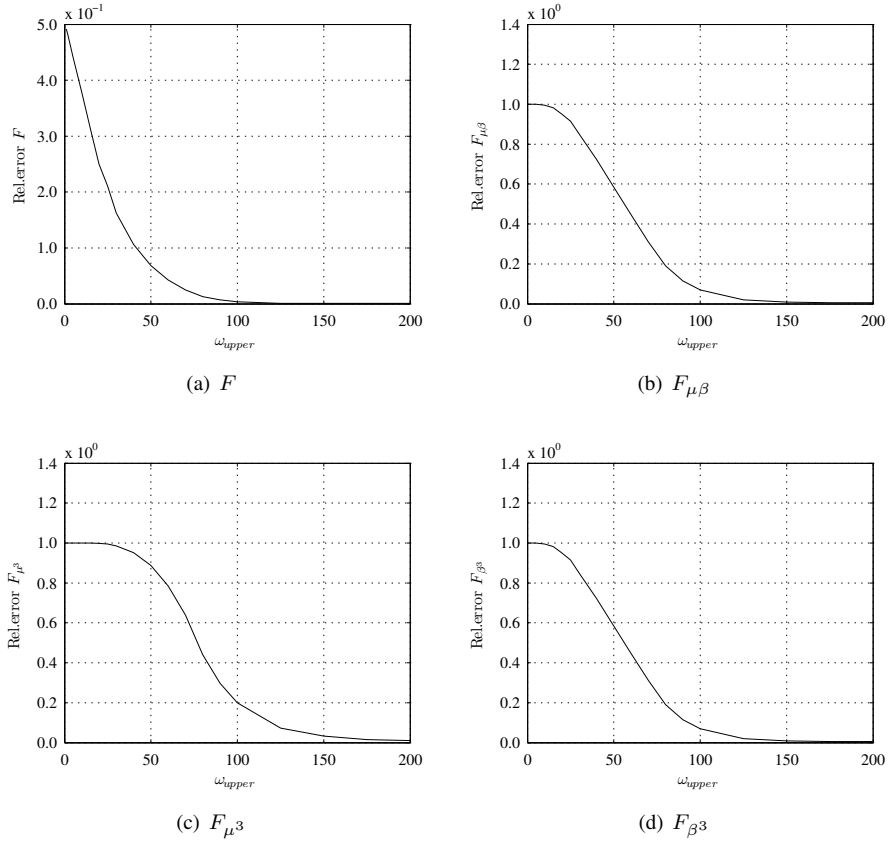
(i) $F_{\mu\beta^2}$ (j) F_{β^3}

Figure 4.1: *Tabulated principal Green function derivatives (cont.)*

field points are close tbcaptiono the calm water free surface and when the distance between them is large. The amplitude of the oscillatory behaviour due to the distance R is to some extend countered by the $R^{-3/2}$ in the leading term. Still, the integration routines need to be able to cope with these oscillations with sufficient accuracy.

In order to check the procedure for calculating the tabulated principal Green function integrals, checks have been carried out by comparing the tabulated values with direct numerical integration of the Green function derivatives. As the Green function derivatives contain an improper integral this comparison has been carried out by stepwise increasing the upper integration limit of the direct numerical integration from 1 upwards until the relative error between the tabulated values and the result of the direct numerical integration became small enough.

Figure 4.2 shows the result of this comparison with on the vertical axis the relative error and on the horizontal axis the the value used for the upper integration limit ω_{upper} for four of the ten principal Green function derivatives. The relative error was computed by using the values of each derivative F for the full β-range $[0, 20]$ with step size 0.01. This resulted in



(a) F (b) $F_{\mu\beta}$

(c) F_{μ^3} (d) F_{β^3}

Figure 4.2: *Relative error numerical integrated Green function derivatives with respect to tabulated Green function derivatives for increasing value of the upper integral limit ω_{upper} at $\mu = 0.05$*

two vectors each containing the integral values corresponding to each value of β, one for the tabulated principal Green function integrals (denoted $\boldsymbol{F_{tab}}$) and one for the direct numerical integration (denoted $\boldsymbol{F_{int}}$). The relative error was computed as given in (4.15).

$$\varepsilon = \frac{|\boldsymbol{F_{int}} - \boldsymbol{F_{tab}}|}{|\boldsymbol{F_{tab}}|} \tag{4.15}$$

For the direct numerical integration use was made of the 10-point Gauss and 21-point Kronrod integration rule. The comparison has been carried out for $\mu = 0.05$ and the full β-range of the tables $[0, 20]$. The low μ-value was chosen such that the highly oscillating behaviour was captured in the comparison, as can be seen in the figure 4.1. Not all results are shown in figure 4.2 but still the most extreme derivatives, $F_{t\mu^3}$ and $F_{t\beta^3}$, are included in the figure.

The figure shows that the results of the direct numerical integration convergence to the the tabulated values of the principal Green function derivatives when the upper integration limit of the direct numerical integration is sufficiently high. This confirms the correctness of the tabulated principal Green function values.

Series approximation

Although the table interpolation method is very efficient for the computation of the Green function derivatives, it is limited by the fact that the range of values of β is unbounded and the fact that relatively high resolution is needed in β to capture the oscillations occurring in the derivatives (refer to figure 4.1). For this reason the table interpolation method is limited to lower β-values (below 20) and above 20 use will be made of series approximation described in the current section. The limit of 20 is arbitrary. Nevertheless, well below 20 series approximation breaks down, whereas around 20 the derivatives computed with both methods coincide, as can be seen in figure 4.3. The series approximation method is based on the work of Newman (1992).

The free surface part of G_t is rewritten in spherical coordinates (R, θ) in a non-dimensional form as $\Re\{F(R,\theta)\}$, with F:

$$F = -4i \int_0^\infty \omega^2 e^{i\omega\beta - \omega^2 \cos\theta} J_0\left(\omega^2 \sin\theta\right) d\omega \tag{4.16}$$

In this equation $\omega = k^{1/2}$, β are defined as they were in the previous section. The cosine term equals μ: $\cos\theta = \mu$, and $\sin\theta = \eta$. F is a complex form of F defined in the previous section. The computational domain consists of: $(0 < \beta < \infty,\ 0 \leq \theta \leq \pi/2)$. Newman (1992) showed that for large values of β (he used τ instead of β) F can be approximated with asymptotic expansions:

$$F = f_0 + f_1 + f_2 \tag{4.17}$$

where:

$$f_0 \simeq -4 \sum_{n=0}^{n_{max}} \frac{(2n+2)!}{n!} \beta^{-2n-3} P_n^0(\cos\theta) \tag{4.18}$$

$$f_1 \simeq 0 \quad \text{is exponentially small and can be neglected} \tag{4.19}$$

$$\begin{aligned} f_2 \simeq & \frac{-4i}{\sqrt{2\sin\theta}} e^{-1/4\beta^2 e^{-i\theta} - i\theta/2 + i\pi/4} \\ & \sum_{n=0}^{n_{max}} \left(\frac{i}{\sin\theta}\right)^n \sum_{m=0}^{n} d_{nm} \omega_2^{1-2m-2n} e^{-im\theta} \end{aligned} \tag{4.20}$$

The upper limits n_{max} and m_{max} should be chosen sufficiently large. In practice values of 15 or higher can be shown to yield sufficient accurate results (omitted here). Furthermore, d_{nm} is defined as follows:

$$\begin{aligned} d_{00} =& 1 \\ d_{0m} =& 0 \quad \text{for} \quad m > 0 \\ d_{nm} =& c_n \frac{(2m+2n-2)!}{(2n-2)! 2^{2m} m!} \quad \text{for} \quad n \geq 1 \end{aligned} \tag{4.21}$$

The leading term c_n is defined as:

$$\begin{aligned} c_n &= \frac{\left[\Gamma\left(n+\frac{1}{2}\right)\right]^2}{\pi 2^n n!} \\ \Gamma(n+1/2) &= \frac{1 \cdot 3 \cdot 5 \cdot 7 \cdot \ldots \cdot 2n-1}{2^n} \sqrt{\pi} \end{aligned} \tag{4.22}$$

And finally the definition of ω_2:

$$\omega_2 = \frac{1}{2}\beta i e^{-i\theta} \tag{4.23}$$

In order to obtain the same ten derivatives of F with respect to μ and β as in the previous section, it is necessary to obtain the derivatives of f_0 and f_2. The derivatives of Legendre functions in f_0 and its derivatives can be obtained from Abramowitz and Stegun (1972, section 8.5). Combination of recurrence relations yields:

$$\frac{dP_v^\mu(z)}{dz} = \frac{1}{z^2-1}\left(-(\nu+1)\,z P_\nu^\mu(z) + (\nu+\mu+1)\,P_{\nu+1}^\mu(z)\right) \tag{4.24}$$

Substitution of $\nu = n$, $\mu = 0$ (note that this is not the same as μ defined in the previous section), and $z = \mu$ (note that this is μ as defined in the previous section) yields:

$$\frac{dP_n^\mu(\mu)}{d\mu} = \frac{n+1}{\eta^2}\left(\mu P_n^0(\mu) - P_{n+1}^0(\mu)\right) \tag{4.25}$$

Using this the appropriate derivatives of f_0 can be obtained straightforwardly. To obtain the derivatives of f_2, f_2 is rewritten as a multiplication of two terms, the exponential term f_{2A} and the summation term f_{2B}:

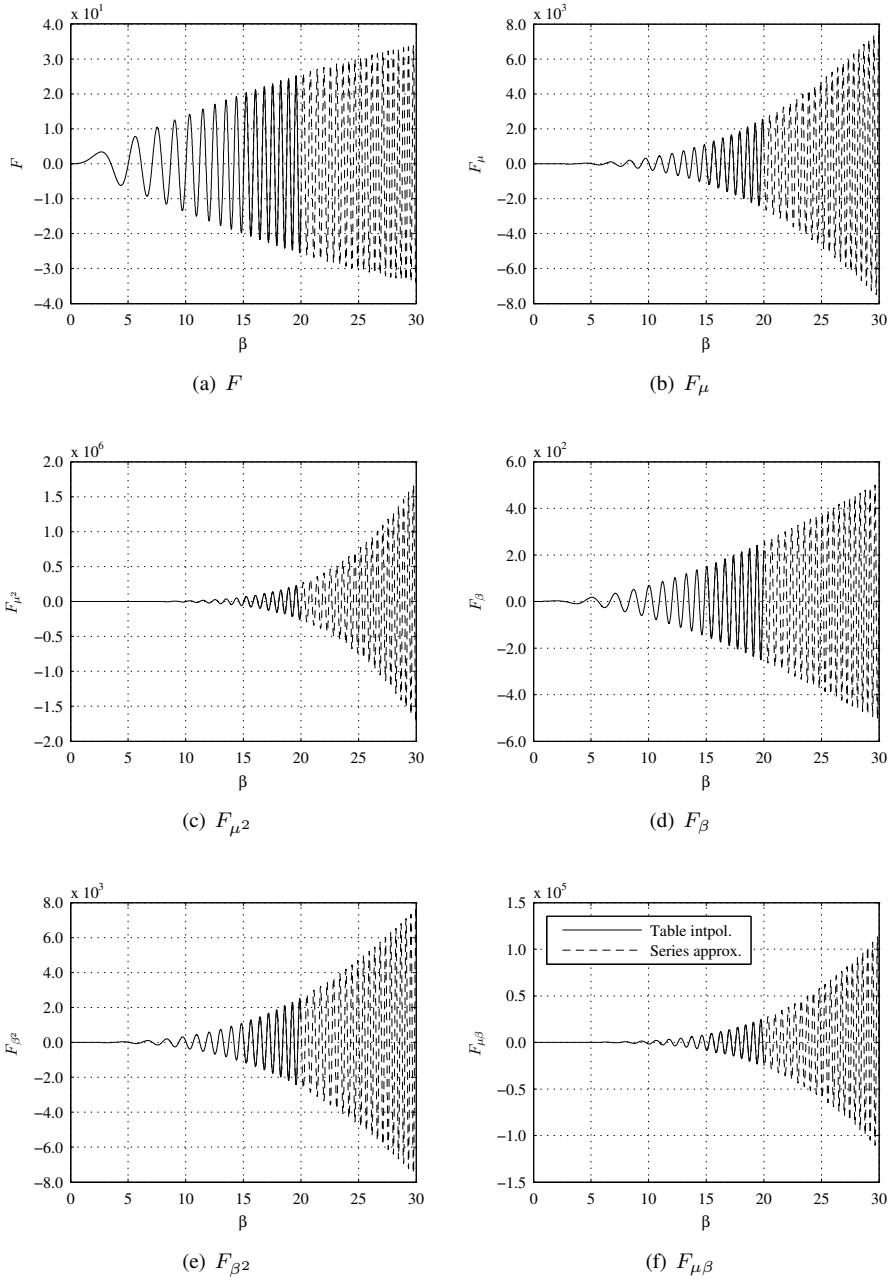
$$\begin{aligned} f_2 =& f_{2A}\cdot f_{2B} \\ f_{2A} =& \frac{-4i}{\sqrt{2\eta}} e^{-1/4\beta^2\mu} e^{i\left(\frac{1}{4}\beta^2\eta - \frac{1}{2}\arccos\mu + \frac{\pi}{4}\right)} \\ f_{2B} =& \sum_{n=0}^{n_{max}} \left(\frac{i}{\eta}\right)^n \sum_{m=0}^{n} d_{nm} \left(\frac{1}{2}\beta(i\mu+\eta)\right)^{1-2m-2n} (\mu - i\eta)^m \end{aligned} \tag{4.26}$$

Application of the chain rule for differentiation and differentiating the appropriate terms finally results in the derivatives of f_2 with respect to μ and β up to the third derivatives. Due to the expansive expressions that are the result of these differentiations, details are omitted here.

Comparison tabulated values and series approximation

In figure 4.3 the principal Green function derivatives based on the first method, table interpolation, and based on the second method, series approximation are compared to verify the implementation of the asymptotic expansions described in the previous section. The principal Green function derivatives have been determined by table interpolation for $0 \leq \beta \leq 20$ and by series approximation for $15 \leq \beta \leq 30$. In both cases μ equaled 0.001; again a low value of μ was chosen for the comparison to capture the most extremely oscillating behaviour of the Green function derivatives. In the figure the value of the principal derivative is plotted on β.

Clearly, there is no significant difference between both graphs for the part that the graphs overlap. The series approximation distinctly carries forward the behaviour of the table interpolated data to larger values of β. Together with the comparison of the table interpolation with the results of direct numerical integration presented previously, this gives a clear indication that the implementation of both the table interpolation and the series approximation is correct.

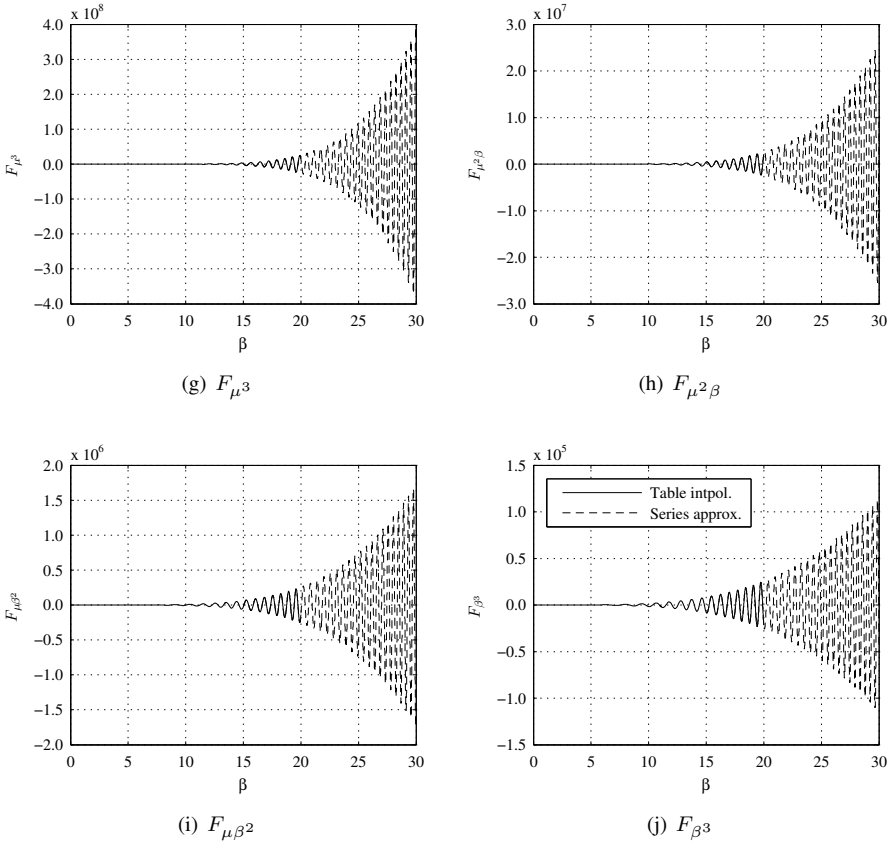


(a) F (b) F_μ

(c) $F_{\mu 2}$ (d) F_β

(e) $F_{\beta 2}$ (f) $F_{\mu\beta}$

Figure 4.3: *Tabulated and asymptotic expressions Green function derivatives for* $\mu = 0.001$



(g) F_{μ^3} (h) $F_{\mu^2\beta}$

(i) $F_{\mu\beta^2}$ (j) F_{β^3}

Figure 4.3: *Tabulated and asymptotic expressions Green function derivatives for* $\mu = 0.001$ *(cont.)*

4.2.2 Rankine and biplane image part

The Rankine and biplane image part is given by the first part of the free surface Green function repeated below from (3.38). Figure 4.4 shows the orientation of the source and doublet panels and their biplane images. The doublet element is modelled by using the equivalent vortex ring element, where vortex line segments are placed along the edges of the panel and their strength is equal to the doublet strength of the panel.

$$\begin{aligned} G^0(p,q) &= \frac{1}{R} - \frac{1}{R_0} \\ R &= \sqrt{(x_0-\xi)^2 + (y_0-\eta)^2 + (z_0-\zeta)^2} \\ R_0 &= \sqrt{(x_0-\xi)^2 + (y_0-\eta)^2 + (z_0+\zeta)^2} \end{aligned} \tag{4.27}$$

The minus sign in front of the biplane term indicates that for the source panel the biplane-image consists of the source panel mirrored in the $z_0 = 0$-surface with a negative source

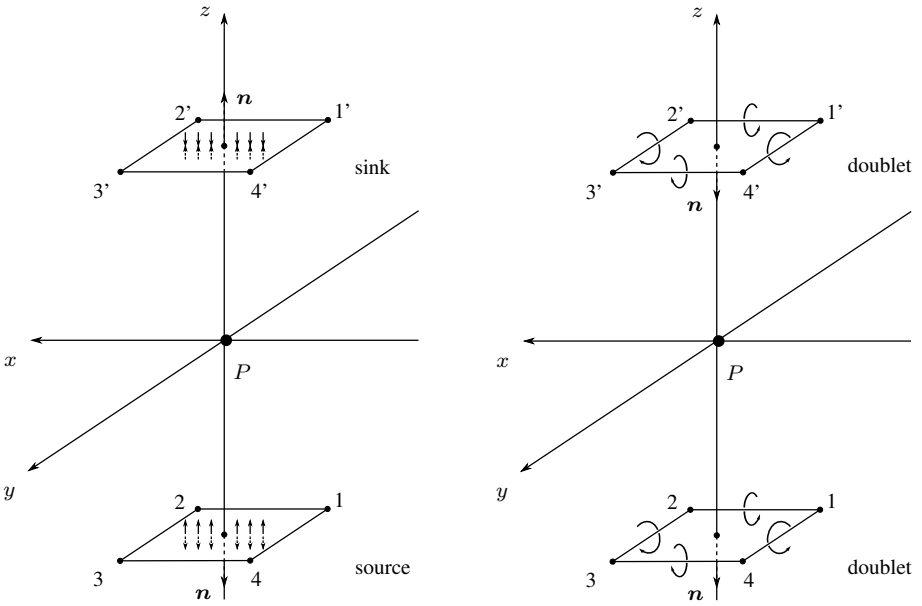


Figure 4.4: *Source panel (left) and doublet panel modelled as four vortex line elements (right) and their images (top)*

strength, or in other words: a sink. For a doublet panel the resulting biplane image can be seen as the mirrored panel with its vortex line segments reversed, so that they are oriented identically to the original element. The different orientation of source and doublet biplane images is also indicated in the figure by the normal direction of the biplane elements, although the orientation of the normal of the source/sink panel is of minor importance as its strength is indiscriminate with respect to its normal direction.

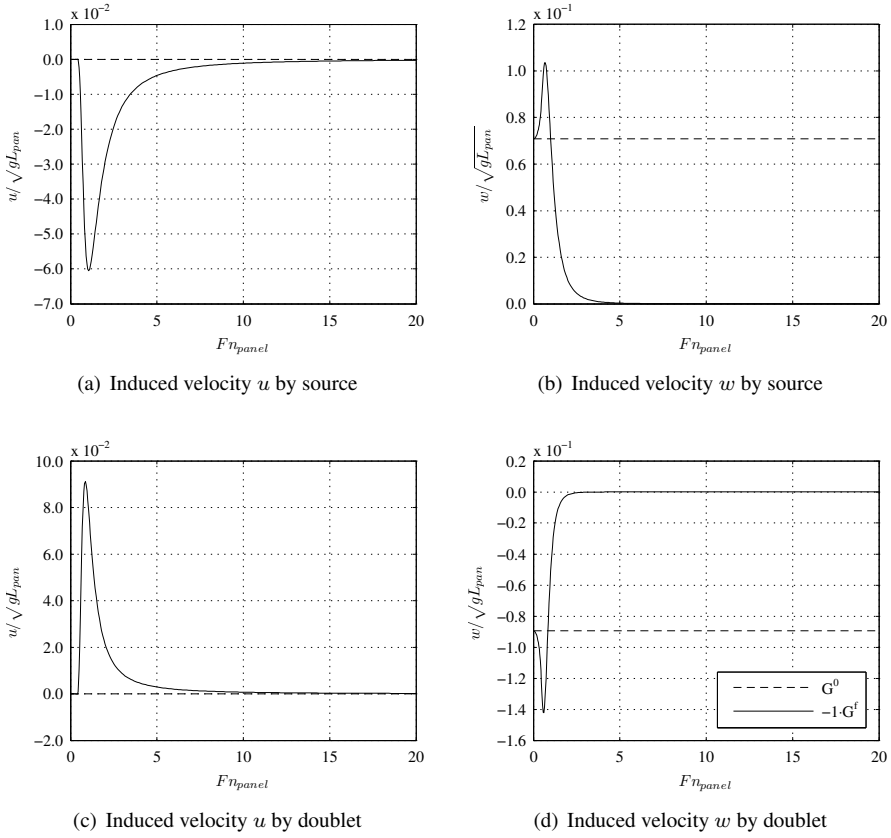
4.2.3 Zero and high Froude number limits

To check the correctness of the Rankine and biplane part implementation, use can be made of the behaviour of the Green function at very low Froude numbers and very high forward speed Froude numbers. These are the so-called zero and high forward Froude number limits of the Green function. It can be shown that the free surface memory term approaches $2/R_0$ for very low Froude numbers and approaches zero for very high Froude numbers, resulting in the following approximations:

$$G \approx \frac{1}{R} + \frac{1}{R_0} \quad \text{for} \quad Fn \to 0 \tag{4.28}$$

$$G \approx \frac{1}{R} - \frac{1}{R_0} \quad \text{for} \quad Fn \to \infty \tag{4.29}$$

In order to study this behaviour, a constant strength singularity panel was considered to be oriented horizontally and submerged at one panel diameter with its normal pointing down-



(a) Induced velocity u by source

(b) Induced velocity w by source

(c) Induced velocity u by doublet

(d) Induced velocity w by doublet

Figure 4.5: *Induced Rankine and biplane velocities (solid lines) and (negative) free surface memory velocities (dashed lines) by a source panel and by doublet panel on a free surface point plotted on the panel Froude number*

wards. The induced velocity of the panel at a point P in the free surface straight above the panel centroid was computed for a range of panel length Froude numbers for a source distribution and for a doublet distribution. Figure 4.4 shows this situation for the case where only a Rankine panel and a biplane image are present. In the case of figure 4.4 the sign of the biplane image is negative; this is occurring when the panel Froude number approaches infinity in (4.29). When the panel length Froude number approaches zero the strength of the biplane image is simply reversed.

At both zero and infinite panel Froude number the horizontal induced velocity u at P equals zero, as both the Rankine panel $(1/R)$ as its biplane image $(1/R_0)$ (be it positive or negative) are symmetrical with respect to P. In between zero and infinity the free surface memory term G_f will be the only contribution to the horizontal induced velocity at P. At zero Froude number both the Rankine panel and its biplane image induce velocities at P that are equal in strength but opposite in sign, cancelling each other out. At infinite Froude number

the opposite occurs; both the Rankine panel and its image produces induced velocities equal in strength and sign; equalling the situation depicted in figure 4.4.

The correctness of this behaviour is confirmed when consulting the free surface boundary condition applied to steady cases with constant forward speed U_{vel}, (3.28). Evident is that for forward speed tending to infinity the vertical induced velocity becomes irrelevant and only the horizontal induced velocity needs to tend to zero by using a negative strength biplane image. Meanwhile, for nearly zero forward speed the vertical induced velocity needs to tend to zero, as its multiplication factor tends to be very large, this is achieved by using a positive strength biplane image.

Figure 4.5 presents the induced horizontal and vertical velocities at point P by the G^0-terms (solid lines) and the G^f-terms (dashed lines), for the a constant strength source panel and a constant strength doublet panel plotted on the panel Froude number. The induced velocities by the G^f-terms are plotted negatively, so that when the dashed and solid lines cross each other the total induced velocity equals zero. The expected trends are visible: although difficult to see in the figure, at Froude number zero the Rankine and biplane terms cancel the induced velocities due to the free surface memory terms, whereas at high Froude number the free surface memory terms tend to zero and only the Rankine and biplane image induced velocities remain. This provides an excellent test of the implementation of both the G^0-terms as the G^f-terms.

4.2.4 Truncation of the free surface memory effects

The induced velocities due to the free surface memory part of the Green function (the G^f-part) contain an improper integral, e.g. an integral with an integration limit at infinity, as can be seen in for example (3.56). To numerically compute this integral it needs to be (1) discretised and (2) truncated. This raises the question how to successfully discretise and truncate these integrals so that the integrals are accurately and efficiently represented in the numerical solution.

In fact the memory terms are oscillating functions over the past time with decreasing amplitude. How quickly the amplitude decreases depends on the forward speed in relation to the panel size and the time step (influencing the distance between the collocation point and the past time panels) and the location of the panel and the collocation point with respect to each other and the free surface.

To deal with the past time integrals numerically, two considerations are important. First, the length of the memory effects that are included in the computation needs to be long enough so that the truncation of the memory effects is not noticeable. Second, the number of time steps within the included part of the memory effects needs to be sufficient to correctly resolve the oscillating behaviour.

In this section the truncation of the memory effects is studied by using the same panel set-up as in the previous sections. Again a (source) panel was submerged at one panel diameter and positioned with its normal pointing downwards. The induced velocity by this panel on a collocation point located above its centroid in the free surface was computed for a range of panel Froude numbers, from very small ($Fn_{panel} = 0.008$) to high ($Fn_{panel} = 20$). Assuming 50 panels over the length of a ship results in ship length Froude number range of $Fn = 0.001$ to $Fn = 2.8$.

The truncation error at each panel Froude number was now found by using a very high number of history steps (8000) and computing at each time step the influence of that time step at the collocation point. Looping over the 8000 steps and summing at each past time step the induced velocity *before* the current time step the result was compared to the result of the entire past time history. (4.30) shows the calculation of the induced velocities at the collocation point with a summation over the time up to past time step jt. The two integrals are the Gauss-Kronrod approximation of the local past time integral (over time step it) and the source panel integration.

$$\begin{aligned} u^f_{jt} &= \sum_{it=0}^{it=jt} \sigma_{it} \int_{\tau(it-1)}^{\tau(it)} \int_S \frac{\partial^2 G^f}{\partial\tau\partial x}\, dS\, d\tau \\ v^f_{jt} &= \sum_{it=0}^{it=jt} \sigma_{it} \int_{\tau(it-1)}^{\tau(it)} \int_S \frac{\partial^2 G^f}{\partial\tau\partial x}\, dS\, d\tau \\ w^f_{jt} &= \sum_{it=0}^{it=jt} \sigma_{it} \int_{\tau(it-1)}^{\tau(it)} \int_S \frac{\partial^2 G^f}{\partial\tau\partial x}\, dS\, d\tau \end{aligned} \tag{4.30}$$

The truncation error is computed as a relative error by dividing the difference of the total induced velocity up to time step jt and up to the maximum time step N_{hist} (8000 in this case) over the total induced velocity due to G^0- and G^f-terms:

$$\varepsilon\,(jt) = \frac{\left| \sqrt{{uf}^2_{jt} + {vf}^2_{jt} + {wf}^2_{jt}} - \sqrt{{uf}^2_{N_{hist}} + {vf}^2_{N_{hist}} + {wf}^2_{N_{hist}}} \right|}{\sqrt{\left(u^0 + {uf}_{N_{hist}}\right)^2 + \left(v^0 + {vf}_{N_{hist}}\right)^2 + \left(w^0 + {wf}_{N_{hist}}\right)^2}} \tag{4.31}$$

Still two factors remain important. First, again the resolution of the time steps should be sufficient to deal with the oscillation frequencies in the memory functions. Second, the length of the time history (number of history steps times the magnitude of the time step) should be sufficient long to successfully compare the summations before and after each time step (as again a truncation error occurs here); or jt should not approach N_{hist} too closely as the error estimate will become unreliable.

The time step where the memory integral can be cut, is the time step jt where ε becomes smaller than a certain threshold value (here set at 0.001). The included history length is named t_{cut}, while the original entire time history is named t_{hist}. Figure 4.6 shows t_{hist} and t_{cut} for the panel Froude number range. The value of t_{hist} is determined by the multiplication of the number of history time steps ($N_{hist} = 8000$) by the time step. The magnitude of the time step is chosen as follows: generally it is found that the time step should be set in such manner that the distance that is travelled by the body (or in this case the panel) in one time step equals one panel length. The result is that the spatial and temporal discretisations are of the same order of magnitude. In formula:

$$dt = \frac{L_{pan}}{U_{vel}} \tag{4.32}$$

From figure 4.6 can be concluded that for values of the panel Froude number between 0.18 and 0.60 it is nearly impossible to decrease the truncation error withfromin a reasonable

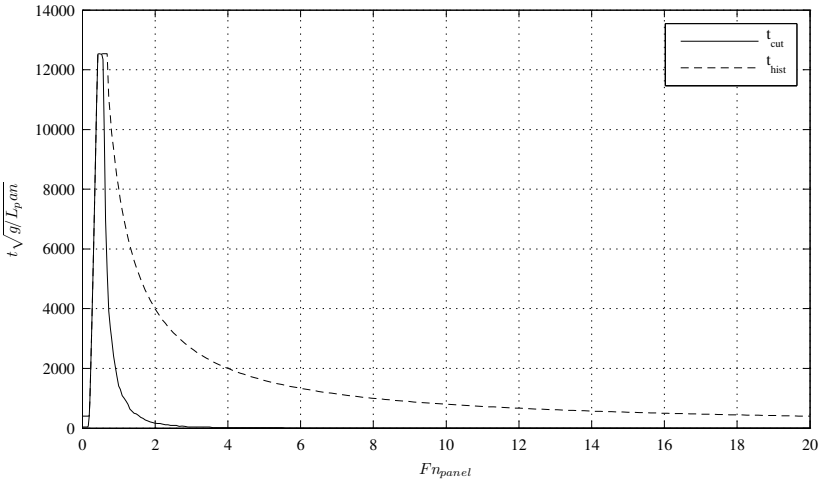


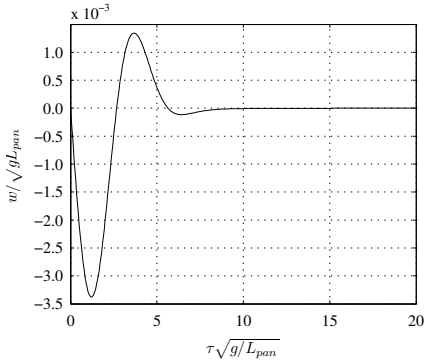
Figure 4.6: *History length and cut off length for* $\varepsilon < 0.001$ *based on panel Froude number.*

history length. This can be seen in the figure by the steep slope of the curves and the fact that both lines (for t_{cut} and t_{hist}) coincide. At these panel Froude numbers the oscillations in the memory effect do not disappear within a reasonable history time and are possibly not resolved accurately enough. In this study no attempt is made to extend t_{hist} even further to arrive at a value for t_{cut}. For practical purposes it sufficient to know that at certain (relatively low) panel Froude numbers and panel submergence it is nearly impossible to successfully truncate the free surface memory integrals.

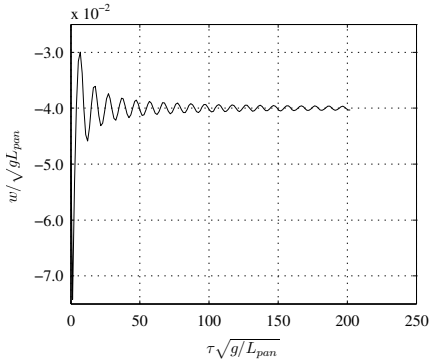
Whether the solution for a complete ship is impaired by this behaviour depends on how many panels are relatively close to the free surface, on their orientation, and on their panel Froude number. Especially for relatively slow ships fitted with large transom sterns close to the calm water intersection problems may arise. In the computation there are a number of provisions made to filter the influences of panels affected by this behaviour. Whether or not this approach is successful depends on the aggressiveness of the filtering and the relative amount of the affected panels. Further study into this behaviour is outside the scope of this work.

To illustrate the different behaviour of the free surface memory functions over the past time in figure 4.7 (truncated) time histories over the past time of the vertical induced velocity w^f are shown. It is clear that for very low and higher panel Froude numbers hardly any oscillating behaviour is visible and the influence dies out very quickly over the history. In contrast, at a panel Froude number of 0.396 the function oscillates rapidly and this oscillation hardly dies out.

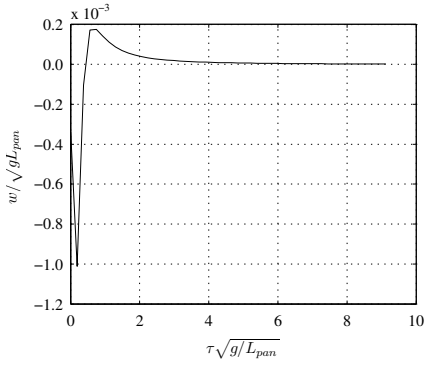
To conclude this section, figure 4.8 shows the amount of time steps necessary in the truncated evaluation of the memory effect on the basis of the Froude number over the ship length. This Froude number is computed from the panel Froude number by assuming that a ship is discretised using 50 panels over the ship's length. At the same time the time step is computed



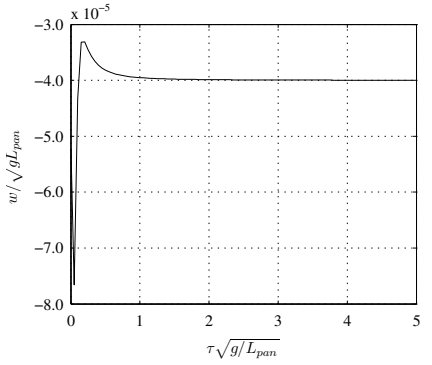
(a) Time history of induced w^f-velocity over past time for $Fn_{panel} = 0.008$



(b) Time history of induced w^f-velocity over past time for $Fn_{panel} = 0.396$



(c) Time history of induced w^f-velocity over past time for $Fn_{panel} = 5.370$



(d) Time history of induced w^f-velocity over past time for $Fn_{panel} = 19.16$

Figure 4.7: *Time history of the memory effect due to a source panel at one panel diameter below the free surface on a free surface point*

using (4.32). The result is that above a (ship) Froude number of 0.35 to 0.40 100 history time steps are sufficient to accurately resolve and compute the induced velocities due to the free surface memory effects with a small truncation error.

It is important to note that this is only an indication of the necessary past time length to be included. When performing calculations at is advisable to check the resolution and the length of the past time memory function by using the appropriate output of the computer code.

4.3 Submerged foils

Next, the computational method was applied to fully submerged foils advancing through calm water. The application of the method to the relatively simple problem of a steady advancing submerged foil provided a limited validation of the method. The potential flow lift and drag

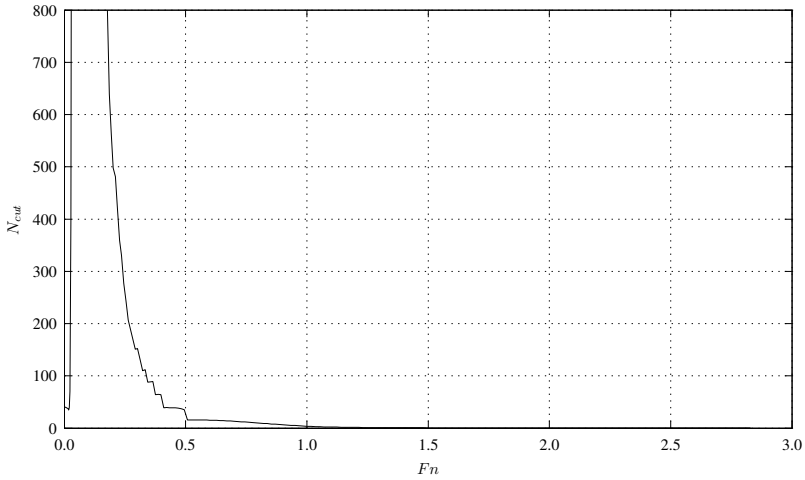


Figure 4.8: *Indication of the number of necessary history time steps for* $\varepsilon = 0.001$ *based on ship Froude number (assuming that 50 panels are used over the entire ship length)*

coefficients as well as the pressure distribution are studied in this section. First, deeply submerged foils are considered in steady flow and the results of the calculations are compared with two-dimensional calculations. Second, calculations of finite aspect ratio foils in proximity of the free surface are compared with published results of measurements for both steady and unsteady flow conditions.

4.3.1 Deeply submerged foils in steady flow

A NACA 0012 foil, with a symmetric section with the maximum thickness of 12% of the chord at 30% of the chord, was modelled both in the computational method presented in this thesis and in XFOIL (Drela and Youngren 2001). In the calculations the free surface Green function calculation was deliberately switched off to save calculation time and only the G^0-part (including the biplane image) of the influence function remained. It has been verified that indeed switching off the free surface part of the Green function did not influence the calculation results, providing that the foil was submerged deep enough.

XFOIL is an interactive program for the design and analysis of subsonic isolated air foils freely available in the public domain under a GNU license (Drela and Youngren 2001). It is capable of performing both viscous as inviscid two-dimensional analysis of air foils. The general XFOIL methodology is described by Drela (1989). The method applied here was based on two-dimensional fully inviscid potential flow theory. The foil was modelled using vortex elements with linear strength in XFOIL. No viscous and boundary layer thickness corrections have been applied and no free surface effect was present within the computations performed with XFOIL.

The two-dimensional panel discretisations for both computational methods are depicted

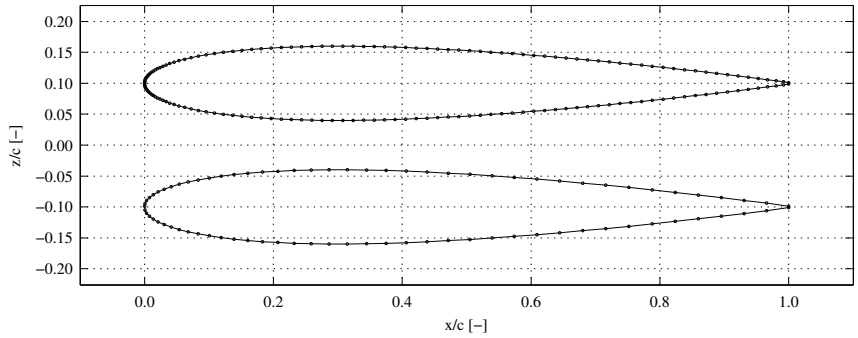
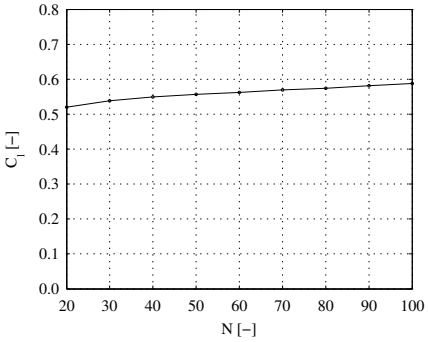


Figure 4.9: *NACA 0012 foil chord-wise panel discretisation for XFOIL (top, 159 panels on circumference) and for the computational method (bottom, 80 panels on circumference)*

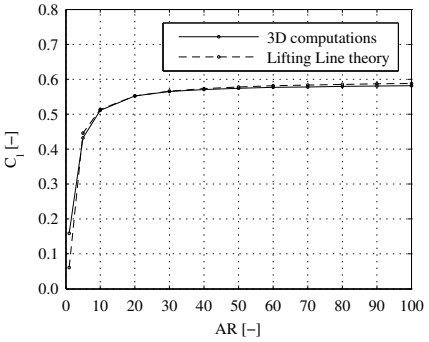
in figure 4.9. For the XFOIL calculations the standard suggested 160 nodes on the foil circumference were used and were sufficient to ensure a converged solution. For the calculations with the computational method presented in this thesis up to 100 panels were used on the circumference. A higher number proved not feasible within the memory requirements, especially considering the fact that to approach a two-dimensional solution high foil aspect ratios needed to be used in the three-dimensional calculations. In order to keep the panel aspect ratio at an acceptable level a relatively large number of span-wise panels was necessary. In these computations typically 80 panels were used on the entire chord-wise circumference and 20 span-wise panels with een aspect ratio of 100. For both panel geometries a cosine panel refinement towards the leading edge was applied, in order to resolve the high and low pressure peaks near the leading edge. A slight gap of 0.2% of the chord was left at the trailing edge in both cases.

To ensure the validity of the comparison between the results of both methods, first a convergence study was carried out. The dependence of the lift coefficient, computed with the computational method of this thesis, on the aspect ratio AR, the submergence depth h/c, and the number of chord-wise panels N was studied. The results of this are shown in figures 4.10(a), 4.10(b), and 4.10(c).

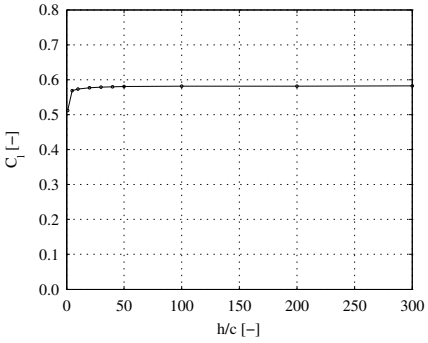
Instead of computing the lift coefficient based on the pressure distribution over the entire foil, only pressure distribution at the mid span is considered. This is done to improve the comparison between the 3D and the 2D computations. The mid span lift coefficient is defined as the lift coefficient based on the chord-wise pressure distribution at the mid span, on the longitudinal centreline of the foil. The mid span lift coefficient is computed by integrating the vertical contribution of the pressure coefficient C_p over the mid span panel strip with constant width B_{pan}. In (4.33), L is the lift force, U the uniform flow velocity, n_z the vertical component of the surface normal, and s a coordinate that follows the surface of the foil. The minus sign appears due to the definition of the normal, that is directed into the fluid.



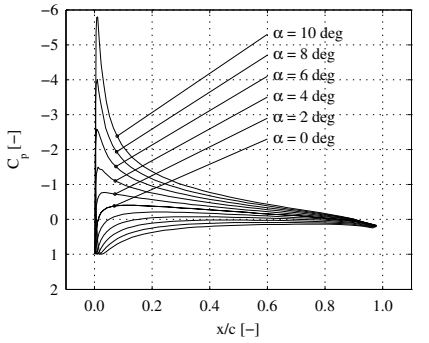
(a) Influence of number elements over the chord on the lift coefficient $AR = 100$, $h/c = 1000$, $\alpha = 5°$



(b) Influence of aspect ratio on the lift coefficient $N = 80$, $h/c = 1000$, $\alpha = 5°$



(c) Influence of submergence depth on the lift coefficient $AR = 100$, $N = 80$, $\alpha = 5°$



(d) Influence of angle of attack on pressure distribution $AR = 100$, $N = 80$, $h/c = 1000$

Figure 4.10: *Lift coefficient convergence study for deeply submerged NACA 0012 foil*

$$\begin{aligned} L &= -1/2\rho U^2 \cdot \int_s C_p n_z dA = -1/2\rho U^2 \cdot \int_s C_p n_z ds \cdot B_{pan} \\ C_l &= \frac{L}{1/2\rho U^2 \cdot B_{pan} c} = -\frac{\int_s C_p n_z ds}{c} \end{aligned} \tag{4.33}$$

In a similar way the (pitch) moment coefficient about a reference point can be computed. In (4.34), (x_{ref}, z_{ref}) is the moment reference point. In the case presented here, the reference point is located at the quarter chord point on the foil centerline. Due to the fact that the chord length was set to unity, direct comparison of these coefficients with the output of XFOIL was possible.

$$C_m = -\frac{\int_s C_p \left(n_z \cdot (x - x_{ref}) - n_x \cdot (z - z_{ref})\right) ds}{c^2} \tag{4.34}$$

Figure 4.10(a) shows the influence of the number of elements on the chord-wise circumference N on the mid span lift coefficient. Calculations with an N of up to 100 have been performed. Although the lift coefficient seems to be almost converged to about 0.58, still a slight increase seems to be possible when increasing N. Yet in practice this is hardly practical, as a further increase of N would yield panels with unrealistically long and narrow panels. The increasingly worsening numerical properties would cause a degradation of the accuracy of the results and could finally cause the solution to break down. One way of overcoming this is to increase the number of span-wise elements M with the increase of the number of chord-wise elements. Unfortunately this leads to a too high memory consumption; clearly there is a trade-off between increasing N and M, the panel aspect ratio, and the memory requirements. The limits of approaching two-dimensional results with a three-dimensional method seem to have been reached here. For the remainder of the calculations $N = 80$ has been selected.

Figure 4.10(b) shows the influence of the foil aspect ratio on the calculated lift coefficient. Above the aspect ratio of 80 the lift coefficient seems to be converged. It should be remarked that the aspect ratio obviously is part of the aforementioned trade-off; the aspect ratio strongly influences the panel shape for a given value of N and M. The dashed line is the prediction of the three-dimensional lift coefficient based on the two-dimensional lift coefficient and lifting line theory for finite wings of rectangular plan form; this line will be referred to later on in this section.

Figure 4.10(c) shows the influence of the submergence depth, expressed as the ratio of the submergence depth and the chord length. At a depth of $h/c = 10$ the influence of the free surface on the lift coefficient has already nearly disappeared. Although the induced velocities due to the free surface memory effects are excluded in these computations, still the G^0 (Rankine) biplane term is present, causing the lift coefficient to reduce when the foil is positioned relatively close to the free surface. Finally, figure 4.10(d) shows the chord-wise distribution of the pressure at the centreline of the foil under different angles of attack.

Accordingly, a $AR = 100$ NACA 0012 foil was selected at a depth $h/c = 1000$ with 80 elements along the chord for comparison of the outcome of the model presented here with two-dimensional potential flow theory. Based on figure 4.10 the results of the three-dimensional computations were assumed to be reasonably converged for comparison with the two-dimensional case.

Figure 4.11 shows a comparison of the chord-wise pressure distribution at the foil centreline computed with both methods. The solid line shows the pressure distribution according to the three-dimensional computational method, the dashed line the pressure distribution computed with the two-dimensional method (XFOIL). Especially the suction peak near the leading edge is somewhat underestimated by the three-dimensional method, either due to three-dimensional effects, or due to too low panel density in that region. Also near the trailing edge some small differences are visible, probably due to the lower panel density in the three-dimensional computations. Nevertheless these small differences, the chord-wise pressure distributions are in satisfactory agreement.

In figure 4.12 the lift coefficient is compared for a range of angles of attack. The lift slope of the line computed with the two-dimensional method corresponds to $0.120\ 1/deg$ and of the three-dimensional computations line to $0.114\ 1/deg$, a difference of 5%. An approximation of the influence of the three-dimensional effects can be made by using lifting line theory to compute the lift slope for finite wings $C_{l\alpha}$ based on the lift curve slope for infinite wings a_0.

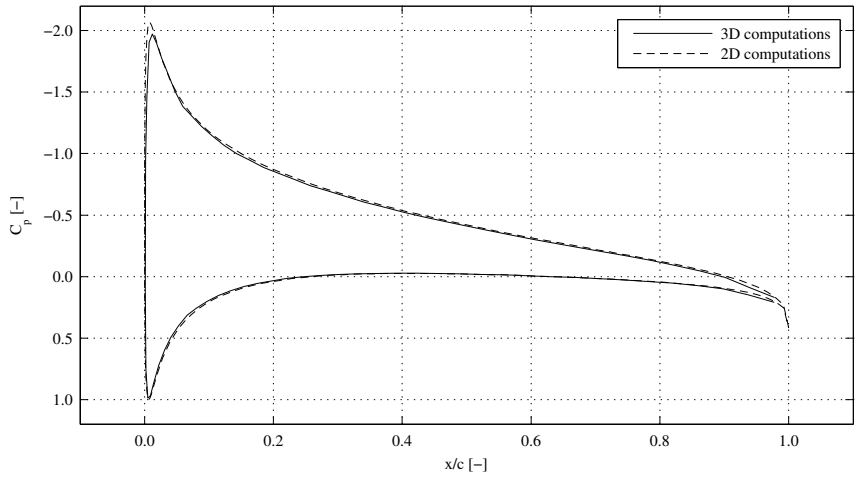


Figure 4.11: *Comparison of the computed pressure distributions at an angle of attack 5 deg of a deeply submerged NACA 0012 foil, for three-dimensional and two-dimensional computations*

This can be done using (4.35), derived by Stewartson (1960) for large aspect ratio rectangular wings:

$$C_{l\alpha} = a_0 \left\{ 1 - \frac{a_0}{4\pi AR} \left[\log \frac{8AR}{a_0} + 1 + \gamma \right] \right\} + O\left(AR^{-2}\right) \tag{4.35}$$

Using (4.35) with $AR = 100$, $a_0 = 0.120\ 1/deg$, and γ Euler's constant, a three-dimensional lift slope of $C_{l\alpha} = 0.117\ 1/deg$ is the result, accounting for already half of the 5% difference between the two-dimensional and three-dimensional calculations. As a confirmation, this study is extended to the range of aspect ratios studied in figure 4.10(b). The result is the dashed line labelled 'Lifting Line theory', that shows satisfactory resemblance to the three-dimensional numerical computations. The only remarkable differences occur at very small aspect ratios and at very large aspect ratios. The difference for aspect ratios well below 10 can be attributed to the fact that (4.35) was derived as an approximation for large aspect ratio wings. The difference for large aspect ratio wings may be caused by unrealistically shaped panels mentioned previously.

Finally, figure 4.13 shows a comparison of the moment coefficient about the quarter chord point for the same range of angles of attack. Both curves again agree reasonably close. Clearly, the three-dimensional computations result in a more irregular shaped curve. A number of factors play a role here. First, the coarser chordwise panel discretisation of the three-dimensional computations causes deviations, particularily due to the integration over the height of the foil. Second, three-dimensional effects may ceuase differences. Third, the panel shape (with very narrow panels) may cause irregularities in the solution, as explained before. Fourth, the value of the moment coefficient is relatively small due to the fact that the center of pressure is located very close to the quarter chord point. The coefficient is built up

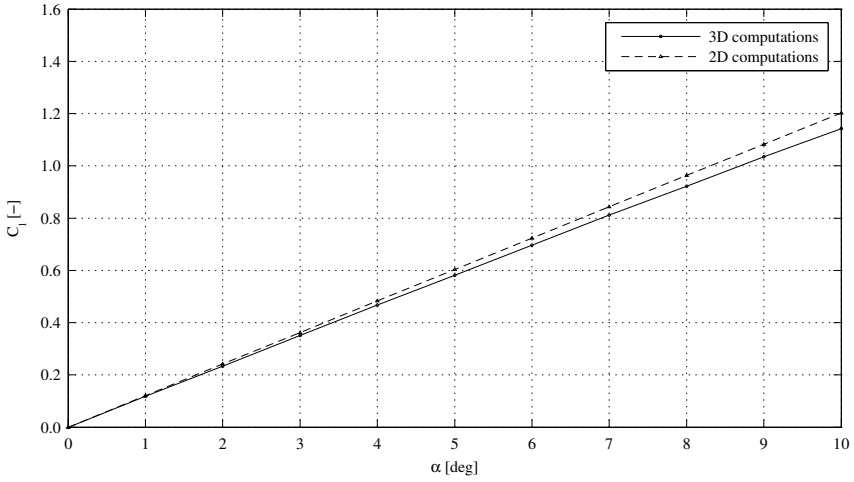


Figure 4.12: *Comparison of the computed lift coefficient at a range of angles of attack of a deeply submerged NACA 0012 foil, for three-dimensional and two-dimensional computations*

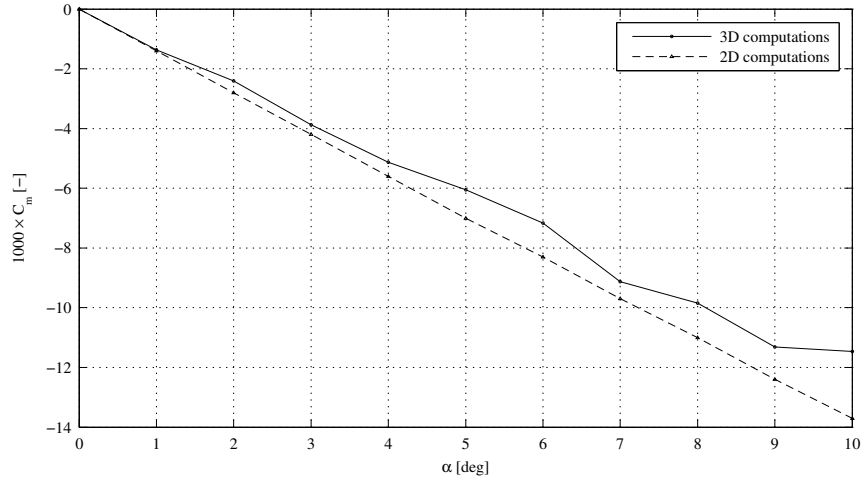


Figure 4.13: *Comparison of the computed (pitch) moment coefficient at a range of angles of attack of a deeply submerged NACA 0012 foil, for three-dimensional and two-dimensional computations*

of panel contributions that are relatively large and that cancel each other to a large extend. Relatively small errors in these contributions may then cause relatively large errors in the moment coefficient.

In conclusion, the remaining differences in the lift and the moment coefficients should mainly be sought in imperfections of the numerical properties, i.e. the panel shape and relatively low number of chord-wise (and span-wise) panels as previously pointed out. Considering the fact that the three-dimensional geometry is stretched to the utmost to approximate two-dimensional flow, this result is satisfactory and gives a good indication of the correctness of the implementation of the source and doublet Rankine and biplane terms as well as the matrix solution.

4.3.2 Foils in proximity of the free surface

In this section the free surface part of the Green function is introduced in the computations. In the previous section only the Rankine (and biplane) terms or G^0-terms were taken into account and it was shown that the source-doublet model with wake sheet could be used to adequately, within the limits of three-dimensional theory, compute the lift on an infinite aspect ratio deeply submerged foils. In the current section the lift characteristics of fully submerged foils in proximity of the free surface are surveyed.

Experimental data

Wilson has published extensive results of an experimental investigation of the steady and unsteady results of an aspect ratio 6, rectangular plan form hydrofoil towed near the free surface (Wilson 1983). These experimental results will be used here as a benchmark. The aim of the experimental study of Wilson was ‘to provide steady and unsteady lift and drag force data for foil-alone performance specifically covering a low Froude number range of interest’. Special care was taken to guarantee a turbulent boundary layer by operating the foil at sufficient high Reynolds numbers and by turbulence stimulation near the leading edge by means of a piano wire. The support system was designed as a forward-leading sting support to minimise hydrodynamic interference. The Froude number range with chord Froude numbers from 1.22 to 4.23, was selected such that the results of the experiments could be applied directly to practical applications on hydrofoil craft and foil-based motion control systems.

Wilson showed that the relation between angle of attack of the foil and the lift remains linear down to submergence to chord ratios of 0.25. For this reason, the comparison between the computational results and the experiments can be limited to comparing the lift curve slope and zero lift angle for a range of depth Froude numbers and submergence to chord ratios. When setting up his steady flow vortex lattice based method Van Walree (1999) used the same data to verify whether his method correctly estimated the free surface effect on the lift generated by the foil. As his method and the method presented in this thesis share the same free surface Green’s function it is expected that it is possible to match his favourable results here. The main difference between both methods is that the VLM of Van Walree only applies singularity elements on the camber line of the foil section, whereas the current method is a fully three-dimensional method solving the normal flow condition on the actual body surface using panels employed on the same surface.

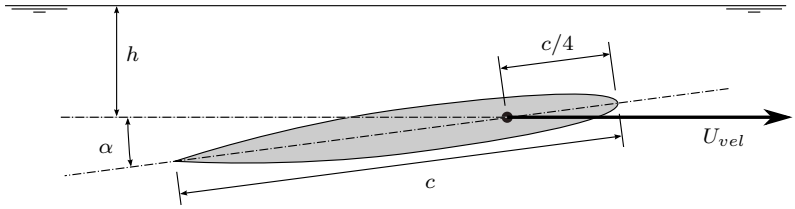


Figure 4.14: *Hydrofoil towed in proximity of a free surface*

The geometry and particulars of the foil are presented in table 4.1 and figure 4.14. Wilson's experiments also include tests with flap deflection angles and unsteady tests in regular waves; both are not considered here, instead the main focus is on the unflapped steady tests.

Table 4.1: *Hydrofoil geometry and particulars (Wilson 1983)*

Section shape		NACA 64A010
Chord	c	0.406 m
Span	s	2.438 m
Thickness ratio	t/c	0.10
Aspect ratio	AR	6
Submergence ratio	h/c	0.25, 0.5, 1.0, 2.0, 4.0
Angle of attack	α	0-10 deg

Computations

In the computations presented in this section no empirical viscous correction was applied. The foil was positioned exactly with its quarter chord point at the location specified by Wilson and the angle of incidence around this point. The support struts of the foil in the towing tank were not modelled in the computations, assuming that the experiment was set-up in such way that their influence on the flow around the foil can be neglected.

Before computing the lift slope curve for a range of depth Froude numbers and submergence depths, first computations were performed to ensure convergence of the results with respect to:

1. Number of chord-wise panels N;
2. Number of span-wise panels M;
3. Free surface memory integral truncation;
4. Wake sheet truncation.

The number of chord-wise and span-wise panels N and M are indicated in figure 4.15. As indicated in the figure again a cosine refinement towards the leading edge was applied in order to resolve the rapid pressure and velocity variations near the leading edge.

The convergence computations were performed for a chord Froude number $F_{n_c} = 3.0$, submergence $h/c = 0.5$, and angle of incidence $\alpha = 2°$. For this case the influence of the free surface effects was strong, as the foil was positioned relatively close to the free surface, where the Green function memory terms show a strong oscillatory behaviour. The velocity was in

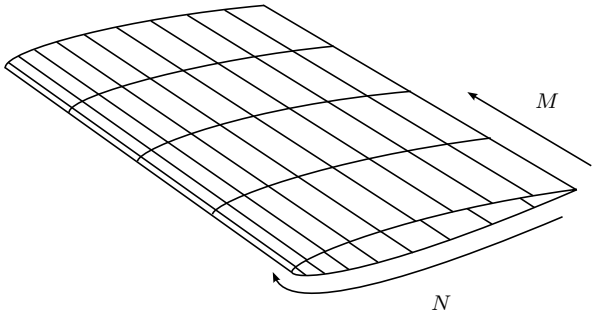


Figure 4.15: *Chord-wise and span-wise number of panels N and M and cosine spacing towards the leading edge*

the lower range of the computations. It is expected that the outcome of this convergence study can be applied to the full computational parameter range.

Figures 4.16 and 4.17 show the convergence of the computed lift and induced drag on respectively the chord-wise and the span-wise number of panels. The convergence of the lift on the chord-wise panel distribution shows a similar trend as has been observed earlier for the high (infinite) aspect ratio foil: a relatively slow convergence, although convergence seems to be slightly better in the current case, with a finite aspect ratio.

Although for the nearly infinite aspect ratio case the span-wise panel distribution was of relatively minor importance, for the current aspect ratio of 6 there is a larger influence of the number of span-wise panels. This importance can mainly be attributed to the much larger influence of the tip vortexes, and stresses the need to correctly resolve their influence on the span-wise velocity and pressure distribution. Again, similar to the infinite aspect ratio case, there was a possibility that the convergence was skewed due to an increasingly unfavourable panel aspect ratio when the chord-wise number of panels increases faster than the span-wise number of panels.

The computed drag, presented with the dashed lines in figures 4.16 and 4.17, consisting of induced and wave drag, is very sensitive to the chord-wise panel distribution, whereas being insensitive to the span-wise panel distribution. The dependence of the drag on the chord-wise panel distribution can be attributed to the importance of sufficient resolution in the frontal projection of the foil to capture the rapid pressure variations in particular near the leading edge, but also near the trailing edge.

Based on figures 4.16 and 4.17 a panel mesh was chosen with 40 chord-wise panels and 16 span-wise panels. Although the computed lift and drag were not fully converged yet, it was assumed that especially the lift curve slope could be computed with sufficient accuracy, especially as the lift curve slope was based on the difference of the result of two subsequent calculations at two angles of attack, together with the fact that the convergence did not show oscillatory behaviour, but rather shows a one-sided approach of the converged result. It may be that the computed zero lift angle and the induced drag could be improved by using more chord-wise and span-wise panels.

Another factor in the choice for $N = 40, M = 16$ was due to the rapid increase of the memory requirements and the computation time when the number of panels was pushed be-

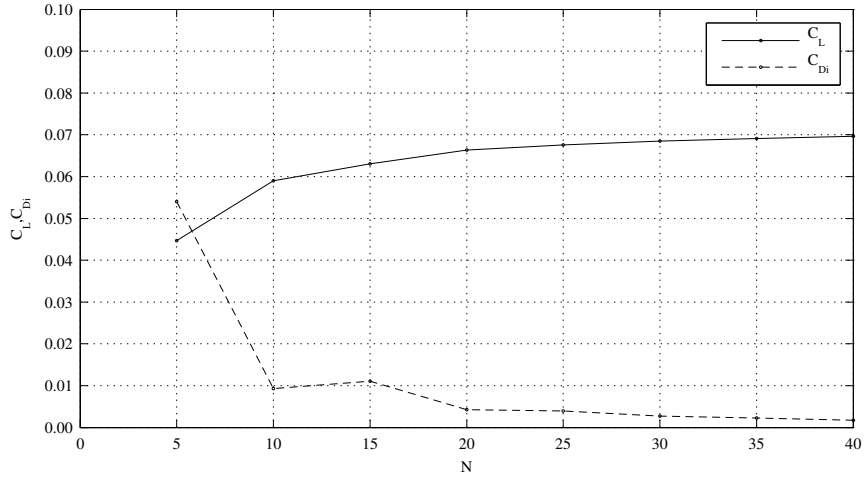


Figure 4.16: *Convergence of the computed lift and drag on the chord-wise number of panels N for $F_{n_c} = 3.0$, $h/c = 0.5$, $\alpha = 2^\circ$, and number of span-wise panels $M = 12$*

.

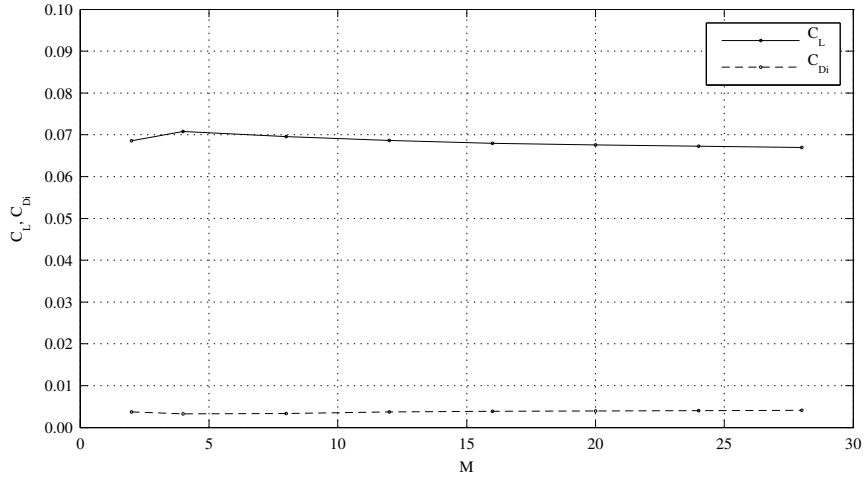


Figure 4.17: *Convergence of the computed lift and drag on the span-wise number of panels M for $F_{n_c} = 3.0$, $h/c = 0.5$, $\alpha = 2^\circ$, and number of chord-wise panels $N = 30$*

.

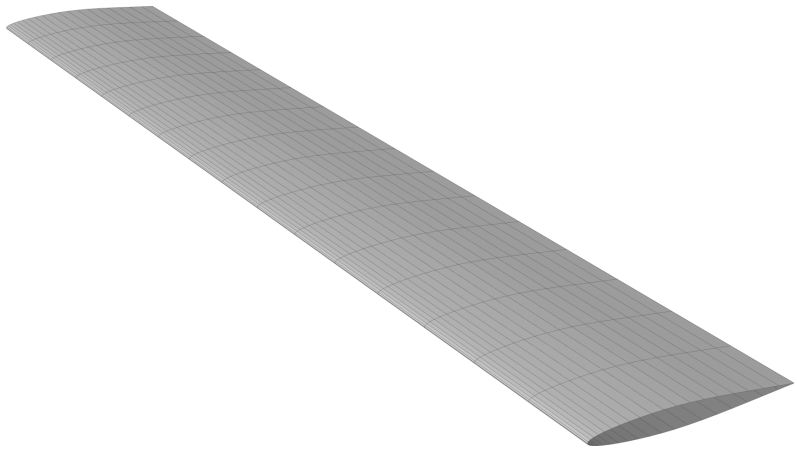


Figure 4.18: *Panel mesh of an aspect ratio 6 foil with the NACA 64A010 foil section,* $N = 40$*,* $M = 16$

yond these values. It is believed that this choice gave an acceptable balance between accuracy and computational effort. The results shown below support this assumption. The resulting panel mesh is depicted in figure 4.18.

To conclude the convergence study, the dependence of the lift and drag on the history length were studied. In these computations both the number of memory effect (or history) time steps and the number of wake time steps were kept constant at 100 steps before truncation. Computations were performed for a range of time step values. In this way the length of the history and wake effects that were included was varried over a wide range.

Already in section 4.2.4 it was demonstrated that care needs to taken that enough history length is included to avoid truncation errors. Other computational results, omitted here, showed that for these steady cases the computed velocities, pressures and loads could be affected significantly when truncation errors were present in the history and wake contributions. In the steady case however, the computational results were insensitive to the resolution (i.e. the number of history time steps for a given history and wake length), allowing for the use of time step variations in order vary the memory effect length. Figure 4.19 shows that in this particular case the lift and drag are converged for a history length of around 20 chords lengths.

Applying the previous, the main parameters have been determined for the simulation. Computations were now performed for a range of depth Froude numbers of 1.0 to 10.0 and for all 5 submergence ratios of Wilson's experiments and for two angles of attack: 0° and 2°, allowing the computation of the lift curve slope $dC_L/d\alpha$ in figure 4.20 and computing the zero lift angle in figure 4.21 as well as the C_D-C_L^2-curve for small angles of attack presented in figure 4.22.

Figure 4.20 shows the comparison of the calculated and the computed lift curve slopes. In order to reduce the effect of viscosity on the experimental lift, both calculated and experimental lift curve slope are divided over the lift curve slope at the highest submergence ratio $h/c = 4$. At this submergence the free surface effect on the lift is negligible, as the value of the lift coefficient becomes independent to the Froude number. The result is a close agree-

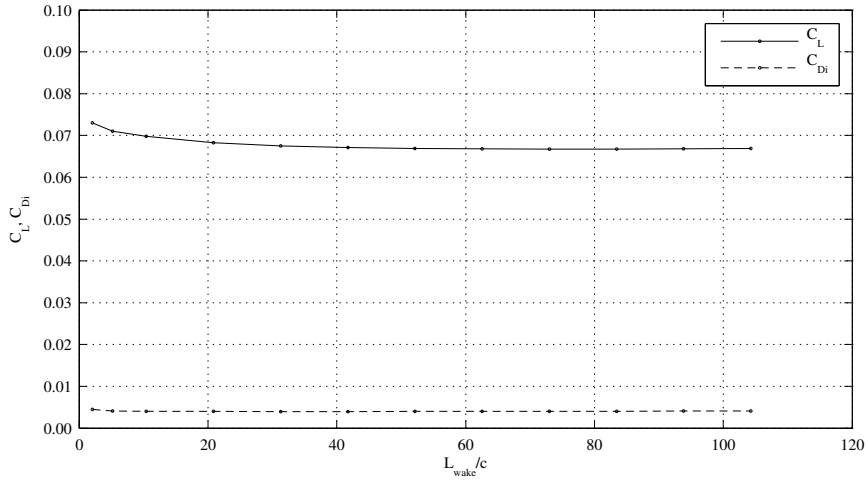


Figure 4.19: *Convergence of the computed lift and drag on the wake sheet length for* $F_{n_c} = 3.0$*,* $h/c = 0.5$*, and* $\alpha = 2^\circ$

ment between experiments and computations for the lift curve slope, a good indication for the correct implementation of source, doublet and wake sheet Rankine, biplane and free surface memory terms.

In figure 4.21 the experimental and computed zero lift increments are presented. Although both the decreasing trend for increasing Froude number and the value range of the zero lift angle are reasonably well predicted by the computations, the absolute values of the zero lift angle are over-predicted, especially for low foil submergence and for high submergence depth Froude numbers.

Two factors do play a role in this case. First, the linearisation of the free surface boundary condition influenced the calculations, especially near the free surface, i.e. for low foil submergence. Second, the fact that the computed lift was possibly not fully converged yet for the chosen number of panels on the foil and still seemed to be increasing at the chosen chord-wise number of panels may be of influence on the predicted zero lift angle. The latter has been checked by increasing the number of chord-wise panels, at the cost of the number of span-wise panels, nevertheless no significant improvement was observed.

Figure 4.22 presents the C_D/C_L^2-curve. Although it was difficult to accurately extract these values from the published results by Wilson and they were obtained from the total drag by Wilson using empirical expressions for the viscous drag components, the comparison presented in figure 4.22 shows an acceptable agreement between experiments and computations. Only for the lowest foil submergence ratio of $h/c = 0.25$ (left out of the figure for clarity) the computed drag shows very high values. Again this can be probably attributed especially to the linearisation of the free surface condition, that can have significant influence on the velocity and pressure distribution on the foil for this very low submergence ratio. Moreover,

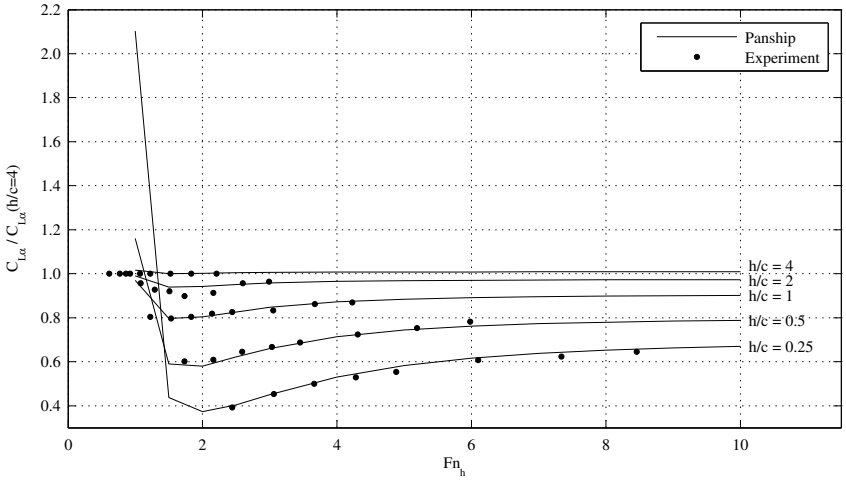


Figure 4.20: *Comparison experimental and calculated free surface influence on lift curve slope*

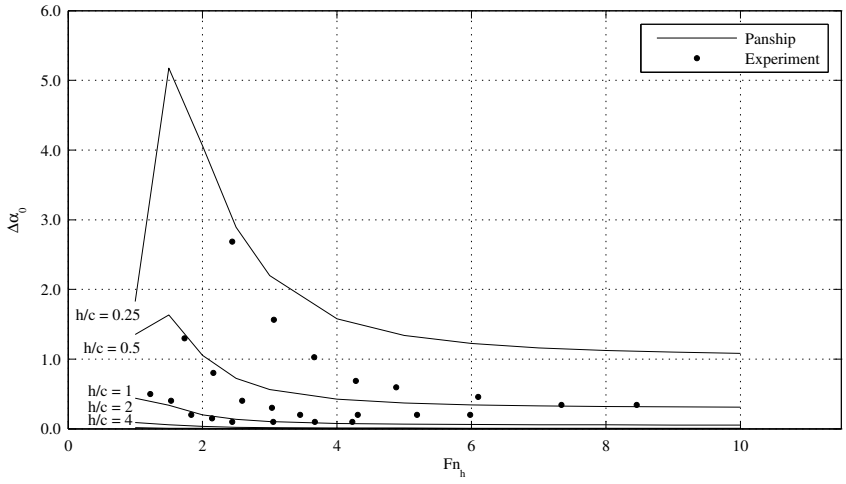


Figure 4.21: *Comparison experimental and calculated free surface influence on zero lift angle*

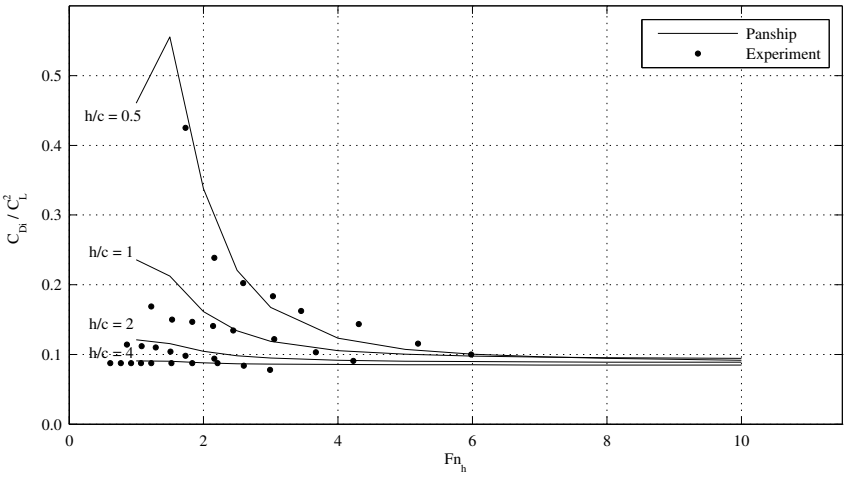


Figure 4.22: *Comparison experimental and calculated free surface influence on induced drag*

especially the drag is very sensitive to the geometric discretisation as demonstrated earlier in this section.

To inspect the effect of the linearisation of the free surface boundary condition, the free surface disturbance due to the foil was investigated. From the previous graphs can be concluded that at a submergence depth Froude number of $Fn_h = 2.00$ the free surface effect on the lift is the largest. Figure 4.23 shows the free surface disturbance generated by the foil at the five submergence depths from $h/c = 0.25$ to $h/c = 4.00$ at this particular Froude number for two chords ahead of the foil to 8 chords behind the foil.

Note that the vertical dimension is magnified with respect to the horizontal scale and that the foil is only plotted for reference purposes at the correct horizontal location, but not at the correct vertical location, nor scale. The magnification of the free surface level is however identical for all five wave profiles.

Logically, at the lowest submergence of $h/c = 0.25$ the generated free surface waves are largest; they have nearly disappeared at the highest foil submergence. Nevertheless, the disturbance amplitude does never exceed the submergence depth and reaches at the maximum 15% of the chord, meaning that at least the foil does not (partly) emerge. The wave length of the disturbance increases when the submergence depth increases. This can be attributed to keeping constant the depth Froude number for all foil submergence depths; consequently the forward speed increases when the depth increases, resulting in longer waves.

In conclusion, computations of the free surface influence on the lift and drag of a foil near the free surface show satisfactory agreement between computed values and experiments, indicating that the implementation of the free surface influence terms in the code is without significant errors. Especially the computed lift shows excellent agreement with experimentally obtained values. The computed drag, although showing reasonable agreement with the

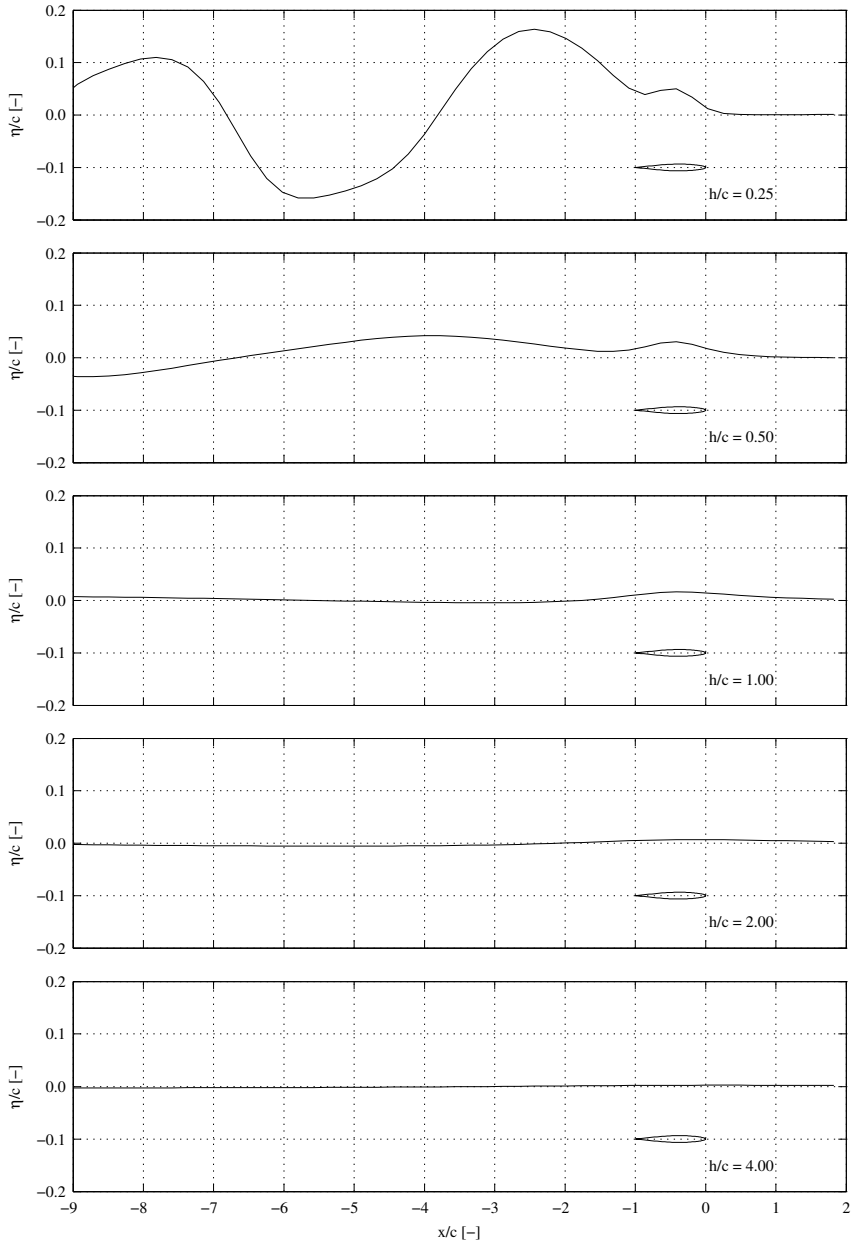


Figure 4.23: *Free surface disturbance at foil centreline at 5 submergence depths at a depth Froude number of* $Fn_h = 2.00$

experiments, is very sensitive to the chosen geometrical discretisation.

4.4 Transom flow model

In section 3.6.3 a transom flow condition was introduced to model the flow around a fully ventilated transom. In the current section the implementation of this model and the influence of parameter variations on the computed pressures and loads is studied. This is done by comparing three different methods to deal with fully ventilated transom flow with the outcome of Savitsky's empirical model to compute the lift on prismatic planing hulls.[1].

The three methods that were used to model transom flow within the computational method presented here are:

1. Plain source distribution without any modification to take into account the flow around the dry transom.
2. Plain source distribution with an empirical pressure modification towards the transom based on the work of Garme (2005), as introduced in section 1.2.3. This model will be further elaborated in section 4.4.2.
3. Combined source-doublet distribution with wake sheet and pressure condition on the transom edge, as introduced in section 1.2.3 and elaborated in section 3.6.3.

In all three cases no panels were distributed on the transom. The total vertical force obtained by the three methods is compared to the outcome of Savitsky's empirical model (Savitsky 1964). This is done in order to determine whether the same overall behaviour is captured, and whether the introduction of the transom flow model poses any improvement or different behaviour than the other transom flow models. To do this, a 15 degrees deadrise prismatic wedge was considered at a 5 degrees trim angle. The wedge was kept fixed in its reference position. Its sides above the chine were vertical. The total vertical force was considered, along with the load distribution over the length of the wedge for a range of panel Froude numbers. The main dimensions of the wedge are presented in table 4.2.

Table 4.2: *Wedge geometry and particulars*

Length keel	L_k	10.00 m
Beam on chine	B_c	2.40 m
Length over beam ratio	L/B_c	4.17
Deadrise angle	β	15°
Trim angle	τ	5°

The dimensions of the wedge were chosen in such way that the speed range was compatible with both the speed range of the computational method ($0.5 \leq Fn \leq 1.2$) and the speed range of Savitsky's empirical model ($0.60 \leq C_v \leq 13.00$). C_v is the speed coefficient, or transom beam Froude number. The choosen speed range is indicated in table 4.3.

[1] A less complete version of this study has already been published (De Jong and Van Walree 2008)

Table 4.3: *Speed range*

V	Fn	C_v
$[m/s]$	$[-]$	$[-]$
5	0.50	1.03
6	0.61	1.24
7	0.71	1.44
8	0.81	1.65
9	0.91	1.85
10	1.01	2.06
11	1.11	2.27
12	1.21	2.47

4.4.1 Savitsky's empirical model

Applying Savitsky's empirical model, the wetted length on the chine L_c can be computed, as well as the mean length over beam ratio of the below chine area λ. This is done by taking into account pile-up using a pile-up factor determined by Wagner as $\pi/2$, meaning that the actual wetted width of a wedge section is $\pi/2$ times the calm water wetted width. Refer to figure 4.24 for the nomenclature for Savitsky's empirical model,

$$L_c = L_k - \frac{b}{\pi}\frac{\tan\beta}{\tan\tau} \tag{4.36}$$

$$\lambda = \frac{L_k + L_c}{2} \tag{4.37}$$

For the wedge considered here λ equaled 3.68. Using λ the total lift coefficient (hydrostatic force plus hydrodynamic force) of an equivalent flat planing surface can be found using the following empirical formulation from Savitsky, applicable for $0.60 \leq C_v \leq 13.00$, $2^\circ \leq \tau \leq 15^\circ$, and $\lambda \leq 4$:

$$C_{L_0} = \tau^{1.1}\left[0.0120\lambda^{1/2} + 0.0055\frac{\lambda^{5/2}}{C_v^2}\right] \tag{4.38}$$

Savitsky formulated another empirical formula to compute the lift of deadrise planing surfaces, based on the lift of a zero deadrise planing surface:

$$C_{L_\beta} = C_{L_0} - 0.0065\beta C_{L_0}^{0.60} \tag{4.39}$$

Finally, Savitsky also proposed a simple empirical formulation to compute distance of the centre of pressure forward of the transom, again based on the mean wetted length over beam ratio λ and speed coefficient C_v:

$$LCP = \left(0.75 - \frac{1}{5.21\frac{C_v^2}{\lambda^2} + 2.39}\right)\lambda b \tag{4.40}$$

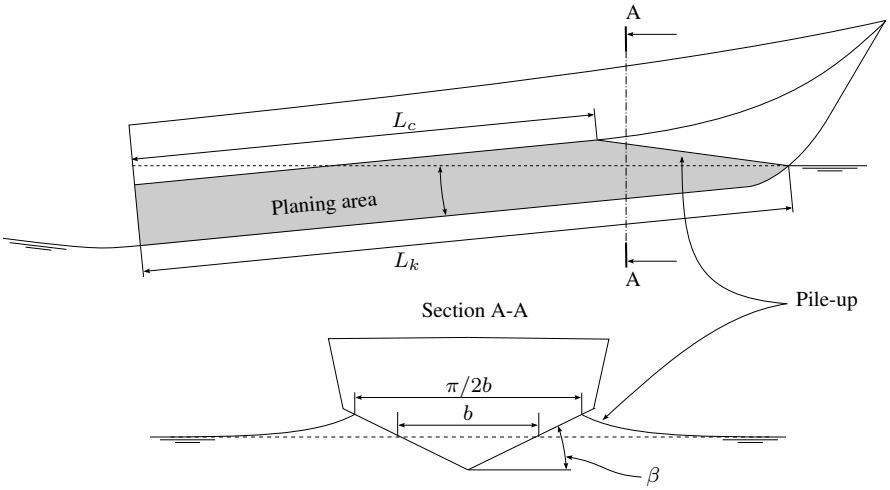


Figure 4.24: *Nomenclature for Savitsky's empirical model*

4.4.2 Empirical near-transom pressure correction

Garme (2005) proposed the usage of a pressure reduction function that reduces the pressure over a length a towards the transom to zero, refer to figure 4.25. Based on pressure measurements on several stations towards the transom he adopted the following strip-wise force reduction function:

$$f_{red} = \tanh\left(\frac{2.5}{a}x_1\right) \tag{4.41}$$

He used this function in his two-dimensional high frequency added mass model (similar to the work of Zarnick (1978) and Keuning (1994)), nevertheless it can be easily applied to computed three-dimensional pressure distributions, by applying (4.41) directly to the computed total pressure distribution. The reduction length a was found by fitting the calculated trim and sinkage of his model to experimental data of a wide variety of high speed ships. For speeds higher than $C_v \approx 2$ Garme (2005) proposed the following reduction length, where B_T is the waterline width on the transom:

$$\begin{aligned} a &= a' B_T C_v \\ a' &= 0.34 \end{aligned} \tag{4.42}$$

For lower speeds the value of the coefficient a' in (4.42) becomes less clear. For low speeds both rise and trim are over-predicted using 0.34; a value of 0.90 instead of 0.34 at $C_v \approx 1$ seems plausible when studying the appropiate figure in Garme (2005). For the computations presented here, a' is set in the following way, interpolating for C_v between 1 and 2:

$$a' = \begin{cases} 0.35 & \forall \quad C_v \geq 2 \\ -0.55C_v + 1.45 & \forall \quad 0.9 \leq C_v < 2 \\ 0.90 & \forall \quad C_v < 0.9 \end{cases} \tag{4.43}$$

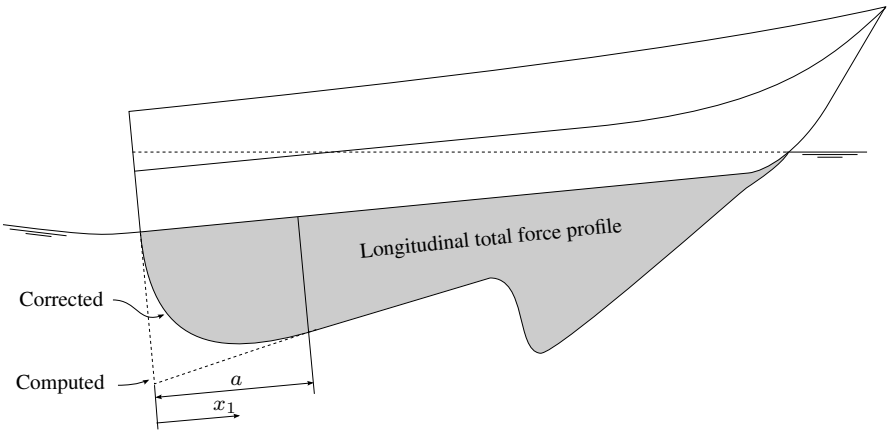


Figure 4.25: *Nomenclature for empirical near-transom pressure correction*

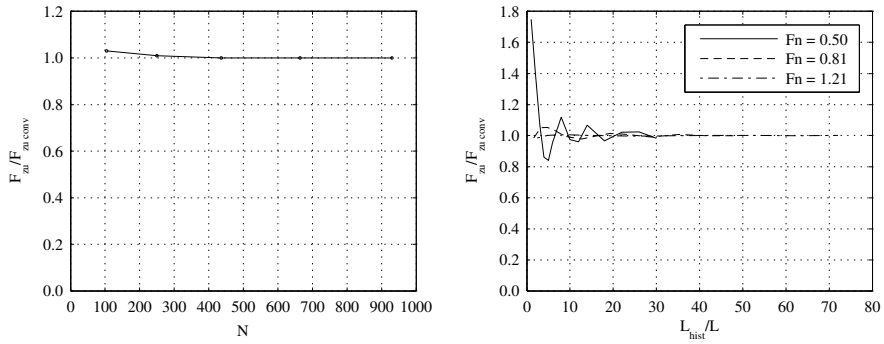
4.4.3 Computations

Numerical convergence

Before performing the comparison described above, first a numerical study was carried out to ensure convergence on the spatial discretisation, the time step and the history and wake lengths, similar to what was done in the previous section for submerged foils. Figure 4.26(a) shows the influence of the number of panels on the hydrodynamic vertical force, i.e. excluding the speed independent hydrostatic force. The hydrodynamic force at each discretisation is divided over the converged value: convergence is reached when this value reaches 1. Relatively quick convergence takes place when the number of panels increases; above 450 to 500 panels the hydrodynamic force is converged. The convergence test was performed for an intermediate forward speed of $Fn = 0.81$.

Figure 4.26(b) shows the convergence of the lift for a range of values for the history length for the lowest, a medium, and the highest forward speed in the speed range. In these calculations the number of time steps in the history length and the wake length were kept constant, whereas the time step was varried. On the horizontal axis the distance travelled in the entire history before truncation is divided over the ship's length. It can be concluded that especially at the lower forward speed convergence becomes difficult: 25 ship lengths of history were necessary before the hydrodynamic force was less than 1% from its converged value. At the medium speed, this was reduced to 16 ship lengths, whereas at the highest forward speed only 6 ship lengths were necessary.

Using these lengths the temporal length of the memory effects and wake sheet that need to be included were obtained. Based on the forward speed and selecting an arbitrary number of history time steps, the time step was determined. The number of history time steps for steady forward speed is of relatively minor importance, as the strength for each wake panel becomes constant for steady problems and the integration routine already takes into account the variation of the influence functions over the wake panels. However, the aspect ratio and the relative size of the panels may have numerical consequences. For this reason typically still



(a) Number of panels

(b) History length and velocity (Froude number 0.81)

Figure 4.26: *Convergence of hydrodynamic force*

100 to 200 number of history and wake time steps were used, avoiding numerical problems more than sufficiently.

Finally the resulting panel representation for the planing wedge is depicted in figure 4.27. In this figure the reason for the slow convergence on the history length can be found. Due to the wedge shape with relatively low trim and deadrise angles, a large number (if not most) of elements are close to the waterline. This led to low μ values in the principal Green function derivatives, resulting in heavily oscillating behaviour that disappeared only slowly over the history length.

A factor of importance could be that in order to create an easier to generate panel mesh with enough resolution to resolve the rapidly varying pressure along the forward waterline, a constant number of panels was chosen for each transverse panel row. The result was that in the bow region, as well as around the waterline intersection of the chine, large numbers of relatively small panels are located very close to the waterline. This may have increased the oscillating behaviour of the Green function derivatives even further.

Transom flow segment length and panel refinement

This section focuses on the particulars of the transom flow condition introduced in section 3.6.3. The condition makes use of combined source-doublet elements on the hull, together with a wake sheet extending from the transom. The unknown strengths of the first wake panel row (i.e. the panels attached to the transom) are used to enforce a pressure condition near the transom edge. This condition was introduced by Reed et al. (1991); refer to section 3.6.3 for the computational details.

In order to reduce the computational load of the transom flow condition use was made of the fact that only over a limited stretch of hull in front of the transom the doublet elements have an actual strength to satisfy the condition. On the remaining part of the hull the doublet strength reduced to zero, making it unnecessary to include doublet panels on this part of the hull and computing their influence. In this manner a significant reduction of Green function evaluations was achieved. The part of the hull where combined source-doublet elements were

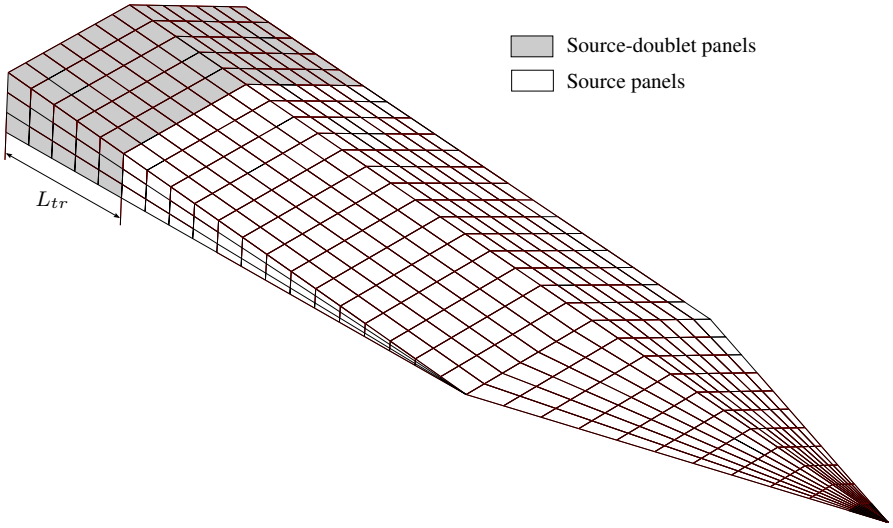


Figure 4.27: *Panel mesh of a wedge with* 15° *deadrise and* 5° *trim consisting of 528 panels*

applied for use with the transom flow condition is termed the 'transom flow segment'. This segment, having a length of L_{tr}, is indicated with grey shading in figure 4.27.

Figure 4.28 presents the influence of the length of the transom flow segment in front of the transom on the longitudinal vertical force profile for a Froude number of 0.81. This force profile was computed summing the vertical total force on the panels of each transverse panel strip and diving it over the length of the strip. For presentation in the figure the vertical force per unit length f_{zstrip} was made non-dimensional with the weight of the zero-speed displacement Δ and the ship's length.

In the figure four force profiles are shown, with a transom flow segment stretching over 10%, 20%, 30%, and 40% of the wedge's length. For the lowest segment length a clear discontinuity is visible in the corresponding force profile. When using a transom flow segment of 20% and 30% of the wedge's length only a small discontinuity is visible, whereas at 40% the discontinuity has practically disappeared. In general it has been found that a 1.5 to 2 times times the reduction length a of Garme can be used as a reasonable estimator for the minimum length of the transom flow segment. In this case ($Fn = 0.81$, $C_v = 1.65$) this would lead to a transom segment length of about 30 to 40% of the ship's length.

Examining the dependence of the lift force and its longitudinal distribution on the longitudinal panel refinement shows that the size of the final panel has a relatively large influence. Figure 4.29 shows five longitudinal force profiles for the same longitudinal panel discretisation of 40 panels. In the second profile, denoted '40+1', the final panel row (the panel row adjacent to the transom edge) was split into two rows, and this procedure was carried on towards 4 times splitting the last panel row, resulting in '40+4'.

Although the character of the force distributions remains largely the same, the total lift increases significantly when refining towards the transom, with the longitudinal location of the centre of pressure moving aft. Part of the change is caused by moving the point where the condition is satisfied -at the centroid of the final panel row- closer to the correct position

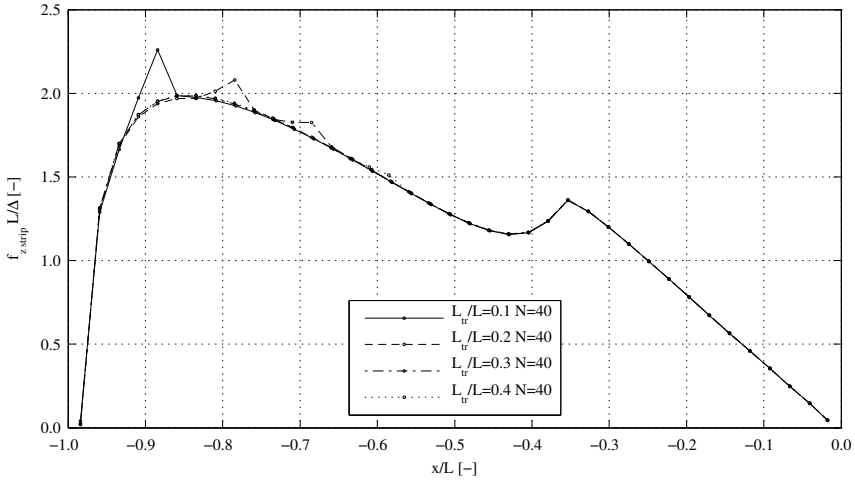


Figure 4.28: *Influence of length transom segment on longitudinal vertical force distribution*

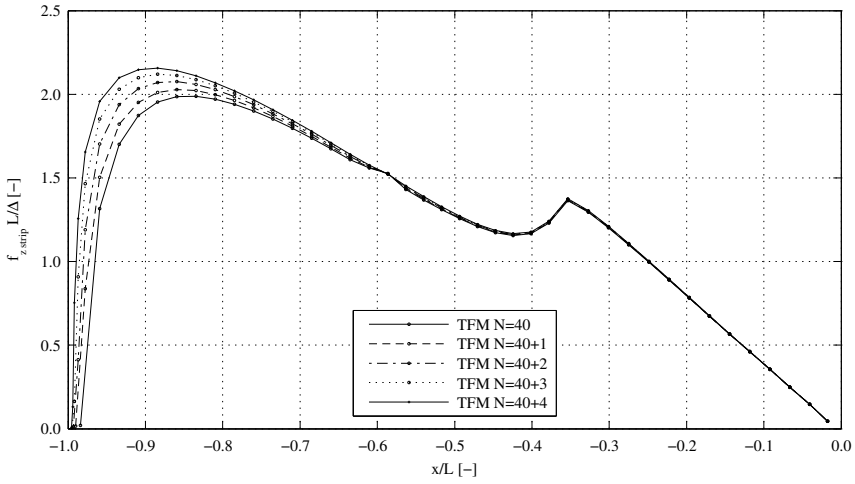


Figure 4.29: *Influence of transom segment panel refinement on longitudinal vertical force distribution*

at the transom edge. Nevertheless, this does not explain the increase of the vertical force entirely, as one would expect only a smooth extension of the force profile aft.

To investigate this behaviour further, the same panel refinement procedure was carried out for the same high speed wedge, but applying a source-only formulation in absence of the transom flow condition. The resulting force profiles are shown in figure 4.30. A near-perfect convergent behaviour was the result -by refining the aft panels the force profile is consistently extended towards (in this case) zero at the transom edge. The force profile forward of the panel refinement was entirely unaffected by the panel refinement, resulting in nearly coincident lines in the figure. This behaviour may be expected in a potential flow, that tends to develop high flow velocities near discontinuities as pronounced edges and knuckle lines, whereas in a real flow the viscous nature of the fluid would limit or soften this tendency. In this case, the pressure due to the source distribution seems to approach zero, this, however, may be a coincidence.

Due to this behaviour, the doublet solution, that was solved after the source solution in order to satisfy the transom flow condition, resulted in ever decreasing doublet strengths as the panels near the transom were increasingly refined. This can be attributed to the fact that the pressure due to the source solution already approached the atmospheric value that the condition was trying to enforce. The result was that the flow acceleration towards the transom edge due to the doublet solution with the transom flow condition was diminished. The resulting pressure distribution started to approach the distribution already found by solely solving the (refined) sources in absence of the transom flow condition.

The questions that remain are whether the diminishing effect of the transom flow condition when refining the panels are (1) only due to the behaviour of the source-only solution and (2) what the physical relevance is of this behaviour. To investigate these questions a number of additional calculations were carried out, focused on suppressing the flow acceleration towards the transom caused by the panel refinement in the source-only solution.

Several techniques can be applied to suppress the acceleration. Figure 4.31 shows the result of a number of these techniques. The techniques applied here are inspired by the fact that one is to some extent free to choose how to divide the solution over the source and doublet strength on each doublet panel. It is possible however, to make a suboptimal choice that results in a numerically unfavourable and inaccurate result, a fact that is explained by Hunt (1980). The techniques that are shown in the figure are:

1. To fix the source strength of the combined source-doublet panels on the transom flow segment at the total incoming flow at each panel due to the forward ship speed, the incident wave and the body induced memory effects.
2. To compute the source strengths by actually solving the sources as in the already proposed method, but applying a dummy segment at the transom that continues the body smoothly behind the transom. This effectively inhibits the source solution to produce the flow acceleration at the transom edge by moving the discontinuity aft, away from the transom edge.
3. To apply source-doublet panels on the entire submerged geometry and fixing the source strength of the entire body at the total incoming flow at each panel due to the forward ship speed, the incident wave and the body induced memory effects.

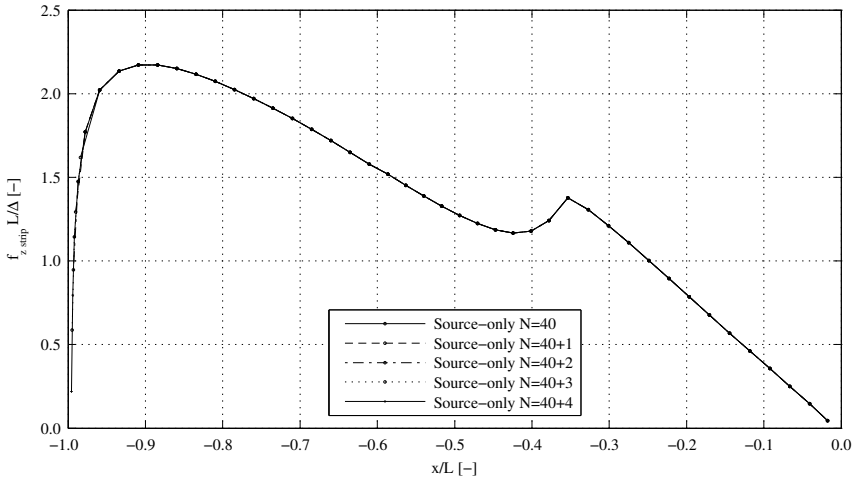


Figure 4.30: *Influence of transom segment panel refinement on longitudinal vertical force distribution - source only formulation without transom flow model*

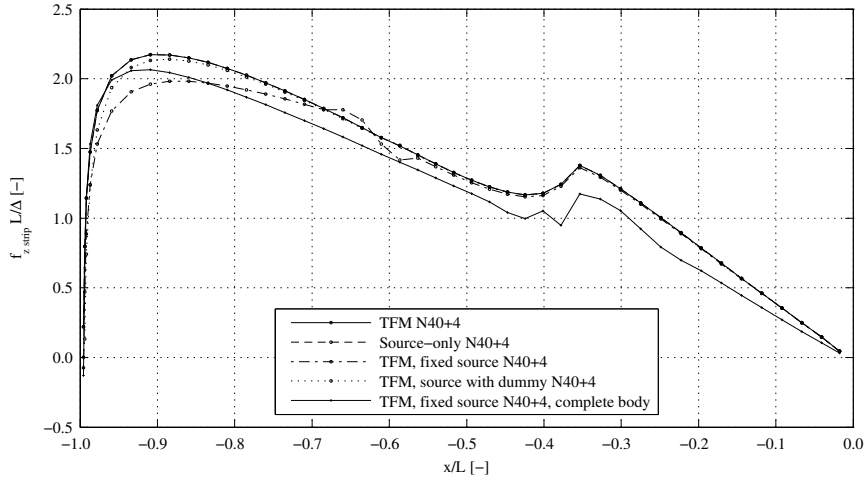


Figure 4.31: *Influence of transom segment panel refinement on longitudinal vertical force distribution - variety of choices for determining source strength*

In the figure the results of these three choices are compared to the outcome of the source-only solution of figure 4.28 and of the transom flow model solution of figure 4.29 for 40 longitudinal panel strips that are split 4 times near the transom to create the panel refinement.

Although not shown here, all three techniques showed a similar convergence behaviour with respect to the panel refinement as the original transom flow method of figure 4.29. The first approach somehow results in lower pressures near the transom, at the cost of a clear discontinuity at the forward edge of the transom flow segment. Some effort has been invested to devise derived approaches that gradually switch from fixing source strengths by satisfying the normal flow condition to fixing them by presetting them to the incoming flow when moving aft of the forward edge of the transom flow segment by using linear interpolation between both or even by applying cosine interpolation. It appears that the more successful one is in removing the discontinuity, the more the resulting force profile reflects the one already found with the original transom flow method.

The second approach, applying a dummy segment in the source-only solution before solving the transom flow condition surprisingly results in nearly the same force profile as the one already found with the original transom flow method. This shows that although the acceleration of the flow towards the transom was suppressed in the source solution (this has been verified) still the second transom flow solution exerted the same acceleration on the flow towards the transom, when the panels were refined. In other words, the diminishing flow acceleration when refining the panels near the transom can not solely be attributed to the source panels, but also exists in the doublet solution combined with the transom flow condition.

The final approach again results in a similar convergence behaviour, nevertheless now the resulting force profile is lower over the entire body length. Additionally, the force profile shows some irregular behaviour, especially near the point where the chines penetrate the water surface. This may indicate that the solution that is obtained in this approach is the result of a non-optimal distribution of the normal flow condition over the source and doublet strengths. No further attempt is made here to quantify this.

Other factors of importance could be the aspect ratio of the refined panels and the relative size of adjacent panels near transom edge. This in particular relates to the relative sizes of the panels just forward of the transom edge and the first wake row panels just aft of the transom edge, as these are closely linked to one another for the computation of the longitudinal induced velocity due to the $d\mu/dx$-term. The influence of the panel aspect ratio has been closely scrutinised and it has been ruled out that this has any significant effect on the results presented here. The second aspect has been ruled out by pre-setting the panel size of the first wake row elements equal to the size of the adjacent refined body panels. Only a very localised influence has been observed on the pressure profile when the first wake row element became much larger than the last body panel. In particular the pressure of the second panel in front of the transom edge could show a negative spike in this case.

For the remainder of this work, where use was made of the transom flow condition presented here, no extensive panel refinement near the transom edge was applied. By not applying panel refinement towards the transom edge the effect of the suction towards the transom is felt over a larger distance in front of the transom, in agreement with empirical data and formulations as shown in the next section. In spite of this it should be noted that this effect may be artificially introduced into the solution and in this way may represent an arbitrary and

opportunistic choice that may introduce undesirable grid dependence into the solution and hence the results of this should be critically assessed. This alone warrants further research into the numerical details of this particular formulation and into alternative approaches that may better represent the effect of transom flow into the numerical solution.

As a final note, this effect has not been been found by Reed et al. (1991) who originally introduced this condition, although they do mention that when using a double body basis flow before adding the transom flow condition they needed to take special measures in order to prevent the flow from turning at the sharp corner at the transom edge. They achieved this by using a dummy wedge behind the hull in a very similar way as described in one of the approaches presented above.

Comparison of transom flow methods with empirical data

Next, three methods of dealing with transom flow were compared to the outcome of the empirical model for computation of the lift (the total vertical force) on a wedge devised by Savitsky (1964). The panel distribution used for all three methods was nearly identical and consists of 528 panels, with 30 longitudinal panel strips, depicted in figure 4.27. No panels were used on the transom stern, that in all cases was considered fully ventilated. Numerical results without any transom flow model, just using a plain source distribution are denoted 'No TFM', using the empirical transom flow model proposed by Garme are denoted 'Empirical TFM', and results of the newly proposed transom flow model, based on the work of Reed et al. (1991) are labelled 'TFM condition', and the empirical estimate using Savitsky's model 'Savitsky'.

Figure 4.32 shows the longitudinal strip-wise force distributions of the three approaches within the numerical method for a Froude number of 0.81. The strip-wise force near the bow is not affected by the transom flow approach that is applied. The plain source distribution does not reduce the pressure to atmospheric at the transom, where both other models do achieve the pressure reduction. The other two methods cause a significant reduction of the lift near the transom, causing the overall lift to decline and a forward shift of the centre of pressure (the point of attachment of the lift force).

The transom flow condition causes a reduced pressure over the entire aft-body, whereas the empirical pressure reduction affects a region closer to the transom, within the reduction length. Nevertheless the extent from the transom of *significant* pressure reduction is similar. The empirical pressure reduction maintains an atmospheric pressure exactly at the transom edge (the forces on the strip centres are depicted), whereas the transom flow condition reduces the pressure to zero at the centroid of the final panel row. Finally, although the transom flow condition still could benefit from a slightly longer transom flow segment in front of the transom as there is still a small discontinuity visible, its force distribution is much smoother than the empirically corrected distribution.

The comparison of the lift for the entire speed range for the three methods with the outcome of Savitsky's empirical model is presented in Figures 4.33 and 4.34. The lift is divided by the still water displacement weight of the wedge. The plain source distribution without transom flow model results in too much lift compared to Savitsky. The empirical pressure correction and the transom flow condition result in lift curves of similar magnitudes reducing the difference with Savitsky's empirical model with roughly 50 %, the transom flow condition

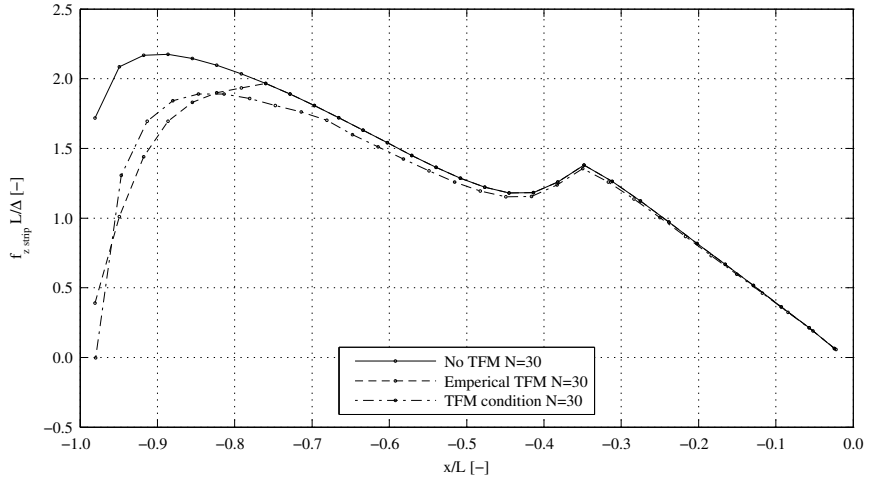


Figure 4.32: *Influence of transom flow model on longitudinal vertical force distribution*

being slightly lower at higher speeds. The transom flow condition results in a slightly more smooth curve than the empirical pressure reduction. This could partly be attributed to the more or less arbitrary choice for the reduction length coefficient a' for a C_v between 1 and 2 ($Fn < 1$).

The location of the centre of pressure, presented in figure 4.34, shows a similar picture. Again both the empirical transom flow method and the transom flow condition perform better than the plain source approach and again the transom flow condition shows a smoother behaviour that is slightly better than the empirical transom flow method. The centre of pressure, as predicted previously, makes a forward shift due to the addition of a transom flow model.

Although the location of the centre of pressure fits with the empirical model when using a transom flow model (be it empirical or based on a pressure condition), still the magnitude of the lift force is over-predicted. Although the empirical model also may have its flaws and care has to be taken when studying differences between it and the computational model, the reason of the different magnitude of the lift may be found in figure 4.35. This figure shows a three-dimensional representation of the total pressure coefficient plotted on the xy-surface. The pressure distribution depicted is computed applying the transom flow condition. A number of observations can be made:

- There is a small discontinuity in the pressure at the end of the transom flow segment, small enough not to affect the overall pressures and forces, as has been already noted when studying the force profiles.
- The pressure at the transom is zero exactly at the centroids of the final panel row, as enforced by the condition.
- The pressures at the sides, at the chines and along the forward waterline, do not tend to zero.

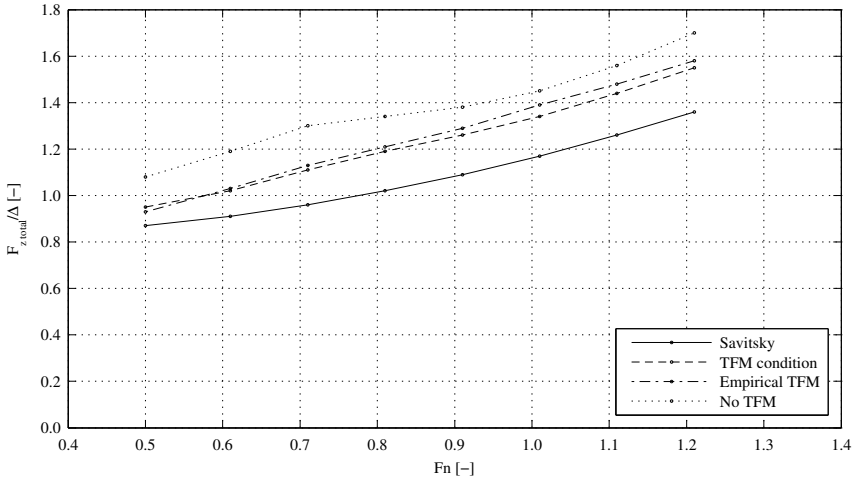


Figure 4.33: *Influence of transom flow model on total vertical force*

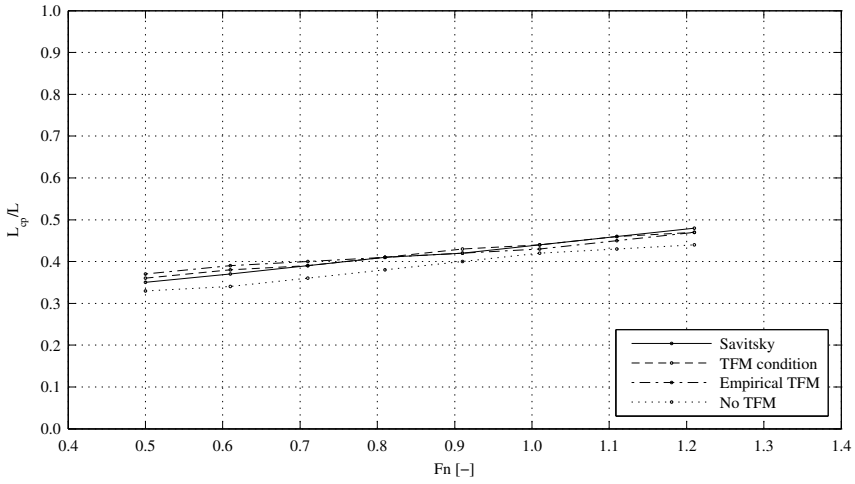


Figure 4.34: *Influence of transom flow model on longitudinal centre of pressure*

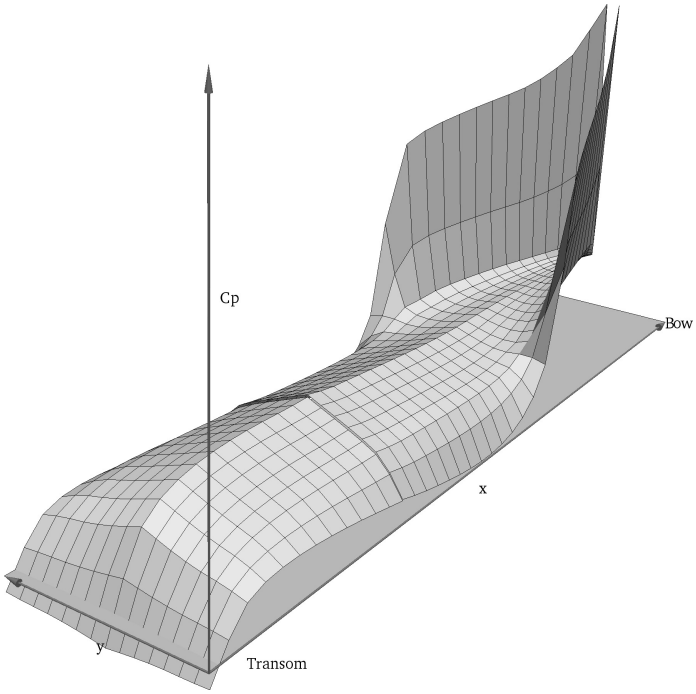


Figure 4.35: *Representation of the total pressure on the wetted surface with transom flow condition*

The final point is due to the way of representing the pressure by taking the pressures at the panel centroids and interpolating and extrapolating at the edge to the panel corner points. In addition to this, no conditions exist along the waterline and along the chines to deal with separating flow. In a real flow the wedge would experience significant spray forming, at least along the stagnation regions at the forward waterline and in all probability as well along a significant part of the chine. This would alleviate the pressure on the bottom of the wedge, lowering the overall lift.

In conclusion the empirical transom flow method and the transom flow condition cause a similar improvement of the computed pressures over the plain source method without transom flow model, when compared to the outcome of the empirical model of Savitsky. Although the transom flow condition is not dependent on a to some extend arbitrary coefficient that has been obtained by fitting another computational model by Garme (2005) to empirical data, the transom flow condition is sensitive to the discretisation near the transom and more computationally demanding. The latter objection has been overcome to a large extend by only applying doublets on a small part of the hull.

Finally, the main attraction of the transom flow condition is that the resulting flow remains a valid potential flow, satisfying all boundary conditions. This makes it especially interesting as it deals with instationary flows, such as ship motions in waves. The empirical transom flow method does not necessarily satisfy the boundary condition or even the Laplace equation, as it is a post-solution modification of the pressure, possibly invalidating its interaction with ship

motions.

To improve the flow at high speeds a spray model along the waterline may be considered for future work, although its interaction with the linearised free surface and the free surface Green function would complicate the successful introduction of such spray model significantly.

As already mentioned, the dependence of the transom flow condition on the near-transom panel discretisation is a source of concern, warranting more research into the fundamentals of this particular condition and the search for alternative methods that are viable within the context of the applied free surface linearisation.

4.5 Free surface elevation

In section 3.7.3 a method was introduced to compute the free surface elevation of both the incident waves and the waves generated by the disturbance potential due to diffraction and radiation. In the current section the resulting wave profile around a ship is studied.

First a Wigley travelling at constant forward speed in calm water is considered. Although the forward speed is lower than the speed range considered for the method presented in this thesis, this provides still a good case to test the free surface elevation computation due to availability of suitable comparison material, both experimentally as numerically. Next, the study is extended to high speed craft.

4.5.1 Wigley hull at constant forward speed in calm water

In the 1980s a cooperative research program was commissioned by the Sixteenth ITTC Resistance Committee to set-up a standard database for ship resistance and the flow around the hull. Part of this research was carried out in Japan and reported by Kajitani et al. (1983). In the current section the wave profile for a Wigley parabolic hull travelling at constant forward speed fixed in its reference position with zero trim and sinkage published by said authors will be used as experimental comparison material for the wave profile obtained by the computational model presented in this thesis. Additionally the computed wave profile will be compared to the outcome of two double body flow methods, first the linear double body flow method of Dawson (1977) and second the non-linear double body flow method Rapid (Raven 1996).

According to Kajitani et al. (1983) the parabolic Wigley hull form shape used in their experiments is given by (4.44), while the main hull parameters are given in table 4.4. For the forward speed a Froude number of 0.316 was selected, as for this Froude number also numerical results have been published by for instance Raven (1996).

$$y = \frac{B}{L}\left(1 - \left(\frac{2x}{L}\right)^2\right)\left(1 - \left(\frac{z}{D}\right)^2\right) \tag{4.44}$$

One major difficulty in computing the wave elevation around a ship using the theory outlined in section 3.7.3 is that it is not possible to straightforwardly compute the Green function memory influences exactly on the calm water waterline. One reason for this is that when the distance R between source and field point becomes zero both the dimensionless parameters μ and β, introduced in section 4.2.1 and repeated below, become infinite.

Table 4.4: *Wigley hull geometry*

Length over beam ratio	L/B	10.00
Length over draft ratio	B/T	16.00
Block coefficient	C_b	0.444
Midship coefficient	C_m	0.667
Deadrise angle	β	0°
Trim angle	τ	0°

$$\begin{aligned}
\mu\left(p,q,t-\tau\right) &= -\frac{z_0+\zeta}{R}, \quad \mu \in [0,1] \\
\beta\left(p,q,t-\tau\right) &= \sqrt{\frac{g}{R}}\left(t-\tau\right), \quad \beta \in [0,\infty\rangle \\
R &= \sqrt{\left(x_0-\xi\right)^2+\left(y_0-\eta\right)^2+\left(z_0-\zeta\right)^2}
\end{aligned} \tag{4.45}$$

This happens for instance for the waterline integrals, both for the current time contribution of a waterline element on a free surface evaluation point located on this waterline element as for past time contributions of waterline elements on free surface evaluation points that happen to be located on (or very near to) these waterline elements at some point in the history. In this case both μ and β contain divisions over zero and the result is that no valid values are obtained for the Green function derivatives.

Still, in the case that the distance R between the free surface evaluation point (the field point) and the source panel becomes small, but not zero (or least that up to the third power of R the value is larger then the machine precision) and the source panel is located very close to the free surface then μ tends either to 1 or to zero, depending on the vertical distance $z_0+\zeta$. If μ tends to 0, then still problems may occur, as the Green function derivatives show highly oscillating behaviour for the near history, as can be observed in figure 4.1. Especially for lower forward speeds and for source panels near the free surface, spatially resolving these oscillations becomes impossible within the current panel integration method and numerical errors may occur in the Green function derivatives computed on the free surface. This problem may be augmented in case the strengths of the panels that are close to the free surface evaluation point become large.

The spatial panel integrations are carried out by splitting the panel in sub-panels and computing the Green function memory influences and continuing splitting the sub-panels until the influences are converged. In the current code this is done in a maximum of 6 steps up to 144 sub-panels per panel. In most cases this is more than sufficient, however in above mentioned scenarios this is a limiting factor that was almost always observed when the computed wave profiles showed large irregularities.

In this section two ways of overcoming these numerical problems are studied. The first approach is to position the free surface evaluation points *on* the calm waterline and filtering undesired large influences. The filtering approach is as follows: when the distance between a (sub)panel centroid and the evaluation point, the radius R, becomes smaller than a pre-set threshold value R_{min} and the vertical distance $z_0+\zeta$ becomes smaller than another pre-set threshold value z_{min}, indicating that both points are located near the calm water surface, then

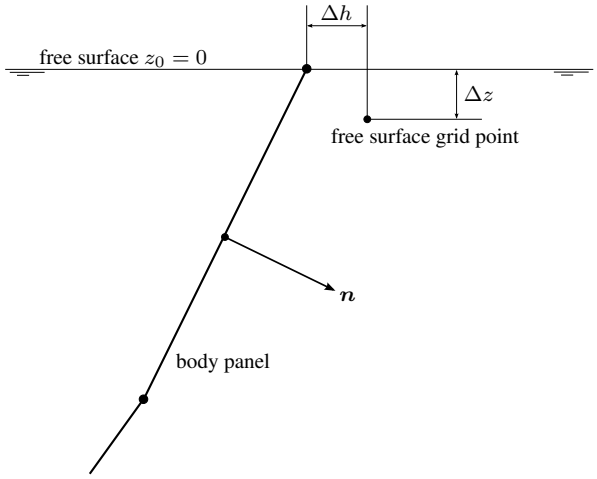


Figure 4.36: *Horizontal and vertical shift of free surface evaluation points, repeated from figure 3.9*

filtering is applied. This filtering is carried out by artificially enlarging the vertical distance $z_0 + \zeta$ prior to computing μ, β, and R for use in the Green function derivative computation. The artificial increase equals z_{min} when R is zero is smoothly reduced to 0 by using a cosine function when R approaches R_{min}.

The second approach is to shift the free surface evaluation point slightly downward with Δz and outward with Δh from the calm waterline as shown in figure 4.36. Now the chance of R becoming zero is next to impossible, as this could only happen when for some history time step the centroid of a sub-panel is located *exactly* on the free surface evaluation point, while also the chance that R becomes small for near history is smaller and the oscillations of the Green functions become less severe when moving away from the calm water surface. The drawback is of course that further down from the free surface the applicability of the free surface boundary condition to compute the elevation worsens, while at the same time moving horizontally away from the body the free surface profile is offset backwards with respect to the body and the wave height is lowered.

Both the shift and the filter thresholds are expressed in terms of the local panel diagonal. Typical values are:

- a fraction of the panel diagonal for Δz, Δh,
- a few panel diagonals for R_{min},
- and a fraction of the local panel diagonal for z_{min}.

A panel convergence study resulted in 980 below water panels. Using cosine refinement towards bow and stern showed slightly better results compared to constant length panels. The resulting panel mesh is depicted in figure 4.37. A relatively large time step corresponding to 2.5 panels forward travel each time step has been chosen with 100 history time steps to avoid truncation errors due to the oscillations in the Green function derivatives. These are relatively large due to the low forward speed of $Fn = 0.316$.

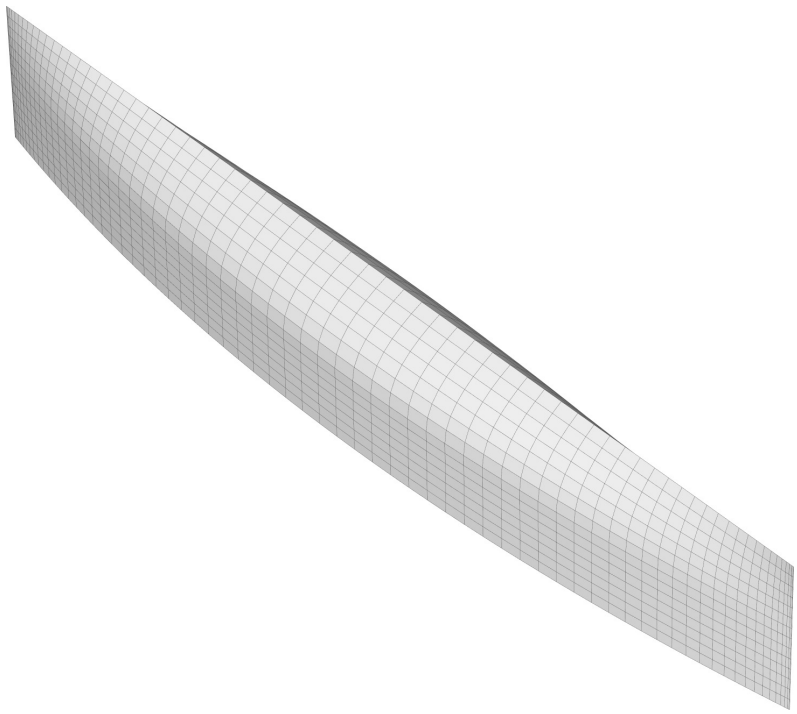


Figure 4.37: *Panel mesh of a Wigley with longitudinal cosine refinement, 980 below water panels*

Figures 4.38 and 4.39 show the wave profiles along the hull of the Wigley that are the result of the first approach. The strength of the filtering was increased by increasing the filtering distance R_{min} from 1 to 4 local panel diagonals, keeping z_{min} at a fixed value of 1 local panel diagonal. Figure 4.38 shows the resulting wave profiles for the Wigley with a constant longitudinal panel spacing and figure 4.39 shows the resulting wave profiles for the Wigley with panel spacing that was cosine refined towards the bow and stern, as depicted in figure 4.37.

Both figures indicate very similar behaviour. The bow wave is well predicted, especially considering the fact that the method applied a linearised free surface boundary condition. This will become even more clear further on in this section where the results of other potential flow methods are compared with the results presented here. Behind the bow wave a number of small oscillations can be observed in the predicted wave profiles compared to the experimental wave profile. In particular around the midship a sawtooth like appearance can be observed in the predicted wave profiles.

Although overall both panel meshes resulted in a very similar appearance of the wave profile, there was one main difference. When using a constant panel spacing the numerical instabilities along the central part of the waterline were gradually filtered to a smooth wave profile when R_{min} was set to 4 local panel diagonals, whereas by using a cosine spacing this did not happen. The reason behind this was that due to the cosine spacing and the fact the the filter radius R_{min} was set to 4 times the local (source) panel diagonal, the filter distance

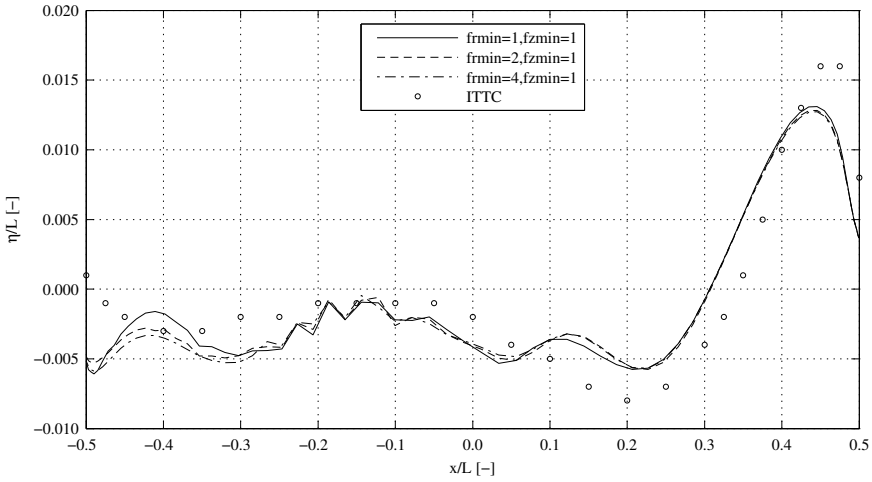


Figure 4.38: *Influence of Green function filtering on free surface profile, rectangular panel mesh*

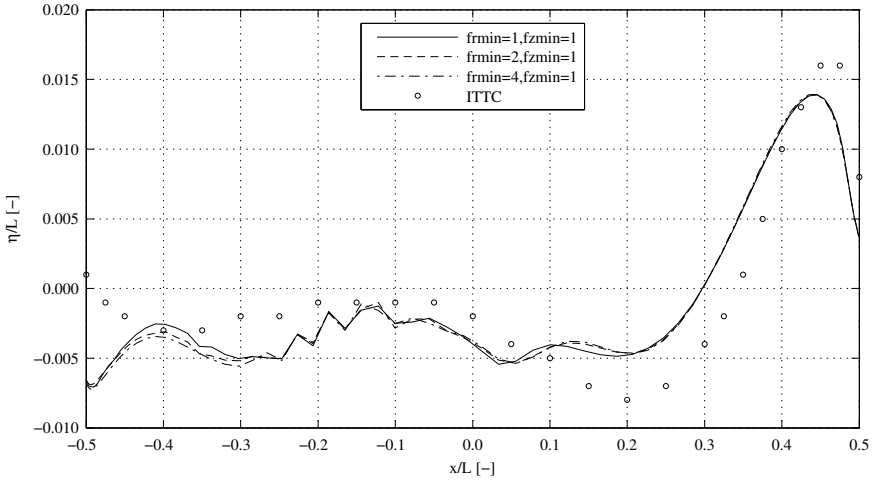


Figure 4.39: *Influence of Green function filtering on free surface profile, panel mesh with longitudinal cosine refinement*

-in a dimensional sense- became smaller when the source panel size decreased. The result was that the influence of the panels near the bow (and near the stern) was less filtered for the cosine refined mesh. Of course this 'problem' is easily solved by formulating the filter radius in a different way, that is not dependent on the local panel size.

Nevertheless, this provides a clue to what the main source is of the small oscillations in the wave profile. Apparently these are mainly caused by the memory effects of the relatively strong bow panels, especially those that are located near the waterline. Along the simulation time their memory effects pass by all the other panels, influencing the local wave height due to truncation errors in the panel integration that appear when the horizontal distance and the submergence is relatively small. Their effect is further magnified when the source panel strength is large, for instance for panels in the bow area. Making sure that the influences of these panels are sufficiently filtered, results in a smooth estimated wave profile along the hull.

The second approach to suppress irregularities in the wave profile due to the free surface memory effect integrations was by shifting the free surface collocation points downward into the fluid and outward, away from the body panels. To investigate this systematically, the free surface collocation points were shifted from the calm waterline on a line at 45 degrees downward and outward from the body from one panel diagonal to 0.01 times the panel diagonal and for each of these shifts the wave profile was computed. No other filtering procedure was applied. Typically the free surface points were chosen at the waterline vertically above the closest hull panel collocation point. This procedure is schematically depicted in figure 4.40.

The resulting wave profiles are depicted in figure 4.41 for the panel mesh with cosine spacing towards stern and bow. The results with regular panel spacing are not shown as they present a nearly identical picture. It can be concluded that the method is successful in suppressing the irregularities that appeared in the previous approach, except for the case that the shift equals less than 0.1 times the panel diagonal, where some disturbances (in the form of small oscillations) are present.

When moving the free surface points further away from the body and deeper into the fluid the wave height of the bow wave diminishes. The location of the wave peaks at the bow, at 15% behind amidships and at the stern seems to unaffected by the shift for values until one panel diagonal and are predicted reasonably well, albeit delayed with respect to the experiments. This delay equals about 10% of the ship's length for the first wave through behind the bow wave and the subsequent wave peak and reduces a few percent when the free surface points are moved closer to the body and free surface.

In this particular case the shifts of 10% to 20% of the panel diameter seem to yield the best results. Virtually no oscillatory disturbances are present while sacrificing only a relatively small amount of the bow wave height. At the largest shift of one panel diameter the stagnation pressure near bow and stern become visible. This is due to the cosine refinement and is not visible when using regular panel sizes instead of cosine refinement. Compared to the previous approach, using a filter procedure, the current approach using a simple shift of the free surface grid points seems to be more successful in obtaining a reasonable wave profile along the hull without oscillatory disturbances due to numerical difficulties.

Another, more efficient, approach to compute the free surface deformation along the waterline is to use the information already available at the collocation points of the body panel adjacent to the waterline. This does not require the definition of separate free surface collocation points and avoids the additional computation of induced velocities and potentials on the free

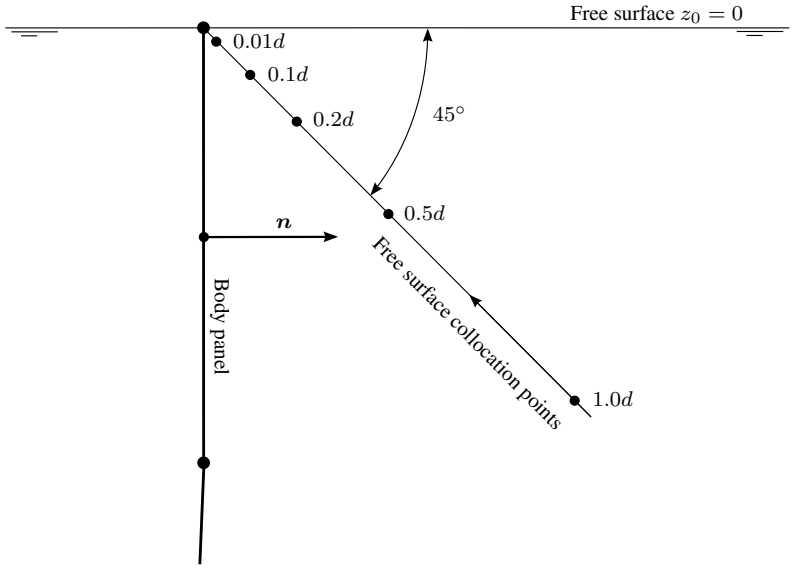


Figure 4.40: *Diagonal shift free surface grid points*

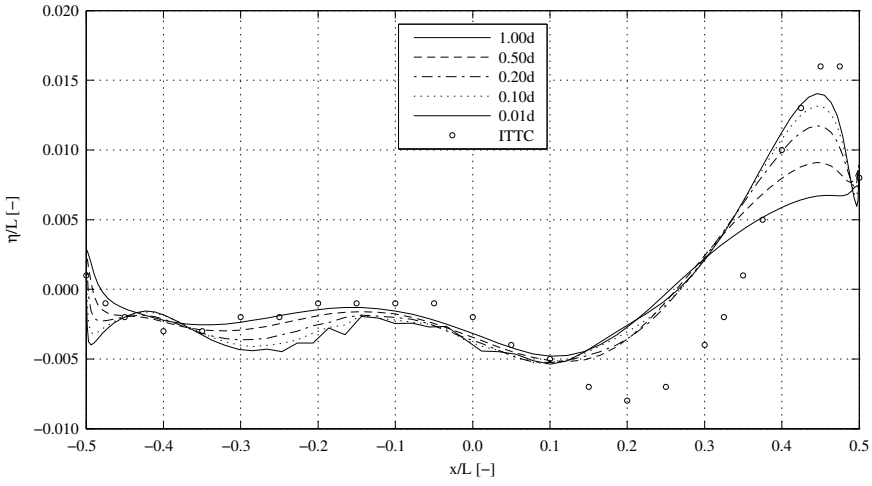


Figure 4.41: *Influence of diagonal free surface grid point shift on free surface profile, panel mesh with longitudinal cosine refinement*

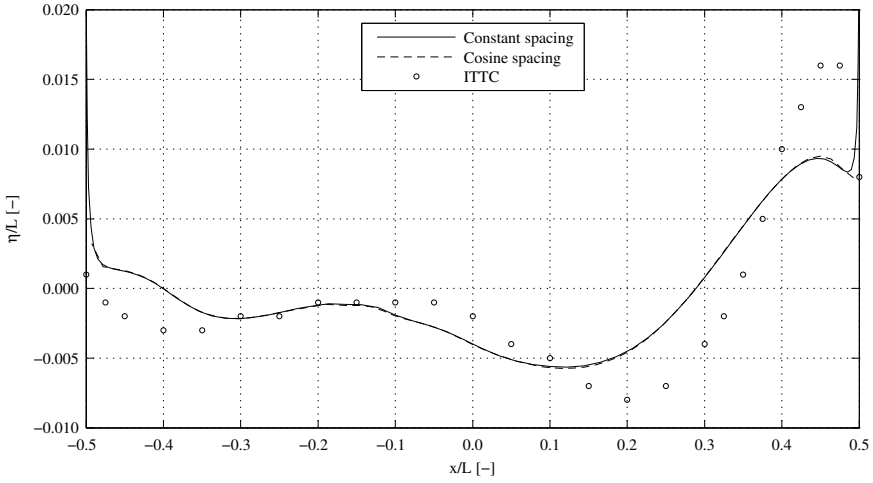


Figure 4.42: *Computation free surface profile on collocation points of upper panel row*

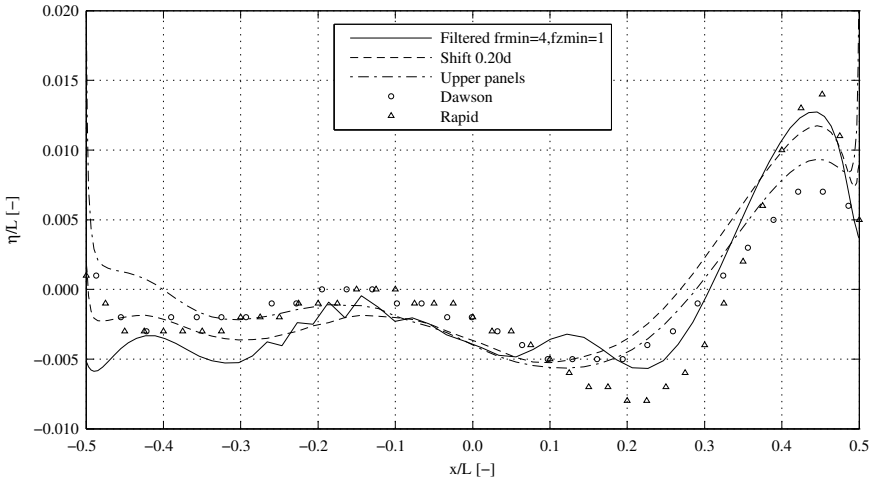


Figure 4.43: *Comparison of the free surface profile computed by different methods*

surface grid points. The drawback is again that the free surface boundary condition is not computed exactly on the calm water free surface but instead at some distance below it. The advantages are a stable solution without additional numerical difficulties and fast evaluation while reducing the computer memory requirements and run time as no new information is needed to compute the free surface elevation.

Figure 4.42 shows two wave profiles computed in this way, on for the panel mesh using cosine refinement towards the bow and stern and one using a constant panel size. The lines are nearly identical, the only difference being the stagnation pressure near the bow and stern that can be observed in the computations with the refinement mesh but are absent in the computation with the regular mesh. Not very surprisingly the results show close agreement with the results where the free surface grid points are submerged at one half and one panel diameter in figure 4.41, with a reduced bow wave height and the location of the subsequent wave through and peak is predicted about 10% of the length of the ship too far aft.

Finally, the wave profile computed with each of the three approaches presented above (free surface elevation computed at free surface grid points with either (1) filtering or (2) a shift applied, and (3) free surface elevation computed at upper panel row) is compared to results obtained with the Dawson method (Dawson 1977), a double body flow method with a linearised free surface boundary condition, and with Rapid (Raven 1996), an iterative potential flow method using a double body basis flow with non-linear free surface boundary conditions in figure 4.43. Both methods are Rankine panel methods with panels distributed over the body and a part of the free surface. The results for Dawson were computed specifically for this comparison, whereas the results of Rapid were taken from the work of Raven (1996).

For clarity the ITTC experimental results are not included in the figure, but as can be seen in Raven (1996) and by comparison with the previous figures and the current figure the hull wave profile computed with Rapid is in near perfect agreement with the results of the ITTC experiments. The Dawson results, that lack some significant digits in the output values due to the old implementation that was available, significantly under-predicts the bow wave and the subsequent trough yet following the Rapid results closely for the aft half of the body.

Studying the wave profiles computed with the method presented in this thesis the following can be observed:

1. The wave profile computed using the information at the upper body panel collocation points shows a very similar behaviour to the results computed with the Dawson method, with a under-predicted bow wave and subsequent trough. There are some deviations in the aft part.
2. The other two approaches (filtering or shifting the free surface points) predict the bow wave height better, but perform worse for the remaining part.
3. The approach employing a diagonal shift to the free surface grid points shows a more consistent wave profile with almost no oscillatory disturbances or additional short waves.
4. On the other hand, the approach employing filtering shows a closer agreement, especially at the bow. But at the same time seems to contain additional short waves, possibly caused by the filtering procedure itself, although the oscillatory disturbances are successfully eliminated.

The predictions using the Green function method of this thesis seem to suffer especially in the aft half of the body. The Wigley shape may be an important factor, as its shape means that

the body at the past time locations passes through the body at the current time instance. This means that the chance that panels (history and current time) are located close to each other is relatively large and may occur in a relative large part of the history time frame. Added to this, the relatively low forward speed and associated large Green function oscillations may increase the numerical difficulties. Nevertheless, the prediction of the bow wave is better than that using the Dawson method. This is a surprise, as both methods use a very similar free surface linearisation.

4.5.2 Wave profile of a high speed ship

Based on the previous section it is difficult to choose the right method to obtain the free surface wave around a ship making use of the computational method presented here. Evaluating the influence functions on the free surface makes filtering or grid point displacement necessary to avoid large numerical oscillatory disturbances due to the difficulties of the numerical integration of the Green function derivatives for field and source points that are located close to each other and to the free surface. Using the influence functions of the hull panels adjacent to the calm water free surface gives much more robust results (denoted 'upper panels' in figure 4.43), that are less accurate than the previous method but still they are close to the results of the Dawson method. Another advantage that this second approach does not result in additional computational time or memory requirements as it makes use of influence functions that are already available.

Evaluating the free surface elevation on the upper panel row has however a drawback when the forward speed of the ship increases. This increase causes high pressure regions to be formed around the forward part of the waterline, as long as the waterline width increases along the length. Figure 4.35 shows these high pressure regions clearly on a wedge that is run at a high forward speed. The collocation points of the upper panels are generally located within the region of high pressure, leading to a over-estimation of the free surface wave at their location. This over-estimation increases with forward speed, due to increase in the stagnation pressure.

An indication of this over-estimation is given in figure 4.44 for a 55 metre high speed vessel sailing in calm water. The figure shows the wave profile along the waterline for two approaches. The first approach computes the free surface on a free surface grid, but with a displacement of 10% of the local panel diameter away from the body and the free surface. The second approach makes use of the upper body panels. For both approaches the ship was fixed in the same reference position. Already at a relatively low forward speed of 25 knots (Froude number 0.55) a significant difference is visible in the forward part of the ship for both approaches.

As noted in the previous section the wave elevation along the aft body of the Wigley was in all probability affected by the fact that past time instances of the body passed through the waterline of the aft body. For the high speed ship, with a nearly prismatic aft body, this is not the case and less numerical disturbances are present in the predicted free surface profile.

Figure 4.45 shows for the same situation a represention of the computed free surface elevation on a free surface grid around the vessel. At the stern an interesting feature is visible. The free surface computation has been performed applying the transom flow condition at the transom edge (with wake sheet extending aft from the transom). Yet, the free surface does not match

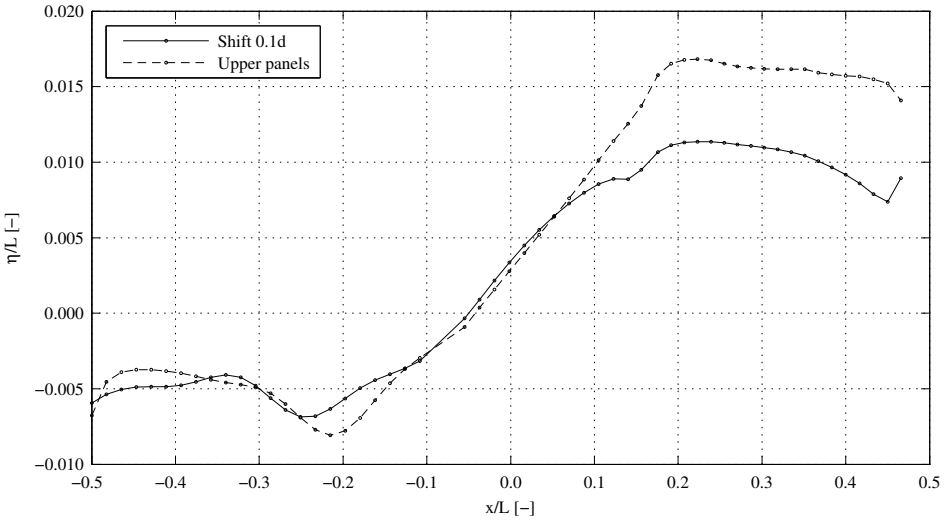


Figure 4.44: *Computed free surface profile for 55 metre fast vessel sailing at 25 knots using two different approaches*

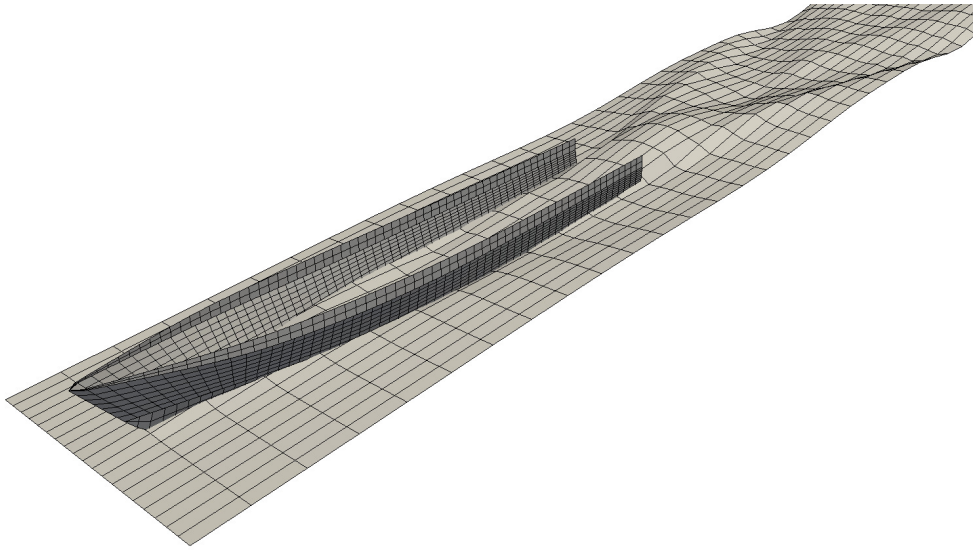


Figure 4.45: *Representation of the computed wave elevation due to a 55 metre fast vessel sailing at 25 knots (Froude number 0.55) in calm water using a crude grid on the free surface*

the transom edge; apparently the influence of the transom flow condition is not 'felt' at the free surface above it.

4.6 Convergence study for seakeeping computations

This section descibes a convergence study aimed at quantifying the influence of panel refinement, time step size, and memory truncation for the practical application for determining the seakeeping behaviour of a high speed ship. The Enlarged Ship Concept that was introduced in chapter 2 was used in this study. The following chapter will present validation computations where the computational method is applied to this same ship and the closely related Axe Bow Concept. Applying the lessons learnt in this section ensured sufficiently converged results were obtained during the validation computations.

To complete this study, computations were performed with a panel representation of the Enlarged Ship Concept both in calm water and in regular waves. In the calm water computations the ship was kept fixed at its reference position and the convergence of the horizontal and vertical forces, and the pitch moment was investigated. In the regular wave computations the ship was allowed to heave and pitch, and the response amplitudes and phase angles of the heave and pitch motions were investigated. The convergence study in regular waves was added to ensure that the inclusion of waves and motions did not detoriate the convergence of the computations.

The calm water convergence study was performed for the following range of parameters:

- Three forward speeds: 25, 35, and 50 knots; Froude numbers 0.55, 0.77, and 1.10.
- Two discretisations:
    1. Source-only panels with an empirical transom flow model.
    2. Source-doublet panels with the pressure based transom flow model.
- A range of time step sizes from 0.01 seconds to 0.40 seconds with a constant number of time steps of 100 before memory length truncation.
- A range of number of submerged panels, expressed as the number of transverse panel strips over the length of the geometry, from 20 to 70 strips.

The convergence behaviour in calm water was studied by plotting the relative error ε (with respect to the converged value) for the heave force, the surge force (resistance), and the pitching moment on the number of panels N and memory effect truncation length L_{hist}/L made dimensionless with the ship length. A logarithmic scale is used for the horizontal axis. The converged values were taken equal to the values at the largest number of panels or the largest truncation length computed, resulting in a a relative error of 0 at the largest number of panels and truncation length.

Meshes were generated using 20 to 70 transverse panel strips over the length of the ship, resulting in 128 to 1226 panels on the entire hull. In the previous chapter, it was already demonstrated that the steady hydromechanic forces are insensitive to the magnitude of the time step, providing that the memory length truncation -measured in time and not in the number of time steps- is kept constant, while the magnitude of the time step is kept reasonable. This enables the memory effect truncation to be studied by solely changing the time

step size, while keeping the number of time steps before the memory effects are truncated constant. This kept the computer memory requirements, as well as the computational time, constant.

A selection of the results of these computations are depicted in figure 4.46, presenting the worst case scenario in terms of convergence. This worst case scenario was encountered at the medium forward speed of 35 knots (Froude number 0.77), while applying the source-doublet discretisation with transom flow condition.

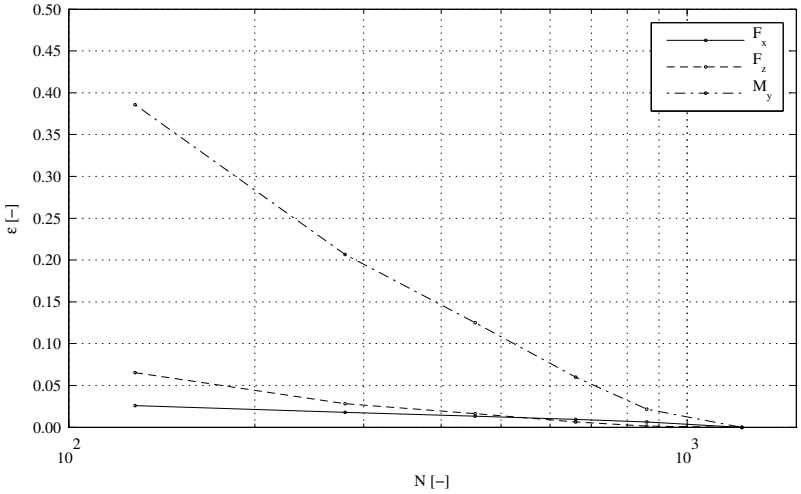
Based on the top figure, showing the convergence of the forces based on the number of submerged panel strips, the pitching moment (defined with respect to the centre of gravity) seems to converge slower than the two forces. At 60 longitudinal panel strips, resulting in 800 to 900 panels on the submerged geometry, both forces differ less than 1 percent of the converged value. The slower convergence of the pitching moment may have been caused by the fact that the magnitude of the pitching moment with respect to the center of gravity was relatively small and built up of relatively larger but opposite hydrostatic and hydrodynamic components. The fact that the convergence in terms of number of panels was worst when using source-doublet panels instead of plain source panels, may be attributed to the dependence of the transom flow condition on the near transom panel discretisation. This problem was already discussed in section 4.4 of this thesis.

The memory truncation convergence, depicted in figure 4.46(b), shows a satisfactory convergent behaviour. The magnitude of the memory length is determined by the time step times the number of history time steps. The time step in turn is determined by a number of factors. First of all it seems very logical to choose the time step in such way that the ship travels a distance equal to its characteristic panel size during each time step. This results in wake panels that are of similar size as the body panels, resulting in a wake strength discretisation that is of the same order as the body discretisation, while the distance between past time geometries is of the same order as the panel size as well. For steady problems, where the wake strength becomes independent of the time, as have been studied in the previous chapter, this is of minor importance, for unsteady problems however this does become important.

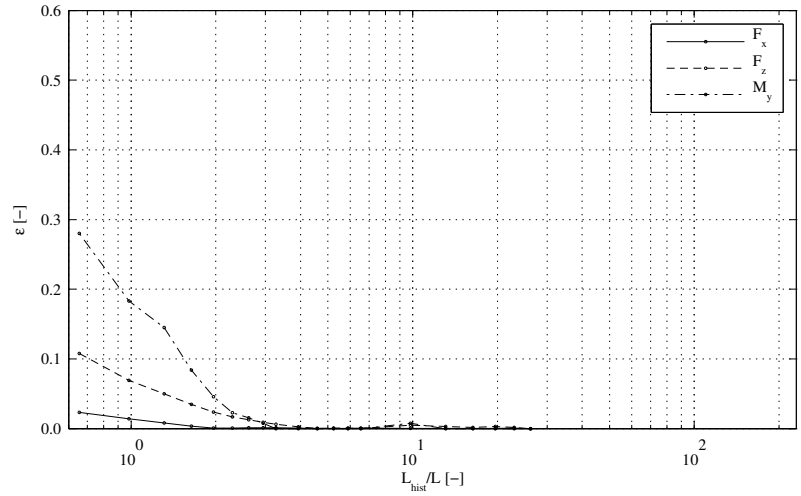
The second factor influencing the choice for the time step is the aforementioned length of the memory effects and wake sheet before truncation. These lengths are determined by the number of history time steps and wake sheet panel rows multiplied with the time step. Minimum lengths have been discussed in section 4.2.4, other factors are the required computer memory and computational time. For the case presented here, a geometry with 60 panel rows at Froude number 0.77, this results in a time step of 0.054 seconds. Using 100 history time steps, figure 4.46(b) shows that the horizontal and vertical forces, and pitching moment are within 1 percent of the converged value.

Whereas the convergence study in calm water is sufficient for checking the convergence of the influence (Green) functions, motions and waves may cause variations of the singularity strengths. These variations may lead to different convergence behaviour and only requiring the influence functions to converge may not be enough to ensure numerical convergence for the hydrodynamic solution. Moreover, it is necessary to require a minimum number of panels to describe a wave length; typically minimal 7 panels per wave length are chosen.

Figure 4.47 presents the dependence on the number of panels of the relative error ε of the heave and pitch motion responses (RAOs) and phase angles for the ESC. The ship was free to heave and pitch while sailing with a forward speed of 25 knots in regular head waves.

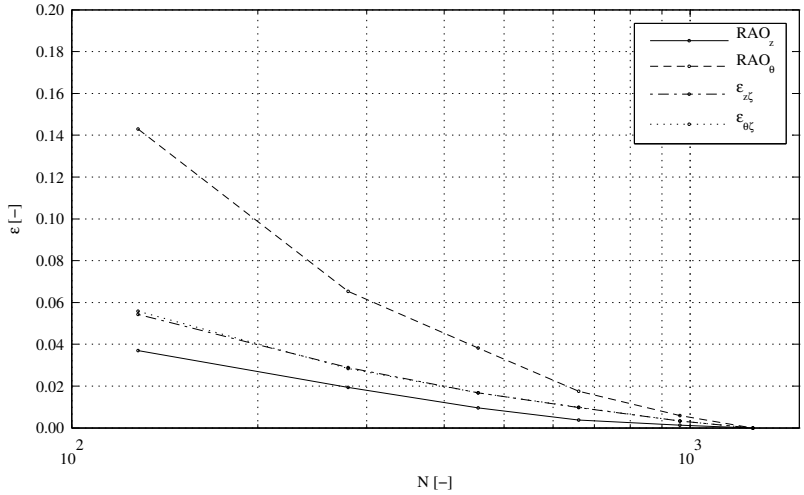


(a) Influence number of panels

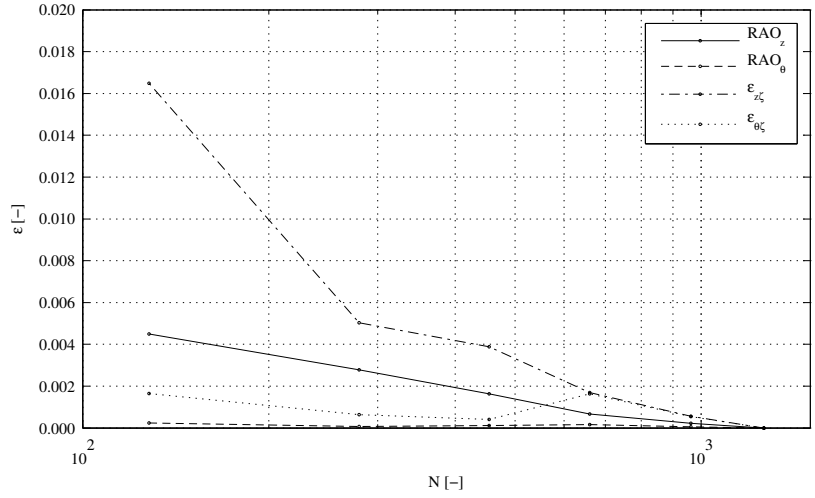


(b) Influence memory effect truncation length

Figure 4.46: *Convergence of the steady total vertical and horizontal force, and pitching moment*



(a) $\omega = 0.80\, rad/s$



(b) $\omega = 1.30\, rad/s$

Figure 4.47: *Influence number of panels on convergence of the heave and pitch responses in phase angles in regular waves*

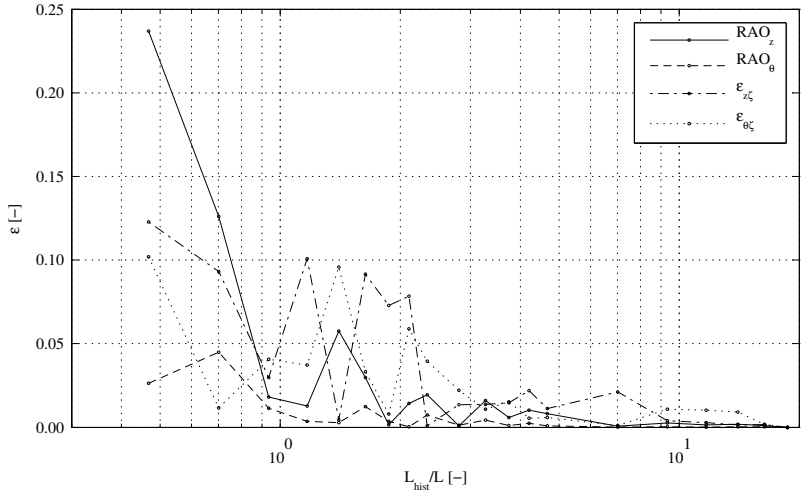
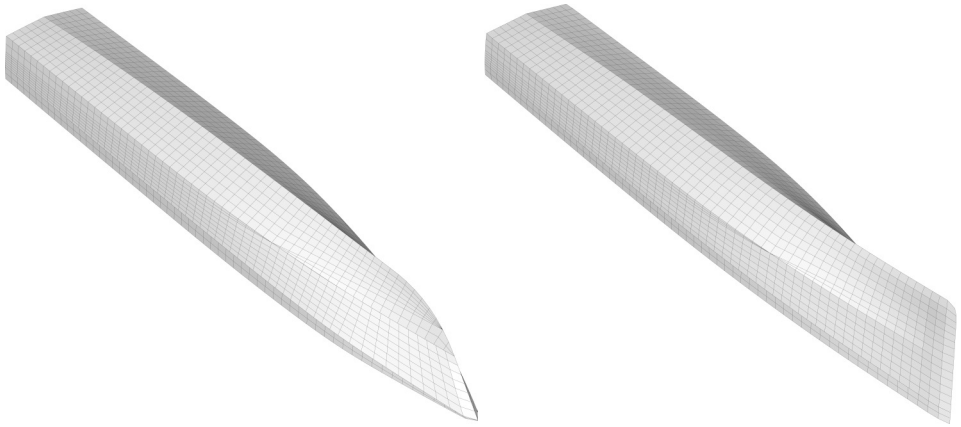


Figure 4.48: *Influence memory effect truncation length on convergence of the heave and pitch responses in phase angles in regular waves*



(a) Enlarged Ship Concept (b) Axe Bow Concept

Figure 4.49: *Panel meshes of Enlarged Ship Concept and Axe Bow Concept, both consisting of 60 longitudinal panel strips yielding about 900 below water panels*

The convergence is expressed as the relative error with respect to the converged value made dimensionless with 1 for the response amplitude operators and with 2π for the phase angles. Figure 4.47(a) shows the convergence on the number of panels for a wave frequency of 0.8 rad/s, in the resonance region of the ship motions. Figure 4.47(b) shows the convergence for a wave frequency of 1.3 rad/s, the minimum wave length that was studied in the validation presented in the next chapter. The wave height was set to one meter in both cases.

The relative error of the RAOs at the higher wave frequency is much smaller than at the lower wave frequency. This is caused by the very small values of the RAO and their differences at the higher wave frequency. The convergence behaviour is very comparable to the convergence of the forces in calm water on the number of panels shown before. Based on these figures a choice for 900 panels or more on the wetted surface seems to yield sufficiently converged results.

Figure 4.48 shows the dependence on the memory effect trunction length of the same relative error of the heave and pitch RAOs and phase angles in the same circumstances for a wave frequency of 0.8 rad/s. This particular study has been performed in the same way as for the calm water case, by adapting the time step between 0.01 and 0.40 seconds. The result of this simple approach is, to some extent, a more confused behaviour, especially for the phase angles. The most likely cause of this behaviour seems to be the fact that changing the time step does not only affect the truncation length, but also influences the time resolution of the unsteady behaviour. Nevertheless, the figure shows that for truncation lengths corresponding to about 2 ship lengths or higher, the results are sufficiently converged.

The final panel geometries of the Enlarged Ship Concept and the Axe Bow Concept are depicted in figure 4.49 and were used in the remaining validation computations in this chapter. All computations were carried out on a quad core Intel® Xeon® CPU running at 2.33 GHz with 4 GiB of memory. An indication of the calculation time can be given as follows. For a model consisting of 900 panels 2 seconds runtime were needed per time step, with a time step of 0.08 seconds this resulted in 25 seconds computational time for 1 second real time. This number is dependent on the amount of panels used (900 in this case), time step size (0.08 seconds in this case), forward speed (Froude number 0.55 in this case), and length of the memory effects included in the computations (100 steps in this case). Under these circumstances, a full irregular simulation of 30 minutes real time will take 12.5 hours to complete.

4.7 Discussion

The first part of this chapter dealt with the verification of the numerical computation and approximation of the Green function derivatives for determining the potential flow panel influence fuctions. The evaluation of these derivatives is performed in the computational method by combining two methods: series approximation and interpolation of pre-computed generalised Green function tables. In sections 4.2.1 the workings of both methods were detailed and their numerical implementation was successfully verified by comparing the values of the principal derivatives computed by table interpolation, series interpolation, and direct numerical evaluation.

The next part considered the verification of the implementation of the Rankine and biplane parts (section 4.2.2) by checking the zero and infinite Froude number limits of the

induced velocities for a single panel submerged close to the free surface (section 4.2.3). With this the verification of the kernel of the implementation, the computation of the influence functions, is successfully completed; i.e. the core of the implementation of the method may be assumed to be correct and an idea of the correct usage of the core is obtained. In addition, the truncation of the free surface memory integrals was studied (section 4.2.4) and general guidelines for the truncation time of these integrals were presented in the chapter.

The application of the method to simple problems with known solutions (section 4.3) was performed in order to study the implementation of the computational method in a broader sense; forming the start of a validation process. First the method was applied to a deeply submerged infinite aspect ratio foil. The resulting pressures and forces were compared to the outcome of a well-accepted two-dimensional potential flow solver, with successful results. Next, the method was applied to a finite aspect ratio foil proceeding at constant forward speed near the free surface and compared to published results of measurements. This comparison showed good results for the pressure distribution, free surface effect on the lift and drag and the zero lift angle. With this, the method was successfully applied to simple problems with and without free surface influences.

Next, the attention was turned toward the numerical study of the extensions of the basic method. First, in section 4.4, a study was performed on the implementation of the transom flow condition, proposed in chapter 3. This study was completed by considering a fixed wedge proceeding at high forward speeds and comparing to the outcome of an empirical method by Savitsky (1964). The proposed transom flow condition performed slightly better than a simple empirical near-transom pressure correction method and both provide a significant improvement over the original computational method without transom flow model.

Although the transom flow condition is better embedded into the solution than adapting the pressure distribution with an empirical near-transom pressure correction, it was shown to suffer from grid dependence when continuous refining the panels towards the transom edge. At this point it is unclear how to resolve this grid dependence. It may be caused by still missing some physical aspects of the flow leaving the transom and the condition may need to be adapted in the future. One possibility may be to study the flow lines of the flow past the transom and to pose conditions on their curvature as has been proposed by several authors (Raven 1996), although the linearisation of the free surface boundary condition may pose difficulties for such an approach.

Other improvements in the computation of the vertical force and its attachment point can possibly be found in providing flow conditions on the waterline and hard chines. Again the free surface linearisation may, however, also prevent a successful implementation of these improvements.

In section 4.5, the free surface elevation along the hull due to the steady forward speed was considered for a relatively slow Wigley hull and for a fast vessel. Two approaches for the computation of the free surface elevation were discussed. The first was using a free surface grid to evaluate the influence functions on, the second was simply using the flow information already known on the hull panels adjacent to the calm water free surface.

The first approach was shown to have some difficulties with the accurate evaluation of the Green function derivatives causing oscillatory disturbances in the computed free surface. These disturbances could be removed by either filtering or by placing the free surface grid points a short distance away from the hull panels and the free surface. The second approach

did not have these difficulties and was more computational efficient, but however less accurate. Moreover when applied to high speed ships, the second approach caused a large over-estimation of the free surface elevation in the fore part of the waterline due to the large stagnation pressures.

The final section dealt with convergence with respect to the number of panels and the time step and memory effect truncation length of the computational method applied to a high speed ship. First, the study was focused at the body fixed in its reference position in calm water at a number of forward speeds. Convergence of the computed forces is found for panel geometries with 60 panels along their length and for time step sizes equivalent to time the ship under consideration takes to travel a distance equal to one panel length, while using 100 history and wake time steps.

Finally, a convergence study was carried out in regular waves, as convergence in calm water may not be sufficient to ensure convergence for unsteady (wave and motion) problems. It was demonstrated that convergence of results as RAOs and relative phase angles on the number of panels and the truncation length was achieved under comparable conditions in terms of number of panels and truncation length.

Chapter 5
Validation

5.1 Introduction

After completion of the verification of the computation of the influence functions, a limited validation using simple problems, and the study of computational details, such as the transom flow modelling and free surface elevation in chapter 4, chapter 5 continues with describing the validation stage for calm water and full seakeeping simulations, with the ship being free to perform motions. The validation study was setup using the results of the convergence study presented in section 4.6 as a guideline.

The validation of the computational method, developed in chapter 3 and detailed in chapter 4, was performed by using the results of the towing tank experiments presented in chapter 2. Part of these results were obtained during the FAST I research project, in particular the calm water results and the results of the experiments in irregular seas. The experiments in regular head waves were especially performed for the validation presented here. The validation was completed using for two design concepts, already introduced previously, the Enlarged Ship Concept and the Axe Bow Concept. Their main dimensions are presented once again in table 5.1.

Table 5.1: *Main particulars FAST conceptual designs*

Quantity	**Symbol**	**Unit**	**ESC**	**ABC**
Length waterline	L_{wl}	m	55.00	55.00
Beam on waterline	B_{wl}	m	8.46	8.46
Maximum draft	T_{max}	m	2.66	4.39
Baseline draft	T_{base}	m	2.66	2.42
Volume of displacement	∇	m^3	516.00	517.40
Wetted area	S	m^2	480.58	512.84
Vertical position CoG	KG	m	3.85	3.53
Longitudinal position CoG[a]	LCG	m	22.49	24.36
Metacentre height	GM	m	1.52	1.52
Pitch radius of gyration	k_{yy}	m	13.75	13.75

[a] The longitudinal position of the centre of gravity is defined with respect to the aft perpendicular.

Although the computational model is capable of dealing with full six degrees of freedom

simulations in waves, the discussion in this chapter will be focused on the seakeeping behaviour in head waves. Particularly the behaviour in head waves is often seen as the most determining for the safety, operability and crew and passenger comfort aboard high speed vessels. As pointed out in chapter 2, also the behaviour of high speed vessels in following and stern quartering seas are of great importance for the safety of these vessels, in particular the occurrence of bow diving and broaching. The validation of the code for stern-quartering and following waves is currently ongoing and the first results are reported by Van Walree and De Jong (2008) and Van Walree and Carette (2010).

The validation process was performed in a stepwise fashion. First, calm water computations were performed (section 5.2) in order to find the trim and sinkage reference positions of both design concepts at constant forward speed. Second, simulations were performed in regular head waves (section 5.3). These two steps were aimed at testing the influence of the various input parameters and the influence extensions to basic method, such as the transom flow condition and pressure stretching, to select the most appropiate combination of parameters and extensions. The parameters and extensions that were investigated are:

- Empirical coefficients, such as the viscous cross flow drag coefficient (section 3.8.2).
- Transom flow modelling (sections 3.6.3 and 4.4).
- Free surface elevation and subsequent pressure modification (sections 3.7 and 4.5).
- Time-dependent added mass (section 3.7).

The third step was to apply the lessons drawn from the previous steps, in particular from the computations in regular head waves, to the validation study of both design concepts in irregular head waves (section 5.4). The final steps form the true validation of the seakeeping method for applications in head waves.

The main goal of this chapter is to evaluate whether the computational method presented in this thesis is able to adequately describe and predict the seakeeping behaviour of high speed vessels in waves; and whether it is possible to distinguish the seakeeping behaviour of both design concepts, ESC and ABC, using the results of the computational model. These topics will be discussed in detail in section 5.5.

A similar study, but much more limited in scope, has been published earlier by De Jong and Van Walree (2009). That study did not include computations in regular head waves and the comparison of the data was less complete. Due to the addition of the regular head waves more insight was gained in which parameters settings and extensions were resulting in better results. This better insight led to more favourable results of the comparison with experimental data, compared to the previous study in De Jong and Van Walree (2009).

The experimental data presented in the graphs of this chapter is accompanied by 95% confidence bounds. The determination of these confidence bounds is detailed in appendix D.

5.2 Calm water trim and sinkage

Although it is not the main goal of the computational model to accurately predict the trim and sinkage, it is important to investigate the trim and sinkage prediction for a number of reasons. First of all, a good prediction of trim and sinkage (and rise) may indicate that

the computational model successfully captures the calm water behaviour and the developed pressure distribution under the hull of the vessel. Second, the trim and rise at forward speed may introduce a relatively large change in submerged geometry. This change may cause a significantly different motion behaviour of the vessel in waves, making correct prediction of sinkage and trim paramount.

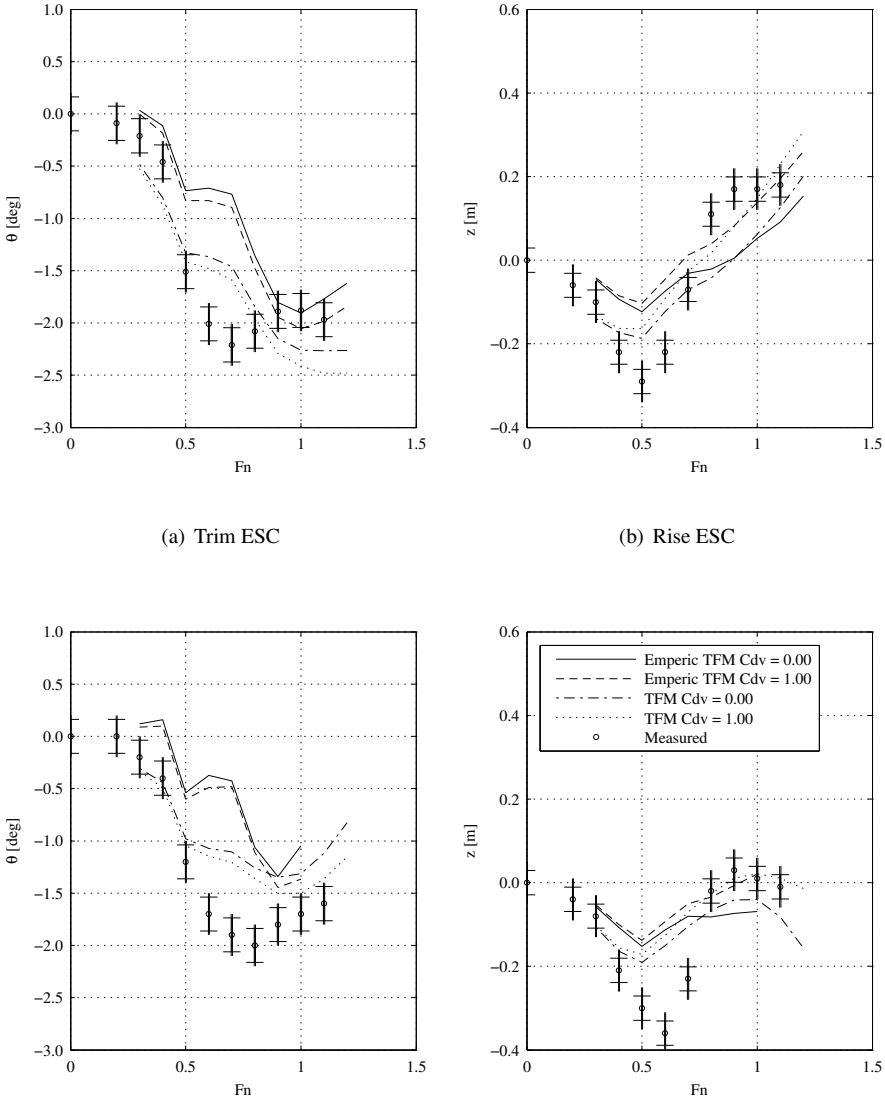
In body-linear seakeeping computations the forward speed dependent trim and sinkage may result in significant different submerged geometries with respect to the zero speed hydrostatic balance. This is of importance especially for high speed ships, that experience a relatively large forward speed dependent trim and sinkage due to the large dynamic pressures developed on the hull. The difference between zero-speed and forward speed reference positions and resulting geometries may have significant influence on the results of the seakeeping analysis. This problem is of course limited to the body-linear approach; in the body-exact approach it is automatically taken care of during simulation.

The calm water trim and sinkage -or for high speed ships rise- are defined respectively as the steady rotation about the body-fixed y-axis and the vertical displacement at the centre of gravity. In the computational model the trim and sinkage were determined in an iterative fashion; subsequent calm water runs were performed and the final orientation of the ship of each run was used to adapt the panel geometry input for the next run, until convergence was reached. Convergence criteria were based on the input trim and sinkage being close enough to the output trim and sinkage of one run, and were typically set to 0.1 degree for the trim and 1 percent of the draft for the rise.

To speed up the iterative process, the trim and sinkage used as input for the new iteration cycle were determined taking the average of the previous two iterations. Typically up to 4 iterative steps were necessary to obtain trim and sinkage values that were within the above stated convergence criteria. The iterative process was performed for a series of forward speeds and the converged trim and sinkage of the previous forward speed was used as first estimator for the next forward speed.

Figure 5.1 presents a comparison of the measured and computed trim and sinkage for the Enlarged Ship Concept (top) and the Axe Bow Concept (bottom). To investigate the influence of the transom flow model on the predicted trim and sinkage, computations were performed with two different panel discretisations: one with source-only panels applying the empirical near-transom pressure correction to take into account transom flow, and one with source-doublet panels with wake sheet applying the transom flow pressure condition at the transom edge. Furthermore, the influence of the empirical cross flow drag was taken into account by performing computations with both panel models for two different values of the cross flow drag, 0.00 and 1.00.

The figures show that the cross flow drag tends to increase both the trim angle (a negative trim angle means bow up) and the rise. The effect grows stronger with increasing forward speed. The force due to the cross flow drag is based on the vertical component of the local relative flow velocity with respect to the ship surface and points in the same direction (refer to section 3.8). Especially near the bow, the relative flow velocities are strong and directed outward and upward and tend to increase with forward speed. This is in accordance with the two-dimensional wedge analogy so often used for high speed ships and bow impact in waves. The result is an additional trimming moment and a net force acting upward.



(a) Trim ESC

(b) Rise ESC

(c) Trim ABC

(d) Rise ABC

Figure 5.1: *Comparison running trim and rise for Enlarged Ship Concept (top) and Axe Bow Concept (bottom)*

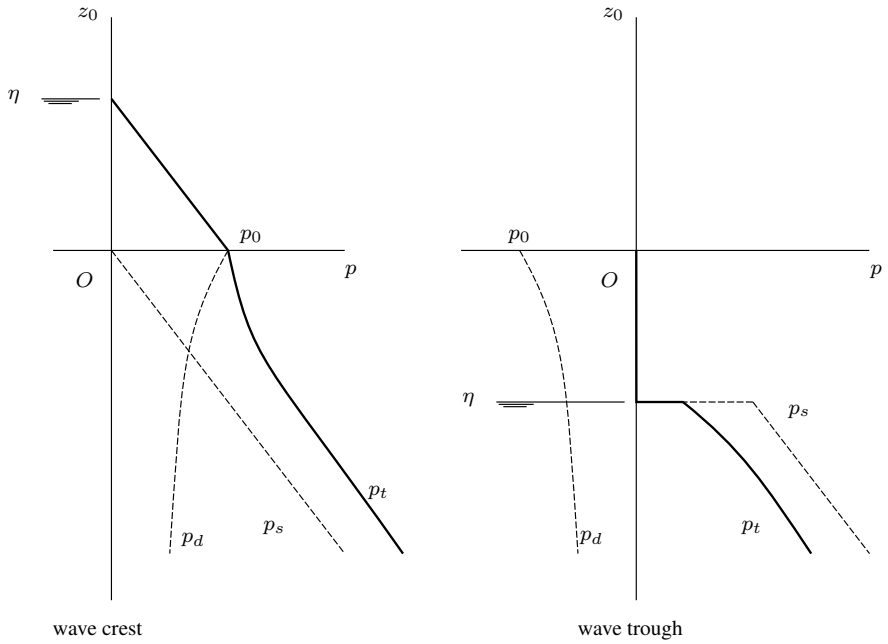


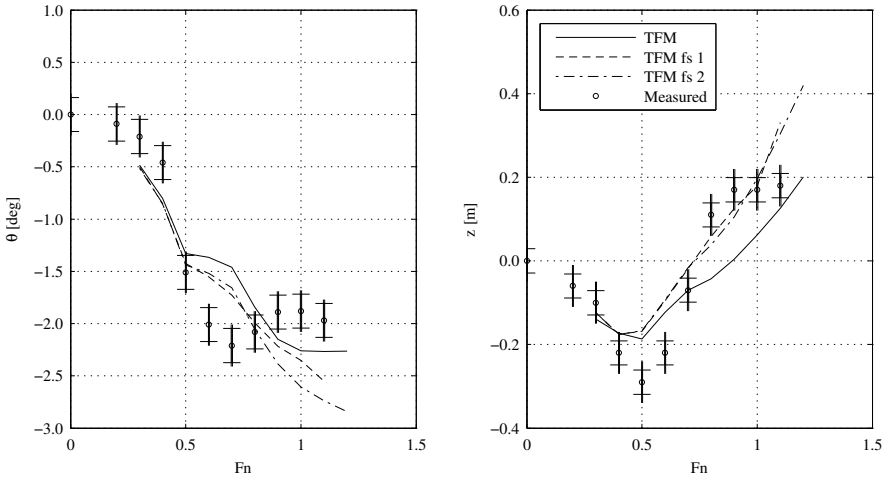
Figure 5.2: *Vertical pressure distribution for alternative method, wave crest - left, wave trough - right*

The usage of the transom flow condition increases the magnitude of the trim angle even further and smooths the relation between trim angle and Froude number significantly, particularly around a Froude number of 0.5 for the Axe Bow Concept. The effect on the rise is less pronounced, but for both concepts and for both the trim and the rise the results are improved in comparison to the plain source distribution with the empirical near-transom pressure correction.

For both design concepts generally the trim angle in the speed range between Froude 0.5 and 1.0 is under-estimated. For both concepts in this range the measured trim angle shows a clear maximum that is not present in the computed results. The rise is estimated closer, however the peak in the initial sinkage around Froude 0.5 is in all cases also under-estimated. Nevertheless, the method seems to be able to capture at least part of the differences between both design concepts. It does predict a smaller (negative) trim angle and no (positive) rise for the Axe Bow and a significant rise (nearly 10 percent of the draft) for the Enlarged Ship Concept at high forward speeds.

To investigate the effect of the free surface disturbance by the steady wave system of the ship at forward speed a number of additional computations were performed. In these computations the free surface disturbance was computed using the method outlined in section 3.7.3 and the pressure was modified in two different ways using the computed free surface elevation:

1. Using the stretching method (section 3.7.6, figure 3.11).
2. Using an alternative method where the pressure on the linearised submerged body surface was set to zero where it emerged above the disturbed free surface and a linear



(a) Trim ESC (b) Rise ESC

Figure 5.3: *Comparison running trim and rise, influence free surface elevation and pressure modification*

hydrostatic pressure was applied on the original above water body surface that submerged below the disturbed free surface (figure 5.2).

Figure 5.3 shows the results of these computations for the Enlarged Ship Concept. The first (solid) line marks the results of the computation with the transom flow condition without free surface disturbance influence, the second line (denoted 'fs1') the results using pressure stretching, and the third (denoted 'fs2') the results using the alternative method.

It turns out that the inclusion of the free surface disturbance does not provide a clear improvement of the calm water predictions. Especially for the highest forward speeds, it causes a significant over-prediction of both trim and sinkage, where the previous computations and the measurements show platforming. In the mid velocity range only limited improvement of the trim prediction is visible. The clear peak in the measured trim angle is not captured by the computations.

5.3 Regular head waves

Before moving to simulations in irregular head waves, a set of simulations were carried out in regular head waves. The main purpose of these simulations in regular waves was to establish the influence of the parameter settings and the different extensions to the computational method on the seakeeping predictions. These extensions entail the transom flow condition, pressure stretching, time-dependent added mass, and the empirical cross flow drag. They were all introduced in chapter 3 and elaborated upon in chapter 4.

The first part of this section will focus on the influence of the parameter variations and the extensions. At this stage the computations were limited to the case of the Enlarged Ship Concept. In the next part the most successful combination of parameters and extensions were applied to perform a comparison of the predictions of the computational method of the ESC and the ABC with measurements. The model experiments in regular head waves presented in in section 2.3.5 were used as validation material.

These tests were specifically setup to enable the comparison of the outcome of the computational method with experiments using a more reproduceable and simple input and therefore more reliable output of both experiments and computations. The use of regular waves removes the stochastic nature of the wave input and allows for a more deterministic comparison, where anomalities are not obscured by differences in wave realisations.

As explained in chapter 2, these regular wave tests consisted of runs in regular head waves with the ESC and ABC at two forward speeds, 25 knots and 35 knots, a range of frequencies, and three wave steepness ratios (1/60, 1/30, and 1/20). Table 5.2 shows the range of the wave frequency, wave period, the wave length, and the encounter period, for easy reference when observing the graphs presented in this section.

Table 5.2: *Regular waves; wave length, frequencies, and periods*

ω	$\omega\,(L/g)^{1/2}$	T	λ/L	$T_e\ 25kts$	$T_e\ 35kts$
$[rad/s]$	$[-]$	$[s]$	$[-]$	$[s]$	$[s]$
0.60	1.42	10.47	3.11	5.86	4.98
0.70	1.66	8.98	2.29	4.68	3.93
0.80	1.89	7.85	1.75	3.83	3.18
0.90	2.13	6.98	1.38	3.20	2.63
1.00	2.37	6.28	1.12	2.72	2.22
1.10	2.60	5.71	0.93	2.34	1.89
1.20	2.84	5.24	0.78	2.03	1.63
1.30	3.08	4.83	0.66	1.79	1.43

The first goal of this work was optimizing the prediction of the heave and pitch motions. In case this optimisation process is successful, one may assume that the global rigid body acceleration levels are acceptable as well. The occurrence of peaks in the vertical acceleration is quite unlikely to be predicted by the current code as no mechanism has been put into place to specifically address these peaks. Their occurrence is related to the time derivative of the added mass term (Keuning 1994). To compute this derivative requires an accurate method working at a small time resolution. This has not been implemented yet in the current computational method. The implementation of a time-dependent added mass term in the body-linear solution (section 3.7.2) only includes the time dependence of the added mass in a quasi-static fashion. The body-exact solution however, can include this particular time derivative directly. The question that remains is whether the time step used in the body-exact solution for global rigid body motions is sufficiently small to adequately resolve peaks in the vertical acceleration levels.

Figures 5.4 and 5.5 present the influence of a number of methods within the computational code on the heave and pitch responses, and compare these responses to the measured responses for the Enlarged Ship Concept for three different values of the wave steepness at 25

knots forward speed (a Froude number of about 0.55). The calm water reference positions at forward speed presented in the previous section were used to orient the linear submerged panel geometry for the solution of the boundary value problem. The Froude-Krylov and hydrostatic pressures were evaluated on the instantaneous submerged geometry, essentially applying the blended pressure method presented in section 3.7.6 (except when applying pressure profile stretching).

In chapter 2, section 2.3.5, it was already mentioned that for the vessels under consideration the heave and pitch motions could be adequately represented by RAOs. This type of analysis also offers the possibility to distinguish the behaviour near resonance, where more extreme motions occur, and the low and high frequent motions. The analysis is identical to the one applied to the measured data described in section 2.3.5.

Nevertheless, it is important to be aware that the linear analysis may result in the loss of non-linear features in the computed and measured signals. For this reason, the fit of single frequency regular sine-signals to the measured and computed signals was watched closely during the analysis of the data presented here. Likewise in the analysis presented in chapter 2, behaviour that was checked for included the occurrence of higher and lower order frequencies in the measurements as well as non-harmonic behaviour.

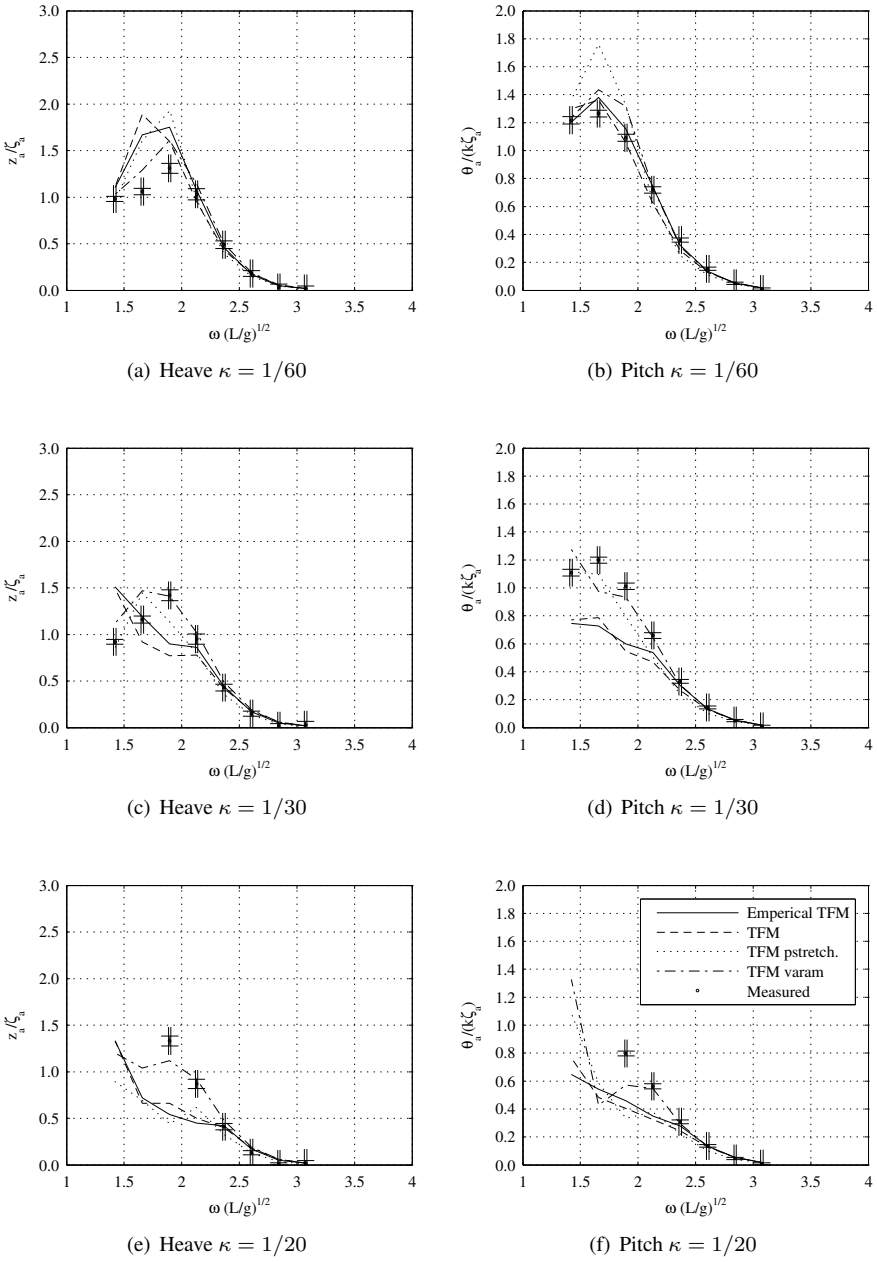
Figures 5.4 and 5.5 show the computed response amplitudes and phase angles applying the following approaches in the computational code:

1. Plain source panels, using the empirical near transom pressure correction, denoted 'Empirical TFM'.
2. Source-doublet panels with wake sheet, using the transom flow condition, denoted 'TFM'.
3. Approach #2 combined with computation of the free surface elevation due to the incoming and the disturbance waves (diffracted and radiated waves) and pressure stretching, denoted 'TFM pstretch'.
4. Approach #2 combined with a time dependent added mass term, denoted 'TFM varam'.

Approaches #1 and #2 produce very similar results, although the inclusion of the transom flow condition seems to cause a slight reduction of the motions for the most part of the frequency range. At the lowest wave steepness (the top two graphs) the responses computed by applying approaches #1 and #2 follow the measured results reasonably close, especially for the pitch motion. The heave motion is over-predicted for frequencies less than the non-dimensional resonance frequency of around 2.

Moving to higher wave steepness values the predicted results quickly deteriorate, especially around and below the resonance frequency. The motion response was extremely under-predicted. By studying the heave and pitch time traces and animations of the ship motions the cause of this behaviour became apparent. First of all, the computed motion time traces showed a lower order frequency response, indicating leaking of energy at the wave frequency to other frequencies. This leakage resulted in lower motion responses at the wave frequency itself. The measured signals do not feature this behaviour.

The mechanism behind this behaviour can be found in the body linear computation of the dynamic pressures. The hydrostatic and incident wave pressures were set to zero on the emerged parts of the hull. However, the boundary value problem still produced hydrodynamic pressures on the now emerged linearised body surface, caused by the rigid body motions and

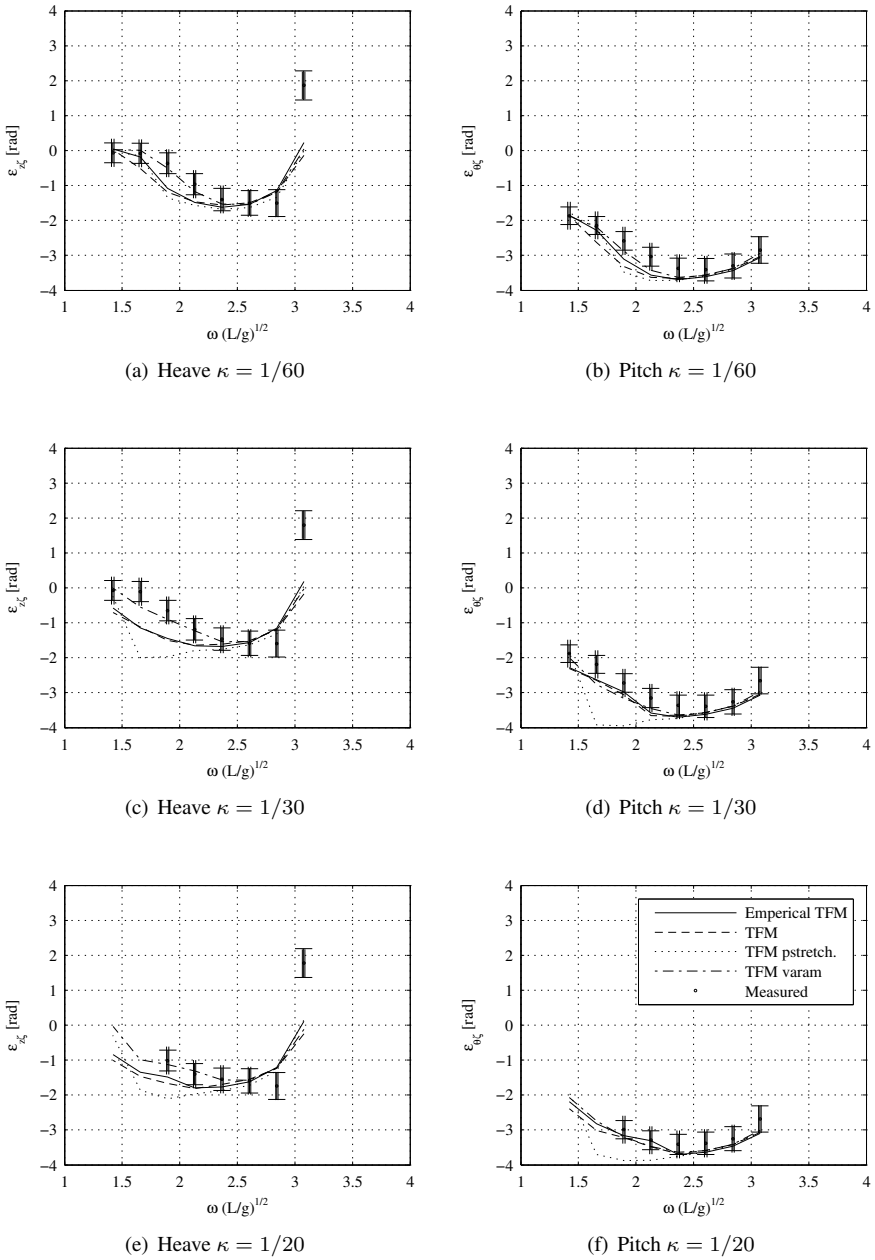


(a) Heave $\kappa = 1/60$ (b) Pitch $\kappa = 1/60$

(c) Heave $\kappa = 1/30$ (d) Pitch $\kappa = 1/30$

(e) Heave $\kappa = 1/20$ (f) Pitch $\kappa = 1/20$

Figure 5.4: *Comparison heave and pitch responses ESC at 25 kts for constant wave steepness*



(a) Heave $\kappa = 1/60$ (b) Pitch $\kappa = 1/60$

(c) Heave $\kappa = 1/30$ (d) Pitch $\kappa = 1/30$

(e) Heave $\kappa = 1/20$ (f) Pitch $\kappa = 1/20$

Figure 5.5: *Comparison heave and pitch responses ESC at 25 kts for constant wave steepness*

the steady forward speed. These pressures resulted in a net upward force slowing down the downward motion and in the case of extreme wave steepness caused the ship to 'skip' every other wave according to the computations. This behaviour led to the reduced motion response at the encounter frequency and a motion component at half the encounter frequency.

A possible solution seemed to be setting the pressure to zero on the part of the instantaneous hull surface above the incoming wave surface, or even better the disturbed wave surface. In this way the upward force decreases when the ship emerges from the water, possibly preventing the skipping of waves. Another resolution could be found by applying the pressure profile stretching method. This method achieves essentially the same result in a more complicated fashion, by attempting to match the different pressure components into a smooth total pressure distribution. This particular method was introduced in section 3.7.6.

Of both approaches, only the results of the pressure stretching approach (approach # 3) are shown in figures 5.4 and 5.5. The responses at the smallest wave steepness of 1/60 showed significant over-prediction around the resonance frequency. When only considering the amplitude responses, the pressure stretching approach seemed to perform significantly better than approaches #1 and #2 at 1/30 wave steepness, while exhibiting under-prediction at the 1/20 wave steepness. Nonetheless when studying the phase angles in figure 5.5, it can be observed that the pressure stretching produced relatively large differences in the predicted phase angles with respect to the measurements, especially around the resonance frequency at the wave steepness of 1/30 and 1/20.

Additionally, when studying the time traces of the heave and pitch motions, the pressure stretching exhibited the same wave skipping as was observed previously at the highest wave steepness. Simply setting the pressure to zero above the instantaneous waterline showed similar results. It can be concluded both approaches are not helpful in improving the results of the seakeeping predictions.

The deviation of the stretched pressure distribution is often too large with respect to the computed one and lacks a meaningful relation with the physical reality. Other authors applied pressure profile stretching to the computation of the wave loads on large vessels, where the wave and motion amplitudes are small in comparison to the ship dimensions. Blandeau et al. (1999) for instance apply pressure stretching to FPSOs. In such cases the difference between the computed and the stretched pressure distributions is much smaller. Because of the relatively large waves (both in length as in height) in comparision to the size of high speed vessels, the resulting large shifts in wetted surface cause significant distorsion of the dynamic pressures (including the undisturbed wave pressures). This distorsion may explain the large phase differences as well.

Another solution may be found by using the time dependent added mass described in section 3.7.2 (approach #4). Instead of pre-computing the added mass matrix for the body-linear calm water submerged geometry in its reference position, the added mass was now computed for the instantaneous location of the submerged panels below the flat calm water surface. This was done regardless of whether the panels were part of the body-linear panels or orginally were above water panels.

The results are marked in figures 5.4 and 5.5 by the dash-dotted line and show a clear improvement over all other lines. In nearly all cases the results show a better agreement with the measurements; with the exception of the largest wave heights occurring when the wave steepness equals 1/20 and at low wave frequencies. It is observed from the time traces that

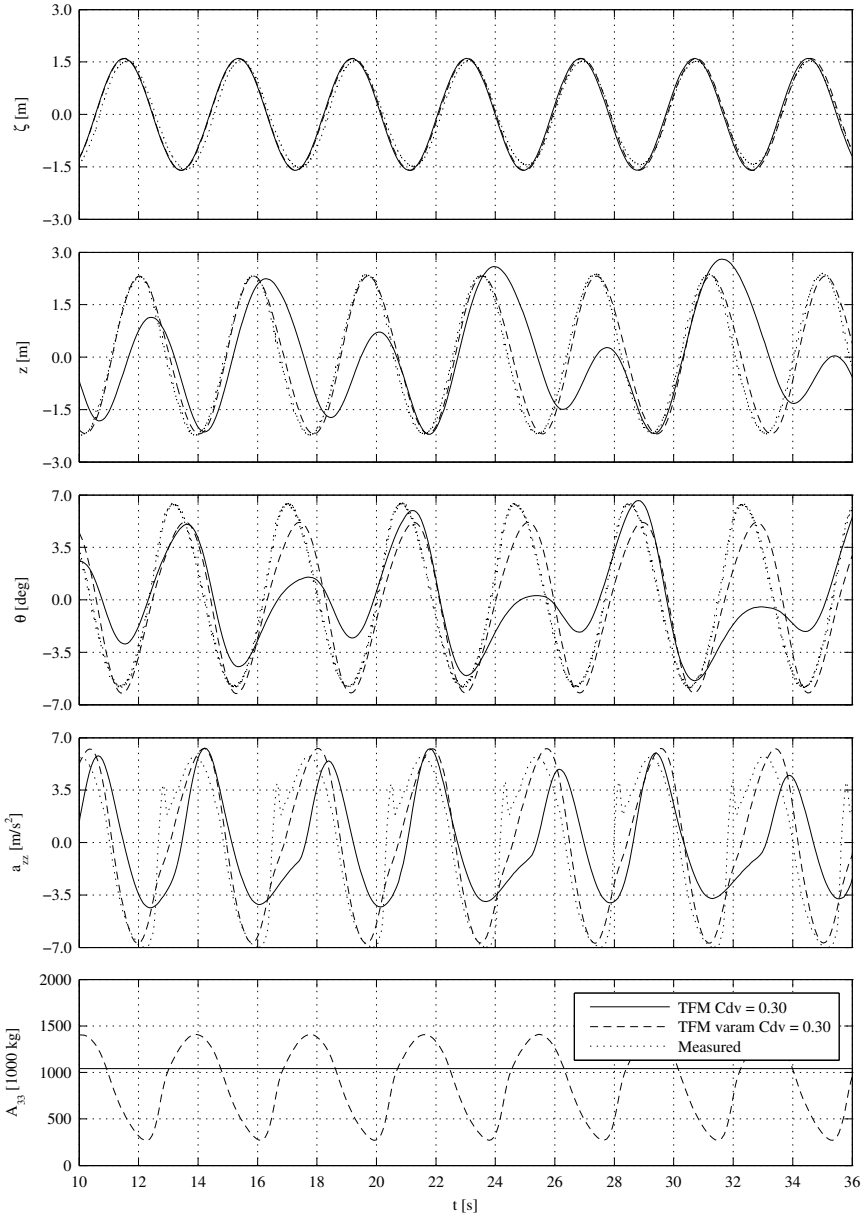


Figure 5.6: *Comparison time traces of computations with and without variable added mass and measurements, ESC at 25 kts,* $\kappa = 1/30$, $\omega(L/g)^{1/2} = 1.9$

the lower order harmonic visible in the other approaches (#1, #2, and #3) nearly disappeared. Moreover, the computed phase angles show a clear improvement, especially for the heave motion.

In fact, this method is well in line with the blended pressure approach. Its implementation follows closely the implementation of the non-linear hydrostatic force. Both are terms that are computed separately from the boundary value solution. They are treated in a non-linear matter, without having large repercussions on the assumptions behind the set-up of the boundary value problem. This is opposite to the implications of the pressure stretching method, where the solution of the boundary value problem is affected without considering the assumptions on which the solution behind it is based.

Figure 5.6 shows a comparison of the time traces of respectively the wave elevation, heave motions, pitch motions, vertical acceleration levels at the centre of gravity, and the time dependence of the heave added mass term. The compututations with the time-dependent added mass are represented by the solid lines, the computations with constant added mass by the dashed lines, and the measurements by the dotted lines. The time traces are of computations and measurements performed at the middle wave steepness for the wave frequency near the motion response peak and a forward speed of 25 kts.

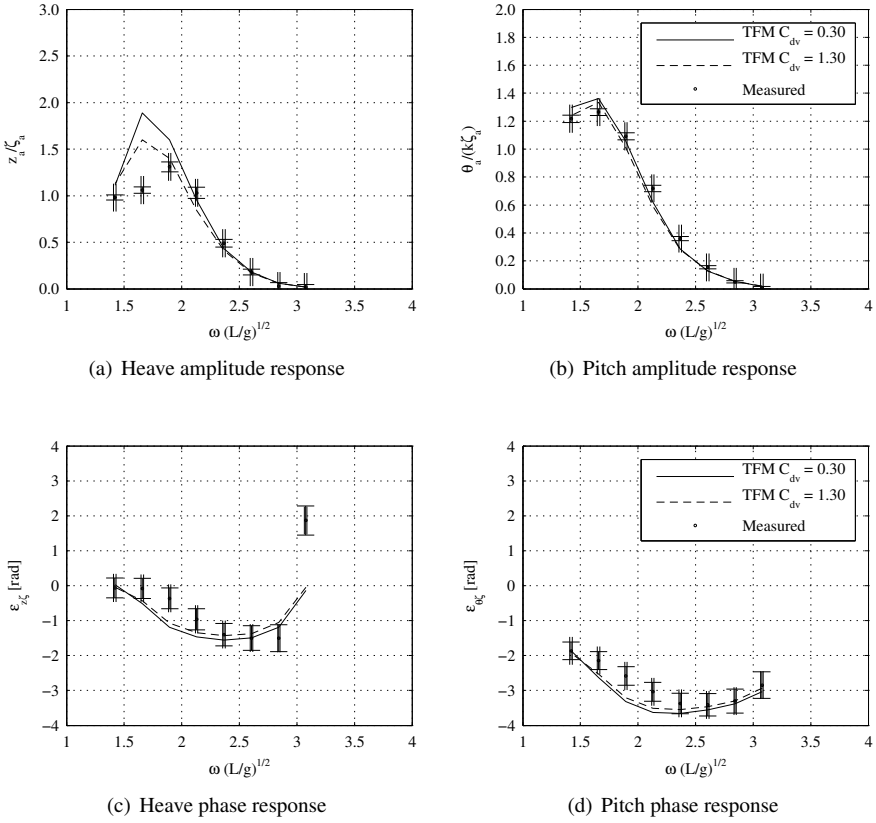
Clearly visible is the lower order component in the motion responses computed with a constant added mass. Both the amplitudes, and the phase angles of the computations with time dependent added mass are in close agreement with the measurements. The exception is the pitch motion amplitude, that is slightly under-estimated, as was already visible in the graphs presented before. Also the vertical acceleration level at the center of gravity is better predicted by the time dependent added mass approach, both in terms of amplitude and of phase angle. The measured signal shows a clear acceleration peak in each cycle associated with impacting the water surface that is not visible in the computed signals.

The final graph in figure 5.6 presents the time dependence of the added mass term for both computations. The time-variant added mass shows in this particular case a variation of 50 percent around the constant value. The (infinite frequency) added mass has not been determined for the measurements.

A parameter that could potentially have a large influence on the extreme motion behaviour is the cross flow drag. All regular wave computations presented until here were performed using a cross flow drag value of 0.30. Figure 5.7 shows the result of increasing this value to 1.30 for approach #2. The effect on the pitch motion is limited, while the heave motion response is reduced by about 15 percent around the motion peak. The phase angles are hardly affected.

More detailed research at larger values of the wave steepness showed however that this increase is not enough to prevent the extreme motion responses caused by the ‘wave skipping’ or by the pressure stretching. Increasing the cross flow drag even further is not recommendable as values far beyond 1.30 lead to unrealistic motion predictions and are very uncommon in literature. A value of 1.00 gives reasonable results for the Enlarged Ship Concept and was used for all computations presented from this point onwards.

Part of the problems of the computational method -the ‘wave skipping’ and the leakage to lower order frequencies- were caused by the way the measurements are set-up. Keeping the wave steepness constant resulted in unrealistic large wave heights for the longer wave lengths of up to six meters or more full scale. Not only the computational results suffered at these



(a) Heave amplitude response

(b) Pitch amplitude response

(c) Heave phase response

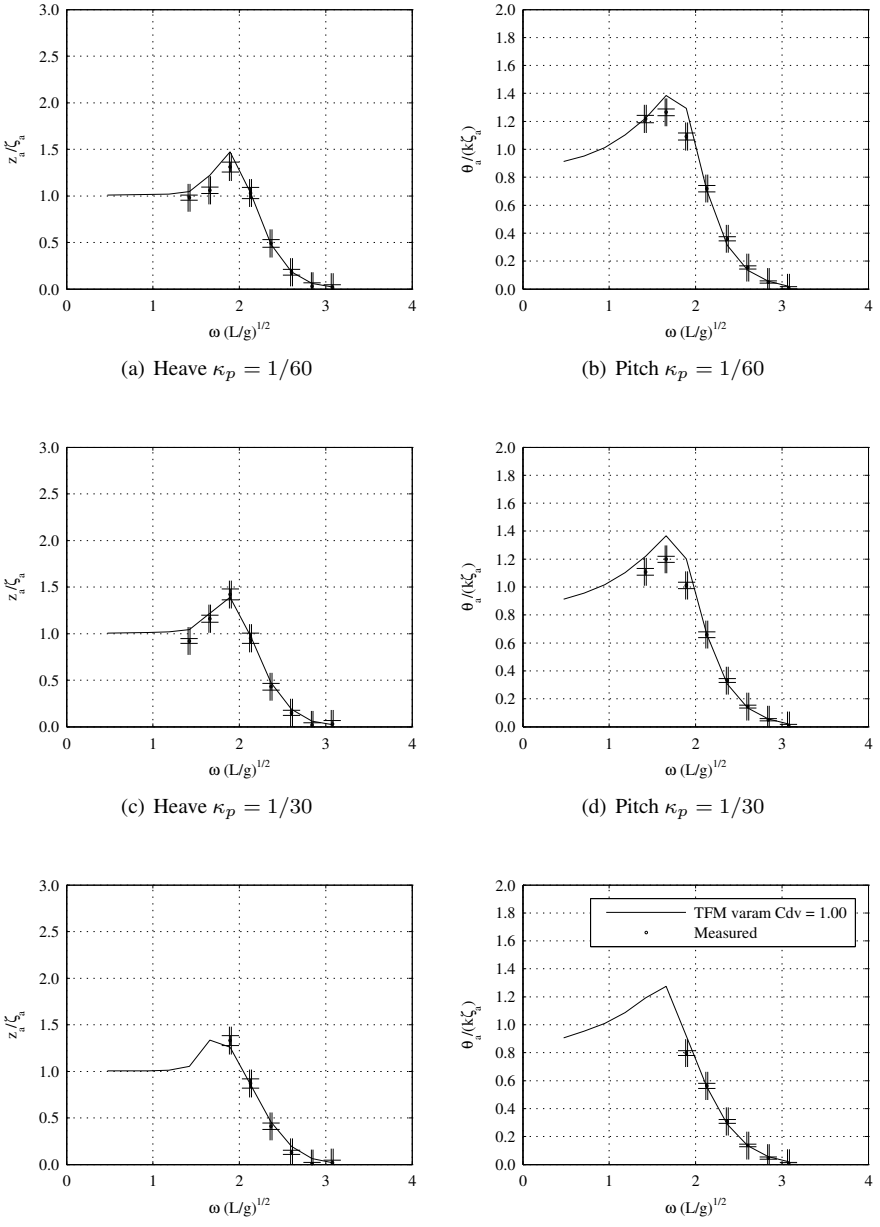
(d) Pitch phase response

Figure 5.7: *Influence C_{dv} on heave and pitch responses ESC at 25 kts ($\kappa = 1/30$)*

large wave heights, but also a number of planned measurements at low wave frequencies were impossible to complete. The reason for this was that neither the model nor the model support bearings were able to cope with the extreme wave heights at these low frequencies caused by keeping the wave steepness constant.

Nonetheless, the model experiments seemed to suffer less from the extremely large wave heights than the computations. To improve this situation, the following graphs were prepared by keeping the wave *height* constant and equal to the wave height at the motion peak. This choice led to a wave steepness equal to the one at the motion peak of the measurements, at a non-dimensional frequency of 1.9. It resulted in larger wave heights at higher frequencies and smaller wave heights at lower frequencies compared to the measurements. The comparison at frequencies higher than the resonance frequency was hardly influenced, and the result at the lower frequencies improved and provided a significantly better picture of the computational outcome.

Figures 5.8 and 5.9 present the heave and pitch responses of the Enlarged Ship Concept at both tested forward speeds for three different wave heights, corresponding with the wave

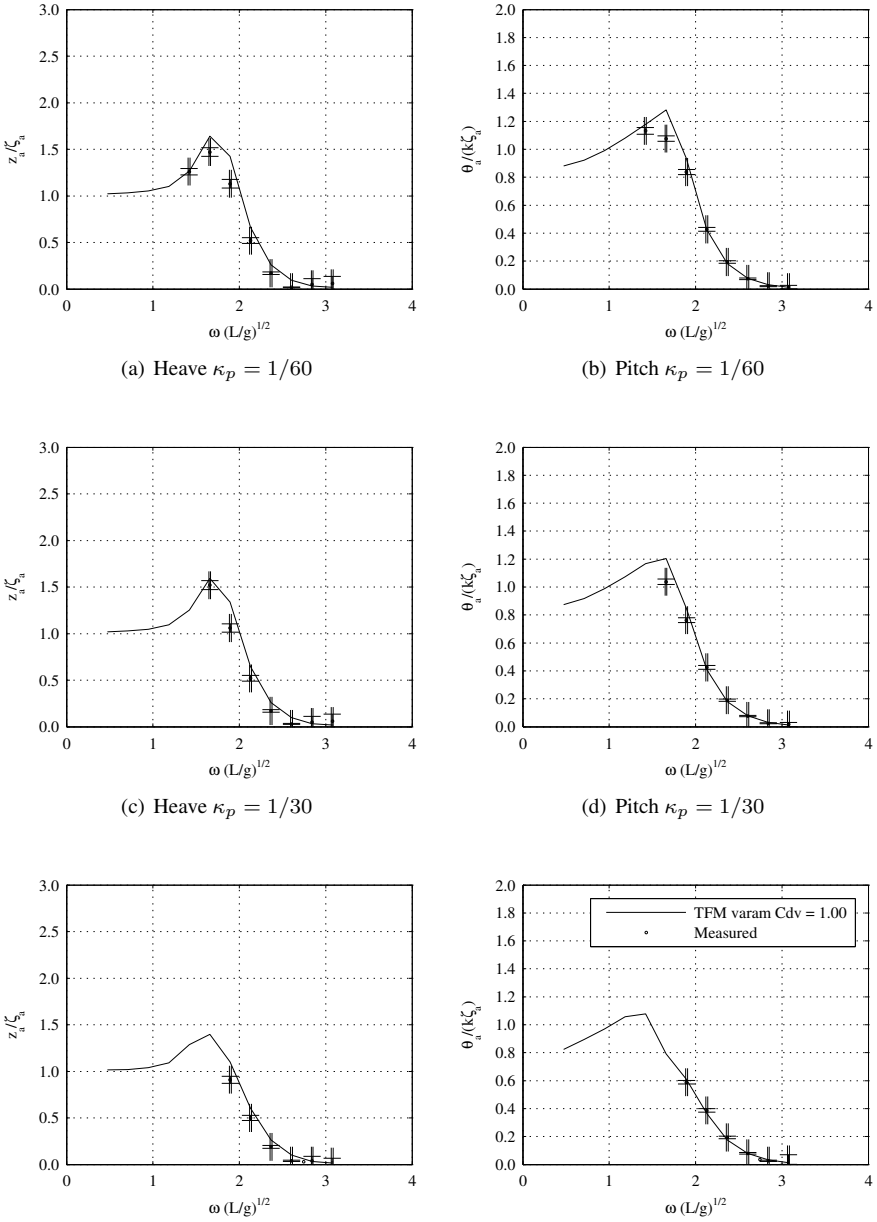


(a) Heave $\kappa_p = 1/60$ (b) Pitch $\kappa_p = 1/60$

(c) Heave $\kappa_p = 1/30$ (d) Pitch $\kappa_p = 1/30$

(e) Heave $\kappa_p = 1/20$ (f) Pitch $\kappa_p = 1/20$

Figure 5.8: *Comparison heave and pitch responses ESC at 25 kts for constant wave height (corresponding with a steepness κ_p at $\omega\,(L/g)^{1/2} = 1.90$)*

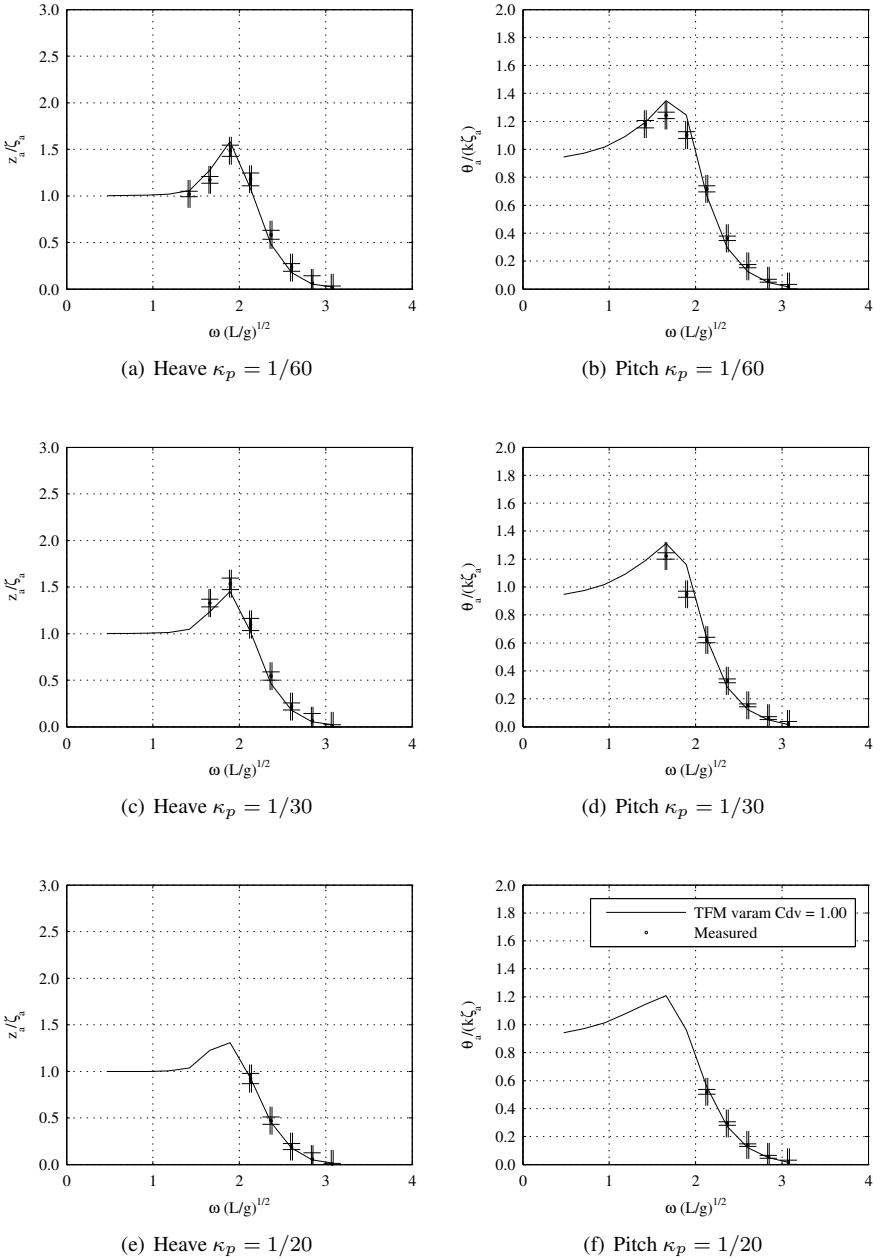


(a) Heave $\kappa_p = 1/60$ (b) Pitch $\kappa_p = 1/60$

(c) Heave $\kappa_p = 1/30$ (d) Pitch $\kappa_p = 1/30$

(e) Heave $\kappa_p = 1/20$ (f) Pitch $\kappa_p = 1/20$

Figure 5.9: *Comparison heave and pitch responses ESC at 35 kts for constant wave height (corresponding with a steepness κ_p at $\omega\,(L/g)^{1/2} = 1.90$)*

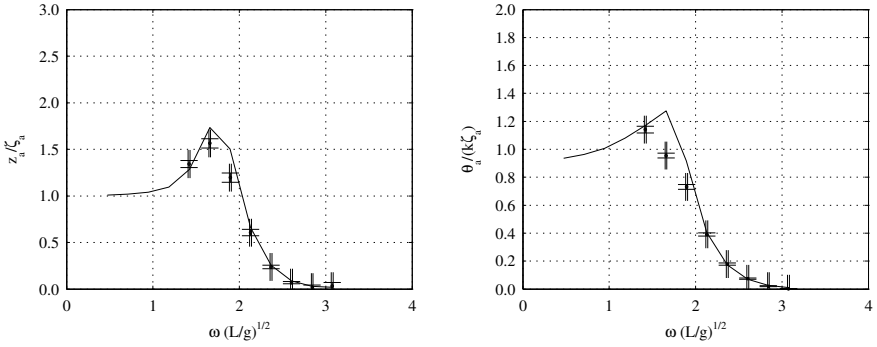


(a) Heave $\kappa_p = 1/60$ (b) Pitch $\kappa_p = 1/60$

(c) Heave $\kappa_p = 1/30$ (d) Pitch $\kappa_p = 1/30$

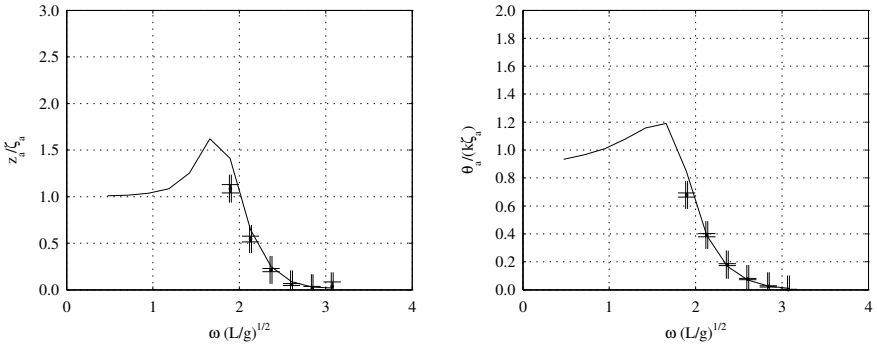
(e) Heave $\kappa_p = 1/20$ (f) Pitch $\kappa_p = 1/20$

Figure 5.10: *Comparison heave and pitch responses ABC at 25 kts for constant wave height (corresponding with a steepness κ_p at $\omega\,(L/g)^{1/2} = 1.90$)*



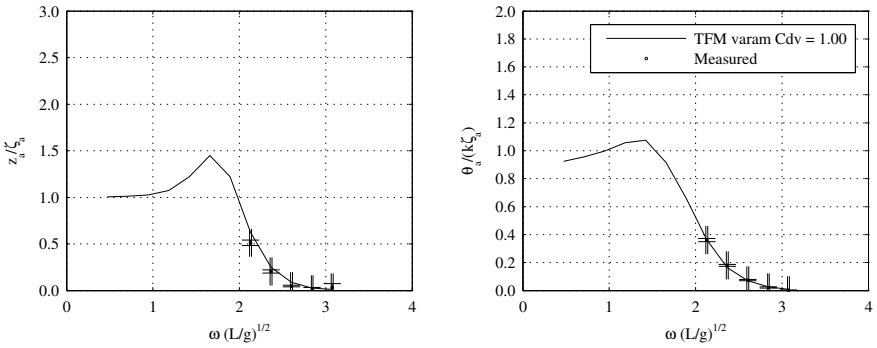
(a) Heave $\kappa_p = 1/60$

(b) Pitch $\kappa_p = 1/60$



(c) Heave $\kappa_p = 1/30$

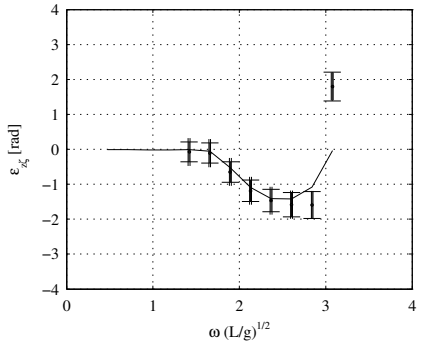
(d) Pitch $\kappa_p = 1/30$



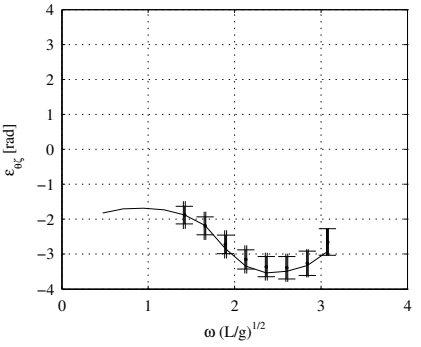
(e) Heave $\kappa_p = 1/20$

(f) Pitch $\kappa_p = 1/20$

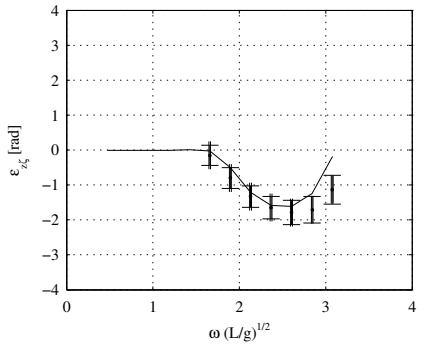
Figure 5.11: *Comparison heave and pitch responses ABC at 35 kts for constant wave height (corresponding with a steepness κ_p at $\omega\,(L/g)^{1/2} = 1.90$)*



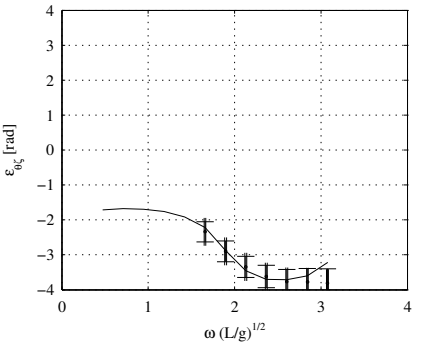
(a) Heave ESC, $\kappa_p = 1/30$, 25 kts



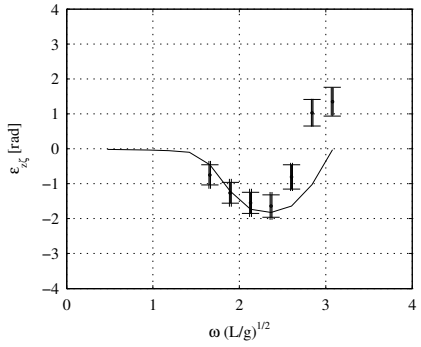
(b) Pitch ESC, $\kappa_p = 1/30$, 25 kts



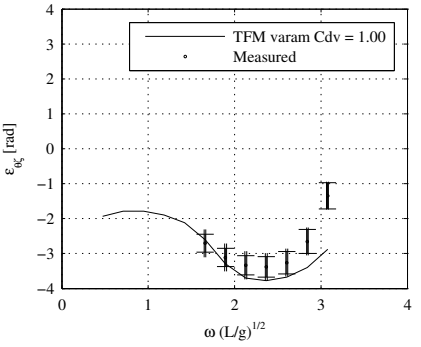
(c) Heave ABC, $\kappa_p = 1/30$, 25 kts



(d) Pitch ABC, $\kappa_p = 1/30$, 25 kts



(e) Heave ESC, $\kappa_p = 1/30$, 35 kts



(f) Pitch ESC, $\kappa_p = 1/30$, 35 kts

Figure 5.12: *Comparison heave and pitch phase angles for constant wave height (corresponding with a steepness κ_p at $\omega\,(L/g)^{1/2} = 1.90$)*

steepness values of 1/60, 1/30, and 1/20 at the motion peak. The same results are depicted in figures 5.10 and 5.11 for the Axe Bow Concept. Finally, a comparison of the computed and measured phase angles for a selection of the results is presented in figure 5.12. In the computations the time-dependent added mass term, transom flow condition, and a cross flow drag coefficient of 1.00 were applied.

The computational results show an excellent agreement with the measurements for both design concepts. The response around the motion peak still shows a limited over-prediction, especially for the pitch motion at the lowest wave height. This could be adapted by an increase of the cross flow drag, but difference is small enough to justify to keep the results as they are.

The Axe Bow Concept suffered relatively more from large motions during the measurements, especially at the highest forward speed. This is visible in the graphs by the fact that at the higher wave steepness less measurement values have been obtained near the motion peak compared to the Enlarged Ship Concept. At the same time, it is only partially visible in the computed results. Nevertheless, at the highest forward speed the motion peaks are marginally higher in the ABC results compared to the results of the ESC.

In general, according to both the computations and the measurements, the two design concepts perform nearly identical in a linear analysis. In this analysis the occurrence of peaks in the vertical accelerations is neglected and therefore not included in the comparison of measurements and computations and of the two design concepts.

5.4 Irregular head waves

The final stage of the validation process presented in this thesis considers the motions and vertical acceleration levels of the Enlarged Ship and Axe Bow Concept designs in irregular head waves. Four cases were selected from the extensive experimental data set of the FAST I research project (chapter 2) covering two forward speeds and two significant wave heights. An overview of these cases is given in table 5.3. An exception was the low wave height at 35 knots of the ABC, with no results available at a significant wave height of 2.0 metres; results obtained at 2.5 metres were used instead.

Table 5.3: *Irregular wave conditions used for validation*

No.	$H_{1/3}$	T_p	U	**Design**
$[-]$	$[m]$	$[s]$	$[kts]$	$[-]$
1	2.0	7.8	25	ESC
2	3.5	7.8	25	ESC
3	2.0	7.8	35	ESC
4	3.5	7.8	35	ESC
5	2.0	7.8	25	ABC
6	3.5	7.8	25	ABC
7	2.5	7.8	35	ABC
8	3.5	7.8	35	ABC

The experimental data was collected by performing repetitive towing tank runs in different temporal parts of a wave realisation with a JONSWAP spectrum with a given significant

wave height and peak period up to a total signal length of 1200 seconds for the 25 knots runs and 900 seconds for 35 knots runs. Typically 300 waves were encountered for each wave condition, based on the peak encounter period.

The measured data - the wave elevation, heave and pitch motions, and the vertical acceleration levels - were sampled at 400 Hz and subsequently digitally low pass filtered at 20 Hz. As stated in section 2.3.6 this way of treating the data provided an acceptable balance between retaining maxima and minima in signals, while removing noise and high-frequent oscillations. Finally, the processing consisted of computing statistical quantities as significant and maximum (positive and negative) values, presented in bar plots, and the construction of Rayleigh plots (refer to section 2.3.6).

As described in chapter 2, the crests and troughs of the signals were obtained by first identifiying the local positive and negative peaks in the time trace following the definitions by Ochi (1973), while supposing a minimum peak time distance of 0.5 seconds. Subsequently, a maximum likelyhood parameter estimate of the Weibull distribution of these peaks was obtained. Finally, the fitted Weibull distribution was used to obtain an estimate for the short term maximum and minimum values in the time trace. With at least 300 peaks in the time trace, the chosen 1/100 probability of exceedance is an arbitrary choice for the short term maximum estimate, but is nevertheless satisfactory for the sake of comparing measured and computed time traces.

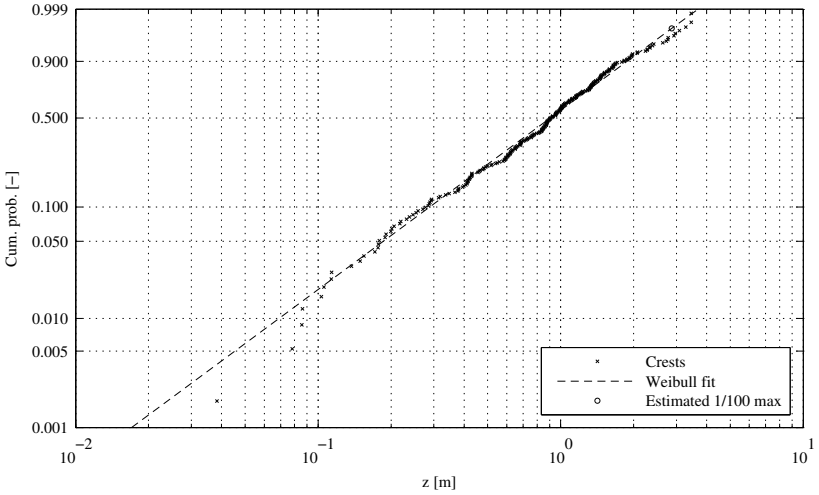
Figure 5.13 shows the Weibull fit and 1/100 maximum values for the heave motion and the vertical acceleration level at the bow of the ESC sailing at 35 knots in a significant wave height of 3.5 metres. The heave crest values are clearly better represented by the fitted Weibull distribution. The estimated maxima are now mostly determined by the statistically more reliable middle section of the data, instead of the tail formed by the higher crests.

The reasoning behind choosing comparing the Weibull estimated maxima over direct comparison of the actual (deterministic) maximum values in the time traces is twofold. First, the measured and computed time traces were not of identical length, changing the probability of exceedance of their deterministic maximum value. Second, both measurements and computations were not performed in the exact same wave realisation and different realisations, likely influencing the maximum value. Moreover, the occurrence of one single maximum value already is of a highly stochastic nature. The Weibull estimated maximum is based on all peaks in the time trace and is therefore statistically a much more reliable estimate.

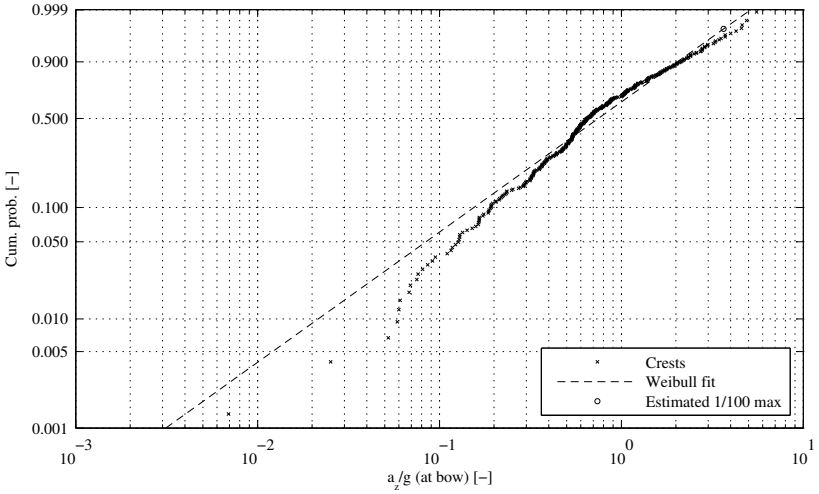
In fact, in the case of a linear system with a narrow banded Gaussian input, the peaks in the output can be shown to be Rayleigh distributed (Longuet-Higgins 1952); the Rayleigh distribution being a special case of the Weibull distribution. For the 1 in 100th maximum value the Rayleigh distribution yields a ratio of 1.5 between the significant value and the maximum value.

The computations were performed applying the lessons learned in the studies presented in the previous sections and the previous chapter. In particular the resulting panels, time step sizes, and memory lengths of the convergence study (section 4.6) were used; while applying the lessons learned of the regular wave computations the following choices were made:

- Cross flow drag value of 1.00
- Time-dependent added mass
- Transom flow condition



(a) Heave



(b) Vertical acceleration at bow

Figure 5.13: *Distribution of measured crests, Weibull fit, and estimated 1/100 maximum value ESC, condition* $T_p = 7.8\ s$*,* $H_{1/3} = 3.5\ m$*, and* $U = 35\ kts$

The computed signals were of similar length (but not identical) as the measured signals; the simulations were performed using 20.000 time steps of respectively 0.078 seconds for 25 knots and 0.054 seconds for 35 knots, resulting in record lengths of respectively 1500 and 1100 seconds, containing 350 to 400 wave encounters.

Apart from the filtering the computed signals were subjected to the same data processing to the one used for the measured signals. All results were made dimensionless to enable direct comparison of measurements and computations. This was done using the desired value of the significant wave height and not the actual realised value.

Table 5.4: *Comparison realised significant wave heights*

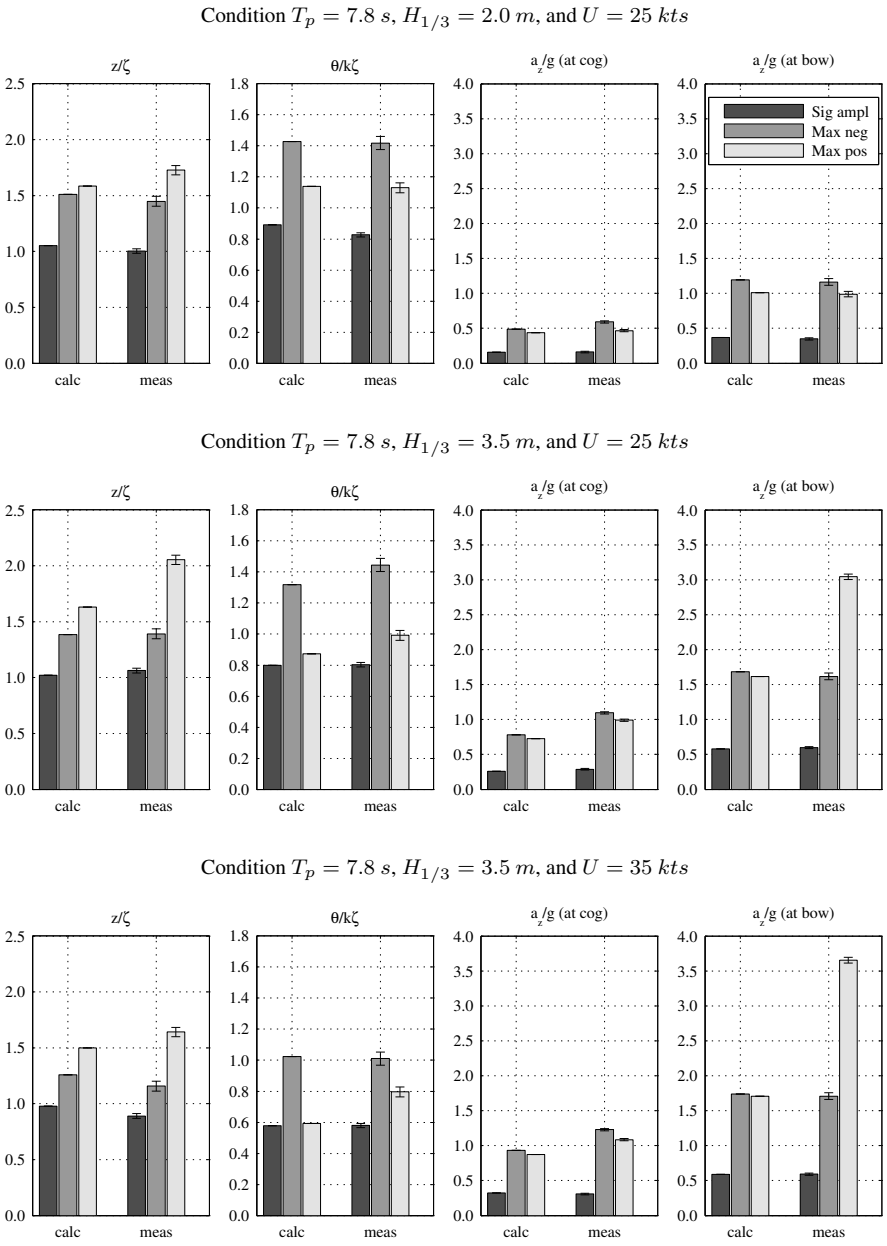
No.	$H_{1/3}$	$H_{1/3\ calc}$	$H_{1/3\ meas}$	U	**Design**
$[-]$	$[m]$	$[m]$	$[m]$	$[kts]$	$[-]$
1	2.00	1.95	2.10	25	ESC
2	3.50	3.42	3.40	25	ESC
3	2.00	1.97	2.10	35	ESC
4	3.50	3.44	3.31	35	ESC
5	2.00	1.96	2.08	25	ABC
6	3.50	3.42	3.33	25	ABC
7	2.50	2.46	2.37	35	ABC
8	3.50	3.44	3.20	35	ABC

Table 5.4 indicates a variation of over 10 percent between the desired and the actual realised significant values of the significant wave height for the measurements and a (one-sided, downward) variation of less than 2 percent for the computations. The main cause of the deviations in the measurements is the difficulty in using wire-type wave probes for measuring the wave elevation at large forward speed. This is caused by spray forming and ventilation around the wires of the wire-type wave probe. The experimental wave spectra were tuned by performing measurements in towing tank at zero forward speed without model, for this reason it is assumed that the desired value of the significant wave height is a more accurate representation than the one measured at high forward speed. For the computations, the deviation in wave heigth is very limited in magnitude and mainly caused by the finite signal length.

Figure 5.14 presents a comparison of the measured and computed significant amplitudes (black), positive maxima (dark grey), and negative maxima (light grey) of three of the four studied cases considering the Enlarged Ship Concept. Figure 5.15 presents the same comparison for the Axe Bow Concept. As stated above the maxima are the 1/100 maximum values obtained by performing a Weibull distribution fit. Each row in both figures shows from left to right the heave response, pitch response, vertical acceleration at the centre of gravity and the vertical acceleration at the bow for one wave condition.

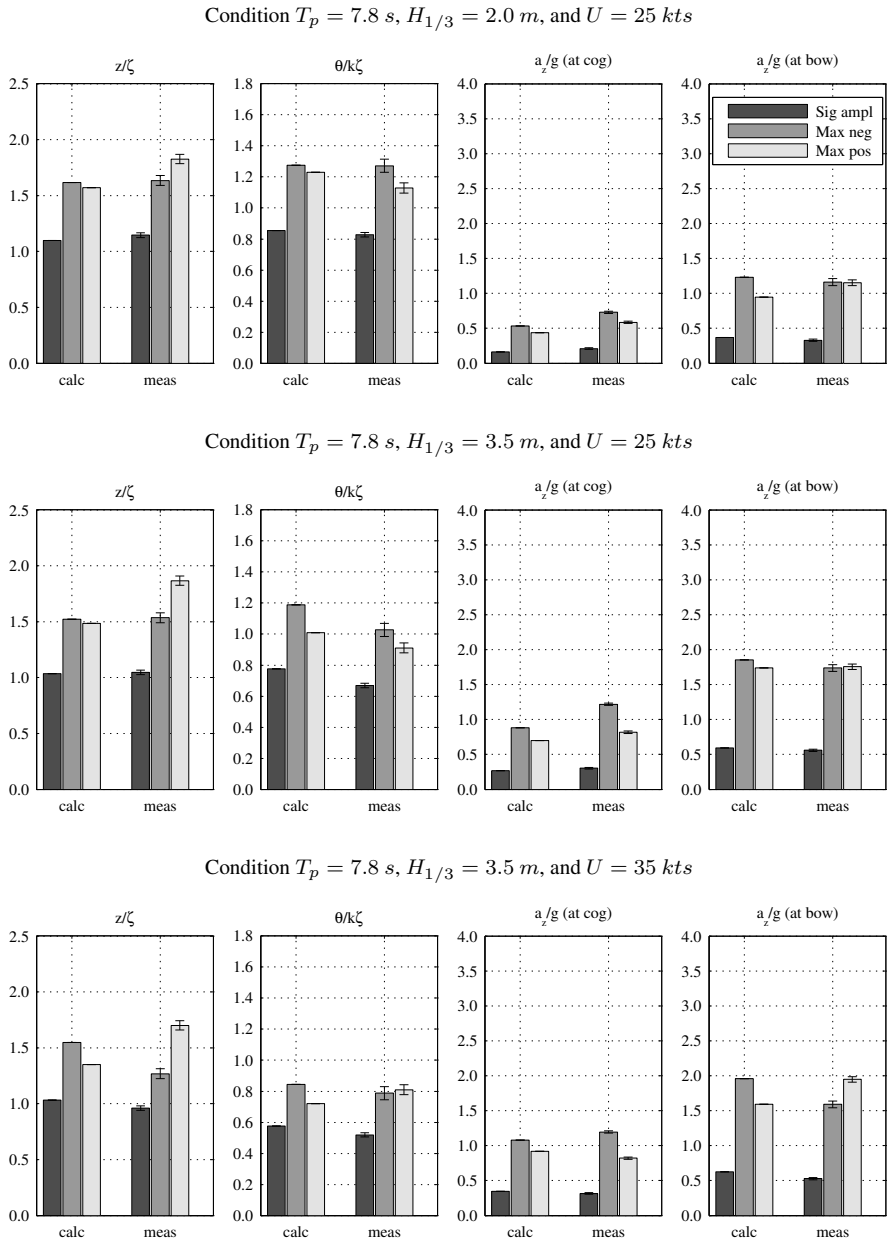
To keep the data presented in the figures conveniently arranged, the lowest wave height at the forward speed of 35 knots is omitted for both design concepts (cases 3 and 7 in table 5.3). The omitted results only confirm the findings derived from the remaining cases.

When only considering the heave and pitch motions, the findings of the regular wave response comparison presented in the previous section are confirmed. The significant amplitudes are adequately predicted in nearly all cases, with in some cases a slight over-prediction of the



(a) Heave motion (b) Pitch motion (c) Vertical acc. CoG (d) Vertical acc. bow

Figure 5.14: *Comparison Enlarged Ship Concept*



(a) Heave motion (b) Pitch motion (c) Vertical acc. CoG (d) Vertical acc. bow

Figure 5.15: *Comparison Axe Bow Concept*

pitch motion. Moreover, also the magnitude of the maxima and minima of the heave and pitch motions are well predicted. The computations do capture the degree of asymmetry (the difference between minimum and maximum values) in the motion responses relatively well, and do show the larger asymmetry of the heave and pitch motions of the Enlarged Ship Concept with respect to the Axe Bow Concept. In that sense the computational method is able to identify the (non-linear) influence of in particular the flared bow of the ESC on the motion responses.

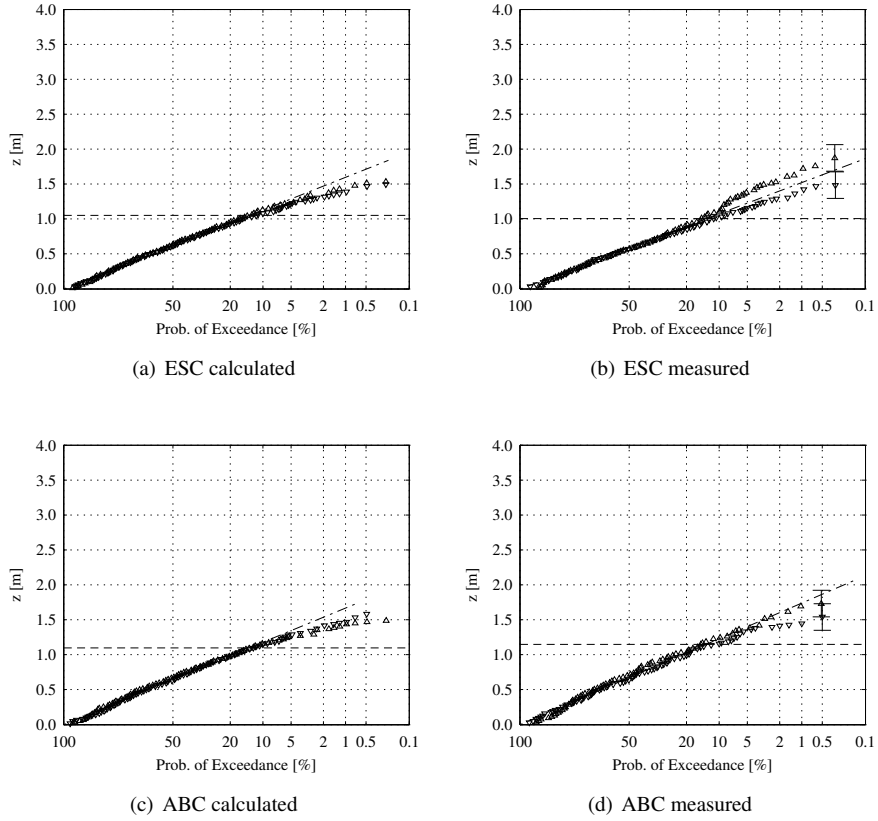
Also, the significant amplitudes of the acceleration levels show a good fit, and hardly show any difference between both design concepts. The occurrence and magnitude of peaks in the vertical acceleration levels is severely under-predicted. The under-prediction is particularly evident in the results of the Enlarged Ship Concept and is associated with the upward acceleration, or better deceleration, of the downward moving ship, in particular the bow, impacting the water surface. The Axe Bow Concept, designed with avoiding slamming in mind, logically suffers less from this under-prediction. The absense of large peaks was to be expected, considering the discussion about the occurrence of maxima (section 2.3.6) and the short-comings of the current computational model in addressing peak responses discussed in the previous section.

Although the peaks in the acceleration levels do not have a noticeable influence on the motion levels, they are a main cause of discomfort on board of the ship and may cause even injury and damage. Therefore their correct prediction is of importance. Within this context, as noted already in chapter 2, it is important to note that it is possible that the vertical acceleration levels are influenced by the structural response of the model. Although the models are expected to be significantly stiffer than their full scale counterparts and the accelerometers are mounted on heavy wooden crossbeams that are tightly integrated in the structure of the model, the impact force may still cause a structural response influencing the measured acceleration levels.

As long as the models are nearly identical in a structural sense -as was the case in the FAST I research program- comparison of the relative performance in terms of the vertical acceleration level is possible. They difference in structural behaviour may however influence the comparison of model scale to full scale and to computations. Additionally, on relatively less stiff full scale ships hydro-elasticity may become important in reducing the actual structural response as well as the rigid body acceleration level.

Following the discussion in chapter 2 regarding the occurrence of peak values, this section is concluded with the presentation of a selection of Rayleigh plots comparing the computed and the experimental outcome. This selection is limited to a comparison of the Rayleigh plots obtained for the least extreme case and for the most extreme case. The least extreme case is formed by the heave and pitch motions of both design concepts at the lowest forward speed and significant wave height. The most extreme case is found in the vertical acceleration level at the bow at the highest forward speed and significant wave height.

As was pointed out in chapter 2, only limiting the time trace analysis to significant values tends to obscure the occurrence of peaks. Similarly, using only the maxima and minima occurring in the time traces for comparison introduces the risk of skewing the comparison of by taking outliers that are statistically irrelevant. This risk increases when the input signals, in this case the wave elevation, are different realisations of the same energy density spectrum. This was the reason for chosing to apply a Weibull estimate for maximum values above.



(a) ESC calculated

(b) ESC measured

(c) ABC calculated

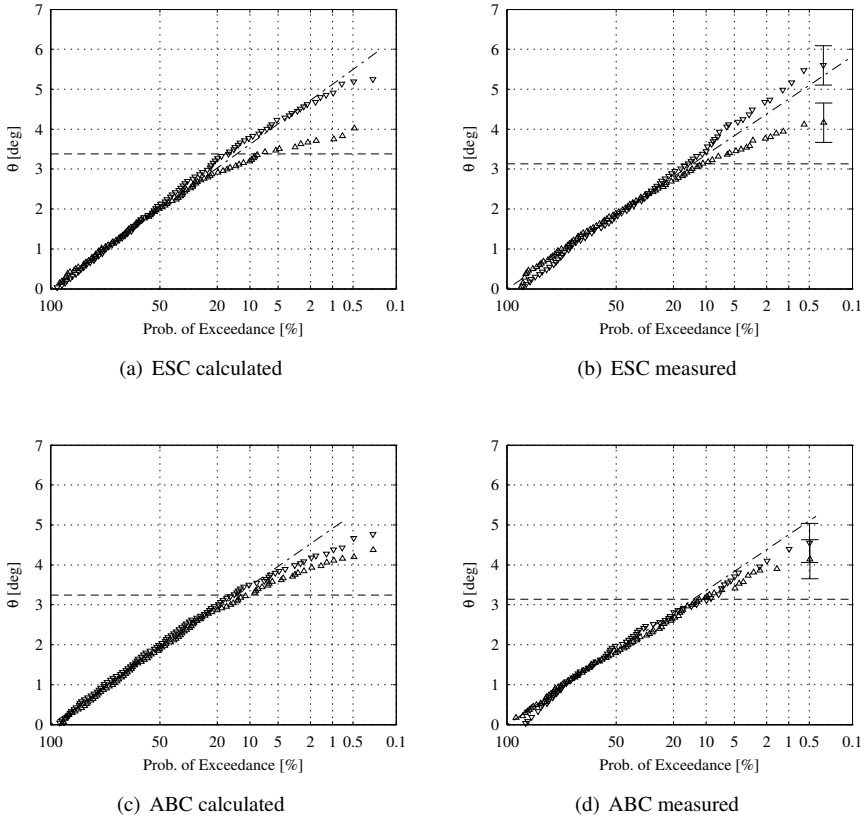
(d) ABC measured

Figure 5.16: *Rayleigh plots heave motion Enlarged Ship Concept and Axe Bow Concept, condition:* $T_p = 7.8\ s$*,* $H_{1/3} = 2.0\ m$*, and* $U = 25\ kts$

Rayleigh plots provide a means to not only compare signals based on standard deviations and maxima, but also show the relation of both, and the degree to which the response signals are linear (refer to section 2.3.6). The Rayleigh plots depicted here are obtained using the procedure outlined in section 2.3.6. As before, the horizontal dashed lines indicate the significant value and the dash-dotted diagonal lines indicate the Rayleigh distribution based on the significant value of the signal.

Figures 5.16 and 5.17 present an overview of the comparison between the measured and computed Rayleigh plots for the heave and the pitch motion of both design concepts in the least extreme wave condition. Measurements and computations compare well. As before, the differences between both design concepts, in particular the asymmetry in the bow-up and bow-down pitch amplitudes of the Enlarged Ship Concept caused by the bow flare, are captured.

Finally, the most extreme case is presented in figure 5.18, showing the Rayleigh plots for the vertical acceleration level at the bow in the most extreme wave condition. Clearly the



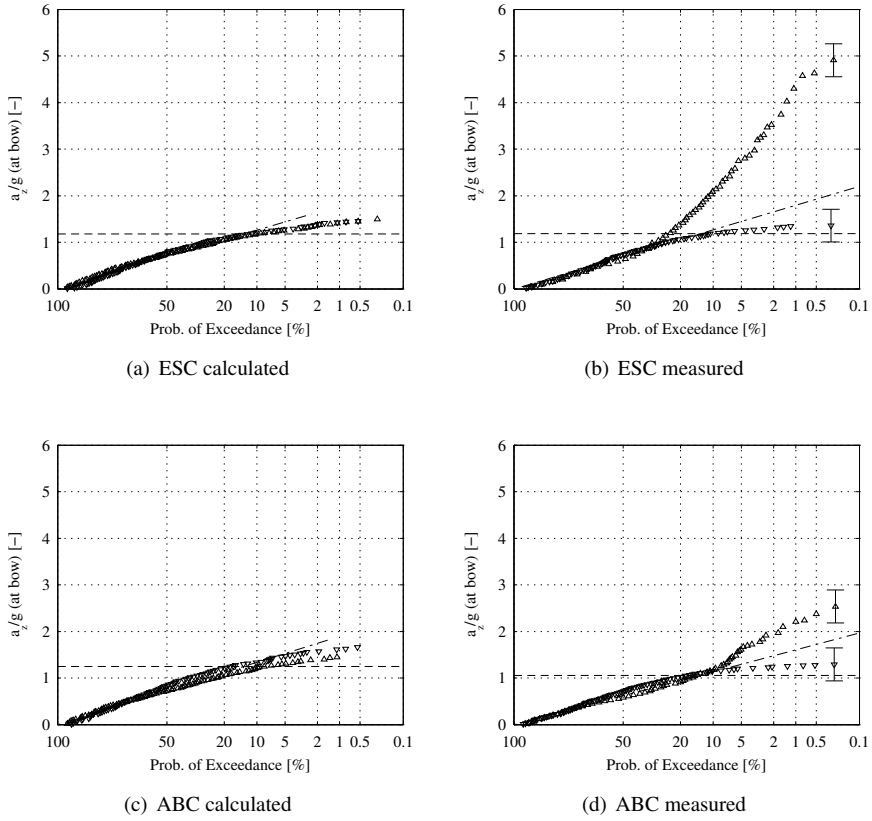
(a) ESC calculated (b) ESC measured

(c) ABC calculated (d) ABC measured

Figure 5.17: *Rayleigh plots pitch motion Enlarged Ship Concept and Axe Bow Concept, condition:* $T_p = 7.8\ s$*,* $H_{1/3} = 2.0\ m$*, and* $U = 25\ kts$

problem of predicting peaks indicated before appears here. Although the significant values as well as the troughs and crests occurring below the threshold of the significant value are predicted well, the computational method entirely misses the occurrence of the higher peaks. The large difference between both design concepts in the magnitude and the frequency of the peaks in the vertical acceleration level is not registered by the method at all. This problem is limited to the acceleration associated with the downward impact of the bow in waves; the deceleration of upward motion of the bow leaving the water surface into the air, governed by the gravity acceleration, is predicted very well.

Similarly to the prediction of the motions in regular waves analysed in section 5.3, the computational model is able to predict the motions of fast ships in irregular head seas with a significant wave height of up to 3.5 metres. The model also is able to quantify the influence of non-linearities in the motion response. Nevertheless, the prediction of the large peaks in the acceleration levels that may occur when sailing in head waves is still non-existent in the computational method and needs improvement.



(a) ESC calculated (b) ESC measured

(c) ABC calculated (d) ABC measured

Figure 5.18: *Rayleigh plots vertical acceleration at bow Enlarged Ship Concept and Axe Bow Concept, condition:* $T_p = 7.8\ s$*,* $H_{1/3} = 3.5\ m$*, and* $U = 35\ kts$

5.5 Discussion

With the presentation of these results, the validation stage within the scope of this thesis is completed. A similar study as the one presented in the current chapter has been published previously for the same computational method as developed in this thesis in chapter 3, with the exception of the material considering regular waves (De Jong and Van Walree 2009). The calm water results given in that paper show similar results as the ones presented in the current thesis. The earlier published results were limited to three forward speeds, whereas in this thesis results are shown for the entire forward speed range. The seakeeping results presented in this thesis are of better quality than the ones presented in earlier publications (e.g. de Jong and Van Walree (2009)). Especially, the introduction of the time-dependent added mass led to a substantial improvement of the outcome of the computational method (section 5.3).

Due to the applied linearisation (body-linear and linearised free surface) in the potential flow solution, the peaks in the vertical acceleration levels are absent in the computations;

whereas in chapter 2 it was shown that the peaks are in fact occurring both in the regular wave experiments as in the irregular wave experiments in head waves. Nonetheless, the global rigid body motions are in close agreement between the experiments and the computations. The main improvement of the seakeeping computations comes from the application of a time-dependent added mass term.

For the computation of slamming, the time derivative of this term is one of the main components, as can already be observed from the work of Wagner and Andersen (2003). To include this derivative would lay the foundation for the simulation of the bow impacting on the water surface and the resulting peaks in the vertical acceleration levels.

This could be used to take the 'blended' approach to the next level by adding a module to the computational method to deal with the impact problem of the fore body with the water surface while solving the rigid body motions with the current computational model. Typically such model would need to be very localised and able to cope with the relative small rise times of the acceleration levels. These rise times generally are of an order of magnitude smaller than the time step used in the current seakeeping analysis. At the same time the impact model should be integrated in the current rigid body solution and its time stepping procedure. Tuitman (2010) developed a similar procedure using a low forward speed seakeeping method for the rigid body motions and a two-dimensional specialised impact model applied at several stations in the fore body to deal with the impact problem.

As a compromise between the current absense of impacts in the computations and the implementation of an impact model, one could use the rigid body motions already available in the current method to estimate the impact velocity of the ship in the water surface to at least predict the occurrence of slamming; without quantifying the exact magnitude of the pressures and the resulting acceleration levels that occur due to the slams. In the literature criteria for the occurrence of slamming may be found. Otherwise criteria for the occurrence of peaks in the vertical acceleration level may be formulated on the basis of time trace analysis of experimental data.

Another option could be to perform detailed computations with specialised viscid or inviscid CFD codes just for the cases that slamming is expected based on the seakeeping predictions by the current code. In that way, the numerical effort spent to incorporate slamming into the predictions is limited to the slamming events, instead of applying advanced and computational demanding codes for the entire time history.

To obtain an even more complete picture of the differences between the computed and experimental data, the next step is to perform direct comparison of time traces obtained using the same wave realisation for experiment and computation. In this way the difficulties associated with comparing statistical data derived from long time traces and the stochastic nature of minima and maxima are avoided.

To be able to generalise the observations and conclusions made in this chapter, it would be opportune to consider a wider range of hull shapes of fast vessels. The ESC and ABC studied in the current work are both slender hulls. It would be interesting to observe the quality of the predictions for more full hull shapes. Also of interest is whether there are changes in the empirical coefficients necessary for the application of the method to non-slender hull forms.

Chapter 6
Conclusions and Recommendations

6.1 Introduction

The research questions of this thesis were introduced in chapter 1 as follows:

1. *What is the limiting behaviour with respect to safety and operability of high speed ships operating in waves?*
2. *What critewerewereria are applied to evaluate the limiting behaviour of high speeds operating in waves?*
3. *Can a numerical method be formulated and implemented for the analysis of the seakeeping behaviour of high speed ships? One that provides more fundamental insight than currently available methods, while remaining practically usable.*

In this final chapter the research questions are addressed followed by a discussion of the recommendations that can be made based on this work. Section 6.2 considers the first two research questions, the identification of limiting behaviour of high speed ships operating in waves and the criteria that are applied to this behaviour, described in chapter 2. Section 6.3 presents the conclusions related to the final question comprising the development, verification, and validation of the computational model discussed in chapters 3, 4, and 5. Recommendations as well as proposed future work will be discussed in section 6.4.

6.2 Limiting behaviour of high speed ships in waves

Chapter 2 describes the results of a series of full scale trials and model experiments for the seakeeping of high speed monohulls carried out for the FAST consortium, a co-operation between the Ministry of Defense of the Netherlands, the U.S. Coast Guard, Damen Shipyards High Speed Craft Department, Damen Schelde Naval Shipbuilding, and MARIN, by the Ship Hydromechanics Laboratory of the Delft University of Technology.

The full scale tests were aimed at formulating limiting criteria for the operation of high speed ships in a seaway. They consisted of data recorded aboard a high speed ship, an 'Enlarged Ship Concept', during normal operation, and interviews with crews of vessels of the same type; supplemented with data gathered aboard Dutch Search and Rescue vessels.

In head and bow quartering seas the main observation was that the crews reacted to peaks occurring in the vertical acceleration level - mainly by means of voluntary speed reduction - irrespective of averages or significant values of the motions and the acceleration levels, both for small and for larger fast vessels. This calls for the use of non-linear seakeeping analysis tools, and conventional limits set to RMS or significant levels do not suffice for high speed ships. In stern-quartering and following seas the limiting behaviour of high speed vessels was found to be characterised by non-linear behaviour such as bow-diving, shipping of green water combined with deck wetness, and broaching possibly followed by capsizing.

As the optimisation of fast ship designs aimed at improving the seakeeping behaviour resulted in significant reduction of the acceleration levels at the wheelhouse, the crew relied on far more indirect feedback such as structural vibrations following an impact at the bow to judge the seakeeping behaviour. Before this optimisation, this feedback consisted of the acceleration levels at the wheelhouse. The less pronounced feedback may lead to an increased risk of structural damage due to bow impacting and shipping of green water on deck, requiring the awareness of the crew to ensure the safety on board these vessels.

The model experiments consisted of the comparison of three designs for a patrol boat for offshore service, based on the Enlarged Ship Concept, the Axe Bow Concept, and the Wave Piercer Concept, in regular and irregular waves, and included head waves, bow- and stern-quartering waves, and following waves. Especially the acceleration levels in head waves were shown to be non-linear with respect to the wave height, in particular due to occurrence of large peaks in the vertical acceleration. This non-linear behaviour invalidates the usage of linear analysis tools and the Rayleigh plot was introduced as an alternative approach to quantify the degree of non-linearity and the occurrence of peaks, both in frequency and in magnitude.

Of the three designs the Axe Bow Concept proved to be the best design in terms of seakeeping behaviour in the conditions tested, having a 100% all year round operability in a North Sea environment. The Wave Piercer Concept performed very well in terms of ship motions and acceleration levels, but suffered heavily from shipping of green water and therefore did not meet the deck wetness requirements.

The operability of fast ships in waves was found to be highly dependent on the occurrence of peaks in the vertical acceleration levels. The measurement of these peaks is highly dependent on how the measurement is actually performed in terms of sensor type and signal processing. Moreover, both the local and global structural properties of the ship or model under consideration and the structural response may have significant influence on the measured acceleration levels. These aspects complicate the correlation of measured acceleration levels between model scale, full scale, and computations. Such comparisons should be performed with caution and special attention should be paid to the mounting of accelerometers.

In conclusion, three areas can be defined as limiting for the safe operation in waves:

1. The occurrence of peaks in the vertical acceleration levels associated with impacting of the fore body of the ship in the waves in head and bow quartering seas. These peaks have a strong non-linear relation with the incoming waves. They may cause fatigue and motion sickness to passengers and crew as well as structural damage, either immediate or in the long term by structural fatigue.
2. The tendency to bow-dive and broach in stern-quartering and following seas.

3. Deck wetness and shipping of green water, which may cause damage to equipment on deck and the superstructure, as well as impair the visibility of the surroundings for the crew.

Regarding the development of criteria for safe operation of fast ships in waves the following conclusions can be drawn:

- Limiting criteria specifically targeted at seakeeping of high speed ships in head seas should be focused on peaks occuring in the vertical acceleration levels at the bow and at the wheelhouse. The maximum accepted vertical acceleration levels were found to be $0.8g$ at the wheelhouse and $2.0g$ at the bow respectively ($1.3g$ and $2.5g$ for vessels smaller than approx. 20 metres in length).
- The application of criteria based on peak levels, instead of averages or significant levels, invalidates the use of linear seakeeping analysis tools such as Response Amplitude Operators and the application of conventional seakeeping criteria to significant (acceleration) levels.
- Other areas where criteria are applied include the behaviour in stern-quartering and following waves, the tendency to bow-dive and to broach, and deck wetness and the shipping of green water.
- Explicit quantification of threshold values only exists for peak levels of the vertical accelerations. For the other phenomena no clear measurement procedures and associated verifiable limits are defined.

6.3 Development, verification, and validation of a computational model

The second part of the research consisted of the development (chapter 3), verification (chapter 4), and validation (chapters 4 and 5) of a computational model as a tool for analysing the seakeeping behaviour of high speed ships. In the setup of the model the lessons learned in the experimental part of the research were applied. The aim of the computational method is to provide designers of fast vessels, operating at moderate to high speeds, a method that gives more fundamental insight in to the seakeeping behaviour than currently widely-used methods such as linear strip theory.

The computational method consists of a non-linear time domain simulation approach with respect to the ship's motions using a time-domain free surface Green function to include the linearised free surface effects. Although theoretically not necessary, the use of a linearised approach for the hydrodynamic forces with respect to body boundary condition was chosen to improve the computational efficiency of the method. The actual body position is retained in the calculation of hydrostatic pressures and the incident wave pressures. This type of approach is known as a blended method.

A number of extensions to the basic method were proposed in chapter 3 to make the method more applicable for high speed ships. A transom flow condition was proposed to force the flow to leave the transom stern smoothly at high ship speeds. Another extension dealt with pressure evaluation techniques, from a fully linear aproach, a blended approach, to pressure profile stretching of the linear pressure to the exact submerged body surface.

Pressure stretching in particular, relied on the computation of the free surface elevation due to both the incoming waves and the disturbance waves generated by the body. Finally, a time-dependent added mass term was proposed.

Verifications in order to ensure correctness of the method, within the limits of its assumptions,were carried out in chapter 4. These verification ranged from detailed verification of the set-up and solution of the potential flow method to verification and partly validation of the transom flow condition and the computed free surface elevation. Satisfactory results were obtained for the application of the method to deeply submerged foils, as well as to the free surface effects on foils operating in proximity of the free surface, proving the correctness of the code. The chapter was concluded with a convergence study specifically aimed at high speed ships.

The transom flow condition was shown to modify the near-transom pressure distribution as expected, yet an unresolved grid dependence was found. The steady free surface elevation around a Wigley hull travelling in calm water was reasonably well predicted, but suffered from inaccuracies due to numerical instabilities in influence evaluations near the free surface. A number of approaches were introduced to overcome these difficulties by means of filtering or grid point displacements.

The validation presented in chapter 5 was limited to the motions and vertical accelerations levels in head waves of two design concepts: the Enlarged Ship Concept and the Axe Bow Concept, using validation data from the experiments already presented in chapter 2. As discussed in the previous section, the most important limitation to the operability of these vessels lies in the occurrence of peaks in the vertical acceleration level in head seas. Nevertheless, the method is capable of solving motions in all six degrees of freedom.

In the first part of the chapter the calm water reference position was compared to experimental data. Although the trend of both the trim and rise were satisfactory captured, there existed significant differences in the comparison of the values obtained with the computations compared to the measured values. The differences between the two tested design concepts were of a similar nature, in both the measurements and the computations. Nevertheless, the running trim and sinkage may have a significant influence on the hydrodynamic behaviour of high speed vessels in waves and therefore further improvement of the estimation of the calm water trim and sinkage should be attempted.

Following the calm water tests, a set of computations and comparisons was performed in regular head waves. The main aim of this comparison was to find the optimal parameter settings and program options to successfully predict the motions in head waves. A number of methods introduced in chapter 3 were applied and their results were compared. The main findings were as follows:

- The method applied in its most basic form gives a too extreme motion response around the resonance frequencies of heave and pitch and an extreme non-linear response.
- The transom flow model, based on a pressure condition solved at the transom edge, yields comparable results to an empirical transom pressure modification.
- Modification of the pressures by means of simple pressure adaptation or pressure profile stretching worsens the motion predictions severely and should not be done for high speed ships.

- The use of a time dependent added mass term instead of a fixed added mass term significantly improves the motion predictions, especially near and below the resonance frequency, and prevents the wave 'skipping'.
- No peaks in the vertical acceleration, associated with the impact of the bow in the water surface, are predicted by the computational method.

Applying the lessons learned with the regular wave computations, finally simulations were performed in irregular head seas. The comparison with experimental data by means of comparing significant values and maxima and minima showed good agreement for the heave and pitch motions and the significant acceleration levels at the bow and at the centre of gravity. Using the method it was possible to distinguish the motion behaviour of both tested design concepts in both the measurements as the computations. Nevertheless, the occurrence of peaks in the vertical acceleration levels was entirely overlooked by the computational method, although the occurrence and the magnitude of these peaks forms the main difference between the seakeeping behaviour of both design concepts.

Summarising, it can be concluded that the computational method developed in this thesis is able to predict the motion responses in head waves of the two tested high speed design concepts satisfactory. The prediction of peaks in the vertical acceleration levels due to impact of the fore body in the water surface is lacking. Nevertheless, the occurrence of these peaks is a phenomenon that frequently occurs when sailing at high speeds in (head) waves and is determining for the operability and safety of fast ships.

Compared to current 'industry standard' methods applied to the seakeeping of high speed ships, particularily linear strip theory and strip theory for planing vessels, the method developed has a number of advantages. These include the fact that with this method a more fundamental three-dimensional pressure distribution is obtained, that includes the effects of forward speed and three-dimensional flow. Another advantage is that the method is able to cope with all wave directions and motions in all six degrees of freedom.

The computational method provides a good basis to be expanded upon by approaches specifically targeted at slamming. Such approaches would complement the already satisfactory (non-linear) rigid body motions predicted by the seakeeping simulations. Possible approaches to deal with the prediction of slamming and the resulting peaks in the vertical accelerations are discussed in the next section.

6.4 Recommendations and future work

Based on the work presented in this thesis a number of recommendations and suggestions for future work can be made. First recommendations will be made for experimental techniques and criteria development. Finally, the further development of the computational method presented in this thesis will be discussed.

6.4.1 Experimental techniques and criteria development

As stated in the conclusions in section 6.2, only for the peak levels of the vertical accelerations were explicit threshold values defined, while more types of limiting behaviour -bow-diving, shipping of green water, and broaching- were identified. Further research is needed to develop

criteria for these other aspects. The process to achieve this should include a number of steps. As a first step, more knowledge should be obtained of the fundamental underlying principles. This should be followed by identifying measurable quantities directly associated with the phenomena under consideration. The final step would be to determine limiting values for these quantities. In fact, a research project is ongoing in further developing criteria for safe and comfortable operation of fast ships in waves. The main focus of this project is on the gathering and analysis of full scale data on SAR and patrol vessels and the experience of operators and crew.

Regarding the peaks occurring in the vertical acceleration level at the bow and at the wheelhouse, continuous attention should be paid to the correct measurement of these acceleration levels in terms of sensor choice and installation, signal processing, and the influence exerted by structural responses.

As the crew gets less direct feedback as to how severe the environmental conditions are, due to the ongoing optimisation of the seakeeping behaviour of new designs, the risk of structural damage increases. This aspect is important and should be given attention when providing crews training and feedback on how to safely operate this kind of vessel. Another possibility could be to provide additional information to the crew while operating the ship, for instance by monitoring stress levels of the bow structure and providing this information to the crew in real time.

Although not discussed in this thesis, one aspect of collecting experimental data for development and validation of computational codes is the measurement of the pressure distribution on high speed vessels operating in calm water or in waves. Obtaining suffienciently accurate pressure distributions would enable validation of computational codes on a deeper level than just motions and loads. Unfortunately model experiments performed during the research were encumbered by problems related to the relatively small dynamic pressure variations due to rigid body motions on top of very large steady pressures. Moreover, there were difficulties related to the translation of discrete point measurements of a rapidly varying pressures to the pressure distribution on a hull. Significant effort needs to be spent in devising an optimal measurement set-up and procedure to enable accurate measurement of pressures at high forward speeds.

6.4.2 Computational method

Regarding the further development of the computational method presented in this thesis the first step is to extend the validation of the code. One option is to proceed to direct time trace validation, where the measured experimental wave elevation is used to perform the computations. This work is planned and may be published shortly after completion of this thesis. Additionally, the validation and application of the method to the other wave headings than head seas should be pursued. The first steps have already been taken in this direction (Van Walree and De Jong 2008; 2011). Finally, the validation could be made more general by the inclusion of a wider range of hull forms. The current hull forms are very slender and it would be interesting to study the application of the method to non-slender hull forms, or even multi-hulls.

The main area of improvement of the computational method put forward in this thesis is the prediction of peaks in vertical acceleration level due to slamming; impacting of the fore body

in the water surface. The first step is to use the current model to obtain the relative velocity of impact of the bow in the water surface and compare this to suitable empirical threshold values. This procedure would at least enable the frequency of impact that a particular ship experiences in a particular sea state to be obtained. The empirical threshold level for the impact velocity can be obtained from literature; for instance Dessi and Ciappi (2010) have published recently about this topic. Another option is to inspect the extensive experimental data set of the FAST research by relating the occurrence of peaks to the vertical rigid body velocity at the bow.

In order to enable the determination of the magnitude of the acceleration levels due to slamming more rigorous methods should be applied. Either a semi-empirical or simplified numerical model can be integrated in to the current method. Such model could be activated when the ship is expected to experience a slam, or afterwards after the relative velocity has exceeded a threshold, by going back a few time steps. A more detailed computation with a smaller time-resolution to resolve the short rise time of the acceleration level would then be performed before proceeding with the original computations. Tuitman (2010) and Hermundstad and Moan (2009a;b) proposed similar procedures. Another possibility is to perform slamming computations separate from the current method using the results of the current method as boundary or initial conditions by applying a detailed and computational expensive CFD method only for these particular situations.

Another improvement of the current method would be the improvement of the computational efficiency by using a more analytical approach instead of time consuming numerical integration for the Green function time and panel integrations. Although no trivial task, work is ongoing to achieve this improvement, with good a chance of success. Additionally, a significant improvement of the computational efficiency would enable the potential flow solution to be moved from the body-linear approach to the body-exact approach. The body-exact approach could yield substantial enhancement of the computational method, equivalent to or better than the improvement achieved in this thesis where the added mass term was moved from the body-linear approach to the body-exact approach.

The transom flow condition to model a dry transom that was introduced in the computational approach was shown to perform similarily to an empirical near-transom pressure correction. Although correctly adapting the pressure, the transom condition was shown to suffer from grid dependence. A solution may be found in closer examining the flow lines of the flow passing the transom and to pose additional, or improved, conditions on them as suggested by Raven (1996). The outcome of such improvement is uncertain, due to the limitations posed by the linearised free surface boundary condition. A better way of dealing with transom flow could also be instrumental in improving the estimation of the calm water trim and sinkage.

Part of these recommendations, in particular the slamming problem and the efficiency of the method, will be considered in a follow-up research project, the FAST III research project.

Appendices

Appendix A

Reynolds Transport Theorem

The rate of change of a scalar, vector, or tensor quantity $\eta(\boldsymbol{x}, t)$ in a volume $V(t)$ with a moving boundary $S(t)$ is dependent on the rate of $\eta(\boldsymbol{x}, t)$ in the deforming volume $V(t)$ and the flux of $\eta(\boldsymbol{x}, t)$ over $S(t)$ due to relative velocity $\boldsymbol{V}_r = \boldsymbol{V}(\boldsymbol{x}, t) - \boldsymbol{V}_S(\boldsymbol{x}, t)$ of the fluid with respect to S:

$$\frac{d}{dt}\int_{V(t)} \eta(\boldsymbol{x}, t)\, dV = \frac{\partial}{\partial t}\int_{V(t)} \eta(\boldsymbol{x}, t)\, dV + \int_{S(t)} \eta(\boldsymbol{x}, t)\, \boldsymbol{V}_r \cdot \boldsymbol{n}\, dS \tag{A.1}$$

where $\boldsymbol{n}$ the outward pointing normal on S, $\boldsymbol{V}$ the fluid velocity, and $\boldsymbol{V}_S$ the velocity of the boundary S. The first term on the right hand side can be rewritten using a three dimensional form of the Leibniz integration rule (refer to for example Gradshteyn and Ryzhik (1980):

$$\frac{\partial}{\partial t}\int_{V(t)} \eta(\boldsymbol{x}, t)\, dV = \int_{V(t)} \frac{\partial}{\partial t}\eta(\boldsymbol{x}, t)\, dV + \int_{S(t)} \eta(\boldsymbol{x}, t)\, \boldsymbol{V}_S \cdot \boldsymbol{n}\, dS \tag{A.2}$$

Combined with the first equation this results in:

$$\frac{d}{dt}\int_{V(t)} \eta(\boldsymbol{x}, t)\, dV = \int_{V(t)} \frac{\partial}{\partial t}\eta(\boldsymbol{x}, t)\, dV + \int_{S(t)} \eta(\boldsymbol{x}, t)\, \boldsymbol{V} \cdot \boldsymbol{n}\, dS \tag{A.3}$$

Using Gauss' divergence theorem on a arbitrary function (scalar or vector) $\boldsymbol{F}$:

$$\int_{V(t)} \nabla \cdot \boldsymbol{F} dV = \int_{S(t)} \boldsymbol{F} \cdot \boldsymbol{n}\, dS \tag{A.4}$$

the boundary integral in (A.3) can be replaced by a volume integral:

$$\frac{d}{dt}\int_{V(t)} \eta(\boldsymbol{x}, t)\, dV = \int_{V(t)} \frac{\partial}{\partial t}\eta(\boldsymbol{x}, t) + \nabla \cdot \eta(\boldsymbol{x}, t)\, \boldsymbol{V}\, dV \tag{A.5}$$

This result is the Reynolds transport theorem and relates the rate of change of quantity $\eta(\boldsymbol{x}, t)$ within $V(t)$ equals the rate of change of $\eta(\boldsymbol{x}, t)$ with time and the flux of $\eta(\boldsymbol{x}, t)$ over the moving boundary $S(t)$ of $V(t)$.

Appendix B

Time Derivatives in Moving Reference Frames

B.1 Convective derivative

To obtain the convective derivative, also know as the material or substantial derivative, of a scalar or vector quantity of a particle that moves in a fluid flow the chain rule of differention has to be applied. This is caused by the fact that when observing the flow from the perspective particle moving through the domain, its properties become functions of both position and time.

For the velocity potential the convective derivative $\frac{d}{dt}$ is given by the following relation, where $\frac{\partial}{\partial t}\Phi\left(\boldsymbol{x},t\right)$ is the derivative of the potential moving with the particle, while $\frac{\partial}{\partial t}\Phi\left(\boldsymbol{x}_0,t\right)$ (or when the coordinates are dropped) is the local time derivative of the potential at the space-fixed location at time t of the particle.

$$\frac{\partial}{\partial t}\Phi\left(\boldsymbol{x},t\right)=\frac{d}{dt}\Phi\left(\boldsymbol{x}_0,t\right)=\frac{\partial\Phi}{\partial t}+\frac{\partial\Phi}{\partial x}\frac{\partial x}{\partial t}+\frac{\partial\Phi}{\partial y}\frac{\partial y}{\partial t}+\frac{\partial\Phi}{\partial z}\frac{\partial z}{\partial t} \tag{B.1}$$

Or in vector notation:

$$\frac{d}{dt}\Phi\left(\boldsymbol{x}_0,t\right))=\frac{\partial\Phi\left(\boldsymbol{x}_0,t\right)}{\partial t}+\nabla\Phi\left(\boldsymbol{x}_0,t\right)\cdot\boldsymbol{V} \tag{B.2}$$

A similar relation is obtained for the convective derivative of a vector quantity such as the fluid velocity $\boldsymbol{V}\left(x,y,z,t\right)$ at the location of the particle:

$$\frac{\partial}{\partial t}\boldsymbol{V}\left(x,y,z,t\right)=\frac{d}{dt}\boldsymbol{V}=\frac{\partial\boldsymbol{V}}{\partial t}+\boldsymbol{V}\cdot\nabla\boldsymbol{V} \tag{B.3}$$

The 'convective' term $\boldsymbol{V}\cdot\nabla\boldsymbol{V}$ takes the form of a tensor derivative. This form does not only take into account the translation of the reference frame but also rotation and deformation or stretching due to the fluid motions.

B.2 Bernoulli equation in a moving reference frame

Once the flow is determined by solving the potential flow formulation, the unsteady Bernoulli equation is used to calculate the resulting pressures. The unsteady Bernoulli equation is

defined as follows in the inertial (earth fixed) frame of reference:

$$\frac{p-p_\infty}{\rho}+\frac{\partial\Phi}{\partial t}+\frac{1}{2}\left(\nabla\Phi\right)^2-gz_0=0 \tag{B.4}$$

In this equation the potential $\Phi\left(x_0,y_0,z_0,t\right)$ is defined in the earth fixed (inertial frame). The numerical solution is setup in such way that the potential and its derivatives are obtained on the panels that are moving with the ship through the domain. Fortunately, the magnitude of the term $\left(\nabla\Phi\right)^2$ is independent of the reference frame and no transformation is needed to obtain this term. The time derivative of the potential on the contrary is dependent on the reference frame and the chain rule for differentiation needs to be applied to relate the time derivative in the moving (ship or body fixed) reference frame to the time derivative in the inertial frame. This leads to a similar form for the time derivative as given in the previous section for the convective derivative. Now however the 'particle' is not moving with the fluid flow but instead the velocity of the individual collocation points $\dot{\boldsymbol{\delta}}$ needs to be taken into account in (B.2).

$$\frac{\partial}{\partial t}\Phi\left(x,y,z,t\right)=\frac{d\Phi}{dt}=\frac{\partial\Phi}{\partial t}+\nabla\Phi\cdot\dot{\boldsymbol{\delta}} \tag{B.5}$$

The velocity at the individual collocation points $\dot{\boldsymbol{\delta}}$ can be written as, where $\boldsymbol{r}$ is the position vector of the collocation point to the center of rotation, mostly the center of gravity, $\boldsymbol{V}$ the translation velocity of the center of rotation (center of gravity) of the body and $\boldsymbol{\Omega}$ the rotational velocity vector of the body, leading to (3.17) in chapter 2.

$$\dot{\boldsymbol{\delta}}=\boldsymbol{V}+\boldsymbol{\Omega}\times\boldsymbol{r} \tag{B.6}$$

The left hand side term $d\Phi/dt$ of (B.5) is obtained at the collocation points on the body, that move due the translations and rotations of the rigid body. The local time derivative at the current time location of the collocation point, the *inertial* time derivative, $\frac{\partial\Phi}{\partial t}$ needs to be used in the Bernoulli equation. Substitution in (B.4) gives:

$$\frac{p-p_\infty}{\rho}+\frac{d\Phi}{dt}-\nabla\Phi\cdot\left(\boldsymbol{V}+\boldsymbol{\Omega}\times\boldsymbol{r}\right)+\frac{1}{2}\left(\nabla\Phi\right)^2-gz_0=0 \tag{B.7}$$

B.3 Euler equations of motion

Consider a body-fixed frame with local translational velocities $\boldsymbol{V}=[u,v,w]$ and rotational velocities $\boldsymbol{\Omega}=[p,q,r]$ and a space-fixed frame with velocities $\dot{\boldsymbol{x}}_0=[\dot{x}_0,\dot{y}_0,\dot{z}_0]$.

To transform body-fixed vectors to earth fixed vectors we apply Euler rotations. These are given as a series of rotations of ψ, θ, ϕ around the intermediate body-fixed axes (in that specific order) then vectors can be transformed using the transformation matrix $\boldsymbol{ABC}$, with:

$$\boldsymbol{A}=\begin{bmatrix}\cos\psi & -\sin\psi & 0\\ \sin\psi & \cos\psi & 0\\ 0 & 0 & 1\end{bmatrix} \tag{B.8}$$

$$\boldsymbol{B}=\begin{bmatrix}\cos\theta & 0 & \sin\theta\\ 0 & 1 & 0\\ -\sin\theta & 0 & \cos\theta\end{bmatrix} \tag{B.9}$$

$$\boldsymbol{C} = \begin{bmatrix} 1 & 0 & 0 \\ 0 & \cos\phi & -\sin\phi \\ 0 & \sin\phi & \cos\phi \end{bmatrix} \tag{B.10}$$

Additionally we need the relation between the time derivatives of the Euler angles and the body-fixed rotation vector $\boldsymbol{\Omega}$ (Etkin and Reid 1995):

$$\begin{aligned} \frac{d\phi}{dt} &= p + q\sin\phi\tan\theta + r\cos\phi\tan\theta \\ \frac{d\theta}{dt} &= q\cos\phi - r\sin\phi \\ \frac{d\psi}{dt} &= (q\sin\phi + r\cos\phi)\sec\theta \end{aligned} \tag{B.11}$$

Now the space-fixed velocity vector becomes:

$$\begin{bmatrix} \dot{x}_0 \\ \dot{y}_0 \\ \dot{z}_0 \end{bmatrix} = \boldsymbol{ABC} \begin{bmatrix} u \\ v \\ w \end{bmatrix} \tag{B.12}$$

We apply Newton's second law for linear momentum to a body under an external force $\boldsymbol{F}$:

$$\boldsymbol{F} = m\frac{d\boldsymbol{V}}{dt} \tag{B.13}$$

To obtain the acceleration vector expressed in the body-fixed reference frame the chain rule needs to be applied, due to the rotational motion of the body fixed frame.

$$\frac{d\boldsymbol{V}}{dt} = \frac{\partial \boldsymbol{V}}{\partial t} + u\frac{\partial \boldsymbol{i}}{\partial t} + v\frac{\partial \boldsymbol{j}}{\partial t} + w\frac{\partial \boldsymbol{k}}{\partial t} \tag{B.14}$$

$$\frac{d\boldsymbol{V}}{dt} = \frac{\partial \boldsymbol{V}}{\partial t} + \boldsymbol{\Omega} \times \boldsymbol{V} \tag{B.15}$$

It can be proven that $\frac{\partial \boldsymbol{i}}{\partial t} = \boldsymbol{\Omega} \times \boldsymbol{i}$, etcetera for $\boldsymbol{j}$ and $\boldsymbol{k}$ (Meriam and Kraige 1998). Substituting this in Newton's second law for linear momentum we obtain the linear equations of motion expressed in the body-fixed frame. Note that the force has been decomposed in a weight part and a external force part (hydrodynamic or aerodynamic, or any other external force). m denotes the total mass of the object (ship).

$$\begin{aligned} m\left(\dot{u} + qw - rv\right) &= X - mg\sin\theta \\ m\left(\dot{v} + ru - pw\right) &= Y + mg\cos\theta\sin\phi \\ m\left(\dot{w} + pv - qu\right) &= Z - mg\sin\theta\cos\phi \end{aligned} \tag{B.16}$$

Similarily conservation of angular momentum in the body fixed frame can be used to obtain the Euler equations for angular motion. An external moment $\boldsymbol{M}$ is working on the body.

$$\boldsymbol{M} = \frac{d\boldsymbol{H}}{dt} \tag{B.17}$$

The time derivative of the angular momentum vector expressed in the body fixed velocities is given below. Note that again the chain rule is applied due to the rotational motion of the body fixed frame.

$$\frac{d\boldsymbol{H}}{dt} = \frac{\partial \boldsymbol{H}}{\partial t} + H_x \frac{\partial \boldsymbol{i}}{\partial t} + H_y \frac{\partial \boldsymbol{j}}{\partial t} + H_z \frac{\partial \boldsymbol{k}}{\partial t} \tag{B.18}$$

Using the definition of the angular momentum vector $\boldsymbol{H}$ and the assumption that the body-fixed reference axes are the principal axes of inertia:

$$\begin{aligned} \boldsymbol{H} &= I\boldsymbol{\Omega} \\ I &= \begin{bmatrix} I_{xx} & 0 & 0 \\ 0 & I_{yy} & 0 \\ 0 & 0 & I_{zz} \end{bmatrix} \qquad \boldsymbol{\Omega} = \begin{bmatrix} p \\ q \\ r \end{bmatrix} \end{aligned} \tag{B.19}$$

Again using $\frac{\partial \boldsymbol{i}}{\partial t} = \boldsymbol{\Omega} \times \boldsymbol{i}$, etcetera for $\boldsymbol{j}$ and $\boldsymbol{k}$ the following is obtained:

$$\begin{aligned} \frac{d\boldsymbol{H}}{dt} &= \frac{\partial \boldsymbol{H}}{\partial t} + \boldsymbol{\Omega} \times \boldsymbol{H} \\ \frac{d\boldsymbol{H}}{dt} &= \frac{\partial \boldsymbol{H}}{\partial t} + \boldsymbol{\Omega} \times I\boldsymbol{\Omega} \end{aligned} \tag{B.20}$$

Expanding the terms and substitution in (B.14) yields the Euler equations for angular motion in the body fixed reference frame:

$$\begin{aligned} \dot{p} + qr\,(I_{zz} - I_{yy}) &= K \\ \dot{q} + rp\,(I_{xx} - I_{zz}) &= M \\ \dot{r} + pq\,(I_{yy} - I_{xx}) &= N \end{aligned} \tag{B.21}$$

B.3.1 Body to space-fixed transformations

From (B.16) can be concluded that the body-fixed acceleration vector equals:

$$\begin{bmatrix} \ddot{x} \\ \ddot{y} \\ \ddot{z} \end{bmatrix} = \begin{bmatrix} \dot{u} \\ \dot{v} \\ \dot{w} \end{bmatrix} + \begin{bmatrix} qw - rv \\ ru - pw \\ pv - qu \end{bmatrix} \tag{B.22}$$

To find the relation between body-fixed and space-fixed linear accelerations, let us limit our analysis to 2D. We retain x, z, θ, dropping the remaining terms. The (body fixed) equations of motion become:

$$\begin{aligned} M\,(\dot{u} + qw) &= X - Mg\sin\theta \\ M\,(\dot{w} - qu) &= Z - Mg\cos\theta \end{aligned} \tag{B.23}$$

The space-fixed velocity vector:

$$\begin{aligned} \dot{x}_0 &= u\cos\theta + w\sin\theta \\ \dot{z}_0 &= -u\sin\theta + w\cos\theta \end{aligned} \tag{B.24}$$

The space-fixed acceleration vector is the time derivative of the space fixed velocity vector:

$$\begin{aligned} \ddot{x}_0 &= \dot{u}\cos\theta - u\dot{\theta}\sin\theta + \dot{w}\sin\theta + w\dot{\theta}\cos\theta \\ \ddot{z}_0 &= -\dot{u}\sin\theta - u\dot{\theta}\cos\theta + \dot{w}\cos\theta - w\dot{\theta}\sin\theta \end{aligned} \tag{B.25}$$

The time derivative of the Euler angle θ simply reduces to q in 2D, enabling us to write:

$$\begin{bmatrix} \ddot{x}_0 \\ \ddot{z}_0 \end{bmatrix} = \begin{bmatrix} \cos\theta\sin\theta \\ -\sin\theta\cos\theta \end{bmatrix} \begin{bmatrix} \dot{u} \\ \dot{w} \end{bmatrix} + \begin{bmatrix} \cos\theta\sin\theta \\ -\sin\theta\cos\theta \end{bmatrix} \begin{bmatrix} qw \\ -qu \end{bmatrix} \tag{B.26}$$

Comparing this vector to the body-fixed acceleration vector we can easily obtain the difference between both vectors:

$$\begin{bmatrix} \ddot{x}_0 \\ \ddot{z}_0 \end{bmatrix} = \boldsymbol{B}\left(\begin{bmatrix} \dot{u} \\ \dot{w} \end{bmatrix} + \begin{bmatrix} qw \\ -qu \end{bmatrix} \right) \tag{B.27}$$

$$\begin{bmatrix} \ddot{x}_0 \\ \ddot{z}_0 \end{bmatrix} = \boldsymbol{B}\left(\begin{bmatrix} \ddot{x} \\ \ddot{z} \end{bmatrix} \right) \tag{B.28}$$

The 3D equivalent being:

$$\begin{bmatrix} \ddot{x}_0 \\ \ddot{y}_0 \\ \ddot{z}_0 \end{bmatrix} = \boldsymbol{ABC}\left(\begin{bmatrix} \dot{u} \\ \dot{v} \\ \dot{w} \end{bmatrix} + \boldsymbol{\Omega} \times \begin{bmatrix} u \\ v \\ w \end{bmatrix} \right) \tag{B.29}$$

$$\begin{bmatrix} \ddot{x}_0 \\ \ddot{y}_0 \\ \ddot{z}_0 \end{bmatrix} = \boldsymbol{ABC}\left(\begin{bmatrix} \ddot{x} \\ \ddot{y} \\ \ddot{z} \end{bmatrix} \right) \tag{B.30}$$

This means that the space fixed acceleration vector is simply the transformation from the body fixed frame to the space fixed frame of the body fixed acceleration vector. It is nevertheless wrong to assume that the body fixed acceleration vector equals the simple time derivative of the body fixed velocity vector as that is not the inertial acceleration vector necessary for applying Newton's second law. The chain rule needs to be applied to obtain the inertial acceleration vector.

Appendix C

Potential Flow Details

C.1 Elimination of the free surface integral

The integral over the free surface in chapter 3, (3.48) would require an expensive numerical evaluation, as the free surface is unbounded. This integral can be replaced by a more simple expression. First, recall the free surface boundary condition (3.26). Using the definition of a free surface normal, one can write:

$$\frac{\partial}{\partial n} = \frac{\partial}{\partial z_0} = -\frac{1}{g}\frac{\partial^2}{\partial t^2} = -\frac{1}{g}\frac{\partial^2}{\partial \tau^2} \tag{C.1}$$

Using this expression, the integral over the free surface in (3.48) can be rewritten as:

$$\int_{S_F(\tau)} \left(\Phi^d G_{\tau n} - G_\tau \Phi^d_n\right) dS = -\frac{1}{g}\int_{S_F(\tau)} \frac{\partial}{\partial \tau}\left(\Phi^d G_{\tau\tau} - G_\tau \Phi^d_\tau\right) dS \tag{C.2}$$

Differentiation and integration on the free surface integral in the right hand side of (C.2) can be interchanged by using the Reynolds Transport Theorem. This theorem is detailed in appendix A. Here in particular the form given by (A.2) is applied in two dimensions, with the following substitutions:

The surface S_F for the domain Ω

The intersection of S_F with the free surface $l_w(\tau)$ for Γ

The two dimensional normal velocity V_N for the inner product $\boldsymbol{v}_\Gamma \cdot \boldsymbol{n}$

The past time τ for t

The function $-1/g\left(\Phi^d G_{\tau\tau} - G_\tau \Phi^d_\tau\right)$ for $\eta(\boldsymbol{x}, t)$

V_N is the two dimensional normal velocity of the body at $l_w(\tau)$ in the plane of the linearised free surface. Rearranging the free surface integral in the right hand side of (C.2) can be expressed as:

$$-\frac{1}{g}\int_{S_F(\tau)} \frac{\partial}{\partial \tau}\left(\Phi^d G_{\tau\tau} - G_\tau \Phi^d_\tau\right) dS = -\frac{1}{g} \left[\frac{\partial}{\partial \tau}\int_{S_F(\tau)} \left(\Phi^d G_{\tau\tau} - g G_\tau \Phi^d_\tau\right) dS - \int_{l_w(\tau)} \left(\Phi^d G_{\tau\tau} - G_\tau \Phi^d_\tau\right) V_N dL\right] \tag{C.3}$$

The remaining task is to eliminate the free surface integral in the right hand side of (C.3). This elimination removes the need for solving the free surface and the potential solution can be obtained by solely solving over the surfaces of interest (submerged hull, lifting surfaces and their wake). Integration of this term with respect to time yields:

$$-\frac{1}{g}\int_0^t \frac{\partial}{\partial\tau}\int_{S_F(\tau)}\left(\Phi^d G_{\tau\tau}-gG_\tau\Phi^d_\tau\right)dSd\tau = -\frac{1}{g}\int_{S_F(\tau)}\left(\Phi^d G_{\tau\tau}-gG_\tau\Phi^d_\tau\right)dS\Big|_{\tau=t} + \frac{1}{g}\int_{S_F(\tau)}\left(\Phi^d G_{\tau\tau}-gG_\tau\Phi^d_\tau\right)dS\Big|_{\tau=0} \quad \text{(C.4)}$$

The $\tau = t$-contribution can be rewritten by using the following:

$G^f_n\big|_{\tau=t} = 0$ using the definition in (3.38)
$\Phi^d G_{\tau\tau}\big|_{\tau=t} = -g\Phi^d G_n\big|_{\tau=t} = -g\Phi^d G^0_n\big|_{\tau=t} - g\Phi^d G^f_n\big|_{\tau=t}$ using (C.1)
$\Phi^d G_{\tau\tau}\big|_{\tau=t} = -g\Phi^d G^0_n$ combining the previous two statements
$G^f_\tau\big|_{\tau=t} = 0$ using the definition of the Green function
$G^0_\tau = 0$ using the definition of the Green function

The $\tau = 0$-contribution can be easily eliminated by considering the initial conditions given in (3.37). What remains is:

$$-\int_0^t \frac{1}{g}\frac{\partial}{\partial\tau}\int_{S_F(\tau)}\left(\Phi^d G_{\tau\tau}-gG_\tau\Phi^d_\tau\right)dSd\tau = \int_{S_F(\tau)}\Phi^d G^0_n dS \quad \text{(C.5)}$$

Integration of (C.3) with respect to time, and substitution of (C.5) in (C.3) yields an expression of the free surface integral for (3.48).

$$\int_0^t\int_{S_F(\tau)}\left(\Phi^d G_{\tau n}-G_\tau\Phi^d_n\right)dSd\tau = \int_{S_F(\tau)}\Phi^d G^0_n dS + \frac{1}{g}\int_0^t\int_{l_w(\tau)}\left(\Phi^d G_{\tau\tau}-G_\tau\Phi^d_\tau\right)V_N dLd\tau \quad \text{(C.6)}$$

The final step in the elimination is to eliminate the G^0-term in (C.6). To achieve this, Green's second identity now is applied on $G^0\left(\boldsymbol{x}_0,\boldsymbol{\xi}\right)$ and $\Phi^d\left(\boldsymbol{\xi},t\right)$, along with the Laplace equation:

$$\int_{S_\infty\cup S_\epsilon\cup S_{FHLW}(t)}\left(\Phi^d G^0_n - G^0\Phi^d_n\right)dS = 0 \quad \text{(C.7)}$$

Again, the contribution on S_∞ tends to zero, however the contribution of S_ϵ will not be zero, as G^0 has a singular point at $\boldsymbol{x}_0 = \boldsymbol{\xi}$. This contribution can be calculated (as detailed by Hunt (1980)) and equals $4\pi T\left(p\right)\Phi^d\left(\boldsymbol{x}_0,t\right)$. Where T is defined as:

$$T(p) = \begin{cases} 1 & p \in V(t) \\ 1/2 & p \in S_{HL}(t) \\ 0 & \text{otherwise} \end{cases} \tag{C.8}$$

Substitution of these results into (C.7) and using that $G^0 = 0$ at S_F yields:

$$4\pi T\Phi^d + \int_{S_{HLW}(t)} \left(\Phi^d G_n^0 - G^0 \Phi_n^d\right) dS + \int_{S_F(t)} \Phi^d G_n^0 dS = 0 \tag{C.9}$$

Combining this result with (C.6) yields an expression for the free surface integral in (3.48); now we can eliminate this free surface integral from the solution.

$$\int_0^t \int_{S_F(\tau)} \left(\Phi^d G_{\tau n} - G_\tau \Phi_n^d\right) dS d\tau = -4\pi T\Phi^d - \int_{S_{HLW}(t)} \left(\Phi^d G_n^0 - G^0 \Phi_n^d\right) dS + \frac{1}{g} \int_0^t \int_{l_w(\tau)} \left(\Phi^d G_{\tau\tau} - G_\tau \Phi_\tau^d\right) V_N dL d\tau \tag{C.10}$$

C.2 Inspection of the waterline integral

In the formulation of the potential flow equations in terms of a source and doublet distribution the waterline integral contains a time derivative of the velocity potential (refer to (3.54) in section 3.6.1). This time derivative can be replaced quite conveniently when using a source only formulation. However when using a combined source-doublet distribution a quite complex integral is the result. Due to this complication some extra attention is given here to this specific integral, repeated below. The method followed here is equivalent to the derivation given by Bingham (1994) for a source-only formulation.

$$-\int_{l_w(\tau)} G_\tau^f \left(\Phi_\tau^{d+} - \Phi_\tau^{d-}\right) V_N dL \tag{C.11}$$

In order to remove the time derivatives we can use the definition of a convective derivative, relating the time derivative travelling with the body (d/dt) to the space-fixed time derivative ($\partial/\partial t$) given in appendix B. The minus sign appears due to definition $\partial/\partial t = -\partial/\partial\tau$.

$$\frac{d\left(\Phi^{d+} - \Phi^{d-}\right)}{dt} = -\frac{\partial\left(\Phi^{d+} - \Phi^{d-}\right)}{\partial\tau} + \boldsymbol{V} \cdot \nabla\left(\Phi^{d+} - \Phi^{d-}\right) \tag{C.12}$$

C.2.1 Source-only formulation

In case of a source-only distribution the following is true for the jump in the potential and the jump in normal derivative of the potential:

$$\left.\begin{aligned} \Phi^{d+} - \Phi^{d-} &= 0 \\ \Phi_n^{d+} - \Phi_n^{d-} &= \sigma \end{aligned}\right\} \forall \quad q \in S_H \tag{C.13}$$

Eq. C.13 is applied on the body. In case $\Phi^{d+} - \Phi^{d-} = 0$ everywhere on the body, then its derivative on the body will equal zero as well:

$$\frac{d\left(\Phi^{d+} - \Phi^{d-}\right)}{dt} = -\left(\Phi_\tau^{d+} - \Phi_\tau^{d-}\right) + \boldsymbol{V} \cdot \nabla\left(\Phi^{d+} - \Phi^{d-}\right) = 0 \tag{C.14}$$

The gradient of $\Phi^{d+} - \Phi^{d-}$ will equal zero as well in the tangential directions everwhere on the body. In this case the gradient term can be rewritten as:

$$\nabla\left(\Phi^{d+} - \Phi^{d-}\right) = \boldsymbol{n}\left(\Phi_n^{d+} - \Phi_n^{d-}\right) \tag{C.15}$$

Substitution of this result in (C.14) leads to:

$$\Phi_\tau^{d+} - \Phi_\tau^{d-} = \boldsymbol{V} \cdot \boldsymbol{n}\left(\Phi_n^{d+} - \Phi_n^{d-}\right) \tag{C.16}$$

And finally, the original integral can be rewritten as given below, by using the definition of σ in Eq. C.13 and $V_n = \boldsymbol{V} \cdot \boldsymbol{n}$.

$$-\int_{l_w(\tau)} G_\tau^f\left(\Phi_\tau^{d+} - \Phi_\tau^{d-}\right) V_N dL = -\int_{l_w(\tau)} G_\tau^f \sigma V_n V_N dL \tag{C.17}$$

C.2.2 Combined source-doublet formulation

In case of combined source-doublet distribution on the body the processing of (C.13) becomes much more complicated. Now the following is true for the jump in the potential and the jump in normal derivative of the potential:

$$\left.\begin{aligned}\Phi^{d+} - \Phi^{d-} &= -\mu \\ \Phi_n^{d+} - \Phi_n^{d-} &= \sigma\end{aligned}\right\} \forall \quad q \in S_H \tag{C.18}$$

Now, $\Phi_\tau^{d+} - \Phi_\tau^{d-}$ is not zero, and the convenient reductions of the source-only formulation do not apply. Instead the definition of the convective derivative contains derivatives of the doublet distribution. Using $\partial/\partial t = -\partial/\partial\tau$ the following is the result:

$$\frac{d\mu}{d\tau} = \left(\Phi_\tau^{d+} - \Phi_\tau^{d-}\right) - \boldsymbol{V} \cdot \nabla\mu \tag{C.19}$$

Substitution results in the following expression. Now no simplifications are possible, as the value of $\mu = \Phi_\tau^{d+} - \Phi_\tau^{d-}$ varries over the body.

$$-\int_{l_w(\tau)} G_\tau^f\left(\Phi_\tau^{d+} - \Phi_\tau^{d-}\right) V_N dL = -\int_{l_w(\tau)} G_\tau^f\left(\boldsymbol{V} \cdot \nabla\mu + \frac{d\mu}{d\tau}\right) V_N dL \tag{C.20}$$

In this equation $d\mu/d\tau$ as well as $\nabla\mu$ need to be evaluated in the body fixed coordinates over the entire memory history. A slight simplification can be obtained by using a constant forward speed $\boldsymbol{V} = [U_{vel}, 0, 0]$.

$$-\int_{l_w(\tau)} G_\tau^f\left(\Phi_\tau^{d+} - \Phi_\tau^{d-}\right) V_N dL = -\int_{l_w(\tau)} G_\tau^f\left(U_{vel}\frac{\partial\mu}{\partial x} + \frac{d\mu}{d\tau}\right) V_N dL \tag{C.21}$$

In most cases in the current code doublet elements are only applied on a small part of the aft-body for use with the transom flow condition introduced in section 3.6.3. For most high speed ships fitted with a transom stern the waterline in this region as (nearly) parallel to the longitudinal axis. When using a body-linear approach V_N will equal (nearly zero) and the contribution of the doublet waterline integral will vanish. For this reason, this integral has been neglected in the computational method. However, when assymetric bodies or symmetric linearised put in a asymmetric position are simulated (for instance when simulating a constant angle of attach in the horizontal plane) or when doublets are distributed near the waterline that is not parallel to the undisturbed waterline this term will be of importance.

Appendix D
Uncertainty Analysis

D.1 Introduction

This appendix details the uncertainty assessment that was performed for the experimental results presented in thesis. The aim was to obtain the uncertainty in the experimental results at a 95% confidence level. The approach follows the ITTC Recommended Procedures and Guidelines for Uncertainty Analysis (ITTC 2002a; 1999) where possible.

Nevertheless, whereas the ITTC documents cited above are aimed at the uncertainty assessment for resistance towing tank tests, additional references have been consulted to help tailor the uncertainty assessment for motions in regular and irregular head waves. Irvine et al. (2008) presented a study into the heave and pitch motions of a surface combatant in regular head waves and includes a uncertainty assessment. (ITTC 2008) are more recent ITTC Recommended Procedures and Guidelines for planar motion mechanism tests, including uncertainty assessment.

In this appendix first the uncertainty assessment approach will be discussed, followed by a description of the procedure followed to quantify the elemental bias and precision limits. Finally, the uncertainty assessment will be discussed for three different sets of experiments:

1. Calm water experiments to obtain the calm water resistance, rise, and trim.
2. Experiments in regular head waves to obtain the heave and pitch responses and phase lags.
3. Experiments in irregular head waves to obtain the heave, pitch, and vertical acceleration levels peak statistics.

D.2 Approach

The discussion in this section is a summary of the methodology outlined in ITTC (2002a). It is assumed that the total uncertainty in the experimental result is composed of a precision (random) component and a bias (systematic) component. The former contributes to the scatter of the data, while the latter contributes to a shift of the mean of the (scattered) measured value with respect to the true value.

Figure D.1, taken from ITTC (2002a), illustrates this. In the figure, μ is the average of multiple readings of the variable X with true value X_{true}; β signifies the bias error. The bell curve illustrates the degree of randomness of the multiple measurements of variable X.

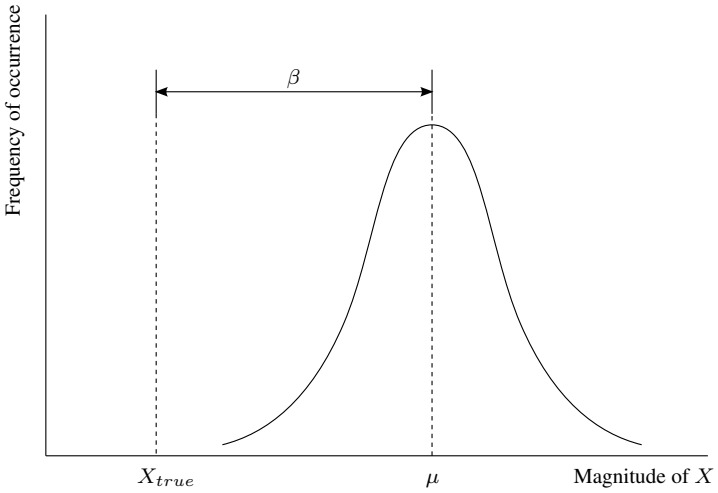


Figure D.1: *Errors in the measurement of a variable X (ITTC 2002a)*

When the precision error (the randomness of the measurement) increases, the bell curve in the figure increases in width. An increase of the bias error results in a larger distance between the true value X_{true} and the average value of all measurements μ.

Usually, the experimental outcome is the result of variables that are measured during an experiment by means of multiple sensors, and that are acquired by a data acquisition setup to be processed and stored digitally. Often, the chain from the sensor to the data acquisition contains additional components that deal with signal conditioning such as amplifiers and filters. Finally, the acquired variables are processed into the final outcome. The data processing usually takes the form of a number of equations that process the individual measured variables into aggregated variables that form the final outcome of the experiment and are represented by tables in graphs. These equations are so-called data reduction eqautions (or DREs).

Also the errors that are contained within the individual measured variables, the elemental errors, are propagated through these elements in the measurement chain to the aggregated variables. In order to quantify the total error, or the total uncertainty, in these final variables one needs to consider how the individual errors propagate through each of the elements in the chain.

This can be done in a few different ways. First, one can consider all the individual steps in the chain and determine how the error propagates through each of these steps. This starts by determining the error in the sensor, by means of experiments or by using the data specified by the manufacturer, followed by determining how the measured signal travels through the data conditioning (filters and amplyfiers) and data acquisition (analog to digital conversion). The final step is the propagation of the errors of different sources through de data reduction equations.

Second, it is sometimes possible to apply a so-called end-to-end method to establish the error in the final outcome. This can be done by taking multiple readings of the same aggregated variable under the same conditions and applying statistics to these multiple readings to obtain the uncertainty in the aggregated variable. By considering the randomness of the

variable the precision component can be obtained. It is more difficult and often practically impossible to obtain the bias error in this way, as one needs to obtain the true value of the aggregated variable. This requires an alternative way of obtaining this true value with at least a known uncertainty, preferable an order of magnitude or more accurate than the measurement procedure under consideration.

A third approach, is the combination of both approaches above. Most preferably, the precision error is obtained by the end-to-end method, a more convenient method than the elementwise approach while being accurate. At the same time the bias error is obtained by a hybrid method, using the end-to-end method for instance in the sensor and data conditioning chain, followed by a elementwise propagation through the data acquisition and data processing. The end-to-end method for the bias error typically makes use of calibration data and specifies the error between the measured calibration data and the calibration curve that is fitted through the calibration data. Added to this are systematic arising from the calibration procedure (for instance the error of the calibration weights used to calibrate a force transducer) and errors that occur further up in the chain.

In the uncertainty assessment presented here, mostly the final, third, approach is applied. One difference is that the precision error is not always obtained by a end-to-end method but rather by the elementwise method, as not all end-to-end precision measurements have been performed, especially not for unsteady wave testing.

It is assumed in the following that the error distributions are well-approximated by the Gaussian distribution. Uncertainty estimates will be performed with a 95% confidence interval using large sample size techniques (as detailed in ITTC (2002a)), and finally that all errors are uncorrelated.

D.2.1 Total uncertainty

The total uncertainty interval $\pm U_i$ about variable X_i is defined as the band around X_i with a 95% confidence level within which the true value lies. The extend of the interval is determined by a combination of the bias error B_i and the precision error P_i of the same variable X_i, both as well with a 95% confidence level:

$$U_i = \sqrt{B_i^2 + P_i^2} \tag{D.1}$$

D.2.2 Bias limits

Bias errors may be assumed to be build up from seperate contributions due to calibration errors, data acquisition errors, data reduction errors, test technique errors, etcetera. Each of these categories may contain multiple elemental sources of bias. If the bias error B_i of variable X_i is caused by M elemental sources of bias with each their own bias contribution to X_i of B_ij then the total bias error B_i may be computed by:

$$B_i = \sqrt{\sum_{j=1}^{M} B_{ij}^2} \tag{D.2}$$

The bias components B_{ij} must by estimated with the best possible information available to the experimenter. Often information supplied by the manufacturer of a sensor contains the

absolute value of the 95% confidence interval, for instance $\pm 0.5^{\circ}C$ for a thermistor. Assuming that this error is normal distributed then one may assume that the standard devitation S_T equals half this value, while using a coverage factor of 2 the bias error again equals $B_T = 2S_T$ or $\pm 0.5^{\circ}C$ (ITTC 2002a).

Another possibility is that the experimenter calibrates elementary sensors himself and obtains a calibration curve. This calibration curve is approximated by a curve fit, in most cases a linear fit. The error between the actual values obtained during the calibration and the linear regression curve is a measure for the bias error. The error that can be use for this is the Standard Error Estimate (SEE) given by Coleman and Steele (1999) as:

$$SEE = \sqrt{\frac{\sum_{i=1}^{N} \left(Y_i - (aX_i + b)\right)^2}{N - 2}} \tag{D.3}$$

where N is the number of calibration measurements, Y_i is the actual value of the calibration at point i with value X_i, and a and b the coefficients of the fitted linear curve. Coleman and Steele (1999) propose that a band of $\pm 2SEE$ holds approximately 95% of the data points, making this band the 95% confidence interval for the fitted calibration curve:

$$B_i = 2SEE \tag{D.4}$$

Added to the bias error in the calibration curve may be the bias error in the calibration procedure (for instance the weight error of the calibration weights used, or in error reading a ruler to obtain a distance against that is used to calibrate a sensor) and the data acquisition error, particularily due to the analog to digitial conversion of the data.

D.2.3 Precision limits

When the end-to-end approach is applied for the estimation of the precision of measured variable X_i, then the precision limit can be obtained by taking the standard deviation S_i of N_i readings of X_i and multiplying by the coverage factor K. The coverage factor is by convention (ITTC 2002a, Taylor and Kuyatt 1993) set equal to 2, its limit for large sample sizes.

$$S_i = \sqrt{\sum_{k=1}^{N_i} \frac{\left((X_i)_k - \bar{X}_i\right)^2}{N_i - 1}} \tag{D.5}$$

$$\bar{X}_i = \frac{1}{N_i} \sum_{k=1}^{N_i} (X_i)_k \tag{D.6}$$

$$P_i = KS_i \tag{D.7}$$

When a mean value of X_i is used in the data processing instead of X_i from a single point measurement then the precision limit decreases as given below, where M is the number of samples over which the mean value is determined:

$$P_i = \frac{KS_i}{\sqrt{N_i}} \tag{D.8}$$

D.2.4 Error propagation

The methods described in the previous sections to obtain bias and precision limits can be used to derive the uncertainty in the elementary sources, before processing them into the aggregated variables that form the experimental results. The last step is to propagate the errors trough the data reduction equations. First we assume that a reduced variable R is obtained from the measured variables X_i (with known bias and precision limits, B_i and P_i) by the following reduction equation:

$$R = r\left(X_1, X_2, ..., X_J\right) \tag{D.9}$$

Then the precision and bias limits of the reduced (or aggregated) variable R can be computed by:

$$\begin{aligned} P_R &= \sqrt{\sum_{i=1}^{J} \left(\vartheta_i P_i\right)^2} \\ B_R &= \sqrt{\sum_{i=1}^{J} \left(\vartheta_i B_i\right)^2} \end{aligned} \tag{D.10}$$

In these equation ϑ_i is the partial derivative of the reduced variable R with respect to the elemental variable X_i:

$$\vartheta_i = \frac{\partial R}{\partial X_i} \tag{D.11}$$

In some cases, when there is a correlation between one or more elemental variables also cross-terms need to be included (Coleman and Steele 1999, ITTC 2002a). This occurs when there is interdependence between the bias errors of different elemental sources. It is assumed that this is not the case here.

D.3 Elemental bias limits

D.3.1 Environment

The gravitational acceleration in the Netherlands, where the experiments have been performed, is on average 9.81 m/s^2, with a variation over the country of 0.0025 m/s^2. The latter is assumed to equal the bias limit in the gravitational acceleration.

D.3.2 Hull geometry

In accordance with the ITTC Guidelines a manufacturing error in the model geometry of $\pm$ 1 mm in all coordinates has been assumed. For the model length this resulted in a bias error B_L of 2 mm. Extending this to the beam and draft, the beam had an error of 2 mm and the draft an error of 1 mm. By assuming the block coefficient $C_b = \nabla/(LBT)$ and the wetted surface coefficient $C_S = S/(\nabla L)$ remain constant the resulting bias error in the wetted surface could be obtained. There are no precision limits associated with the hull geometry.

D.3.3 Model speed

The bias limit of the model speed has been obtained in two different ways. The first way was by computing the SEE with respect to the *desired* value of the forward speed for each of the two given forward speeds and applying (D.4) as no separate method of obtaining the forward speed was available. This led to a rough estimate of the bias error of 0.002 m/s at 2.876 m/s and of 0.009 m/s at 4.026 m/s.

The second approach was to study the actual mechanism of measurement of the forward speed. The speed measurement is performed by obtaining the rotational speed of the engine shaft of the master electrical motor on the towing carriage by means of pulse counting. There are 4096 pulses per revolution, the reduction rate from engine shaft to drive wheel is 14.45:1. The diameter of the engine shaft has been measured and equals 691 mm. This gives 27.26 pulses per millimeter travel of the carriage. Using this information, the forward speed is computed and sent to the data acquisition computer by converting from digital to analog by a 16 bit DA conversion and back to digital at the data acquisition computer by a 16 bit AD conversion with a range of 20 V.

The following error sources have been identified:

- Measurement error of the diameter of the carriage drive wheel: 1 mm
- Resolution of the pulse count system (specified by manufacturer): 0.2 rpm
- Both AD and DA conversion: each were assumed to have an error of 1 bit out of a 16 bit conversion at a 20 V range and a calibration factor of 1 V/(m/s)

All errors in the chain have been converted into bias errors of the forward speed in m/s. They were added to yield the bias limit of the model speed by (D.2), resulting in a bias error of 0.006 m/s. This value is in the same range as the first estimates using the SEE with respect to the *desired* value of the forward speed, but its definition is better founded than the first method, where instead of the *true* value, the *desired* value was used. For this reason 0.006 m/s was used as the bias error B_U of the forward speed.

D.3.4 Wave elevation and frequency

The wave elevation was obtained by two wave probes. One probe was of the wire type, the other of a servo type with a servo controlled vertical rod that follows the free surface profile. The wave height that was used in most of the data processing was obtained by the wire type probe. The servo type probe had a comparable, slightly worse, performance. Its accuracy estimation procedure was nearly identical to the one of the wire type probe.

Before the model was mounted under the towing carriage an extensive series of wave calibrations has been carried out in order to be able to find to correct wave generator control paramters to generate the desired regular waves. This extensive data set was used to estimate the precision and bias limits of the wave height and the wave frequency measurement obtained from the wave probes.

The bias limit of the wave elevation B_{ζ_i} was obtained again by studying the measurement chain. The first bias error was obtained from the calibration data by studying the fit of the linear calibration curve to the data points by means of eqs. (D.3) and (D.9).

The calibration was performed by displacing the wave height sensor vertically along a ruler in and out the water over a range of distances and measuring the output voltage at the amplifier output. Then a reading error of 0.5 mm was assumed in this process. Furthermore a 0.5 degree probe misalignment error between calibration and measurement was assumed and the 16 bit AD conversion was taken into account. These assumptions were converted to error components in the wave height in mm and combined using (D.2).

The wave frequency during the wave calibration tests was obtained by a least squares fitting method of a sine to the measured time trace by the wave probe. Both precision and bias errors of the wave frequency, P_ω and B_ω, were computed using the end-to-end approach. The bias error was obtained by computing the SEE with respect to the *desired* value, as no indepedent, more accurate, means of obtaining the wave frequency were available. This was done over the complete range of wave frequencies, for multiple runs at each frequency. The final results were averaged over the wave frequency.

A final error that needed to be specified is the error in the longitudinal position of the wave probe with respect to the model center of gravity. This quantity is important when computing the relative phase angle between the motions of the model and the incoming wave. This was specified as a bias error B_D of 1 mm. There is no precision error associated with this value.

D.3.5 Motions

The motions of the model were obtained by a realtime dynamic motion tracking system, the Krypton Rodym DMM system. This tracking system consists of a three camera setup mounted on the towing carriage that monitor a number of IR LEDs on a target plate fixed on the model and a separate computer that computes the location and angular orientation of the target plate in three-dimensional space using triangulation. The measurement volume is determined by the field of view of the three cameras and measures about 17 cubic metres. The manufacturer divided this volume in three accuracy zones: 1.5 to 3.0 distance, 3.0 to 5.0 metres distance and 5.0 tot 6.0 metres distance. The first zone is reported to have a $\pm$ 0.1 mm accuracy, the next $\pm$ 0.2 mm and the final zone $\pm$ 0.3 mm.

The bias limits of the heave and pitch motions, B_{z_i} and B_{θ_i}, were again obtained by studying the measurement and data acquisition chain. The measurements were performed in the first accuracy zone, leading to the first bias error of 0.1 mm. An alignment error of the plate of about 0.5 degrees was assumed, leading to a cosine error in the vertical motion. An error in target plate placing of 1 mm both horizonally as vertically was assumed, leading to an error in the vertical motion under rotation.

The LEDs were placed around 100 mm apart, which was used to translate the distance inaccuracy into an angular inaccuracy. The signal was originally digitally sampled at 12 bits, but latter converted to 16 bits. For both conversions an error of 1 bit was assumed. All the individual sources were converted to an error in mm and in degrees for the heave and pitch motion respectively and added using (D.2).

D.3.6 Vertical acceleration levels

These sensors were factory calibrated with a specified accuracy of $0.02g$s. The calibration was checked by performing measurements with sensors in upright and reversed positions, and

90 degrees rotated with respect to the horizontal axis, and was found to be correct. On top of the manufacturer specified accuracy, a bias error due to 0.5 deg misalignment was assumed and a bias error due to the 16 bit AD conversion.

D.3.7 Summary of the results

The results that were obtained applying the procedures for the indivivual components in the measurement setup described in the previous sections are summarised in table D.1.

Table D.1: *Elemental bias limits*

Quantity	Symbol	Unit	Bias limit
Gravitational acceleration	g	m/s^2	0.025
Model length	L_m	mm	2.000
Model wetted surface	S_m	m^2	0.011
Model forward speed	U	m/s	0.006
Wave elevation (wire type)	ζ_i	mm	3.570
Wave elevation (servo type)		mm	5.211
Wave frequency	ω	rad/s	0.015
Position wave probe	D	mm	1.000
Heave motion	z_i	mm	0.193
Pitch motion	θ_i	deg	0.115
Vertical acceleration level cog	a_{zcogi}	m/s^2	0.196
Vertical acceleration level bow	a_{zbowi}	m/s^2	0.196

The values that are presented in the table compare very well with the values published by Irvine et al. (2008), who used a very similar test setup. The main difference between their values and the ones found here are found in the wave elevation. Their bias and precision limits are around 1 mm, here in particular the bias limit is above 3 mm and is mainly caused by the fit of the calibration curve to the data points. Irvine et al. (2008) used wave amplitudes of less than 20 mm, whereas in this research the wave amplitude exceeds 100 mm in a number of cases.

D.4 Elemental precision limits

D.4.1 Model speed

The precision limit of the model speed has been obtained by studying the measured forward speed in a series of subsequent measurement runs averaged over each run at two forward speeds with desired values of 2.876 (21 runs) and 4.026 m/s (20 runs). This gave an estimate for the precision error in the averaged value of the forward speed, and to use this value (for average forward speed) (D.8) should not be applied.

D.4.2 Wave frequency

The wave frequency during the wave calibration tests was obtained by a least squares fitting method of a sine to the measured time trace by the wave probe. Both precision and bias errors of the wave frequency, P_ω and B_ω, were computed using the end-to-end approach. The precision error was obtained by computing the standard deviation of the wave frequency obtained in this way over a number of runs. This was done over the complete range of wave frequencies, for multiple runs at each frequency. The result was averaged over the wave frequency.

D.4.3 Wave height, ship motions and acceleration levels

An end-to-end approach was used to determine the precision errors in the wave height, in the ship motions, and in the acceleration levels. The precision limits were obtained by studying the regular wave runs and splitting each run into 12 equal parts containing at least two harmonic cycles. For each part the standard deviation, the relative phase angle, the minimum value, and the maximum value has been determined and in this way 12 estimates for the same value have been determined. Applying (D.7) with a coverage factor of 2, an estimate of the precision limit of the variables was determined. The procedure was performed for the measurements of one of the two models for the middle wave steepness. Finally, the resulting precision limits were averaged over the wave frequencies.

In this way separate precision limits have been obtained for the standard deviation, the amplitude, the relative phase angle, the minimum value, and the maximum value of the time traces. It was assumed that these limits were applicable for the irregular wave experiments as well. The usual way to do this is to perform one measurement 10 to 12 times instead splitting one measurement in 12 parts. Unfortunately, the former procedure was not executed during the measurements. The splitting of the runs may result in an over-estimation in the precision limits.

The precision limits for the calm water experiments have been obtained by studying the standard deviation of the variables in a set of calm water runs at constant forward speed. Applying (D.7) with coverage factor 2 to the individual measured samples an estimate of the precision limit of the variables was determined. This precision limit should be interpreted as the error in each individual sample. To obtain the precision limit in the averaged measured values either (D.8) was applied.

D.4.4 Summary of the results

Table D.2 presents the elemental precision limits for the forward speed, wave frequency, and the heave and pitch motions for average values, whereas table D.3 presents the results of the precision limits for the minima, maxima, standard deviation, amplitude and phase angle of the unsteady experimental variables.

Table D.2: *Elemental precision limits for averages*

Quantity	Symbol	Unit	Precision limit
Model forward speed	U	m/s	0.009
Wave frequency	ω	rad/s	0.015
Heave motion	z	mm	0.025
Pitch motion	θ	deg	0.001

Table D.3: *Elemental precision limits for averages*

Quantity	Symbol	Unit	Min	Max	Std	Ampl	Phase $[rad]$
Wave elevation (wire type)	ζ	mm	11.01	9.93	2.34	3.29	
Wave elevation (servo type)		mm	11.23	11.78	2.11	2.89	
Heave motion	z	mm	9.40	9.51	0.86	0.99	0.16
Pitch motion	θ	deg	0.50	0.46	0.04	0.05	0.08
Vertical acceleration level cog	a_{zcog}	m/s^2	1.32	1.29	0.12	0.06	
Vertical acceleration level bow	a_{zbow}	m/s^2	3.90	2.99	0.15	0.13	

D.5 Uncertainty assessment

D.5.1 Calm water experiments

The measured calm water trim and rise at the center of gravity on model scale are compared for three design concepts (ABC, ESC, and WPC) in chapter 2 and used as validation data in chapter 5 for the computational model. Also the total resistance of the three design concepts is compared in chapter 2, nevertheless the resistance is not used in the validation process. For this reason, the uncertainty analysis was only performed for the calm water trim and rise and not for the total resistance.

The trim and rise were determined by performing a run and measuring the heave and pitch values and averaging them over the time trace. Next, the time averaged heave and pitch values obtained at zero forward speed (subscript 0) were subtracted from the forward speed values (subscript U) (D.12).

$$\begin{aligned} \Delta z &= z_U - z_0 \\ \Delta\theta &= \theta_U - \theta_0 \end{aligned} \tag{D.12}$$

The computation of the bias and precision limits was done according to (D.13). The elemental precision limits of the averages of the heave, pitch, and the forward speed were taken from table D.2. The factor 2 in (D.13) takes into account taking the difference of the forward speed and zero speed values.

$$\begin{aligned} B_{\Delta z}^2 &= 2\left(\frac{\partial \delta z}{\partial z_i} \cdot B_{z_i}\right)^2 \\ P_{\Delta z}^2 &= 2\left(P_z\right)^2 \end{aligned} \tag{D.13}$$

The resulting trim and rise are plotted on the Froude number. The uncertainty in the Froude number can be computed by using the definition of the Froude number:

$$Fn = \frac{U}{\sqrt{gL}} \tag{D.14}$$

Based on (D.14) the bias error can be obtained as given below, with the partial derivatives obtained analytically.

$$\begin{aligned} B_{Fn}^2 &= \left(\frac{\partial Fn}{\partial U} \cdot B_U\right)^2 + \left(\frac{\partial Fn}{\partial g} \cdot B_g\right)^2 + \left(\frac{\partial Fn}{\partial L} \cdot B_L\right)^2 \\ \frac{\partial Fn}{\partial U} &= \frac{1}{\sqrt{gL}} \\ \frac{\partial Fn}{\partial g} &= \frac{-U}{2g\sqrt{gL}} \\ \frac{\partial Fn}{\partial L} &= \frac{-U}{2L\sqrt{gL}} \end{aligned} \tag{D.15}$$

The bias and precision limits for the trim and rise were found to be independent of forward speed and ship type, whereas the forward speed, in terms of the Froude number, was only slightly dependent on the forward speed. Table D.4 shows the bias and precision limits and the uncertainty of the three variables. The uncertainty is shown as absolute value and as percentage of the range. The uncertainty in the Froude number is the worst case in terms of absolute value, at the highest forward speed.

In particular the trim shows relatively a relatively large uncertainty. This is related to the relatively small magnitude of the trim of less than 2.12 degrees.

Table D.4: *Uncertainty in the full scale trim and rise values*

Variable	**Symbol**	**Unit**	**Range**	**Bias limit**	**Precision limit**	**Uncertainty**	
			$\boldsymbol{R}$	$\boldsymbol{B}$	$\boldsymbol{P}$	$\boldsymbol{U}$	$\%\boldsymbol{R}$
Froude number	Fn	$[-]$	1.10	0.0018	0.0018	0.0025	0.23%
Rise	Δz	$[m]$	0.47	0.0055	0.0008	0.0055	1.17%
Trim	$\Delta\theta$	$[deg]$	2.12	0.1627	0.0014	0.1627	7.67%

D.5.2 Regular head wave experiments

The data obtained during the regular head wave experiments is aggregated into response amplitude operators (RAOs) and relative phase angles with respect to the incoming wave of the heave and pitch motions and the acceleration levels at the bow and the center of gravity. Figure D.2 shows a block diagram of the test procedure and the data reduction for the heave and pitch motions. This figure is setup following the ITTC guidelines.

Based on the data reduction equations, six elementary variables can be distinguished: the longitudinal position of the wave probe D, the model speed U, the gravitational acceleration g, the heave motion observations z_i for each sample i, the pitch motion observations θ_i for each sample i, and finally the wave elevation observations ζ_i for each sample i. The elementary errors associated with these variables have been deliberated in sections D.3 and D.4. As explained previously, no end-to-end precision limit has been obtained for the final outcome

of the experiment and for that reason the precision limit has been obtained in the same way as the bias limit, by propagating the elementary precision limits through the DREs.

The data reduction equations can be used to propagate the elementary errors to the uncertainty in the final outcome, shown in the final block in figure D.2. As an example the response amplitude operator of heave, RAO_z is used to explain the error propagation procedure. The description offered in the current section for the bias limit propagation can be directly for the precision limit propagation.

The heave RAO is determined by dividing the have amplitude z_a over the wave amplitude ζ_a. (D.16) shows the equation to obtain the bias limit for the heave RAO. The derivatives of the heave RAO with respect to the heave and wave amplitudes, corresponding to the ϑ terms in (D.10), can easily be analytically obtained.

$$B_{RAO_z}^2 = \left(\frac{\partial RAO_z}{\partial z_a} \cdot B_{z_a}\right)^2 + \left(\frac{\partial RAO_z}{\partial z_a} \cdot B_{z_a}\right)^2 \tag{D.16}$$

The other two variables in (D.16) are the bias limits of the heave and the wave amplitude, which are given by (D.17) and (D.18).

$$B_{z_a}^2 = \left(\frac{\partial z_a}{\partial z_i} \cdot B_{z_i}\right)^2 + \left(\frac{\partial z_a}{\partial \omega_e} \cdot B_{\omega_e}\right)^2 \tag{D.17}$$

$$B_{\zeta_a}^2 = \left(\frac{\partial \zeta_a}{\partial \zeta_i} \cdot B_{\zeta_i}\right)^2 + \left(\frac{\partial \zeta_a}{\partial \omega_e} \cdot B_{\omega_e}\right)^2 \tag{D.18}$$

In these equations B_{z_i} and B_{ζ_i} are elementary bias limits that can be read from table D.1. The derivatives of z_a and ζ_a with respect to z_i, ζ_i, and ω_e are determined by the harmonic fit equations, that are basically Fourier transforms at a single frequency. These equation, for the heave motion, is given by:

$$z_a = \frac{2}{N}\sqrt{\left(\sum_{i=1}^{N} z_i \cos\left(2\pi\omega_e t_i\right)\right)^2 + \left(\sum_{i=1}^{N} z_i \sin\left(2\pi\omega_e t_i\right)\right)^2} \tag{D.19}$$

and computes the heave amplitude z_a from the individual data samples z_i of sample i at time t_i using a harmonic function with frequency ω_e. As this equation involves summations over a large number of samples, obtaining its derivatives with respect to z_i and ω_e analytically is very cumbersome. To overcome this, a method proposed by Irvine et al. (2008) was applied, approaching these derivatives numerically by a applying a perturbation technique.

First z_a is computed from z_i by (D.19), forming the 'nominal' case, $z_{a\,nom}$. Next, focusing on the first RHS term, one by one the elements of z_i are perturbed by 0.1% before using (D.19) to compute the resulting $z_{a\,per\,i}$ for each sample $i = 1, ..., N$, and the derivative for each i is computed by:

$$\left(\frac{\partial z_a}{\partial z_i}\right)_i \approx \frac{z_{a\,nom} - z_{a\,per\,i}}{0.001 z_{a\,nom}} \tag{D.20}$$

Finally, all these derivatives are summed over $i = 1, ..., N$ to yield the first RHS term in (D.17). A similar procudere is used for the second RHS term. However, now no summation is necessary as ω_e only needs to be perturbed once. The derivative is approximated by:

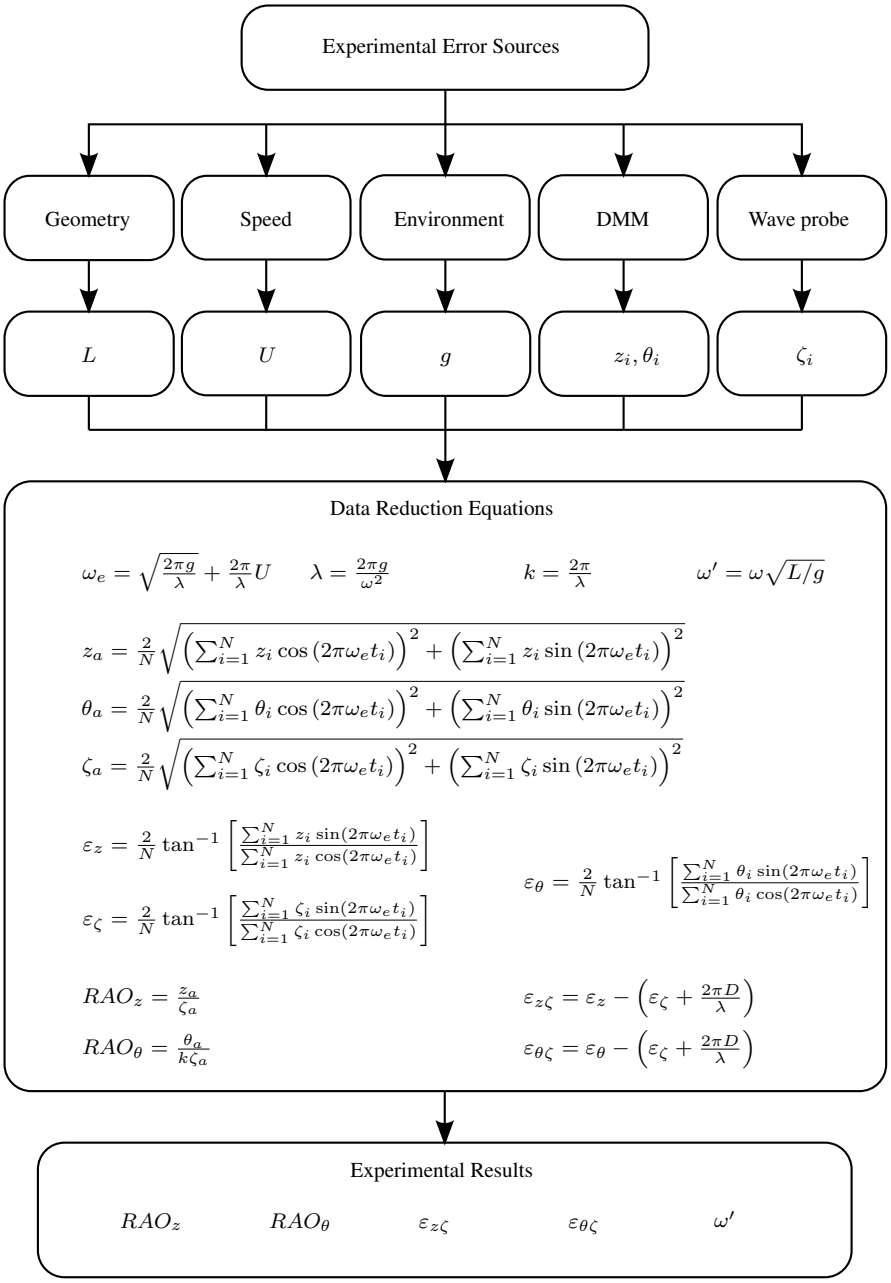


Figure D.2: *Block diagram of test procedure regular waves for heave and pitch*

$$\frac{\partial z_a}{\partial \omega_e} \approx \frac{z_{a\,nom} - z_{a\,per\,\omega_e}}{0.001\omega_e} \tag{D.21}$$

Now only one term, the bias limit of the encounter frequency, remains in (D.17) and (D.18). This bias limit can be obtained by tracing the elementary variables of ω_e, leading to (D.22) and (D.23). All derivatives in these two equations can be computed analytically and only elementary bias limits remain.

$$B_{\omega_e}^2 = \left(\frac{\partial \omega_e}{\partial \lambda} \cdot B_\lambda\right)^2 + \left(\frac{\partial \omega_e}{\partial U} \cdot B_U\right)^2 \tag{D.22}$$

$$B_\lambda^2 = \left(\frac{\partial \lambda}{\partial \omega} \cdot B_\omega\right)^2 + \left(\frac{\partial \lambda}{\partial g} \cdot B_g\right)^2 \tag{D.23}$$

The same procedure can be applied to ζ_a and a very similar procedure can be used for computing the bias limits associated with the phase angle. Nevertheless, in some cases the numerical approximation of the derivative turned out to be dependent on the magnitude of the perturbation instead of converging for decreasing perturbation magnitude. For instance for $\frac{\partial z_a}{\partial \omega_e}$ a nearly linear behaviour appeared for the derivative with respect to the perturbation percentage, for small values. In other cases only limited irregular behaviour was visible around a relatively large value. In the first case the value of the derivative was obtained at the actual value of of the bias limit of the deriving value, whereas in the second case a mean was taken over a small range of perturbation of $\pm 0.4\%$.

The precision limits were easier to determine, as these were already obtained for the amplitudes and phase angles by the end-to-end method. They only needed to be propagated when determining the RAO values from the amplitudes, and the numerical procedure outlined above was avoided.

The same procedure can be followed for the bias and precision limits of the RAOs and relative phase angles of the pitch motion and the vertical acceleration levels. The main difference with the previous is the form of the final dimensionless expressions of the RAOs:

$$\begin{aligned} RAO_\theta &= \frac{\theta_a}{k\zeta_a} \\ RAO_{a_z} &= \frac{a_{za}L}{g\zeta_a} \end{aligned} \tag{D.24}$$

This means that also the bias and precision limits of k, L, and g need to be included for the bias an precision limits of these variables.

The bias and precision limits being obtained, the total uncertainty in the aggregated variables was computed by applying (D.1). The uncertainty is dependent on the forward speed, the wave frequency, the wave ampltitude (or steepness), and the ship type. The uncertainty assessment has been performed for the Enlarged Ship Concept, for the middle wave steepness of 1/30, yet for all wave frequencies. It was found that the forward speed had only marginal influence on the final uncertainty. It was assumed that the other choices represented the complete data set sufficiently.

The results of the regular wave experiment uncertainty assessment are presented in the tables below. Note that all values presented in the tables below are model scale values or dimensionless values. Table D.5 shows the values and uncertainties of the wave length and some derived wave frequencies (encounter frequency and dimensionless frequency) over the range of wave frequencies. The error of the wave length is largest at 1.5%, whereas the other uncertainties are lower than 1%.

Table D.5: *Uncertainty in the wave length and frequency*

ω	λ	U_λ	ω_e	U_{ω_e}	ω'	$U_{\omega'}$
$[rad/s]$	$[m]$	$[\%]$	$[rad/s]$	$[\%]$	$[-]$	$[\%]$
5.81	1.83	0.7%	15.71	0.3%	3.08	0.4%
5.37	2.14	0.8%	13.82	0.3%	2.84	0.4%
4.92	2.55	0.9%	12.02	0.3%	2.61	0.4%
4.47	3.09	0.9%	10.33	0.3%	2.37	0.5%
4.02	3.81	1.0%	8.76	0.3%	2.13	0.5%
3.58	4.81	1.2%	7.34	0.3%	1.90	0.6%
3.13	6.29	1.3%	6.00	0.4%	1.66	0.6%
2.68	8.58	1.5%	4.79	0.5%	1.42	0.8%

The next table, table D.6, presents the values and uncertainties of the motion and acceleration amplitudes over the wave frequency range and include the effect of the data reduction by means of harmonic analysis of the measured time traces. The relative error is largest for the highest wave frequency and becomes smaller for increasing wave frequency, eventually at values just below 1% for the motions and at 2.5% for wave elevation and the acceleration levels.

Table D.6: *Uncertainty in the motion and acceleration amplitudes*

ω	z_a	U_{z_a}	θ_a	U_{θ_a}	ζ_a	U_{ζ_a}	$a_{za\,cog}$	$U_{a_{za\,cog}}$	$a_{za\,bow}$	$U_{a_{za\,bow}}$
$[rad/s]$	$[mm]$	$[\%]$	$[deg]$	$[\%]$	$[mm]$	$[\%]$	$[m/s^2]$	$[\%]$	$[m/s^2]$	$[\%]$
5.81	0.8	125.4%	0.1	93.57%	33.8	9.8%	0.22	28.2%	0.41	31.1%
5.37	0.8	121.4%	0.3	16.55%	37.4	8.9%	0.18	34.5%	1.41	9.1%
4.92	6.3	15.8%	0.9	5.82%	42.6	7.8%	0.98	6.4%	3.28	4.0%
4.47	22.1	4.5%	2.0	2.61%	48.1	6.9%	2.32	2.8%	5.76	2.3%
4.02	60.0	1.8%	3.9	1.40%	59.6	5.6%	4.52	1.5%	9.35	1.5%
3.58	113.8	1.1%	6.0	1.01%	84.2	34.0%	6.72	1.1%	12.70	1.2%
3.13	122.4	1.0%	7.2	0.89%	112.7	3.0%	5.00	1.4%	10.07	1.4%
2.68	120.1	1.0%	6.0	0.99%	128.5	2.6%	2.93	2.2%	5.04	2.6%

Table D.7 and D.8 show the uncertainty of the final aggregated variables, the RAOs and relative phase angles. The RAOs show for decreasing wave frequency a decreasing error to less than 3 percent for the motions and from to less than 6 percent for the acceleration levels. The acceleration levels contain larger errors, this is mainly caused by the fact that the acceleration level RAOs are made dimensionless with the length and the gravitational acceleration, that contain additional errors on top of the already larger elementary errors.

Table D.7: *Uncertainty in the Response Amplitude Operators (percentages based on ratio of the uncertainty to the actual RAO value)*

	z		θ		$a_{z\,cog}$		$a_{z\,bow}$	
ω	**Value**	U	**Value**	U	**Value**	U	**Value**	U
$[rad/s]$	$[-]$	$[\%]$	$[-]$	$[\%]$	$[-]$	$[\%]$	$[-]$	$[\%]$
5.81	0.02	125.7%	0.01	93.7%	1.83	34.3%	3.38	36.8%
5.37	0.02	121.7%	0.05	17.1%	1.35	38.8%	10.54	19.9%
4.92	0.15	17.6%	0.14	7.0%	6.45	16.8%	21.56	16.0%
4.47	0.46	8.2%	0.35	4.3%	13.55	14.0%	33.57	14.0%
4.02	1.01	5.8%	0.70	3.1%	21.30	11.2%	44.00	11.2%
3.58	1.35	4.1%	0.95	2.2%	22.37	8.0%	42.30	8.0%
3.13	1.09	3.1%	1.12	1.8%	12.43	6.1%	25.04	6.1%
2.68	0.93	2.8%	1.12	2.2%	6.40	5.7%	10.99	5.9%

The relatively large uncertainty in the relative phase angles can again be traced to the phase angle computation when performing the harmonic analysis. Like the amplitude estimation, also the phase angle estimation is highly dependent on the accuracy of the encounter frequency. At the higher wave frequencies the uncertainty is even larger. This is caused by the fact that when the motion amplitudes are small than the error of the motion measurement (that is assumed to be independent of the magnitude of the motion) has a large influence on the estimated phase angle by the harmonic analysis.

Table D.8: *Uncertainty in the (relative) phase angles (percentages based on ratio of the uncertainty to 2π)*

ω	U_{ε_z}	U_{ε_θ}	U_{ε_ζ}	$U_{\varepsilon_{z\zeta}}$	$U_{\varepsilon_{z\theta}}$
$[rad/s]$	$[\%]$	$[\%]$	$[\%]$	$[\%]$	$[\%]$
5.81	5.0%	4.2%	4.3%	6.6%	6.0%
5.37	4.7%	3.9%	3.9%	6.1%	5.5%
4.92	4.3%	3.6%	3.6%	5.6%	5.1%
4.47	3.9%	3.3%	3.3%	5.1%	4.6%
4.02	3.7%	3.0%	3.1%	4.8%	4.3%
3.58	3.6%	2.9%	3.0%	4.7%	4.2%
3.13	3.6%	2.9%	2.9%	4.6%	4.1%
2.68	3.5%	2.8%	2.9%	4.5%	4.0%

Table D.9 shows the contributions of the elemental error sources to the heave RAO. It turns out that the errors are highly dependent on the accuracy of the encounter frequency at which the harmonic analysis is performed, more than on the accuracy of the actual measured motion amplitude. Depending on the wave frequency either the accuracy of the wave frequency determination or the accuracy of the forward speed measurement is more important. The very high wave frequencies form an exception, there the motion amplitude error has a large influence, due to the very small value of the motion amplitude combined with a relatively large error.

Finally, in chapter 2 section 2.3.5 figures 2.15 and 2.19, time traces are shown for the vertical

Table D.9: *Contributions of the elemental errors to the bias error of the heave RAO*

ω	z_i	ζ_i	ω	U
$[rad/s]$	[%]	[%]	[%]	[%]
5.81	56.8%	0.4%	15.1%	27.7%
5.37	63.4%	0.4%	15.4%	20.7%
4.92	4.0%	1.1%	48.8%	46.2%
4.47	0.5%	1.2%	59.8%	38.6%
4.02	0.1%	1.0%	69.6%	29.3%
3.58	0.0%	0.6%	78.6%	20.8%
3.13	0.0%	0.3%	86.3%	13.4%
2.68	0.0%	0.3%	92.0%	7.7%

acceleration level at the bow made non-dimensional with g for respectively the Enlarged Ship Concept and the Axe Bow Concept. The bias and precision limits were computed by (D.25) and the results are presented in table D.10. The table shows for each of the two concepts the uncertainty in the peak values of the non-dimensional vertical acceleration levels.

$$B^2_{a_z/g} = \left(\frac{1}{g} \cdot B_{a_z}\right)^2 + \left(-\frac{2a_z}{g^2} \cdot B_g\right)^2 \tag{D.25}$$

Table D.10: *Uncertainty in peak levels of non-dimensional vertical acceleration level at the bow* $a_{z\,bow}/g$

Design	**Figure**	**Peak value**	B	P	U	U
		[−]	[−]	[−]	[−]	[%]
ESC	2.15	2.6	0.0240	0.0870	0.0902	3.47%
ABC	2.19	1.1	0.0208	0.0870	0.0894	8.13%

D.5.3 Irregular head wave experiments

The data measured during the irregular head wave experiments has been aggregated in two distinct manners:

1. Rayleigh plots showing the crest and troughs (positive and negative peaks) in the time traces.
2. By means of significant amplitudes and maxima and minima obtained by fitting a Weibull distribution to the peak (positive and negative) statistics.

In the former, the data, except for the acceleration levels, is not made non-dimensional and the maxima and minima in the time trace are directly processed into peak statistics without altering the data. For this reason the points in the plots representing peak values contain the same error as individual samples in the time traces. These errors can be directly taken from the elemental bias and precision limits presented in tables D.1 and D.3. For the precision error the error of the maximum and minimum values are taken from the table.

The exception is formed by the acceleration levels. These are made non-dimensional with the gravitational acceleration. As in the previous section the uncertainty could be calculated by using (D.25). As can be seen in this equation the error becomes dependent on the measured value of the acceleration level.

The second manner of presenting the data was by bar plots of the significant amplitudes and Weibull fitted maxima and minima. This is presented in chapter 5 in figures 5.14 and 5.15. Furthermore the data in the graphs was made non-dimensional. The heave responses (significant amplitudes, maxima, and minima) were made non-dimensional by the significant wave amplitude. The pitch responses by the wave number times the significant wave amplitude. Finally, the acceleration levels by the gravitational acceleration.

The uncertainty analysis of the data reduction was split into two parts. First, the propagation of the error through the determination of the significant amplitudes and the Weibull fit procedure was considered. Next, the influence of making the results non-dimensional was taken into account. The procedure has been performed for two different forward speeds, 25 and 35 knots, and two different significant wave heights, 2.0 metres and 3.5 metres, for the Enlarged Ship Concept. It was assumed that changing the model type (from ESC to ABC) does not influence the results of the uncertainty analysis. Thus, in total four measurements were considered.

The propagation of the bias error through the determination of both the significant amplitude (by taking the two times the standard deviation 2σ of a time trace) and the Weibull estimates of the maxima and minima (by fitting a Weibull distribution to the positive and negative maxima and subsequently determining the 1/100$^{\text{th}}$ maximum value) was computed numerically. The precision error of the standard deviation was directly taken from table D.3, the precision errors of the minimum and maximum values from D.3 were treated in identical fashion as the bias errors.

The error propagation procedure was done in a similar way as in the previous section. As an example the standard deviation of the heave time trace will be treated. The bias error in the standard deviation is determined by the bias error in the individual samples in the heave time trace multiplied by the error propagation given as the derivative of the standard deviation to the measured heave time trace.

$$B_{\sigma_z}^2 = \left(\frac{\partial \sigma_z}{\partial z_i} \right)_i^2 \cdot B_{z_i}^2 \tag{D.26}$$

The error propagation coefficient, the first RHS term, is numerically approximated by computing the nominal value of standard devitation of the unperturbed signal and the perturbed values of the standard deviation for each sample $i = 1, ..., N$ in the time trace by perturbating each sample with 1 thousandth and computing the perturbed standard deviation of the perturbed time trace for each individual perturbation. Now the derivative can be approximated by (D.27) for each perturbation (for N samples). Finally, the N derivatives are summed from $i = 1, ..., N$, yielding the final value of the derivative.

$$\left(\frac{\partial \sigma_z}{\partial z_i} \right)_i \approx \frac{\sigma_{z\,nom} - \sigma_{z\,per\,i}}{0.001 \sigma_{z\,nom}} \tag{D.27}$$

The exact same approach was applied to the Weibull fit procedure to obtain the maximum and minimum value in a time trace. The approach was applied to each individual time trace that

was analyzed of the four measurements that were considered. It was found that the values of the propagation coefficient were largely independent on the magnitude and the amount of noise in the signal and on the magnitude of the perturbation, giving confidence in the chosen approach.

Next, the significant amplitudes and maxima and minima were made non-dimensional. As an example the data reduction procedure of the non-dimensional significant amplitudes of the heave and pitch motions is detailed in the following.

Data reduction equation of the heave significant amplitude:

$$z' = \frac{z_{1/3}}{\zeta_{1/3}} = \frac{2\sigma_z}{2\sigma_\zeta} = \frac{\sigma_z}{\sigma_\zeta} \tag{D.28}$$

Error propagation equation of the non-dimensional heave significant amplitude:

$$U_{z'}^2 = \left(\frac{1}{\sigma_\zeta} \cdot U_{\sigma_z}\right)^2 + \left(-\frac{\sigma_z}{2\sigma_\zeta^2} \cdot U_{\sigma_\zeta}\right)^2 \tag{D.29}$$

Data reduction equation of the pitch significant amplitude:

$$\theta' = \frac{\theta_{1/3}}{k\zeta_{1/3}} = \frac{2\sigma_z}{2k\sigma_\zeta} = \frac{\sigma_z}{k\sigma_\zeta} \tag{D.30}$$

Error propagation equation of the non-dimensional pitch significant amplitude:

$$U_{z'}^2 = \left(\frac{1}{k\sigma_\zeta} \cdot U_{\sigma_z}\right)^2 + \left(-\frac{\sigma_z}{2k\sigma_\zeta^2} \cdot U_{\sigma_\zeta}\right)^2 + \left(-\frac{\sigma_z}{2k^2\sigma_\zeta} \cdot U_k\right)^2 \tag{D.31}$$

The uncertainty U in the above can be replaced with the bias limit B and the precision limit P. The approximation of the uncertainties of the standard deviation has been detailed above. The uncertainty of the wave number k has been detailed when describing the uncertainty analysis of the regular wave experiments. Simply the value of k and its uncertainty are taken at the wave peak frequency. All analysis is done at full scale. The data reduction for the Weibull estimated minima and maxima is similar to the above. Again for the data reduction procedure of the acceleration levels one is referred to (D.25).

The results of the dimensional uncertainties in the standard deviations and the Weibull estimated 1/100$^{\text{th}}$ maxima and minima is given in table D.11. The values were determined by taking the average over the four studied measurements as the absolute uncertainties were found to be relatively independent on the forward speed and significant wave height. The ranges of the standard deviation (σ) and the maxima and minima are averaged over the four measurements that were studied during the analysis are included to give an idea of the relative magnitude of the errors.
The final four tables show the uncertainties in the final non-dimensional outcomes of the irregular wave experiments. From the tables can be concluded that the uncertainty levels in the final outcome are independent from the forward speed, but generally dependent on the significant wave height. For larger significant wave height the uncertainty decreases in the maxima and minima. The motions are relatively more accurate than the acceleration levels.

Table D.11: *Uncertainties in the (averaged over four measurements) standard deviations and Weibull estimated maxima and minima (full scale and dimensional)*

Symbol	Unit	σ	U_σ	max	U_{max}	min	U_{min}
z	$[m]$	0.66	0.02	3.04	0.03	-2.32	0.03
θ	$[deg]$	1.83	0.04	5.75	0.06	-8.06	0.07
a_{zcog}	$[m/s^2]$	2.27	0.12	7.45	0.18	-8.83	0.17
a_{zbow}	$[m/s^2]$	4.60	0.15	21.88	0.42	-13.87	0.47
ζ	$[m]$	0.66	0.05	3.07	0.03	-2.67	0.03

D.6 Concluding remarks

The uncertainty assessment presented above is highly dependent on the precise estimation of the bias and precision limits. Especially the precision limits can be most reliably obtained by the end-to-end method, were relevant experiments are repeated 12 times and processed to yield 12 estimates per aggregated variable. The statistics of these 12 estimates can be used to obtain the precision limit as explained above. Due to the fact that no repetition measurements were carried out during execution of the experiments, no such data was available. An alternative method was used, by splitting individual time traces (of regular waves) into 12 parts and analysing these. This, however, in all probability results in an over-estimation of the precision limits. For this reason in order to improve the uncertainty assessment it is recommendable to perform the repetition experiments for a small number of key experiments.

Table D.12: *Uncertainties in the significant amplitudes and Weibull estimated maxima and minima (non-dimensional) for the heave motion*

U^a	$H_{1/3}$	$z'_{1/3}$	$U_{z'_{1/3}}$	z'_{max}	$U_{z'_{max}}$	z'_{min}	$U_{z'_{min}}$
$[kn]$	$[m]$	$[-]$	$[-]$	$[-]$	$[-]$	$[-]$	$[-]$
25.00	2.00	1.00	0.021	1.79	0.041	-1.45	0.044
25.00	3.50	1.06	0.012	2.05	0.022	-1.39	0.019
35.00	2.00	0.87	0.020	1.53	0.037	-1.32	0.042
35.00	3.50	0.89	0.011	1.64	0.020	-1.16	0.018

[a] U without subscript here signifies forward speed

Table D.13: *Uncertainties in the significant amplitudes and Weibull estimated maxima and minima (non-dimensional) for the pitch motion*

U	$H_{1/3}$	$\theta'_{1/3}$	$U_{\theta'_{1/3}}$	θ'_{max}	$U_{\theta'_{max}}$	θ'_{min}	$U_{\theta'_{min}}$
$[kn]$	$[m]$	$[-]$	$[-]$	$[-]$	$[-]$	$[-]$	$[-]$
25.00	2.00	0.83	0.014	1.73	0.032	-1.42	0.042
25.00	3.50	0.80	0.008	0.99	0.013	-1.45	0.017
35.00	2.00	0.62	0.012	0.97	0.022	-0.99	0.032
35.00	3.50	0.58	0.007	0.80	0.012	-1.01	0.015

Table D.14: *Uncertainties in the significant amplitudes and Weibull estimated maxima and minima (non-dimensional) for the vertical acceleration level at the center of gravity*

U	$H_{1/3}$	$a'_{z1/3}$	$U_{a'_{z1/3}}$	a'_{zmax}	$U_{a'_{zmax}}$	a'_{zmin}	$U_{a'_{zmin}}$
$[kn]$	$[m]$	$[-]$	$[-]$	$[-]$	$[-]$	$[-]$	$[-]$
25.00	2.00	0.16	0.012	1.13	0.016	-0.59	0.017
25.00	3.50	0.29	0.012	0.99	0.018	-1.10	0.016
35.00	2.00	0.17	0.012	0.50	0.017	-0.69	0.018
35.00	3.50	0.31	0.012	1.09	0.023	-1.23	0.018

Table D.15: *Uncertainties in the significant amplitudes and Weibull estimated maxima and minima (non-dimensional) for the vertical acceleration level at the bow*

U	$H_{1/3}$	$a'_{z1/3}$	$U_{a'_{z1/3}}$	a'_{zmax}	$U_{a'_{zmax}}$	a'_{zmin}	$U_{a'_{zmin}}$
$[kn]$	$[m]$	$[-]$	$[-]$	$[-]$	$[-]$	$[-]$	$[-]$
25.00	2.00	0.35	0.016	0.47	0.040	-1.16	0.049
25.00	3.50	0.60	0.016	3.04	0.041	-1.62	0.043
35.00	2.00	0.34	0.016	1.24	0.046	-1.17	0.052
35.00	3.50	0.59	0.016	3.65	0.044	-1.71	0.047

Bibliography

M. Abramowitz and I. A. Stegun. *Handbook of Mathematical Functions with Formulas, Graphs, and Mathematical Tables*. Dover, New York, ninth edition, 1972.

T. Armstrong. The future for commercial fast craft - learning from events since FAST'91. In *Proceedings of the 10th International Conference on Fast Sea Transportation*, pages 3–12, 2009.

R. F. Beck and S. J. Liapis. Transient motion of floating bodies at zero forward speed. *Journal of Ship Research*, 21: 164–176, 1987.

R. F. Beck and A. E. Loken. Three-dimensional effects in ship relative motion problems. *Journal of Ship Research*, 33(4):261–268, 1989.

R. F. Beck and A. Magee. Time-domain analysis for predicting ship motions. In *Proceedings of the Symposium on Dynamics of Marine Vehicles and Structures in Waves*, pages 49–56, London, 1990.

R. F. Beck and A. Reed. Modern seakeeping computations for ships. In *Proceedings of the 23rd Symposium on Naval Hydrodynamics*, pages 1–45, 2001.

V. Bertram. Ship motions by Rankine source method. *Ship Technology Research*, 37(4):143–152, 1990.

H. B. Bingham. *Simulating ship motions in the time domain*. PhD thesis, Massachusetts Institute of Technology, 1994.

F. Blandeau, M. Francois, S. Malenica, and X.B. Chen. Linear and non-linear wave loads on FPSOs. In *Proceedings of the 9th International Offshore and Polar Engineering Conference*, pages 252–258, Brest, France, 1999.

J. J. Blok and A. B. Aalbers. Roll damping due to lift effects on high speed monohulls. In *Proceedings of the 2nd International Conference on Fast Sea Transportation*, pages 1331 – 1348, 1991.

J. J. Blok and W. Beukelman. The high speed displacement hull forms - seakeeping characteristics. *Transactions Society of Naval Architects and Marine Engineers*, 92:125–150, 1984.

J. J. Blok and H. W. Roeloffs. The influence of the forebody deadrise on the performance in a seaway. Technical Report 49207-1-HT, Marin, 1989.

J. J. van den Bosch. Tests with two planing boats in waves. Technical report, Ship Hydromechanics Laboratory Delft University of Technology, 1970.

K. Brower and C. Cleary. Top level requirements for a high speed cutter for offshore service. Elc project report, USCG, 2003.

T. Bunnik. *Seakeeping calculations for ships, taking into account the non-linear steady waves*. PhD thesis, Delft University of Technology, 1999.

R. L. Burden and J. D. Faires. *Numerical analysis*. Brooks/Cole, 7th edition, 2001.

Y. Cao. *Computations of nonlinear gravity waves by a desingularized boundary integral method*. PhD thesis, University of Michigan, Ann Arbor, USA, 1991.

M.-S. Chang. Computation of three-dimensional ship motions with forward speed. In *Proceedings of the 2nd International Conference on Numerical Ship Hydromechanics*, pages 124–135, 1977.

A. H. Clément. Computation of impulse response function using differential properties of the time-domain Green function. In *13th International Workshop on Water Waves and Floating Bodies*, pages 21–24, Alphen aan den Rijn, The Netherlands, 1998a.

A. H. Clément. An ordinary differential equation for the Green function of time-domain free-surface hydromechanics. *Journal of Engineering Mathematics*, 33(2):201–217, February 1998b.

E. P. Clement and D. L. Blount. Resistance tests of a systematic series of planing hull forms. *Transactions Society of Naval Architects and Marine Engineers*, 71:491–561, 1963.

H. W. Coleman and W. G. Steele. *Experimentation and uncertainty analysis for engineers*. John Wiley and Sons, New York, 2nd edition edition, 1999.

P. R. Couser, J. F. Wellicome, and D. F. Molland. An improved method for the theoretical prediction of the wave resistance of transom-stern hulls using a slender body approach. *International Shipbuilding Progress*, 45:331–349, 1998.

W. E. Cummins. The impulse response function and ship motions. *Schiffsbautechnik*, vol. 9(47):101–109, 1962.

C. W. Dawson. A practical computer method for solving ship-wave problems. In *Proceedings of the 2nd International Conference on Numerical Ship Hydromechanics*, pages 30–38, 1977.

D. Dessi and E. Ciappi. Comparative analysis of slamming events and induced response for different types of ships. In *PRADS*, 2010.

A. F. J. van Deyzen, J. A. Keuning, and R. H. M. Huijsmans. Motion reduction of small planing vessels using smart control. the influence of thrust control on the operability of planing monohull sailing in head waves. *Submitted to: International Shipbuilding Progress*, 2011.

P. van Diepen. *Wave piercing bow of a monohull marine craft*. U.S. Patent No. 20030089290, 2003a.

P. van Diepen. A flat wave piercing bow concept for high speed monohull. In *Annual Meeting Papers*. Society of Naval Architectures and Marine Engineers, 2003b.

L. J. Doctors and A. H. Day. Resistance prediction for transom stern vessels. In *Proceedings on the 4th International Conference on Fast Sea Transportation*, pages 743–750, Sydney, Australia, 1997.

L. J. Doctors, G. J. Macfarlane, and R. Young. A study of transom-stern ventilation. *International Shipbuilding Progress*, 54:145–163, 2007.

D. G. Dommermuth and D. K. P. Yue. Numerical simulations of nonlinear axisymmetric flow with a free surface. *Journal of Fluid Mechanics*, 178:195–219, 1987.

M. Drela. XFOIL: An analysis and design system for low Reynolds number airfoils. In *Proceedings of the Conference on Low Reynolds Number Airfoil Aerodynamics*, University of Notre Dame, June 1989.

M. Drela and H. Youngren. *XFOIL 6.9 User Primer*. MIT Aero & Astro and Aircraft Inc., November 2001. Available online: `http://web.mit.edu/drela/Public/web/xfoil/xfoil_doc.txt`.

S. X. Du, D. A. Hudson, W. G. Price, P. Temarel, and Y. S. Wu. Numerical predictions of steady flow around high speed vessels with transom sterns. In *Proceedings of the 6th International Conference on Fast Sea Transportation*, pages 17–24, 2003.

B. Etkin and L. D. Reid. *Dynamics of flight: Stability and control*. Wiley, 3rd edition, 1995.

O. M. Faltinsen. Numerical solution of transient nonlinear free-surface motion outside and inside moving bodies. In *Proceedings of the 2nd International Conference on Numerical Ship Hydromechanics*, pages 347–357, 1977.

O. M. Faltinsen and F. Michelsen. Motions of large structures in waves at zero Froude number. In *Proceedings of the International Symposium on the Dynamics of Marine Vehicles and Structures in Waves*, pages 91–106, 1974.

A. Finklestein. The initial value problem for transient water waves. *Communications on Pure and Applied Mathematics*, 10:511–522, 1957.

P. J. Finn, R. F. Beck, and A. W. Troesch. Nonlinear impact loading in an oblique seaway. *Journal of Offshore Mechanics and Arctic Engineering*, 125:190–197, 2003.

G. Z. Forristal. On the statistical distribution of wave heights in a storm. *Journal of Geophysical Research*, 83: 2353–2358, 1978.

G. Z. Forristal. The distribution of measured and simulated wave heights as a function of spectral shape. *Journal of Geophysical Research*, 89:10547–10552, 1984.

G. Fridsma. A systematic study of the rough water performance of planing boats. Technical report, Stevens Institute of Technology, 1969.

G. Fridsma. A systematic study of the rough water performance of planing boats - Part 2 irregular waves. Technical report, Stevens Institute of Technology, 1971.

K. Garme. Improved time domain simulation of planing hulls in waves by correction of the near-transom lift. *International Shipbuilding Progress*, 52(3):201–230, 2005.

J. Gerritsma and W. Beukelman. Analysis of the modified striptheory for the calculation of ship motions and wave bending moments. Report 96S, Netherlands Ship Research Centre TNO, 1967.

I. S. Gradshteyn and I. M. Ryzhik. *Table of integrals, series, and products*. Academic Press, Inc., fourth edition, 1980.

O. Grim. Berechnung der durch Schwingungen eines Schiffskörpers erzeugten hydrodynamischen Kräfte. *Jahrbuch der Schiffsbautechnischen Gesellschaft*, 47:277–299, 1953.

J. Grue and E. Palm. Wave loading on ships and platforms at a small forward speed. In *Proc. 10th OMAE*, pages 255–263, 1991.

P. Guëvel and J. Bougis. Ship motions with forward speed in infinite depth. *International Shipbuilding Progress*, 29 (332):103–117, 1982.

P. Guëvel, G. Delhommeau, and J. P. Cordonnier. Numerical solution of the Neumann-Kelvin problem by the method of singularities. In *Proceedings of the 2nd International Conference on Numerical Ship Hydrodynamics*, pages 107–123, 1977.

R. E. Haring, A. R. Osborne, and L. P. Spencer. Extreme wave parameters based on continental shelf storm wave records. In *Proceedings of the 15th Coastal Engineering Conference*, pages 151–170, Honolulu, USA, July 1976. Am. Soc. Civ. Eng.

O. A. Hermundstad and T. Moan. Efficient method for direct calculation of slamming loads on ships. *Transactions Society of Naval Architects and Marine Engineers*, 117:156–181, 2009a.

O. A. Hermundstad and T. Moan. Practical calculation of slamming pressures in oblique seas. In *Proceedings of the 10th International Conference on Fast Sea Transportation*, Athens, Greece, 2009b.

J. L. Hess and A. M. O. Smith. Calculation of non-lifting potential flow about arbitrary three-dimensional bodies. *Journal of Ship Research*, 8:22–44, 1964.

N. Hogben and R. G. Standing. Wave loads on large bodies. In *Proceedings of the International Symposium on the Dynamics of Marine Vehicles and Structures in Waves*, pages 273–292, 1975.

R.H.M. Huijsmans and A.J. Hermans. The effect of the steady perturbation potential on the motion of a ship salling in random seas. In *Proceedings of the 5th International Conference on Numerical Ship Hydrodynamics*, Hiroshima, 1989.

B. Hunt. The mathematical basis and numerical principles of the boundary integral method for incompressible potential flow over 3D aerodynamic configurations. *Numerical methods in applied fluid dynamics*, pages 49–135, 1980.

R. B. Inglis and W. G. Price. Motions of ships in shallow water. *Transactions of the Royal Institution of Naval Architects*, 122:269–284, 1980.

R. B. Inglis and W. G. Price. A three dimensional ship motion theory - comparison between theoretical predictions and experimental data of the hydrodynamic coefficients with forward speed. *Transactions of the Royal Institution of Naval Architects*, 124:141–157, 1982.

Jr. Irvine, M, J. Longo, and F. Stern. Pitch and heave tests and uncertainty assessment for a surface combatant in regular head waves. *Journal of Ship Research*, 52(2):146–163, June 2008.

ISO. *Evaluation of human exposure to whole-body vibration - Part 3: Evaluation of whole-body z-axis vertical vibration in the frequency range 0.1 to 0.63 Hz*. ISO 2631-3, 1985.

ISO. *Mechanical vibration and shock evaluation of human exposure to whole body vibration - Part 1: General requirements*. ISO 2631-1, 1997.

ITTC. Uncertainty analysis in EFD - Uncertainty assessment methodology. In *ITTC Recommended Procedures and Guidelines*, 22nd International Towing Tank Conference, Seoul/Shanghai, Procedure 7.5-02-01-01, Rev. 00, 1999.

ITTC. Uncertainty analysis - Example for resistance test. In *ITTC Recommended Procedures and Guidelines*, 23rd International Towing Tank Conference, Venice, Procedure 7.5-02-02-02, Rev. 01, 2002a.

ITTC. Sea keeping experiments. In *ITTC Recommended Procedures and Guidelines*, 23rd International Towing Tank Conference, Venice, Procedure 7.5-02-07-02.1, Rev. 01, 2002b.

ITTC. Uncertainty analysis - Example for planar motion mechanism test. In *ITTC Recommended Procedures and Guidelines*, 25th International Towing Tank Conference, Fukuoka, Procedure 7.5-02-06-04, Rev. 00, 2008.

G. Jensen, V. Bertram, and H. Söding. Ship wave-resistance computations. In *Proceedings of the 5th International Conference on Numerical Ship Hydromechanics*, pages 593–606, 1989.

P. de Jong and J. A. Keuning. 6-DOF forced oscillation tests for the evaluation of nonlinearities in the superposition of ship motions. *International Shipbuilding Progress*, 53(2):123–143, 2006.

P. de Jong and F. van Walree. Hydrodynamic lift in a time-domain panel method for the seakeeping of fast ships. In C. Bertorello, editor, *Proceedings of the 6th International Conference on High-Performance Marine Vehicles*, pages 95–105, 2008.

P. de Jong and F. van Walree. The development and validation of a time-domain panel method for the seakeeping of high speed ships. In G. Grigoropoulos, M. Samuelides, and N. Tsouvalis, editors, *Proceedings of the 10th International Conference on Fast Sea Transportation*, volume 1, pages 141–154, October 2009.

P. de Jong, F. van Walree, J.A. Keuning, and R.H.M. Huijsmans. Evaluation of the free surface elevation in a time-domain panel method for the seakeeping of high speed ships. In *Proceedings of the 17th International Offshore and Polar Engineering Conference*, pages 2134–2141, Lisboa, 2007.

C. Judge, A. Troesch, and M. Perlin. Initial water impact of a wedge at vertical and oblique angles. *Journal of Engineering Mathematics*, 48:279–303, 2004.

H. Kajitani, H. Miyata, M. Ikehata, H. Tanaka, and H. Adachi. Summary of the cooperative experiment on Wigley parabolic model in Japan. In *Proceedings of the 2nd DTNSRDC Workshop on Ship Wave Resistance Computations*, pages 5–35, Bethesda, MD, USA, November 1983.

W. von Karman. *The impact of seaplane floats during landing*. Technical Memorandum TN321, NACA, 1929.

J. Katz and A. Plotkin. *Low-speed aerodynamics*. Cambridge University Press, second edition, 2001.

J. A. Keuning. *The nonlinear behaviour of fast monohulls in head waves*. PhD dissertation, Delft University of Technology, Shiphydromechanic Laboratory, 1994.

J. A. Keuning. The application of the enlarged ship concept in a Dutch coast guard cutter. In *Proceedings of the 4th Ausmarine Conference*, pages 55–62, 2000.

J. A. Keuning. Grinding the bow or how to improve the operability of fast monohulls. *International Shipbuilding Progress*, 53(4):281–310, 2006.

J. A. Keuning and J. L. Gelling. The influence of the bow shape on the operability of a fast ship in a seaway. In *Proceedings of the 2nd International Conference on Marine Research and Transportation*, pages 219–234, Ischia, Naples, Italy, June 2007.

J. A. Keuning and J. Gerritsma. Resistance tests of a series of planing hull forms with 25 degrees deadrise angle. *International Shipbuilding Progress*, 29:222–249, 1982.

J. A. Keuning and J. Pinkster. 'The Axebow', a futher improvement on the seakeeping performance of a fast monohull. *Schip en Werf en de Zee*, 12(1):31–36, 2002.

J. A. Keuning and F. van Walree. The comparison of the hydrodynamic behaviour of three fast patrol boats with special hull geometries. In *Proceedings of the 5th International Conference on High Performance Marine Vehicles*, pages 137–152, Launceton, Australia, 2006.

J. A. Keuning and G. L. Visch. The use of a vertical bow fine for the combined roll and yaw stabilization of a fast patrol boat. In *Proceedings of the International Conference on High-performance Marine Vehicles*, pages 107–116, 2008.

J. A. Keuning and G. L. Visch. Combined roll and yaw control on fast ships with an AXE bow in stern quartering and following waves using a vertical magnus rotor. In *Proceedings of the 10th International Conference on Fast Sea Transporation*, 2009.

J. A. Keuning, J. Gerritsma, and P. F. van Terwisga. Resistance tests of a series of planing hull forms with 30 degrees deadrise angle. *International Shipbuilding Progress*, 40:333–385, 1993.

J. A. Keuning, S. Toxopeus, and J. Pinkster. The effect of bowshape on the seakeeping performance of a fast monohull. In *Proceedings of the 6th International Conference on Fast Sea Transportation*, pages 197–212, 2001.

J.A. Keuning and J. Pinkster. Optimisation of the seakeeping behaviour of a fast monohull. In *Proceeding of the 3th International Conference on Fast Sea Transportation*, 1995.

B. K. King, R. F. Beck, and A. R. Magee. Seakeeping calculations with forward speed using time-domain analysis. In *Proceedings of the 17th Symposium on Naval Hydrodynamics*, pages 577–596, 1988.

B. V. Korvin-Kroukovski and W. R. Jacobs. Pitching and heaving motions of a ship in regular waves. *Transactions Society of Naval Architectures and Marine Engineers*, vol. 65:590–632, 1957.

A. N. Krylov. A general theory of the oscillations of a ship on waves. *Transactions of the Royal Institution of Naval Architects*, 40, 1896.

C. Lai. *Three-dimensional planing hydrodynamics based on a vortex lattice method*. PhD thesis, University of Michigan, 1994.

D. R. Lavis. Hovercraft development. In *Proceedings of the 1st International Conference on High Performance Marine Vehicles*, pages ACV1–ACV38, 1992.

S. J. Liapis and R. F. Beck. Seakeeping computations using time-domain analysis. In *Proceedings of the 4th International Conference on Numerical Ship Hydromechanics*, pages 34–54, 1985.

W. M. Lin and D. K. P. Yue. Numerical solutions for large-amplitude ship motions in the time domain. In *Proceedings of the 18th Symposium on Naval Hydromechanics*, pages 41–65, Ann Arbor, 1990.

W. M. Lin, J. N. Newman, and D. K. P. Yue. Nonlinear forced motions of floating bodies. In *Proceedings of the 15th Symposium on Naval Hydromechanics*, pages 33–49, 1984.

A. R. J. M. Lloyd. *Seakeeping: Ship behaviour in rough weather*. Ellis Horwood Limited, Chichester, UK, 1989.

M. S. Longuet-Higgins. On the statistical distribution of the heights of sea waves. *Journal of Marine Research*, 11: 245–246, 1952.

M. S. Longuet-Higgins. On the distribution of the heights of sea waves: Some effects of nonlinearity and finite bandwidth. *Journal of Geophysiscal Research*, 85:1519–1523, 1980.

M. S. Longuet-Higgins and E. D. Cokelet. The deformation of steep waves on water I - A numerical method of computation. In *Proceedings Royal Society London*, volume A350, pages 1–26, 1976.

K. J. Maki, L. J. Doctors, R. F. Beck, and A. W. Troesch. Transom-stern flow for high speed craft. In *Proceedings of the 8th International Conference on Fast Sea Transportation*, St. Petersburg, Russia, 2005a.

K. J. Maki, A. W. Troesch, and R. F. Beck. Qualitative investigation of transom stern flow ventilation. In *Proceedings of the 20th International Workshop on Water Waves and Floating Bodies*, 2005b.

M. Martin. Theoretical prediction of motions of high speed planing boats in waves. *Journal of Ship Research*, 22 (3):140–169, September 1978.

A. Matsuda, H. Hashimoto, and N. Umeda. Capsizing due to bow-diving in following waves. *International Shipbuilding Progress*, 51:121–133, 2004.

J. L. Meriam and L. G. Kraige. *Dynamics*. John Wiley and Sons, 4th edition, 1998.

J. R. Meyer and J. R. Wilkens Jr. Hydrofoil development and applications. In *Proceedings of the 1st International Conference on High Performance Marine Vehicles*, pages HF1–HF24, 1992.

D. E. Nakos, D. C. Kring, and P. D. Sclavounos. Rankine panel methods for transient free surface flows. In *Proceesings of the 6th International Conference on Numerical Ship Hydrodynamics*, pages 613–632, Iowa City, IA., 1993.

NATO STANAG. *Common procedures for seakeeping in the ship design process*. STANAG 4154, 1997.

J. N. Newman. The theory of ship motions. *Advances in Applied Mechanics*, vol. 18:pp. 221–283, 1978.

J. N. Newman. Double-precision evaluation of the oscillatory source potential. *Journal of Ship Research*, 28: 151–154, 1984.

J. N. Newman. The evaluation of free-surface Green's functions. In *Proceedings of the 4th International Conference on Numerical Ship Hydrodynamics*, pages 4–19, 1985.

J. N. Newman. *Wave Asymptotics*, chapter The approximation of free-surface Green's functions, pages 107–135. Cambridge University Press, 1992.

F. Noblesse. The green function in the theory of radiation and diffraction of regular waves by a body. *Journal of Engineering Mathematics*, 16:137–169, 1982.

NORDFORSK. *Seakeeping performance of ships, assessment of a ship performance in a seaway*. Nordic Cooperative Organization for Applied Research, 1987.

M. K. Ochi. On prediction of extreme values. *Journal of Ship Research*, 17(1):29–37, 1973.

T. F. Ogilvie. Nonlinear high-froude-number free-surface problems. *Journal of Engineering Mathematics*, 1(3): 215–235, 1967.

T. F. Ogilvie and E. O. Tuck. A rational strip theory of ship motions: Part I. Technical Report 013, Department of Naval Architecture and Marine Engineering, University of Michigan, 1969.

J. Ooms and J. A. Keuning. Comparative full scale trails of two fast rescue vessels. In *Proceedings of the RINA International Conference on Surveillance, Pilot and Rescue Craft for the 21st Century*, pages S&T 13–25, 1997.

A. J. Oving. Resistance prediction method for semi-planing catamarans with symmetrical demi-hulls. Technical report, Maritime Research Institute Netherlands (Marin), 1985.

J. Pawlowski. A nonlinear theory of ship motions in waves. In *Proceedings of the 19th Symposium on Naval Hydromechanics*, pages 33–58, 1992.

H. C. Raven. *A solution method for the nonlinear ship wave resistance problem*. PhD dissertation, Delft University of Technology, 1996.

H. C. Raven. Inviscid calculations of ship wavemaking — capabilities, limitations and prospects. In *Proceedings of the 24th Symposium on Naval Hydromechanics*, Washington, D.C., 1998.

A. Reed, J. Telste, and C. Scragg. Analysis of transom stern flows. In *Proceedings of the 18th Symposium on Naval Hydrodynamics*, pages 207–219, 1991.

N. Salvesen, E. O. Tuck, and O. M. Faltinsen. Ship motions and sea loads. *Transactions Society of Naval Architects and Marine Engineers*, 78:250–287, 1970.

H. E. Saunders, editor. *Hydrodynamics in ship design*, volume 2. Society of Naval Architects and Marine Engineers, New York, 1957.

D. Savitsky. Hydrodynamic design of planing hulls. *Marine Technology*, 1(1):71–95, 1964.

D. Savitsky. On the seakeeping of planing hulls. *Marine Technology*, 5(2):164–174, 1968.

D. Savitsky and P. W. Brown. Procedures for hydrofdynamic evaluation of planing hulls in smooth and rough water. *Marine Technology*, 13(4):381–400, 1976.

S. M. Scorpio and R. F. Beck. Twodimensional inviscid transom stern flow. In *Proceedings of the 12th International Workshop on Water Waves and Floating Bodies*, Carry le Rouet, France, 1997.

R. Sheinberg, C. Cleary, K. Stambaugh, and J. A. Keuning. Design development and evaluation of affordable high speed naval vessel for offshore service. In *Proceedings of the 9th International Conference on Fast Sea Transportation*, 2007.

W. Sottorf. Experiments with planing surfaces. Technical Report 661, NACA, 1932.

K. J. Spyrou. *Contemporary Ideas on Ship Stability*, chapter Geometrical aspects of the broaching-to instability, pages 47–68. Elsevier, 2000.

B. Starke, H. C. Raven, and A. van der Ploeg. Computation of transom-stern flows using a steady free-surface fitting RANS method. In *Proceedings of the 9th International Conference on Numerical Ship Hydromechanics*, Ann Arbor, Michigan, 2007.

M. St.Denis and W. J. Pierson. On the motions of ships in confused seas. *Transactions Society of Naval Architectures and Marine Engineers*, vol. 61:280–357, 1953.

K. Stewartson. A note on lifting line theory. *Quarterly Journal of Mechanics and Applied Mathematics*, 13:49–56, 1960.

F. Tasai. On the damping force and added mass of ships heaving and pitching. Technical report, Research Institute for Applied Mechanics, Kyushu University, 1959.

B. N. Taylor and C. E. Kuyatt. Guidelines for evaluating and expressing the uncertainty of NIST measurement results. Technical Note 1297, National Institute of Standards and Technology, Gaithersburg, USA, 1993.

A. Thompson. *Boat*. U.S. Patent No. 6116180, 2000.

E. F. Thompson. Results from CERC wave measurement program. In *Proceedings of the International Symposium on Ocean Wave Measurement and Analysis*, New Orleans, USA, September 1974. Am. Soc. Civ. Eng.

R. Timman and J. N. Newman. The coupled damping coefficients of a symmetric ship. *Journal of Ship Research*, 5 (4):1–7, 1962.

R. L. Trillo. High speed over water, ideas from the past, the present and the future. In *Proceedings of the 1st International Conference on Fast Sea Transportation*, 1991.

J. Tuitman. *Hydro-elastic response of ship structures to slamming induced whipping*. PhD thesis, Delft University of Technology, 2010.

M. P. Tulin. The theory of slender surfaces planing at high speeds. *Schiffstechnik*, 4:125–133, 1957.

M. P. Tulin and C. C. Hsu. Theory of high-speed displacement ship with transom sterns. *Journal of Ship Research*, 30, 1986.

N. Umeda. *Contemporary Ideas on Ship Stability*, chapter Effects of some seakeeping/manoeuvring aspects on broaching in quartering seas, pages 423–433. Elsevier, 2000.

F. Ursell. On the vertical added mass and damping of floating bodies at zero speed ahead. In *Proceedings of the Symposium of Ships in Seaway*, 1957.

J.-M. Vanden-Broeck. Nonlinear stern waves. *Journal of Fluid Mechanics*, 96(3):603–611, 1980.

R. van 't Veer. *Behavior of Catamarans in Waves*. PhD thesis, Delft University of Technology, 1998.

W. S. Vorus. A flat cylinder theory for vessel impact and steady planing resistance. *Journal of Ship Research*, 40(2): 86–106, June 1996.

J. H. Vugts. *The hydrodynamic forces and ship motions in waves*. PhD thesis, Delft University of Technology, Shipbuilding Laboratory, 1970.

H. Wagner. Uber Stoss und Gleitvorgange an der Oberfläche von Flüssigkeiten. *Zeitschrifft für Angewandete Mathematik und Mechanik*, 12(4), 1932.

M. K. Wagner and P. Andersen. Effects of geometry on the steady performance of planing hulls. *Ship Technology Research*, 50(2):91–100, 2003.

F. van Walree. *Computational methods for hydrofoil craft in steady and unsteady flow*. PhD thesis, Delft University of Technology, 1999.

F. van Walree. Development, validation and application of a time domain seakeeping method for high speed craft with a ride control system. In *Proceedings of the 24th Symposium on Naval Hydrodynamics*, pages 475–490, July 2002.

F. van Walree and N. F. A. J. Carette. Validation of time domain seakeeping codes for a destroyer hull form operating in steep stern-quartering seas. In *Proceedings of the ITTC Workshop on Seakeeping*, Seoul, Korea, October 2010.

F. van Walree and P. de Jong. Time domain simulations of the behaviour of fast ships in oblique seas. In *Proceedings of the 10th International Ship Stability Workshop*, pages 1–9, 2008.

F. van Walree and P. de Jong. Validation of a time-domain panel code for high speed craft operating in stern quartering seas. In *Proceedings of the 11th International Conference on Fast Sea Transportation*, Hawaii, USA, 2011.

J. V. Wehausen and E. V. Laitone. Surface waves. In *Handbook of Physics*, volume 9. 1960.

M. B. Wilson. Experimental determination of low Froude number hydrofoil performance in calm water and in regular waves. In *Proceedings of the 20th American Towing Tank Conference*, pages 517–574, Hoboken, New Jersey, USA, 1983.

E. E. Zarnick. *A nonlinear mathematical model of motions of planing boats in regular head waves*. Report 78-032, DTNSRDC, March 1978.

R. Zhao and O. M. Faltinsen. Water entry of two-dimensional bodies. *Journal of Fluid Mechanics*, 246:593–612, 1993.

R. Zhao, O. M. Faltinsen, J. R. Krokstad, and V. Aanesland. Wave-current interaction effects on large-volume structures. In *Proceedings of the 5th International Conference on Behaviours of Offshore Structures*, 1988.

R. Zhao, O. M. Faltinsen, and J. V. Aarsnes. Water entry of arbitrary two-dimensional sections with and without flow separation. In *Proceedings of the 21st Symposium on Naval Hydrodynamics*, 1996.

Summary

Seakeeping Behaviour of High Speed Ships

An experimental and numerical study

In recent years, great progress has been made in both the optimisation of the seakeeping behaviour of fast ships and the development of efficient numerical methods for computation of the seakeeping behaviour of ships in general. The study presented in the thesis aims to integrate both developments. First, the key aspects of the seakeeping behaviour of fast vessels are identified, as well as their influence on the operability of these vessels. Subsequently, a numerical approach is developed that is specifically aimed at the seakeeping of fast vessels.

The first step considers an emperical study aimed at qualifying and where possible quantifying the seakeeping behaviour of fast ships both at model scale and at full scale. This study is founded both on liturature and on experimental experience. The second step consideres the formulation, verification, and validation of the numerical method. For validation use is made of the experimental data obtained during the emperical research.

First full scale tests are examined. These tests were performed in order to increase understanding of the seakeeping behaviour of these vessels and to formulate limiting criteria for the operation of these ships at sea. Data has been gathered on several types of fast ships during normal operation and is supplemented with crew interviews. The main observation from these experiments is that the crews reacted to large peaks occurring in the vertical acceleration level, mainly by means of voluntary speed reduction, rather than to averages or significant values of the motions and the acceleration levels. These peaks may cause fatigue and motion sickness to crew and passengers as well as structural damage, either immediate or in the long term by material fatigue.

Besides the occurrence of peaks in the vertical acceleration two more problem areas can be identified. The first problem area is the tendency to bow-dive and broach in stern-quartering and following seas. The second problem area is the occurrence of deck wetness and the shipping of green water that may cause damage to equipment on deck and the superstructure as well as impair the view of the crew. It is found that quantification of threshold values exists only for peak levels of the vertical accelerations. For the other phenomena no specific measurements and associated verifiable limits are defined in order to be able to evaluate criteria.

Next, model experiments are considered, consisting of the hydromechanical comparison of three design concepts a patrol boat for offshore service. The acceleration levels, in particular the occurrence of peaks, in head waves are shown to be non-linear with respect to the wave height. This non-linear behaviour invalidates the usage of linear analysis tools and the Rayleigh plot is introduced as an alternative approach to quantify the degree of non-linearity and the occurrence of peaks.

Using the lessons learned during the emperical study, a computational method for the seakeeping analysis of fast ships is formulated. The chosen approach results in a simulation method that is partly non-linear with respect to the ship's motions. Use is made of a time-domain Green function to include the free surface effects in a linearised fashion. Although theoretically not necessary, it is chosen to linearise the body boundary condition to improve the computational efficiency of the method. At the same time, the actual body position and orientation is retained in the calculation of the hydrostatic pressures and the incident wave pressure.

A number of extensions to the basic code are proposed in the thesis. These extensions include a transom flow condition to force the flow to leave the transom stern smoothly at high ship speeds, a time-dependent infinite frequency added mass, and a pressure evaluation method that uses the computed free surface deformation to adapt the hydrodynamic pressures.

A verification study is described in the thesis to investigate the correct implementation of the numerical solution, followed by validation of the method by means of application of the method to simple problems. The implementation of the transom flow condition shows a modest improvement over a simple empirical near-transom pressure correction method and a significant improvement over the computational method without transom flow model. Nevertheless, an unresolved grid dependence exists in the transom flow condition. A number of methods are investigated to deal with numerical difficulties in the free surface evaluation.

The validation study in chapter 5 of this thesis is limited to trim and sinkage in calm water and the motions and vertical acceleration levels in regular and irregular head waves. First comparisons of computed and experimental results in regular head waves are performed to obtain optimal parameter settings and program options. Next, simulations and comparisons are performed in irregular head seas. The comparisons show that the basic form of the method results in over-estimated motion responses. In its current state, no peaks in the vertical acceleration associated with the impact of the bow in the water surface are predicted by the computational method.

Of the proposed extensions the time-dependent added mass significantly improves the motion predictions, resulting in a satisfactory agreement between experiments and computations. Also the transom flow condition performs reasonably well and yields comparable results to an empirical near-transom pressure correction. The adaptation of the hydrodynamic pressures to the free surface deformation and rigid body motions, especially pressure stretching, severely impaires the predicted motions and causes too extreme responses.

In conclusion, both an experimental and a numerical study into the seakeeping behaviour of fast vessels is performed in this thesis. The experimental study results in the identification of the key aspects of the seakeeping behaviour of fast vessels, particularily the occurrence of large peaks in the vertical accelerations in head seas, and broaching and bow-diving in stern-quartering and following seas. Explicit limits have been formulated for the acceleration levels in head seas, however there are no clear criteria for the other aspects.

The computational method developed in this thesis can satisfactory predict the motion responses in head waves of the two tested high speed design concepts, particularily when used with a time-dependent added mass formulation and a transom pressure condition. It does, however, still lack in the prediction of peaks in the vertical accelerations due to impact of the fore body in the water surface, a phenomenon that frequently occurs when sailing at

high speeds in (head) waves and is the limiting factor for the operability and safety of fast ships.

To improve the method, the computational method can be expanded upon by approaches specifically targeted at slamming. Such approaches would complement the already satisfactory (non-linear) rigid body motions predicted by the seakeeping simulations. Other proposed future work includes the extension of the validation. This could for instance be achieved by including more general wave headings and by moving to direct time trace comparison. Additionally, solving the numerical problems of the transom flow condition and the improvement of the computational efficiency are areas where improvement could be achieved. The latter could enable efficient and more accurate body-exact simulations.

Samenvatting

Zeegangsgedrag van Snelle Schepen

Een experimentele en numerieke studie

De afgelopen jaren is grote vooruitgang geboekt in zowel de optimalisatie van het zeegangsgedrag van snelle schepen als de ontwikkeling van efficiënte numerieke methoden voor de berekening van het zeegangsgedrag van schepen in het algemeen. Het onderzoek dat wordt beschreven in dit proefschrift heeft tot doel om deze beide ontwikkelingen te integreren. Eerst worden de belangrijkste aspecten van het zeegangsgedrag van snelle schepen geïdentificeerd, alsmede de invloed van deze aspecten op de inzetbaarheid van deze schepen. Vervolgens wordt een numerieke aanpak ontwikkeld die specifiek gericht op het zeegangsgedrag van snelle schepen.

De eerste stap omvat een empirisch literatuurstudie en een experimenteel onderzoek gericht op kwalificatie en waar mogelijk kwantificering van het zeegangsgedrag van snelle schepen op zowel modelschaal als ware grootte. Dit onderzoek is zowel op de literatuur als op experimentele resultaten gebaseerd. De tweede stap omvat de formulering, verificatie en validatie van de numerieke methode. Voor de validatie wordt gebruik gemaakt van de experimentele data verkregen tijdens het empierische onderzoek.

Eerst worden ware grootte metingen beschouwd. Deze metingen zijn uitgevoerd om het begrip van het zeegangsgedrag van deze schepen te vergroten en voor het formuleren van limietwaarden voor de inzet van deze schepen op zee. Data is verzameld op een aantal verschillende typen snelle schepen gedurende de normale operatie en is aangevuld met interviews met de bemanningen van deze schepen. De belangrijkste observering die op basis van deze experimenten kan worden gemaakt, is dat de bemanningen reageren op het optreden van grote pieken in de verticale versnelling, voornamelijk door middel van vrijwillige snelheidsreductie, in plaats van op gemiddelden of significante waarden van de bewegings- en versnellingsniveaus. Deze versnellingspieken kunnen vermoeidheid en bewegingsziekte veroorzaken bij bemanning en passagiers en daarmee de inzetbaarheid beïnvloeden. Tevens kan structurele schade ontstaan, zowel direct als op de lange termijn door materiaal vermoeiing.

Naast het optreden van versnellingspieken kunnen nog twee probleemgebieden worden aangeduid. In de eerste plaats het optreden van ‘bow-diving’ en ‘broaching’ in (schuin) achterinkomende golven. In de tweede plaats het overnemen van (groen) water, dat schade aan de apparatuur op het dek en de bovenbouw kan overoorzaken en het zicht van de bemanning kan verminderen. Het blijkt dat er alleem kwantificering van limietwaarden bestaat voor de piekwaarden van de verticale versnellingen. Voor de andere verschijnselen zijn geen specifieke metingen en bijbehorende controleerbare limieten gedefinieerd om criteria te kunnen evalueren.

Vervolgens worden model experimenten beschouwd, bestaande uit de hydromechanische vergelijking van drie concepten voor een patrouilleschip voor zeedienst. De versnellingsniveaus in kopgolven, met name de piekniveaus, blijken niet-lineair te zijn met betrekking tot de golfhoogte. Dit niet-lineaire gedrag verhindert het gebruik van lineaire analyse-instrumenten en de Rayleigh plot wordt geïntroduceerd als een alternatieve manier om de mate van niet-lineariteit en het optreden van de pieken te kwantificeren.

Gebruikmakend van de lessen geleerd gedurende de empirische studie, wordt er een rekenmethode voor de zeegangsanalyse van snelle schepen geformuleerd. De gekozen aanpak resulteert in een simulatiemethode die semi-niet-lineair is met betrekking tot de scheepsbewegingen. Er wordt gebruik gemaakt van een tijdsdomein Green functie om de vrijvloeistofoppervlak-effecten gelineariseerd mee te nemen. Hoewel theoretisch niet nodig, is gekozen voor linearisatie van de lichaamsrandvoorwaarde om de computationele efficiëntie van de methode te verbeteren. Echter, de werkelijke lichaamspositie en -orientatie wordt behouden bij de berekening van de hydrostatische druk en de ongestoorde golfdruk,

Een aantal uitbreidingen van de basiscode worden voorgesteld in dit proefschrift. Deze omvatten een afstroomvoorwaarde om de stroming vloeiend te laten afstromen van de spiegel bij hoge scheepssnelheden, een tijdsafhankelijke oneindige frequentie toegevoegde massa en een drukevaluatiemethode die de berekende vrij vloeistofoppervlak vervorming gebruikt om de hydrodynamische drukken aan te passen.

Een verificatiestudie wordt beschreven in dit proefschrift om de correcte implementatie van de numerieke methode te onderzoeken, gevolgd door validatie van de methode door deze toe te passen op relatief eenvoudige problemen. De uitvoering van de afstroomvoorwaarde aan de spiegel toont een bescheiden verbetering ten opzichte van een eenvoudige empirische drukcorrectie methode en een aanzienlijke verbetering ten opzichte van de oorspronkelijke methode zonder afstroomvoorwaarde. Niettemin blijkt er een onopgeloste gridafhankelijkheid in de afstroomvoorwaarde te bestaan. Een aantal methoden worden onderzocht om numerieke problemen in de vrijvloeistofoppervlak evaluatie op te lossen.

De validatiestudie in hoofdstuk 5 van dit proefschrift is beperkt tot trim en inzinking in vlak water en de bewegingen en verticale versnellingsniveaus in regelmatige en onregelmatige kopgolven. Eerst worden vergelijkingen van berekende en experimentele resultaten in regelmatige kopgolven uitgevoerd om optimale parameterinstellingen en programmaopties te vinden. Vervolgens worden simulaties en vergelijkingen met experimenten uitgevoerd voor onregelmatige kopgolven. Deze vergelijkingen laten zien dat de basisvorm van de methode resulteert in overschatte bewegingsresponsies. Zoals verwacht, worden versnellingspieken veroorzaakt door de impact van de boeg in het wateroppervlak niet voorspeld door de rekenmethode.

Van de voorgestelde uitbreidingen van de basismethode blijkt dat de tijdsafhankelijke toegevoegde massa de bewegingspredicties aanzienlijk verbetert. Dit resulteert in een goede overeenkomst tussen experimenten en berekeningen. Ook de afstroomvoorwaarde presteert goed en levert vergelijkbare resultaten met de empirische drukcorrectie. De aanpassing van de hydrodynamische druk gebruik makend van de vervorming van het vrijvloeistofoppervlak en de actuele lichaamsorientatie, en dan vooral druk ‘stretching’, heeft een sterke negatieve invloed op de voorspelde bewegingen en resulteert in (te) extreme responsies.

Concluderend wordt zowel een experimentele en een numerieke studie naar het zeegangsgedrag van snelle schepen in dit proefschrift uitgevoerd. De experimentele studie resulteert

in de identificatie van de belangrijkste aspecten van het zeegangsgedrag snelle vaartuigen, namelijk het optreden van pieken in de verticale versnelling in kopgolven, en 'bow-diving' en 'broaching' in (schuin) achterin komende golven. Expliciete limieten zijn geformuleerd voor de versnellingsniveaus in kopgolven, echter er blijken geen duidelijke criteria geformuleerd te zijn voor de andere aspecten.

De rekenmethode die in dit proefschrift is ontwikkeld, is in staat om de bewegingsrepons met bevredigende resultaten te voorspellen, met name bij gebruik van een tijdsafhankelijke toegevoegde massa formulering en een afstroomvoorwaarde bij de spiegel. Echter, de correcte voorspelling van pieken in de verticale versnelling ontbreekt nog; een fenomeen dat frequent voorkomt wanneer er met hoge snelheid tegen de golven in wordt gevaren en een bepalende factor is voor de inzetbaarheid van snelle schepen.

Om het rekenmodel te verbeteren zou deze kunnen worden uitgebreid met methoden die specifiek gericht zijn op d berekening van de gevolgen van 'slamming'. Anderevoorgesteld toekomstige werk omvat de uitbreiding van de validatie, bijvoorbeeld door meer algemene inkomende golfrichtingen te beschouwen en door vergelijking van de gemeten en berekende tijdsreeksen. Bovendien zou verbetering kunnen worden bereikt door het oplossen van de numerieke problemen met de afstroomvoorwaarde aan de spiegel en de verbetering van de numerieke efficiëntie van de methode. Dit laatste zou efficiënte en meer accurate lichaamsexacte simulaties mogelijk kunnen maken.

Acknowledgements

First of all, I would like to express my gratitude to my supervisors René Huijsmans and Lex Keuning for their patience and guidance. They have managed to stimulate me to actually finish the thesis, a great accomplishment on its own. René's quick understanding of the finer points of the theoretical work that I carried out has contributed significantly to the quality of the thesis. Lex' enthousiasm for the field of hydrodynamics of high speed ships and of sailing yachts has been a great source of inspiration for me. His common sense and his extensive experience on the matter of ship hydromechanics are highly appreciated.

The FAST II research project was made possible by a consortium consisting of Damen Shipyards High Speed Craft Department, Damen Schelde Naval Shipbuilding, the Ministry of Defense of the Netherlands, and Maritime Research Institute Netherlands. I wish to thank the different members of the steering group for their support and the fruitful discussions during project meetings. I look forward to continue working together with you in the future.

My special thanks to Frans van Walree for his support and guidance. He was always available to answer my plentiful questions and to help me to a deeper understanding of the background of the computational method. Our cooperation has led to a good deal of papers. It has been a pleasure working together.

I would like to thank the thesis committee for their time and effort. I particularily wish to thank Prof. Martin Renilson of the University of Tasmania and Prof. Philip Wilson of the University of Southampton for their extensive and insightful comments regarding the final draft.

Many thanks to the support staff of the Shiphydromechanics Laboratory, Roel den Oude (retired), Rina Moesbergen, Hans van der Hek, Frits Sterk, Guido Visch, Michiel Katgert, Jasper den Ouden, Peter Poot, and Piet de Heer, for their ongoing support with the model tests, fixing things whenever I broke them, and their pleasant company. Piet, many thanks for your reliable secreterial support, even though you are not officially our secretary anymore.

To my officemates and lunchmates for our fruitful, but mostly cheery conversations. Alex and Evert-Jan both have managed to share an office with me for quite a while. I had many theoretical, scientific, and sometimes metaphysical discussions with Evert-Jan and Peter Wellens. It has been great to be able to share experiences and ideas on the matter of hydromechanics of high speed craft with Alex and Albert, who are also working on the field.

Thanks to Jorge Izquierdo Yerón of Universidad Politécnica de Madrid, who helped me out with the thesis during a three month stay at our laboratory. He endured a still very buggy code with grace, providing me, maybe without realising it, lots of useful feedback to debug and improve the code.

I wish to thank my parents, Jan and Elly, for their continuous encouragement and support, and the absolute faith they put in me. I am grateful to my wife, Mónica, and daughter, Isabella, for their love, patience, and support while struggling to finish the thesis. Mónica, it has been wonderful to share the experience of obtaining both our doctor's degrees. We made it.

Curriculum Vitae

Pepijn de Jong was born on January 16th in Leeuwarden, the Netherlands. He attended secondary school at the Slauerhoff College in Leeuwarden, graduating with honors in 1998. Subsequently, he commenced his study Marine Engineering at Delft University of Technology, obtaining his propedeuse with honors in 1999. After an interruption of nearly 8 months in 2001, working as a deckhand on traditional dutch sailing vessels, he completed has bachelor's degree in 2004, again with honors. This was followed by his master's degree in 2005, another time with honors, specialising in Ship Hydromechanics. His thesis was on the topic of non-linear ship motions, by performing and analysing forced oscillation experiments in the towing tank with a model of a navy frigate.

During his study, he was an active member of AEGEE, an international student association, participating in and organising several international activities. Besides this, he was active in the student speed skating association D.S.S.V. ELS and held the position of president of the board of this association in 2002-2003.

April 2005 he commenced a PhD research appointment at the section Ship Hydromechanics and Structures of the Delft University of Technology. The research project was aimed at the development of a numerical tool to evaluate the seakeeping behaviour of fast ships, and involved both experimental and numerical work. The result of this work is presented in this thesis.

During his PhD appointment he was asked to take on the role of tenure-tracked Assistant Professor (Universitair Docent) at the same section in 2007. Due to this appointment, his tasks were broadened and involved teaching ship hydromechanics and working on several smaller research projects. One of these projects was the developement of a Velocity Prediction Program for traditional dutch sailing vessels of the type skûtsje. He continues to hold the position of Assistant Professor. His main focus is the hydromechanics of fast ships.

Journal publications

P. de Jong and J.A. Keuning. 6-DOF forced oscillation tests for the evaluation of nonlinearities in the superposition of ship motions. *International Shipbuilding Progress*, 53(2):123-143, 2006

Other publications

P. de Jong and J.A. Keuning. Test with six degrees of freedom forced oscillator to investigate the non linear effects in ship motions. In *Proceedings of the 8th International Conference on Fast Sea Transportation (FAST)*, Saint Peterburg, Russia, 2005.

P. de Jong, F. van Walree, J.A. Keuning and R.H.M. Huijsmans. Evaluation of the free surface elevation in a time-domain panel method for the seakeeping of high speed ships. In *Proceedings of the 17th International on Offshore and Polar Engineering Conference (ISOPE)*, 2134-2141, Lisboa, Portugal, 2007.

P. de Jong and F. van Walree. Hydrodynamic lift in a time-domain panel method for the seakeeping of fast ships. In *Proceedings of the 6th International Conference on High-Performance Marine Vehicles (HIPER)*, 95-105, Naples, Italy, 2008.

F. van Walree and P. de Jong. Time domain simulations of the behaviour of fast ships in oblique seas. In *Proceedings of the 10th International Ship Stability Workshop (ISSW)*, Dajeon-Seoul, Korea, 2008.

P. de Jong, M. Katgert and J.A. Keuning. The development of a velocity prediction program for traditional dutch sailing vessels of the type skûtsje. In *Proceeding of the 20th International HISWA Symposium on Yacht Design and Yacht Construction*, Amsterdam, The Netherlands, 2008.

P. de Jong and F. van Walree. The development and validation of a time-domain panel method for the seakeeping of high speed ships. In *Proceedings of the 10th International Conference on Fast Sea Transportation (FAST)*, 141-153, Athens, Greece, 2009.

F. van Walree and P. de Jong. Deterministic validation of a time domain panel code for parametric roll. In *Proceedings of the 12th International Ship Stability Workshop (ISSW)*, Washington, USA, 2011

F. van Walree and P. de Jong. Validation of a time-domain panel code for high speed craft operating in stern quartering seas. In *Proceedings of the 11th International Conference on Fast Sea Transportation (FAST)*, Hawaii, USA, 2011.